Integrated chips and optical cavities for trapped ion quantum information processing

by

David R. Leibrandt

B.S.E. Engineering Physics
University of Michigan, 2004

Submitted to the Department of Physics
in partial fulfillment of the requirements for the degree of

Doctor of Philosophy in Physics

at the

MASSACHUSETTS INSTITUTE OF TECHNOLOGY

June 2009

Author .....
Department of Physics
May 20, 2009

Certified by ..
Isaac L. Chuang
Associate Professor, Departments of Physics and EECS
Thesis Supervisor

Accepted by .....
Thomas J. Greytak
Lester Wolfe Professor of Physics, Associate Department Head for Education

Integrated chips and optical cavities for trapped ion quantum information processing

by

David R. Leibrandt

Submitted to the Department of Physics
on May 20, 2009, in partial fulfillment of the
requirements for the degree of
Doctor of Philosophy in Physics

Abstract

Quantum information processing is a new and exciting field which uses quantum mechanical systems to perform information processing. At the heart of the excitement are quantum computation – which promises efficient algorithms for simulating physical systems, factoring, and searching unsorted databases – and quantum communication – which provides a provably secure communications protocol.

Trapped ions show much promise for achieving large-scale quantum information processing. Experiments thus far have demonstrated small algorithms and entanglement of two remote ions. Current work focuses on scaling to large numbers of ions for quantum computation and interconversion between trapped ions and photons for quantum communication. This thesis addresses some of the challenges facing scaling and interconversion for trapped ion quantum information processing.

The first part of the thesis describes the development of scalable, multiplexed ion trap chips for quantum computation. The ion trap chips are based on a new ion trap geometry, called the surface-electrode trap, in which all of the electrodes reside in a single plane. Three generations of surface-electrode traps are designed, fabricated, and tested – culminating with the demonstration of an ion trap chip microfabricated using standard silicon VLSI materials and processes for scalability to small trap size and large arrays of interconnected ion traps.

The second part of the thesis presents an experiment that demonstrates cavity cooling, a method of laser cooling the motional state of trapped ions without decohering the internal qubit state. Cavity cooling is demonstrated for the first time with trapped ions, and for the first time in the parameter regime where cooling to the motional ground state is possible. The measured cavity cooling dynamics are found to agree with a rate equation model without any free parameters.

The third and final part of the thesis presents a theoretical proposal for interconversion between single trapped ion qubits and single photon qubits for quantum communication. The idea is to map the state of the single ion qubit to a superradiant collective state of several ions, which then couples strongly with single photons in an optical cavity.

Thesis Supervisor: Isaac L. Chuang
Title: Associate Professor, Departments of Physics and EECS

Acknowledgments

First and foremost, I want to thank my advisor – Professor Isaac Chaung. Working with Ike has been a valuable experience, and in addition to the standard set of experimental skills he taught me a lot about the process of experimental physics – from formulating an idea, forming collaborations, and raising money to performing the experiment and presenting the results. I further want to thank him for the freedom and encouragement he gave me to work on the cavity cooling experiment, which is somewhat removed from the overall theme of experiments in his group.

I'd also like to thank the other members of my thesis committee – Professors Vladan Vuletić and Edward Farhi. Vladan in particular was very helpful in designing and debugging the cavity cooling experiment, and he taught me a lot of atomic physics along the way.

I had the pleasure of spending a few months working with Richart Slusher at Bell Labs on the design of the SMIT traps, and collaborating with him after I returned to MIT on the testing. Dick's vision and enthusiasm are inspiring.

I owe a lot to my labmates. Christopher Pearson brought me up to speed in Ike's lab while we were working together on the macroscopic ion experiment. Kenneth Brown, Robert Clark, and Jaroslaw Labaziewicz taught me how to build lasers and trap atomic ions, and collaborated with me on the atomic ion experiments described in the first part of this thesis. Along the way we had a lot of fun and became good friends. In addition, I learned a lot of what I know about electronics, both hardware and software, by studying the experimental control systems that Jarek built. Yufei Ge graciously fabricated some ion traps and phase holograms for me. Elizabeth George, in addition to being willing to try to implement an ambitious idea for an ion trap with an integrated optical fiber, convinced me to have fun outside the lab every once in a while, which was valuable for my sanity.

Finally, I want to thank the FedEx delivery person, who once delivered a package that had neither my room number nor my name in the address. Apparently shipping, like ion trapping, has an element of black magic.

This thesis is dedicated to my friends and my family, without whose support it would not have been possible.

Contents

List of Figures

List of Tables

Chapter 1

Introduction

Information processing – the storage, transmission, and manipulation of information – has been around for virtually all of recorded human history. For most of this time, the physical basis of all information processing was classical mechanics, and the information processing which took place can be called classical information processing. The power of classical information processing for computation [Chu36, Tur36] and communication [Sha48] was studied by some of the first computer scientists – Church, Turing, and Shannon – who found that any physical implementation of classical information processing can be efficiently simulated by a mathematical construction called a Turing machine. Following the discovery of quantum mechanics in the early twentieth century, however, scientists slowly realized that as classical mechanics is a limiting case of quantum mechanics, so classical information processing is a limiting case of something else – which is naturally called quantum information processing.

This started a new branch of computer science which set out to learn what advantages quantum information processing might offer over classical information processing. Deutsch defined a mathematical construction called a universal quantum computer which can efficiently simulate any physical implementation of quantum information processing, and found one example of a problem that can be solved in less computational steps on a universal quantum computer than on a Turing machine [Deu85]. While other examples have been discovered since then, the general boundary between problems that can and cannot be solved in less computational steps on a universal quantum computer than on a Turing machine has yet to be established.

Meanwhile, physicists started to think about how quantum information processing might be implemented experimentally. Several physical systems have been proposed – including quantum optics [CY95, O'B07], nuclear magnetic resonance (NMR) [GC97, VSB$^+$01], Josephson junctions [MOL$^+$99, MNAU02], neutral atoms [BCJD99, ALB$^+$07], and trapped ions [CZ95, WMI$^+$98b] – and small computations have been demonstrated. So far, however, none of these physical systems have been shown to be scalable – which for the purpose of this thesis is defined as capable of being extended to build a working, reliable quantum information processor of arbitrary size. This thesis focuses on the trapped ion implementation, and addresses several challenges associated with scaling from small demonstration experiments to quantum information processing systems of practical interest.

This chapter introduces trapped ion quantum information processing and describes the contents of this thesis. Section 1.1 gives a brief overview of quantum information processing, including a description of why it is computationally advantageous and what will be required

for a practical implementation. Section 1.2 gives a history of the trapped ion implementation, and Section 1.3 summarizes the work presented in this thesis and its context within the field of trapped ion quantum information processing. Section 1.4 outlines each of the chapters of this thesis. Finally, Sections 1.5 and 1.6 list the contributions of coworkers to and the publications resulting from this thesis.

1.1 Quantum information processing

Quantum information processing is information processing using quantum mechanical systems [NC00]. The basic unit of quantum information is the qubit, or quantum bit, which is a two-level quantum mechanical system. Unlike classical bits, whose state can be either 0 or 1, the general state of a qubit is a superposition of the states 0 and 1 and can be written $|\psi\rangle = \alpha|0\rangle + \beta|1\rangle$ where α and β are complex numbers satisfying $|\alpha|^2 + |\beta|^2 = 1$. Quantum information can be manipulated by quantum gates, which are linear transformations that act on qubits, and transmitted by quantum channels, which are communications channels that transport qubits between locations. Quantum information processing offers an advantage over classical information processing for several applications.

1.1.1 What's all the hoopla about?

The first proposed application of quantum information processing was quantum simulation [Fey82, Llo96], which is the simulation of quantum mechanical systems. Quantum mechanical systems are hard to simulate using classical information processing. Simply writing down the state of a general quantum mechanical system that consists of n two-level quantum systems requires $\mathcal{O}(2^n)$ bits, and simulating the time evolution for a time T requires $\mathcal{O}(T2^{2n})$ gates. The best classical computers are limited to $n \lesssim 100$. However, if quantum mechanical systems are used simulate other quantum mechanical systems, the computational requirements are reduced to $\mathcal{O}(n)$ qubits and $\mathcal{O}(Tn^2)$ quantum gates [Cla09]. This represents an exponential improvement over classical information processing in both the size of the required computer and the number of computational steps.

The power of quantum information processing can also be applied to general mathematical problems; this application is called quantum computation. One problem in quantum computation that has received a lot of attention is factoring [Sho94]. The best known classical algorithm for factoring is called the number field sieve, which requires $\mathcal{O}(e^{n^{1/3}(\log n)^{2/3}})$ gates to factor an n bit number [CP01]. This is computationally intractable for $n \gtrsim 1000$, and in fact the security of the RSA public key cryptography protocol used widely for secure communication over the internet depends on the difficulty of factoring large numbers. Quantum computation offers a factoring algorithm that requires only $\mathcal{O}(n^3)$ quantum gates, so a moderately sized quantum computer could be used to decrypt secure messages encoded using RSA. Another problem of practical interest for which quantum computation offers an advantage is unsorted database search [Gro96]. While the speedup offered by quantum information processing is less dramatic than for factoring – $\mathcal{O}(\sqrt{n})$ quantum gates versus $\mathcal{O}(n)$ classical gates for an n element database – this speedup has been proven in a mathematically rigorous way. Many more problems have been identified for which quantum information processing offers an advantage over classical information processing; for a comprehensive catalog see the introduction of Reference [Jor08].

It is perhaps appropriate that while quantum information processing takes away the security of RSA and some other public key cryptography protocols, it provides new protocols

for secure communication [BB84]; this application of quantum information processing is called quantum communication [BS98]. Unlike public key cryptography protocols, which all depend on the difficulty of solving particular mathematical problems for their security, quantum communication cryptography protocols depend only on the laws of physics and are provably secure.

1.1.2 DiVincenzo criteria for quantum information processing

While the promise of quantum simulation, quantum computation, and quantum communication are exciting, the experimental requirements for the implementation of quantum information processing are daunting. The primary reason is that quantum mechanical systems are extremely sensitive to noise from the environment, which causes decoherence of the quantum information. At first glance, this might seem to doom quantum information processing to the same fate as analog classical computation, which was found to lose all of its potential advantages over digital classical computation in the presence of noise. Thankfully, quantum error correction [Sho95] and quantum repeaters [BDCZ98] enable arbitrarily large-scale quantum information processing in the presence of decoherence with a constant probability of error, but they require individual quantum gates with error probabilities below what is called the fault tolerance threshold and is estimated to be between 10^{-6} [ABO08] and 10^{-2} [Kni05] (see Reference [Cro05] for a good review of quantum error correction and fault tolerance thresholds). Thus, from an experimental perspective, the problem of scaling is reduced to assembling an arbitrarily large number of qubits and performing quantum gates with an error probability below the constant fault tolerance threshold.

A more detailed list of the experimental requirements for quantum information processing was compiled by David DiVincenzo, and these requirements are called the DiVincenzo criteria. They are [DiV00]:

1. A scalable physical system with well characterized qubits
2. The ability to initialize the state of the qubits to a simple fiducial state, such as $|000\ldots\rangle$
3. Long relevant decoherence times, much longer than the gate operation time
4. A "universal" set of quantum gates
5. A qubit-specific measurement capability

These first five criteria are sufficient to implement a universal quantum computer that can be used to solve any problem in quantum simulation and quantum computation. The following two additional criteria are necessary for quantum communication.

6. The ability to interconvert stationary and flying qubits
7. The ability to faithfully transmit flying qubits between specified locations

While the DiVincenzo criteria 2 through 7 have been demonstrated (although not all in the same physical system), experiments so far are limited to 8 qubits [VSB$^+$01, LKS$^+$05, HHR$^+$05]. The challenge which must be addressed in order to build quantum information processing systems of practical interest is contained in the second word of DiVincenzo criteria 1 – the physical system must be demonstrated to be scalable.

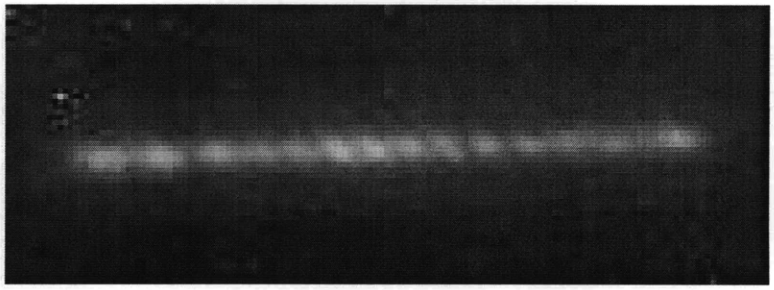

Figure 1-1: Linear Coulomb crystal of ions trapped in an RF Paul trap. Each bright spot is a single laser cooled ion. The ion spacing is roughly 30 μm.

1.2 Trapped ion implementation

Trapped ions are one of the more promising candidate physical systems for large-scale quantum information processing. Quantum information is stored in the electronic or nuclear states of trapped ions and initialization, logic gates, and readout are accomplished by laser-ion interactions. Excellent reviews of the trapped ion implementation of quantum information processing can be found in References [WMI+98b, LBMW03, HRB08].

1.2.1 Demonstration of the DiVincenzo criteria

The DiVincenzo criteria 1 through 5 for quantum computation, with the exception of scalability, have all been demonstrated with trapped ions.

Well characterized qubits are realized by laser cooled ions confined in linear RF Paul traps [WDW78] (see Figure 1-1). Several ions are confined together in a single trap, and the position of each ion is fixed by the potential of the trap and the Coulomb repulsion of the neighboring ions. Each ion holds one qubit of quantum information. The two qubit states are typically electronic or nuclear internal states, which have been very well characterized by atomic physicists for most species of atomic ions. The qubits are coupled by their shared normal modes of motion. The quantum mechanical structure of the motional modes is that of a harmonic oscillator.

Initialization of the external motional states and the internal qubit states is accomplished by sideband cooling and optical pumping [DBIW89]. The probability of success of operations in quantum computation is known as the fidelity. Experiments have achieved fidelities for sideband cooling to the motional ground state as high as 99.9% [Roo00], and fidelities for optical pumping to one of the qubit states as high as 99.991% [MSW+08].

Long decoherence times are achieved by a judicious choice of qubit states, stable local oscillators, and good magnetic field stabilization. The coherence time is fundamentally limited only by the spontaneous emission time of the qubit states, which is $\mathcal{O}(1)$ s for metastable electronic states and $\mathcal{O}(10^{15})$ s for hyperfine states. The experimental limit of the coherence time is usually set by either frequency noise of the local oscillator used to keep track of the qubit phase or magnetic field noise which causes energy shifts of the qubit states. Both of these sources of noise result in a randomization of the qubit phase. Coherence times of $\mathcal{O}(10^3)$ s have been achieved experimentally [BHI+91, FSLC97], which are much longer than typical gate times of $\mathcal{O}(10^{-5})$ s.

Quantum gates are accomplished by laser-ion interactions. Arbitrary single qubit gates and a single two qubit entangling gate are sufficient for universal quantum computation.

The original proposal for quantum computation with trapped ions was based on the two qubit Controlled-NOT (CNOT) gate [CZ95]. The CNOT gate requires that the motional modes of the ions are initialized to the ground state, and the contribution to the gate error due to imperfect ground state cooling is given by the probability of starting in a motional excited state. A few years later an alternative two qubit gate was proposed, called the geometric phase gate, which to first order is insensitive to the initial motional state [SM99]. The geometric phase gate still, however, requires near ground state cooling of the motional modes. (A higher order analysis reveals that the gate error due to imperfect ground state cooling is given by $\approx 0.3\pi^2\eta_{LD}^4 \langle n \rangle (\langle n \rangle + 1)$ where η_{LD} is the Lamb-Dicke parameter which is typically around 0.1 and $\langle n \rangle$ is the expectation value of the number of excitations in the motional mode used for the gate [SM00].) Both the CNOT and geometric phase gates have been implemented experimentally [MMK+95, SKHR+03, LDM+03], with the highest fidelity two qubit gate implementation being a geometric phase gate with a fidelity of 99.3% [BKRB08]

Finally, qubit measurement is based on the method of quantum jumps [CK85, BHIW86]. The qubit states are selected such that one but not both of the qubit states is part of a closed cycling transition, so when the cycling transition laser is applied the ion either scatters many or no photons based on the state of the qubit. The error can be made very small by counting photons for a long time, and measurement fidelities of 99.991% have been achieved experimentally [MSW+08].

The DiVincenzo criteria for quantum computation have been assembled to demonstrate simple quantum algorithms – including teleportation [RHR+04, BCS+04], unsorted database search [BHL+05], and the quantum fourier transform [CBL+05] – and quantum error correction [CLS+04]. The largest trapped ion quantum computation to date demonstrated entanglement of 8 qubits [HHR+05]. While these demonstrations represent enormous advances in trapped ion quantum information processing, they do not demonstrate scalability because the physical systems they use are not extensible to arbitrary numbers of qubits.

The DiVincenzo criteria 6 and 7 for quantum communication, on the other hand, have yet to be demonstrated with trapped ions. Trapped ions are stationary qubits because they must be kept in vacuum and it is difficult to transport them over long distances. Photons are the best flying qubits because they can be transmitted between locations through optical fibers and they move at the speed of light. Theoretical proposals for interconversion between trapped ion qubits and photonic qubits use vacuum Rabi flopping in cavity quantum electrodynamics (cavity QED) [CZKM97, Pel97]. While quantum interconnects between neutral atom qubits and photonic qubits via vacuum Rabi flopping have been demonstrated [BBM+07], and several groups are working on a trapped ion version [GKH+01, MKB+02, RBS+08, HDM+09], quantum interconnects between trapped ion qubits and photonic qubits have yet to be demonstrated.

1.2.2 Scalable architectures and challenges

The original proposal for trapped ion quantum computation, in which all of the ions are in the same trap, is not scalable to arbitrarily large numbers of qubits [CZ95]. This is because the two qubit gates rely on the ability to address one particular motional mode by frequency. As more and more ions are added to the trap, the frequency spacing between the motional modes becomes smaller and eventually it becomes impossible to perform two qubit gates. For typical experimental parameters, this limits the number of qubits to $\mathcal{O}(10)$.

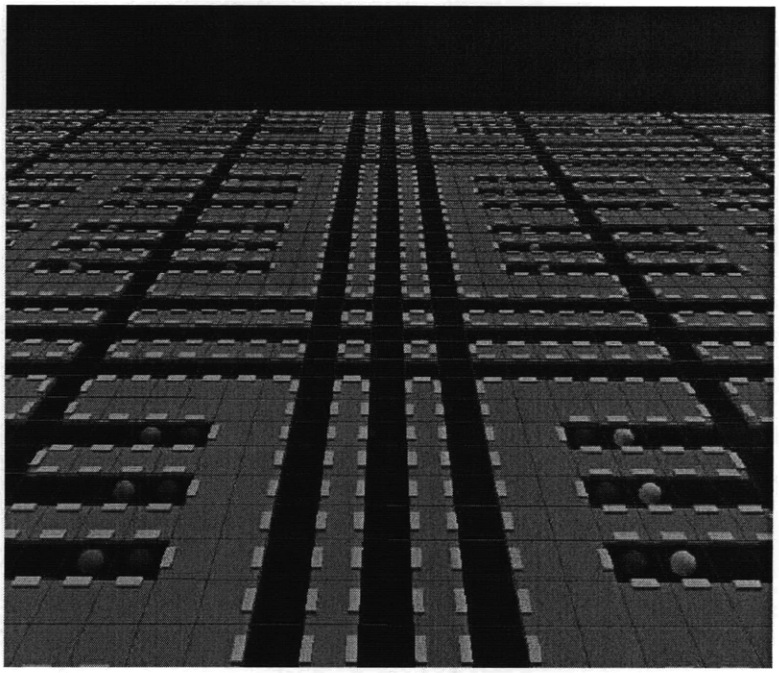

Figure 1-2: Quantum CCD architecture for trapped ion quantum computation. Ions are confined in a multiplexed array of ion traps, and can be moved between traps to perform two qubit gates between arbitrary pairs of ions. Reproduced with permission from Reference [Cro05].

One possible solution to the scaling problem is the quantum charge coupled device (QCCD) architecture for an ion trap quantum computer [WMI+98b, CZ00, KMW02] (see Figure 1-2). In the QCCD architecture, ions are confined in a multiplexed array of ion traps. Two qubit gates are performed between arbitrary pairs of ions by moving the ions into the same trap, performing the gate, and moving the ions back to their storage locations. Some progress has been made in constructing multiplexed ion trap arrays and moving ions between traps [RBKD+02, HOS+06, BVO+09], but much more work remains before large-scale trapped ion quantum computation with the QCCD architecture can be realized.

There are several challenges that need to be addressed in order for large-scale trapped ion quantum computation with the QCCD architecture to be realized [Ste07]:

- Multiplexed ion trap arrays must be designed and built in a way which is scalable to both more traps and smaller trap size. The traps must further be designed such that it is possible to move ions between traps with high success probability and low motional heating due to movement [RBKD+02, HOS+06, BVO+09]. Finally, the intrinsic rate of motional decoherence in the traps must be sufficiently low to allow high fidelity two qubit gates [WMI+98b, TKK+99, DOS+06, LGA+08, LGL+08].

- Quantum non-demolition motional cooling, which is cooling of the motional modes of the ions without decoherence of the internal qubit states, must be implemented in order to periodically recool the ions as they heat up due to either non-adiabatic ion movement or intrinsic motional decoherence [KKM+00, MW01, HMS+08].

- Control electronics and laser delivery optics must be integrated into the traps [KPM+05, KK09] (see Figure 1-3).

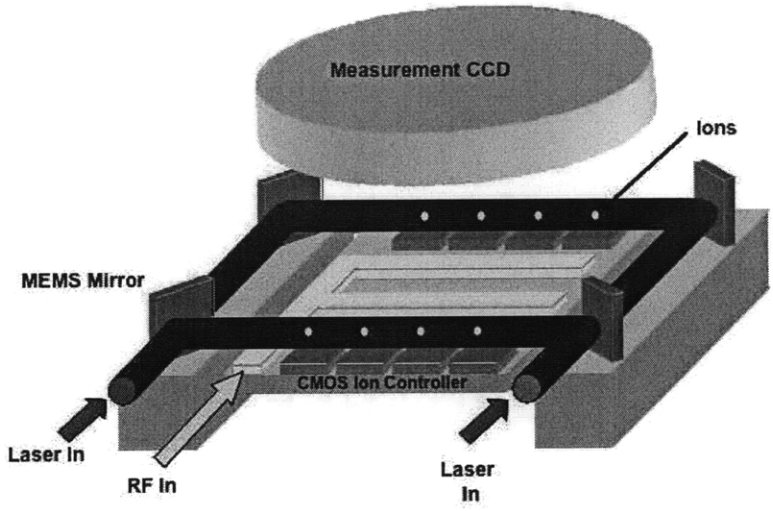

Figure 1-3: Multiplexed ion trap with integrated control electronics and laser delivery optics. Ions are confined above the ion trap chip, which is integrated with electronics that drive the ion trap electrodes and optics that deliver lasers to the trap sites. Reproduced with permission from Reference [KPM+05].

- Last but not least, and equally applicable to either the QCCD or the distributed quantum computation architecture discussed next, is that the gate errors of individual gates must be pushed below the fault tolerance threshold.

Another possible solution to the scaling problem is the distributed quantum computation architecture for an ion trap quantum computer. In this approach, small trapped ion quantum computers are connected by short range quantum communication channels to form a quantum network. The communications channels can either be optical fibers [CZKM97, Pel97, SL00, DR05, DMM+06], as was discussed for long range quantum communication, or superconducting wires [SvdWCL04, TBZ05, DLC+09], which are inherently short range. This thesis considers only optical fiber quantum communication channels.

The challenge which needs to be met in order for large-scale trapped ion quantum computation with the distributed architecture to be realized is high fidelity interconversion between trapped ion qubits and photonic qubits. Interconversion via vacuum Rabi flopping in cavity QED requires that the vacuum Rabi flopping rate, which is the rate of exchanging excitations between the ion and the cavity, is greater than the geometric mean of the spontaneous decay rates of the ion and the cavity [CZKM97, Pel97]. This is called the strong coupling regime. Reaching the strong coupling regime requires that the volume of the cavity is very small, which is difficult to achieve with trapped ions because stray electric charges on the cavity mirrors generate stray electric fields that destabilize the ion trap.

While there are no fundamental obstacles to reaching the strong coupling regime with single ions, one way to make it easier to reach the strong coupling regime is to use collective states of several ions which couple superradiantly to the cavity [Dic54]. Quantum interconnects between collective states of neutral atoms and single photons have been demonstrated [CPKK04, CMJ+05, EAM+05, STTV07], and some progress towards quantum interconnects between collective states of trapped ions and single photons has been made [HDLL+08, HDM+09]. The problem with this approach is that there are no known quantum gates which act on collective states of several ions. Thus the challenge which

needs to be addressed in order for large-scale trapped ion quantum computation with the distributed architecture to be realized is either to reach the strong coupling regime with single ions or to figure out how to perform quantum gates with collective states of several ions.

1.3 Contributions of this work

This thesis provides partial solutions to some of the challenges associated with scaling and interconversion for trapped ion quantum information processing.

1.3.1 Integrated chips

The first part of this thesis focuses on the development of scalable, multiplexed ion trap chips. The approach taken here is to develop a new ion trap geometry called the surface-electrode ion trap, in which all of the electrodes reside in a single plane. This ion trap geometry was proposed by Chiaverini et al. in 2005 [CBB+05] and first experimentally demonstrated by Pearson et al. in 2006 [PLB+06] as a part of this thesis work. The advantage of the surface-electrode geometry is that it is amenable to microfabrication and integration with control electronics and laser delivery optics [KPM+05, KK09]. This thesis proceeds to design, build, and characterize a microfabricated surface-electrode ion trap, which is scalable in a straightforward way to both more traps and smaller trap size.

Included as part of the characterization of ion trap chips is a set of measurements of the motional heating rate in several surface-electrode ion traps. Motivated by the work of Deslauriers et al. [DOS+06] the heating rates are measured with the trap electrodes at room temperature and cryogenically cooled to 6 K, and it is found that the heating rates are suppressed by several orders of magnitude by cryogenic cooling. The motional heating rates at 6 K in the scalable, microfabricated ion trap are low enough to allow two qubit gates with error probabilities below the fault tolerance threshold.

1.3.2 Optical cavities

The second and third parts of this thesis focus on the integration of ion traps with optical cavities.

The second part presents an experimental demonstration of a method of quantum non-demolition cooling. One of the motional modes of a trapped ion is cooled by cavity cooling, in which the cooling proceeds by coherent scattering of photons into an optical cavity [HHG+97, VC00, VCB01]. Because the cooling process is coherent, it is possible to use cavity cooling to cool the motional modes of trapped ions without decohering the internal qubit states. This work is the first demonstration of cavity cooling of trapped ions, and the first demonstration of cavity cooling in the regime where it is possible to cool to the motional ground state.

Finally, the third part of this thesis presents a theoretical proposal for interconversion between single ion qubits and single photon qubits via collective states of several ions. The single photon qubit is first transformed into a collective ion qubit as has been done with neutral atoms [CPKK04, CMJ+05, EAM+05, STTV07]. The new idea is to perform a gate which transforms the collective ion qubit, which interacts strongly with the cavity, into a single ion qubit, which can be used directly for quantum gates. Practical experimental parameters for a potential demonstration experiment are suggested.

It is important to note that this thesis does not address all of the challenges associated with scaling and interconversion for trapped ion quantum information processing, nor does it provide complete solutions to the challenges it does address. First it focuses exclusively on the hardware and underlying physics, and neglects the computer science issues of error correcting codes [Sho95] and computer architecture [Cro05]. Within scaling, the ion trap chips are designed with ion movement and integration of optics and electronics in mind but neither are demonstrated. A method of quantum non-demolition cooling is demonstrated, but the qubit coherence during cooling is not measured in this work. Finally, the challenge of reducing the quantum gate errors below the fault tolerance threshold is only partially addressed by the motional heating measurements; there are other contributions to the gate errors which are dominant in current experiments. Within interconversion, the challenge of performing quantum gates with collective states of several ions is addressed only in theory. Experiments will be needed to determine how well this proposal will work for quantum information processing in practice.

1.4 Outline

The remainder of this thesis is divided into three parts. The first part, about the development of scalable, multiplexed ion trap chips, is presented in Chapters 2 and 3. The second part, about the demonstration of a method of quantum non-demolition cooling, is presented in Chapters 4 and 5. The third part, about interconversion between single ion qubits and single photon qubits via collective states, is presented in Chapters 6 and 7. Figure 1-4 depicts the overall flow of this thesis. In more detail:

Chapter 2 describes the theory and development of surface-electrode ion traps. After a brief review of the theory of RF Paul traps in general, the theory of surface-electrode RF Paul traps is covered. The first experimental demonstration of a surface-electrode ion trap is presented, in which a surface-electrode ion trap is used to trap macroscopic particles. This is followed by a second demonstration experiment, in which a surface-electrode ion trap is used to trap atomic ions. Chapter 2 concludes with a description of the design and fabrication of a scalable, multiplexed ion trap chip.

Chapter 3 is about the evaluation of surface-electrode ion traps for quantum information processing. It begins by presenting the theory of the $^{88}Sr^{+}$ ion, which is used in all of the atomic ion experiments in this work, and the experimental setups used for testing surface-electrode ion traps at both room temperature and at 6 K. Three methods of loading ions into surface-electrode ion traps are explored – electron impact ionization, laser ablation, and photoionization – and photoionization is found to be best. The testing results of both the scalable, multiplexed ion trap chip described in Chapter 2 and some other microfabricated ion trap chips are presented, including measurements of the motional heating rates, and the prospects of surface-electrode ion trap chips for quantum information processing are discussed.

Chapter 4 describes the theory of cavity QED. After the well-established theory of cavity QED of a two-level ion coupled to a single mode of an optical cavity is reviewed, the experimentally relevant case of $^{88}Sr^{+}$ coupled to a cavity with two degenerate polarization modes is discussed. A master equation model is presented, and the deviations from the simple two-level theory are quantified.

Chapter 5 presents the demonstration experiment of cavity cooling, which is one possible method of quantum non-demolition cooling. It begins by describing the experimental

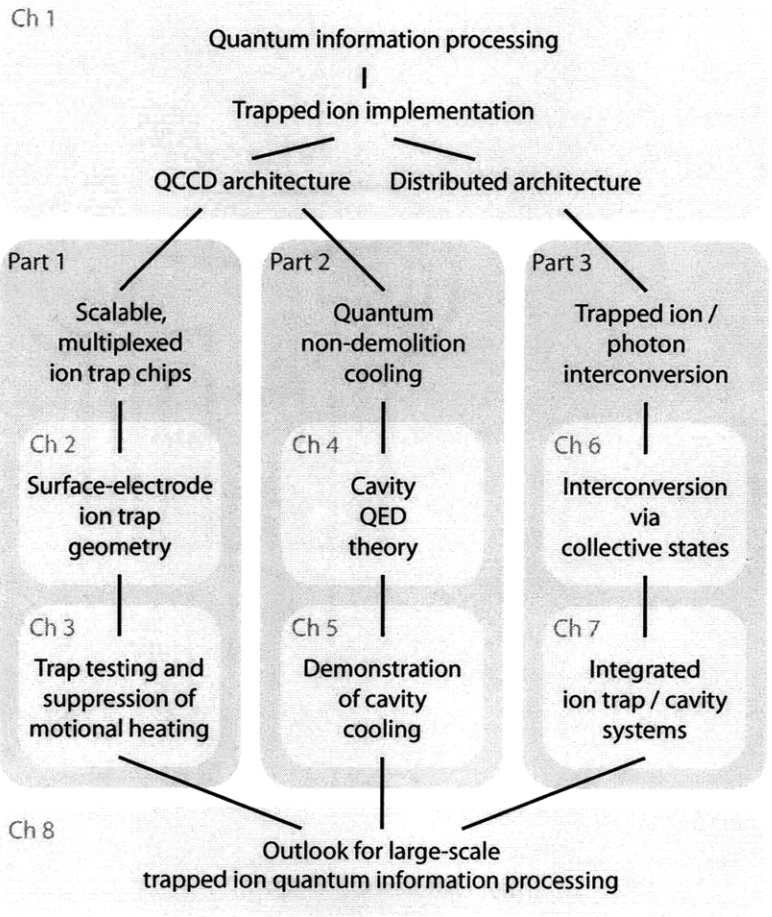

Figure 1-4: Block diagram depicting the overall flow of this thesis. Lines connecting the parts and chapters represent logical flow from the top down.

setup, including a detailed description of the design and a step-by-step procedure for the construction of the high finesse optical cavity. The coupling of the ion to the optical cavity is measured and compared with the theoretical expectation. The spectrum of photon scattering into the cavity, by which cavity cooling takes place, is presented. Finally, the dynamics of cavity cooling are measured and compared with a rate equation model. Chapter 5 concludes by discussing possible follow-up experiments which could demonstrate quantum non-demolition cooling or other interesting physics made possible by cavity cooling.

Chapter 6 is about the theoretical proposal for interconversion between single ion qubits and single photon qubits via collective states. After the procedure for mapping between single photon and collective ion states is reviewed, the new idea for mapping between collective ion states and single ion states is presented. Practical experimental parameters for a potential demonstration experiment with $^{88}Sr^{+}$ are suggested.

Chapter 7 discusses ideas for ion trap chips with integrated optical cavities. A few different geometries are presented and evaluated theoretically as candidate systems for the implementation of interconversion between single ion qubits and single photon qubits via collective states. Preliminary experimental tests of one geometry are attempted but are unsuccessful. A second geometry which looks to be both well suited for the interconversion experiment and experimentally feasible is identified.

Chapter 8 concludes this thesis with a summary of the results and their relevance to the field of trapped ion quantum information processing.

1.5 Contributions of coworkers

While most of the work presented in this thesis is my own, many coworkers contributed to the various parts.

The experimental demonstration of surface-electrode ion traps with macroscopic ions was initiated by Christopher Pearson, who took me on as an apprentice when I joined the Chuang group. Later, Christopher and I were joined by Waseem Bakr, who helped with the data collection. The experimental demonstration of surface-electrode ion traps with atomic ions was carried out primarily by Kenneth Brown, Jaroslaw Labaziewicz, and Robert Clark; my part was to do some numerical modeling of the trap. The project to build a scalable, multiplexed ion trap chip was a collaboration between myself at MIT and Richart Slusher along with many others at Alcatel-Lucent. I helped with the trap design, but the trap was built entirely by the fabrication team at Alcatel-Lucent. The trap testing was carried out by myself and Robert Clark at room temperature and myself and Jaroslaw Labaziewicz at 6 K. Jaroslaw Labaziewicz built the laser system used for most of the atomic ion experiments in this thesis, and Waseem Bakr and Paul Antohi built the cryostat used for 6 K trap testing. Yufei Ge fabricated the other surface-electrode ion traps used for motional heating rate measurements.

The cavity cooling experiment was built and operated primarily by myself, with some help from Yat Shan Au designing and building the cavity and Rhys Hiltner building some electronics. Ziliang Lin performed some calculations of the optical polarizibility of C_{60}^{+}, which we have considered cavity cooling as a follow up experiment.

The idea for mapping between single and collective ion states came out of a lunch discussion between myself and Isaac Chuang. The ideas for ion trap chips integrated with optical cavities benefited from conversations with Jaroslaw Labaziewicz, Taehyun Kim, Jungsang Kim, and Peter Herskind. The experimental test of one geometry was executed

by Elizabeth George, with help from Yufei Ge fabricating the trap and Shannon Wang attempting to trap ions.

1.6 Publications

The following is a list of publications I have coauthored during my Ph.D. studies.

1. *Experimental investigation of planar ion traps*
   C. E. Pearson, **D. R. Leibrandt**, W. S. Bakr, W. J. Mallard, K. R. Brown, and I. L. Chuang
   Phys. Rev. A **73**, 32307 (2006)

2. *Modeling ion trap thermal noise decoherence*
   D. Leibrandt, B. Yurke, and R. Slusher
   Quant. Inf. Comput. **7**, 52 (2007)

3. *Loading and characterization of a printed-circuit-board atomic ion trap*
   K. R. Brown, R. J. Clark, J. Labaziewicz, P. Richerme, **D. R. Leibrandt**, and I. L. Chuang
   Phys. Rev. A, **75**, 15401 (2007)

4. *Laser ablation loading of a surface-electrode ion trap*
   D. R. Leibrandt, R. J. Clark, J. Labaziewicz, P. Antohi, W. Bakr, K. R. Brown, and I. L. Chuang
   Phys. Rev. A **76**, 55403 (2007)

5. *Suppression of heating rates in cryogenic surface-electrode ion traps*
   J. Labaziewicz, Y. Ge, P. Antohi, **D. R. Leibrandt**, K. R. Brown, and I. L. Chuang
   Phys. Rev. Lett. **100**, 13001 (2008)

6. *Temperature dependence of electric field noise above gold surfaces*
   J. Labaziewicz, Y. Ge, **D. R. Leibrandt**, S. X. Wang, R. Shewmon, and I. L. Chuang
   Phys. Rev. Lett. **101**, 180602 (2008)

7. *Demonstration of a scalable, multiplexed ion trap for quantum information processing*
   D. R. Leibrandt, J. Labaziewicz, R. J. Clark, I. L. Chuang, R. Epstein, C. Ospelkaus, J. Wesenberg, J. Bollinger, D. Leibfried, D. Wineland, D. Stick, J. Sterk, C. Monroe, C.-S. Pai, Y. Low, R. Frahm, and R. E. Slusher
   arXiv:0904.2599 & submitted for publication

8. *Cavity sideband cooling of a single trapped ion*
   D. R. Leibrandt, J. Labaziewicz, V. Vuletić, and I. L. Chuang
   arXiv:0905.0148 & submitted for publication

Part I

Ion trap on a chip

Chapter 2

Surface-electrode ion traps

Surface-electrode ion traps, or ion chips, were first proposed by Chiaverini et al. [CBB+05] and subsequently demonstrated by several groups [PLB+06, SCR+06, BLB+06, BCL+07]. Unlike the three-dimensional and quasi two-dimensional traps used for many years in trapped ion quantum information processing, all of the electrodes lie in a single plane and the ions are trapped above the plane of the electrodes.

Surface-electrode ion traps offer several distinct advantages over three-dimensional traps for trapped ion quantum information processing. They are amenible to modern microfabrication techniques, allowing them to be scaled both to smaller trap sizes than are possible with conventionally machined three-dimensional traps and to arrays of arbitrarily large numbers of interconnected traps [BRC+04]. Microfabrication also paves the way to integration with optics [KK09] and electronics [KPM+05], which will be necessary for any truly large-scale quantum information processor. Finally, it is much easier to cryogenically cool surface-electrode ion traps for reduced ion heating rates [DOS+06, LGA+08, LGL+08] and for possible coupling to superconducting detection circuits [BPR+99] or qubits [TRBZ04, TBZ05].

This chapter describes the theory and development of surface-electrode ion traps. Section 2.1 presents the well known theory of three-dimensional ion traps, and Section 2.2 specializes to describe the theory of surface-electrode traps. Section 2.3 presents two proof-of-concept demonstration experiments where simple, non-microfabricated surface-electrode traps are used to trap macroscopic and atomic ions. Finally, Section 2.4 presents the design and fabrication of a scalable, multiplexed surface-electrode trap which is microfabricated on a silicon substrate using standard VLSI techniques.

Sections 2.1 and 2.2 are a review of previous work, while Sections 2.3 and 2.4 are original work. Note, however, that the material in Section 2.4 was done in collaboration with the ion trap foundry program at Alcatel-Lucent, headed by Richart Slusher.

2.1 Ion trap theory

The ion traps used for quantum information processing are called linear RF Paul traps. Because Earnshaw's theorem prevents the use of static electric fields for trapping ions, a combination of static and RF electric fields are applied which combine to form a dynamically stable trap for charged particles. The dynamics of an ion in a linear RF Paul trap are determined by solving the classical equations of motion to obtain an effective, time-independent three-dimensional harmonic oscillator potential called the secular potential. The quantized motion of the ion is that of a three-dimensional quantum harmonic oscillator

with motional frequencies given by the classical calculation. Note that the theory of ion traps has been well covered by many references [Deh67, Pau90, Gho95, WMI+98b, Lab08], so this treatment will omit derivations.

2.1.1 Mathieu equations

The standard linear RF Paul trap has hyperbolic electrodes defined by

$$\frac{x^2 - y^2}{r_0^2} = \pm 1 \tag{2.1}$$

and shown in Figure 2-1. Two of the electrodes are biased at an RF potential $V\cos(\Omega t)$ and the other two are biased at a DC potential U, such that the electric potential in the center of the electrodes is

$$\phi(x, y, t) = \frac{x^2 - y^2}{2r_0^2}\left(U - V\cos(\Omega t)\right) + \phi_0(t) \ . \tag{2.2}$$

The x and y equations of motion of an ion in such a potential take the form of Mathieu equations:

$$\frac{d^2x}{d\tau^2} + \left(a - 2q\cos(2\tau)\right)x = 0 \tag{2.3}$$

and

$$\frac{d^2y}{d\tau^2} - \left(a - 2q\cos(2\tau)\right)y = 0 \ . \tag{2.4}$$

Here $\tau = \Omega t/2$ is a dimensionless time, the Mathieu parameters $q = (2QV)/(mr_0^2\Omega^2)$ and $a = (4QU)/(mr_0^2\Omega^2)$ are dimensionless RF and DC voltages, and Q and m are the ion charge and mass. The motion is stable (i.e., the components of the ion position vector x and y are bounded in time) in regions of Mathieu parameter space. In particular, for $a = 0$ the motion is stable for $0 < q \leq q_{max} = 0.908$. The two-dimensional lowest order stability region is shown in Figure 2-2.

Confinement of the ion along the z direction is provided by two additional endcap electrodes (not shown in Figure 2-1) which are biased at a positive DC potential. This superimposes a weak static electric quadrupole potential

$$\phi(x, y, z) = U_{ec}\left(\frac{z^2}{r_{ec}^2} - \frac{x^2 + y^2}{2r_{ec}^2}\right) \tag{2.5}$$

on top of the stronger RF electric quadrupole potential that confines along the z axis but weakens the confinement along the x and y axes.

2.1.2 Pseudopotential approximation

In the pseudopotential approximation, where $q \ll 1$, the ion motion along axis i can be decomposed into slow, large amplitude secular motion at the secular frequency ω_i and fast, small amplitude micromotion at the RF drive frequency Ω. For an arbitrary electric potential of the form

$$\phi(x, y, z, t) = \phi_{RF}(x, y, z)\cos(\Omega t) + \phi_{DC}(x, y, z) \ , \tag{2.6}$$

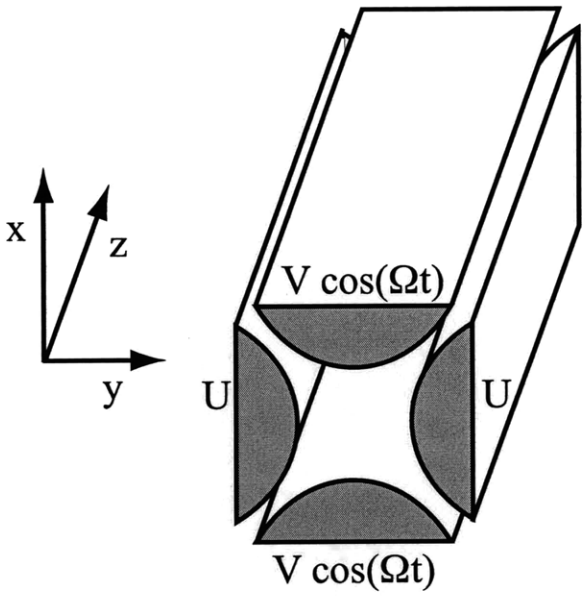

Figure 2-1: Schematic showing the geometry of a four rod linear RF Paul trap which confines a charged particle in two dimensions. The ion is confined in the center of the four electrodes, which are shaped hyperbolically and extend infinitely in the z direction. Confinement along the z direction can be added by two additional endcap electrodes (not shown) which are biased at a positive DC potential.

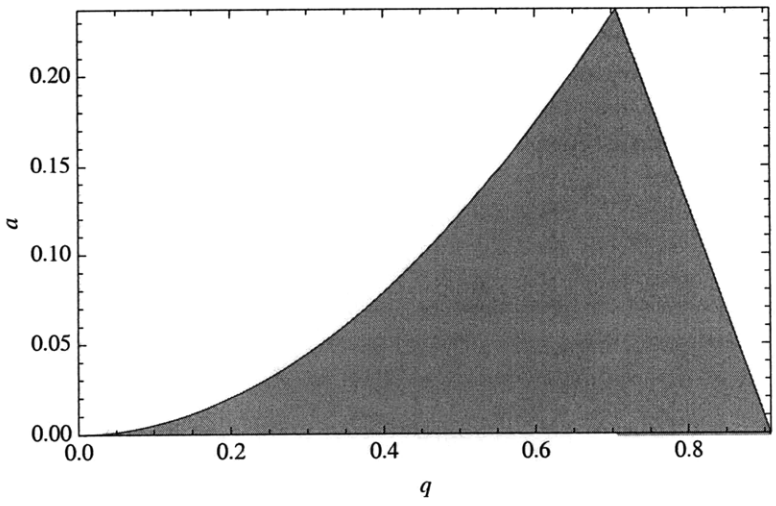

Figure 2-2: Stability region of a linear RF Paul trap in Mathieu parameter space. The region where the ion motion is stable is shaded.

the secular motion is determined by a secular potential

$$\psi_{sec}(x,y,z) = \frac{Q^2}{4m\Omega^2}|\vec{\nabla}\phi_{RF}(x,y,z)|^2 + Q\phi_{DC}(x,y,z) \ . \tag{2.7}$$

The amplitude of the micromotion to first order in q is $\frac{q}{2}|\vec{r}_{sec}|$ where $|\vec{r}_{sec}|$ is the magnitude of the secular displacement from the RF null. Since micromotion causes undesired Doppler shifts of the lasers as seen by the ion, it is important to keep the ion on the RF null.

In practice, for any given trap geometry, the trap parameters are determined by numerically calculating the shape functions $\phi_{RF}(x,y,z)$ and $\phi_{DC}(x,y,z)$ using a boundary element electrostatics solver [Cha] and using them to compute the secular potential. The ion position and orientation of the principal axes of motion, the secular frequencies ω_i, and the trap depth $\psi_{sec,0}$ (defined as the energy an ion would need to escape the secular potential) can all be extracted from the secular potential. For the four rod trap in two dimensions, the secular frequencies and trap depth are given by

$$\omega_{x,y} = \sqrt{\frac{Q^2V^2}{2m^2r_0^4\Omega^2} \mp \frac{QU}{mr_0^2}} = \sqrt{\frac{q^2}{2} \mp a}\frac{\Omega}{2} \tag{2.8}$$

and

$$\psi_{sec,0} = \frac{Q^2V^2}{4mr_0^2\Omega^2} - \frac{QU}{2} = \frac{qQV}{8} - \frac{QU}{2} \ . \tag{2.9}$$

2.2 Surface-electrode geometry

The two-dimensional electric quadrupole potential required for a linear RF Paul trap can also be produced by a set of electrodes which all lie in a single plane [CBB+05]. This ion trap geometry is called a surface-electrode ion trap, and one example is shown in Figure 2-3.

One of the disadvantages of surface-electrode ion traps is that, assuming the electrodes are not transparent, the lasers are constrained to be in the xz plane. It is important to note that with the five electrode surface-electrode ion trap geometry used in this work, if the electrode widths and DC voltages are symmetric with respect to reflections across the xy and yz planes, then one of the principal axes is oriented along the y axis. For laser cooling, only the principal axes which have a non-zero projection of the laser wavevector are cooled. Thus, it is important to break the symmetry either by DC voltages or by geometry.

2.3 Proof of concept

Surface-electrode ion traps were proposed in 2005 [CBB+05] and first demonstrated simultaneously by two groups in 2006 [PLB+06, SCR+06]. One of the first demonstration experiments, which is described in Section 2.3.1, used traps fabricated on printed circuit boards (PCBs) to trap macroscopic charged particles.

While macroscopic charged particles cannot be used as qubits, they can be used to help determine the suitability of surface-electrode ion traps for quantum information processing. First, the difficulty of loading surface-electrode traps (which have trap depths that are only of order 1% that of similarly sized four rod traps) can be tested and loading methods can

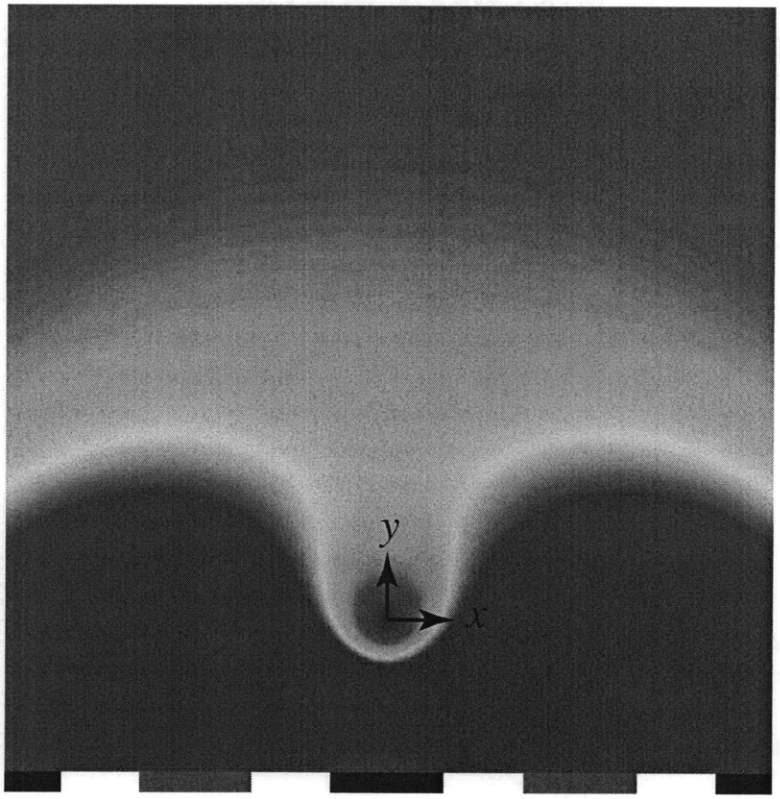

Figure 2-3: Schematic of a surface-electrode ion trap. The ion trap electrodes are shown at the bottom of the figure in red (RF) and black (DC). Ions are trapped at the origin of the coordinate system shown. The secular potential is plotted on a linear color scale as a function of x and y, with blue representing the lowest and red representing the highest secular potential values. Secular potential values higher than twice the trap depth are truncated for clarity. The DC electrodes can be segmented to provide confinement in the z direction. Additionally, the RF electrodes can be made unequal width in order to tilt the principal axes for efficient laser cooling of the y mode of motion.

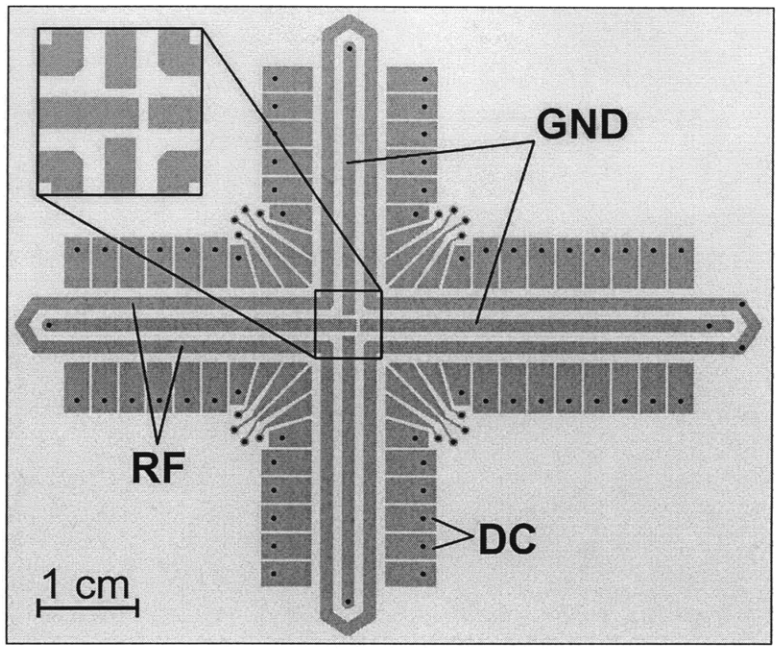

Figure 2-4: Layout of the PCB surface-electrode ion trap used to trap macroscopic charged particles. Ions can be moved between the different arms of the trap by biasing the finely segmented DC electrodes on the outside of the RF electrodes. Opposing electrodes in straight sections of the trap are electrically connected, but near the intersection all the outer and center electrodes are electrically independent for finer control. Electrical connections are made via surface mount headers on the underside. The RF loop at each end helps prevent ions from leaking out axially.

be developed. Second, the ion movement operations required to implement the Kielpinski et al. [KMW02] ion trap quantum computer architecture can be demonstrated and control waveforms worked out. These challenges are both addressed by the experimental demonstration with macroscopic charged particles presented in Section 2.3.1.

Further challenges that must be addressed in order to determine the suitability of surface-electrode ion traps for quantum information processing are that optical access for laser cooling is blocked along the axis orthogonal to the trap substrate, and that ion heating is enhanced by the close proximity of the trap electrodes. These challenges are addressed in Section 2.3.2, which describes a second demonstration experiment in which a PCB surface-electrode ion trap is used to trap atomic ions, and in Chapter 3.

2.3.1 Macroscopic ions

The PCB ion trap used for trapping macroscopic charged particles is shown in Figure 2-4 [PLB+06]. It consists of four branches, identical in cross section to the trap shown in Figure 2-3, which meet in a cross intersection. Ions can be trapped in any of the individual trap regions defined by the segmented outer DC control electrodes, and they can be moved between trap regions and through the cross intersection by varying the DC potentials on the control electrodes. The electrodes are tin coated copper, and the substrate is GML-1000 (a microwave laminate). The three middle electrodes are all 1.27 mm wide, the electrode spacing is 0.89 mm, and the outer control electrodes are 2.5 mm long.

Electrospray ionization (ESI) provides ions to the trap. This technique, commonly used with linear quadrupole filters for mass spectroscopy, applies high voltage to a liquid solution containing the particles to be ionized at a sharp tip. Strong electric fields at the tip blow off fine droplets of solution, and as solvent evaporates from these charged droplets, self-repulsion breaks them up into smaller particles, eventually producing individual charged solute particles. Following Reference [CPK+02], a 5% suspension of 0.44 μm diameter aminopolystyrene spheres is mixed with a 4:1 mixture of methanol and a solution buffered to pH = 3.9, to produce a 0.05% suspension of microspheres. The suspension is placed in a hermetically sealed bottle and pressurized to 50-100 kPa. This forces the liquid through a 0.45 μm filter used to block any clusters of microspheres and out the electrospray tip. The tip itself is made from fused silica capillary tubing, which is heated, stretched to produce a neck, and cleaved to produce a 100 μm opening. A potential of 4 kV is applied directly to the liquid with a copper wire inserted in the fluid near the tip. The mean charge-to-mass ratio of the resulting trapped ions is 1.17×10^{-8} e/amu (electron charges per nucleon mass).

Before 0.44 μm diameter aminopolystyrene spheres were settled on as the macroscopic ion of choice, other ion species were tested. The first ions to be trapped were dextran and TMR-dextran (dextran functionalized by tetramethylrhodamine, which is fluorescent). Both molecules have a molecular weight of $\sim 10^4$ amu, but they were found to clump into large particles such that each ion was made up of many dextran molecules. This resulted in a large variance in the size of the ions. The 0.44 μm diameter aminopolystyrene spheres, on the other hand, were trapped individually. Later, 0.045 μm diameter carboxyl-polystyrene spheres were trapped. These were more difficult to work with experimentally because they scattered less imaging light.

Because surface-electrode traps have such a small trap depth, direct loading from the electrospray plume into the PCB trap is very inefficient. To solve this problem, ions are first loaded into a four rod trap and then transferred to the PCB trap. The DC electrodes of the four rod trap are not segmented, but Coulomb repulsion of the ions in the four rod trap is sufficient to push them into the surface-electrode trap. Note that the four rod trap and the surface-electrode trap must be driven with the same frequency and phase RF in order for this loading scheme to work. Figure 2-5 shows the interface between the four rod trap and the surface-electrode trap. The process of transferring ions from the four rod trap to the surface-electrode trap is nearly 100% efficient.

Electrospray ionization must be performed at or near atmospheric pressure, but experiments on free trapped particles require a vacuum. To accomplish both requirements, both the four rod and surface-electrode traps are enclosed in a custom built clear acrylic box and loaded through an open flange on one side (see Figure 2-6). After loading, the flange is closed and the box is evacuated down to about 0.1 torr. This is in a regime where the ion stability is not affected by aerodynamic drag, but the speed of ion motion in shuttling experiments is significantly affected.

Also shown in Figure 2-6 is a metal plate installed above the trap to increase the trap depth and shield the trap from stray electric fields. Machined slots in this plate allow imaging of the ions from above. This slotted top plate design has the advantage of masking laser scatter, but for more complex trap topologies it might be easier to use a transparent conductor such as indium tin oxide or a thin film of gold [Gor00, GH02, SHKS01]. This could be deposited on a glass plate or directly on the vacuum window or an imaging optic inside the vacuum chamber.

Figure 2-7 shows some macroscopic ions trapped in the PCB surface-electrode trap. Ions are illuminated by a green (532 nm) laser and can be observed either by eye or with

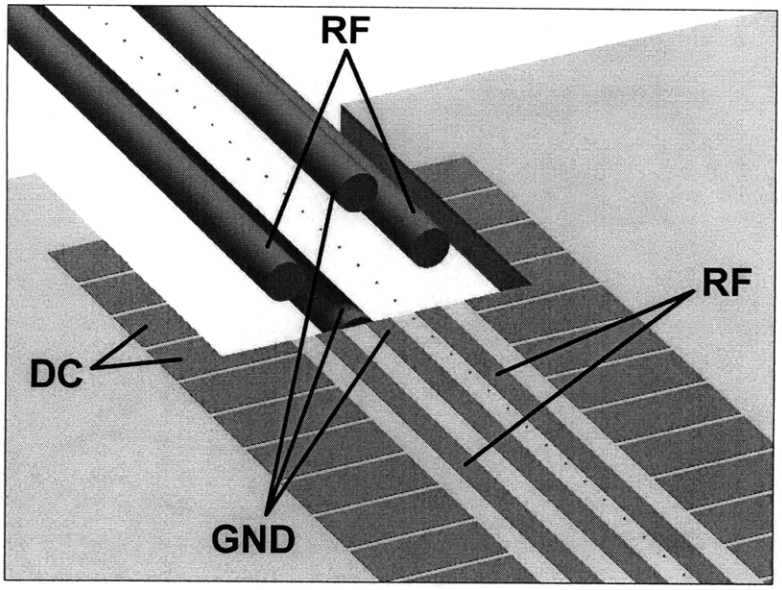

Figure 2-5: Interface between the PCB surface-electrode ion trap and the four rod ion trap used for loading. A slot cut in the surface-electrode trap allows for a common trap axis, drawn as a dotted line. The large macroscopic ions immediately form a linear Wigner crystal in the four rod trap and are pushed into the surface-electrode trap.

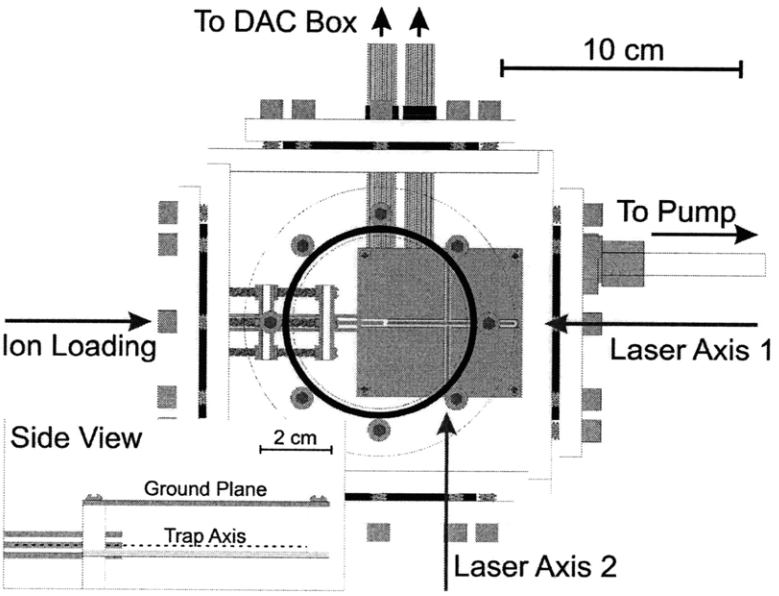

Figure 2-6: Setup for testing PCB surface-electrode ion traps with macroscopic ions. Both the four rod trap used for loading and the surface-electrode trap are mounted in a transparent acrylic vacuum chamber which can be pumped down to about 0.1 torr. Ions are loaded into the four rod trap from the left by electrospray ionization at standard pressure, then a flange is screwed into place and the air evacuated slowly. Two green lasers illuminate the trap axes.

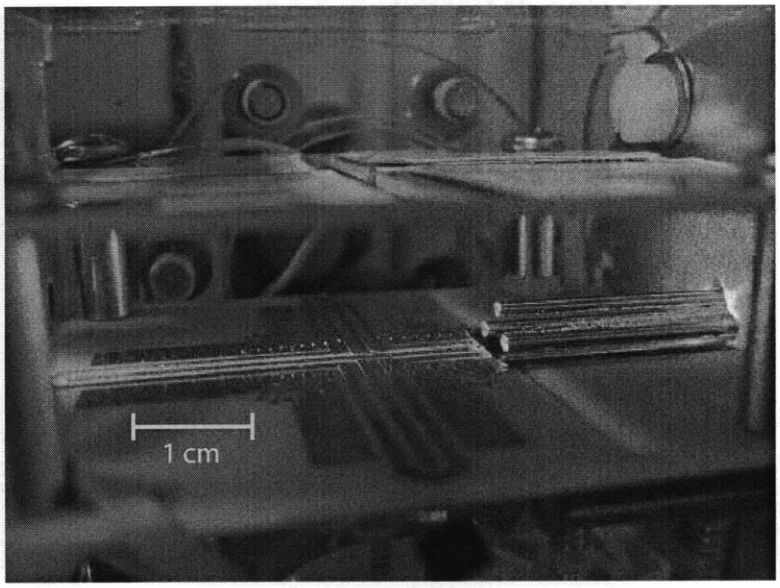

Figure 2-7: Macroscopic ions trapped in the PCB surface-electrode trap. Ions are illuminated by a green laser and imaged using an inexpensive CCD camera. The four rod trap used for loading is visible to the right of the surface-electrode trap.

an inexpensive CCD camera.

The three primitive ion movement operations for quantum information processing are shuttling in one dimension, transport through intersections, and splitting or joining pairs of ions [KMW02]. All three operations have been demonstrated in this trap [PLB+06]. Figure 2-8 shows two CCD images of the same ion, before and after being transported through the cross intersection. To pass through the intersection, the ion must be pushed over the local maxima in the secular potential located near the cross [HOS+06, HYH+08, BVO+09]. In this experiment simple waveforms consisting of square waves on the center control electrodes were used, but more sophisticated waveforms must be used in order to accomplish heating-free transport with atomic ions.

To summarize the results of this demonstration experiment with macroscopic ions,

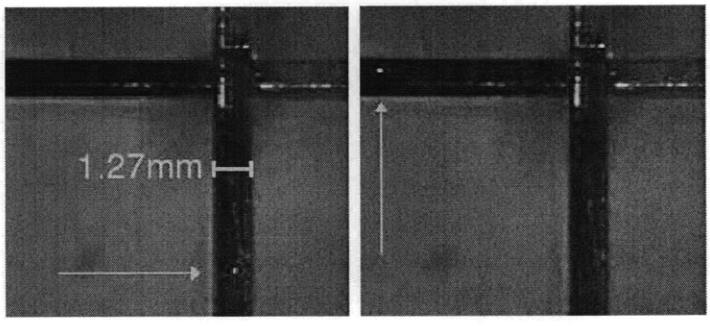

(a) (b)

Figure 2-8: Macroscopic ion passing through a cross intersection in a surface-electrode ion trap. The arrows point to the position of the ion (a) before and (b) after turning the corner. This operation takes about 50 ms.

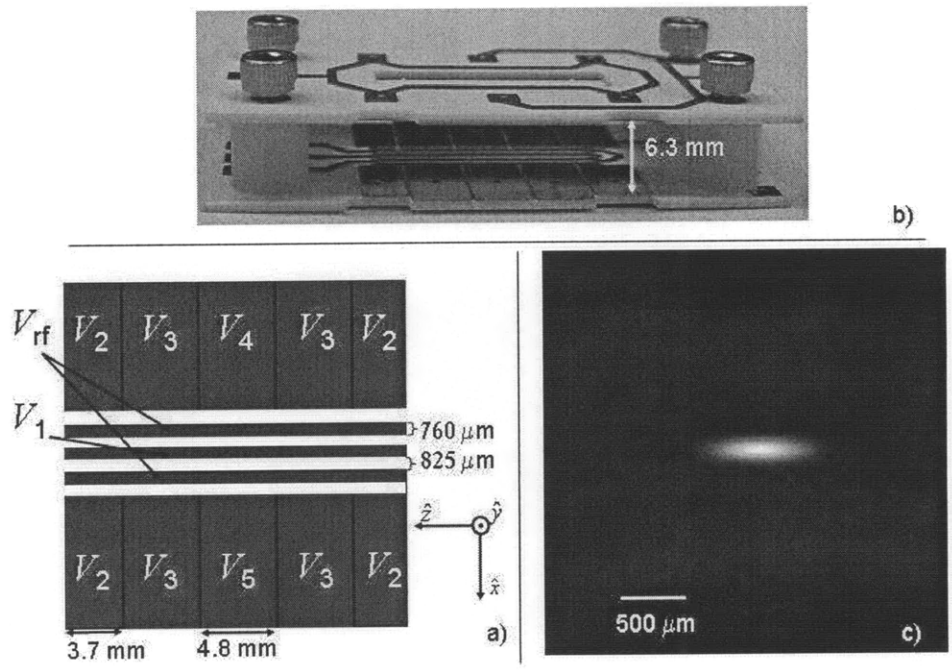

Figure 2-9: PCB surface-electrode ion trap used to trap atomic ions. (a) Photograph showing the surface-electrode trap and an extra top plate electrode mounted 6.3 mm above the trap which shields the trap from stray electric fields. (b) Layout of the trap electrodes, each labeled with the voltage applied; all but V_{rf} are DC. The space between the long electrodes has been milled out and the sides coated with copper. (c) CCD image of a cloud of $^{88}Sr^+$ ions trapped in the PCB surface-electrode ion trap.

surface-electrode ion traps can be efficiently loaded from four rod traps. While in this work the loading was done at atmospheric pressure where aerodynamic drag enhances the ion stability, with a well designed interface the transfer can be made very smooth and should work in vacuum. Further, the quantum information processing ion movement primitives have been demonstrated in a surface-electrode trap in a vacuum low enough that the aerodynamic drag does not affect the ion motional stability.

2.3.2 Atomic ions

The PCB surface electrode ion trap used for trapping atomic ions is shown in Figure 2-9 [BCL+07]. The electrodes are bare copper and the substrate is Rogers 4350B, a low RF loss, low outgassing rate substrate. The substrate between the electrodes is milled out and the vertical sidewalls are coated with copper to avoid exposing the ion to any bare dielectric surfaces. The trap is mounted in a standard UHV chamber and pumped down to 10^{-9} torr.

The trap is loaded with $^{88}Sr^+$ by electron impact ionization of neutral atoms from a resistive oven source (see Section 3.5). It was found experimentally to be unnecessary to load from a four rod trap, so the electron beam overlaps the neutral atom beam at the location of the surface-electrode trap. The ions are laser cooled by two co-propagating lasers at 422 nm and 1091 nm, which address the $^{88}Sr^+$ $S_{1/2} \leftrightarrow P_{1/2}$ and $D_{3/2} \leftrightarrow P_{1/2}$ transitions (see Section 3.1). The scattered 422 nm light is imaged using an electron-multiplying CCD

camera. Figure 2-9(c) shows an image of a cloud of $^{88}Sr^{+}$ ions in the PCB surface-electrode ion trap.

This demonstration experiment showed that it is possible to perform direct loading of atomic ions into a surface-electrode ion trap. The four rod to surface-electrode interface demonstrated in the macroscopic ion experiment has a higher loading efficiency, but it is not necessary. In this particular trap, there was a large enough stray electric field to rotate the ion trap principal axes and allow for laser cooling of all three axes, and so laser cooling in a surface-electrode trap did not present a problem. No unexpected obstacles to the use of surface-electrode ion traps for trapping atomic ions were uncovered.

2.4 Lucent ion trap foundry

Armed with the knowledge that surface-electrode traps seem to be advantageous for large-scale quantum information processing, and that they work for trapping atomic ions, the next step is to design and build a scalable, multiplexed ion trap (SMIT). This goal will be the subject of this section and Chapter 3.

2.4.1 Design goals

The design goals for this program were to build an ion trap with the following properties [KPM+05].

1. The fabrication technology should be scalable, both to smaller trap sizes and to more traps. This requirement equates to microfabrication.

2. The trap should be a multiplexed ion trap array with many trapping zones.

3. Finally, the trap should be capable of integration with electronics and optics. Large electrode counts in future large-scale traps will require integrated electronics for driving the control electrodes and integrated optics for delivering lasers to many trapping zones simultaneously. An important fact to note is that CMOS electronics are damaged if they are heated to above 400 C, so microfabricated ion traps which require processing above 400 C are not compatible with integrated CMOS electronics.

2.4.2 Trap design

The trap design is a surface-electrode ion trap fabricated on a silicon substrate. A cross section of the trap is shown in Figure 2-10. The substrate is a 700 μm thick, highly doped conductive silicon wafer with a resistivity of 0.018 Ω cm. On top of the substrate is a 1 μm layer of aluminum with a resistance of 0.027 $\Omega/\square$ (ohms per square of area), which together with the substrate serves as the electrical ground of the trap. The 1 μm aluminum control electrodes are above the ground on top of a 400 nm layer of silicon nitride, which has a dielectric constant of 7.5. Finally, the 1 μm aluminum RF electrodes sit on top of the control electrodes, but raised up by a 10 μm thick layer of stress balanced silicon dioxide (PETEOS) with a dielectric constant of 4.

The silicon dioxide layer is made as thick as possible in order to minimize the capacitance and increase the breakdown voltage between the RF and the DC electrodes. There is an effective capacitive divider formed by the relatively high capacitance between the DC

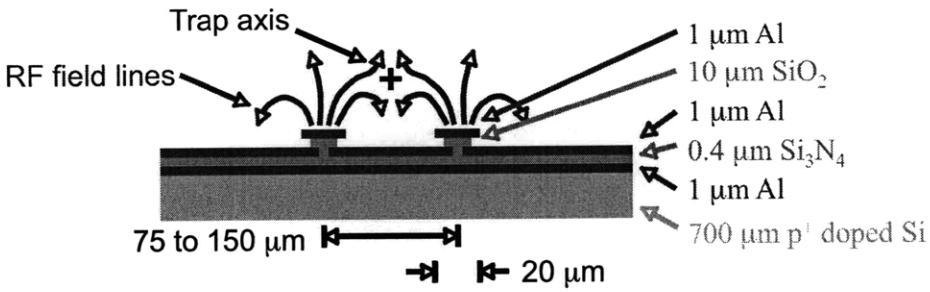

Figure 2-10: Cross section of the SMIT ion trap. DC voltages are applied to the three electrodes in the middle layer of aluminum and RF is applied to the two raised rails in the top layer of aluminum. Ions are trapped at the RF quadrupole null located 39 to 79 μm above the surface of the DC electrodes, indicated by a black cross. Not to scale.

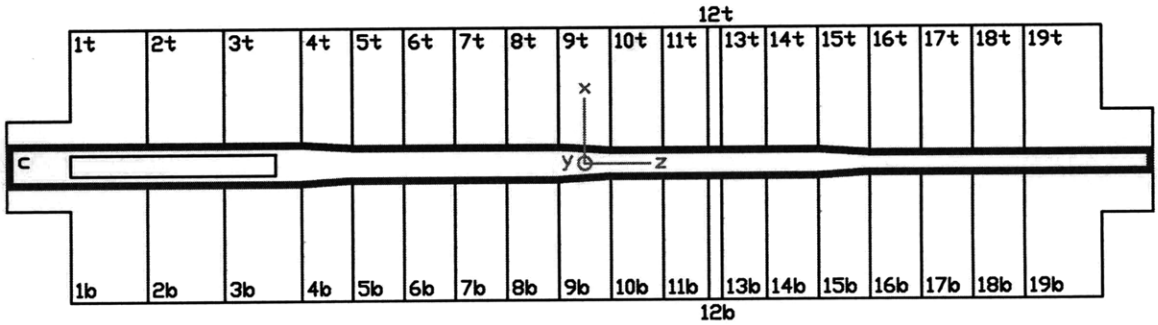

Figure 2-11: Layout of the SMIT ion trap. DC electrodes are drawn and labeled in blue and RF electrodes are drawn in red. The black rectangle is an optional through wafer slot used for loading. The DC electrodes are between 50 μm and 300 μm wide along the trap axis. The RF electrodes are 20 μm wide and are separated by 150 μm, 125 μm, 100 μm, and 75 μm center to center in the four regions going from left to right.

electrodes and the ground layer and the much smaller capacitance between the RF electrodes and the DC electrodes. This capacitive divider effectively RF grounds the DC electrodes.

Some of the traps feature an optional through wafer slot for loading the traps using an atomic beam coming from under the trap. This loading geometry prevents the atomic beam from depositing metal on the trap electrodes and shorting out the trap. The slot is fabricated by chemically mechanically polishing (CMP) the back of the wafer down to 400 μm thick, then dry etching the rest of the way through the wafer. This results in a slot with walls that are slanted less than 5%.

The layout of the trap is shown in Figure 2-11. The trap is a linear array with 40 electrodes and 17 trapping zones. The ion height above the trap surface varies from 39 to 79 μm as the RF electrode spacing varies from 75 to 150 μm. Typical trap voltages for trapping an ion between electrodes 3B and 3T are listed in Table 2.1. These particular trapping voltages result in secular frequencies $(\omega_x, \omega_y, \omega_z)/(2\pi) = (1.7, 2.1, 0.5)$ MHz and a trap depth of 0.025 eV for $^{88}Sr^+$. The principle axis coordinate system is rotated by 14 degrees about the z axis relative to the coordinate system shown in Figure 2-10. This allows efficient laser cooling of all three principal axes.

Electrode	Voltage
RF	155 V at 40.6 MHz
C	0.95 V
2T	6 V
3B	1.3 V
4T	6 V

Table 2.1: Typical operating voltages for the SMIT ion trap. The electrodes not listed are grounded. These voltages trap the ion between electrodes 3B and 3T.

2.4.3 Fabrication and packaging

The traps are fabricated at the New Jersey Nano Consortium (NJNC) microfabrication facility. Figure 2-12 shows some scanning electron microscope (SEM) images of a finished trap.

The finished traps are mounted in 100 pin ceramic pin grid array (CPGA) carriers (Global Chip Materials PGA10047002, see Figures 2-13 and 2-14). Contacts to the electrodes are made by wire bonding at the edge of the chip to 300 by 300 μm aluminum wire bond pads. The trap is mounted in the CPGA on top of a 1.27 mm thick alumina spacer in order to raise the surface of the trap above the CPGA for laser access.

The trap is fixed in the CPGA by either ceramic paste (as in Figure 2-13), low outgassing rate epoxy (EPO-TEK 353ND), or solder (80/20 Au/Sn). The ceramic paste is not a very strong adhesive, and would often crack off during handling. Epoxy is more durable and easier to use, but it limits the UHV bake temperature and there is concern about residue from the epoxy migrating to the trap surface. Solder is the preferred method for attaching the trap to the spacer and the spacer to the CPGA, but it requires evaporating a thin layer of gold on the back of the trap and on both sides of the spacer.

All of the materials and processes are very similar to those used in standard silicon VLSI processing, so scaling will be facilitated by the enormous amount of resources which have been invested in silicon VLSI processing by the classical computer industry. All of the processing steps can be carried out at under 400 C, so future versions of the trap could be fabricated directly on a CMOS ASIC (application specific integrated chip). Silicon VLSI is also compatible with standard MEMS (micro-electro-mechanical systems) optics used by the telecommunications industry.

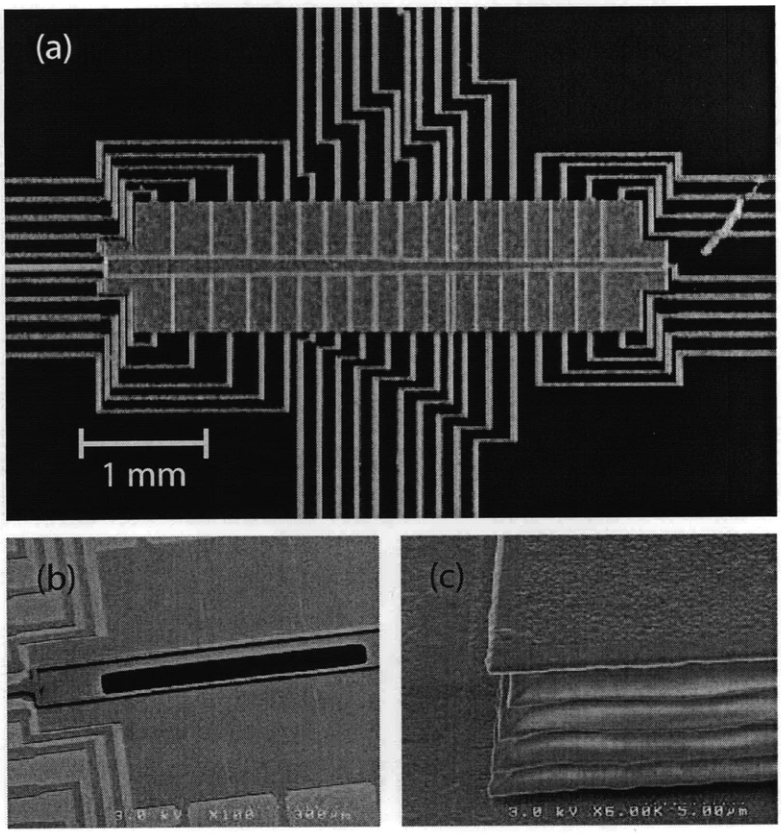

Figure 2-12: Scanning electron microscope pictures of the SMIT ion trap. (a) Trap layout. This particular trap does not have a through wafer loading slot. (b) Through wafer loading slot located in the center electrode in the trap region with the largest RF rail separation. (c) Side view of the 10 μm SiO_2 layer used to raise the RF electrodes above the DC electrodes. The SiO_2 is striated because it is deposited in several layers for stress relief.

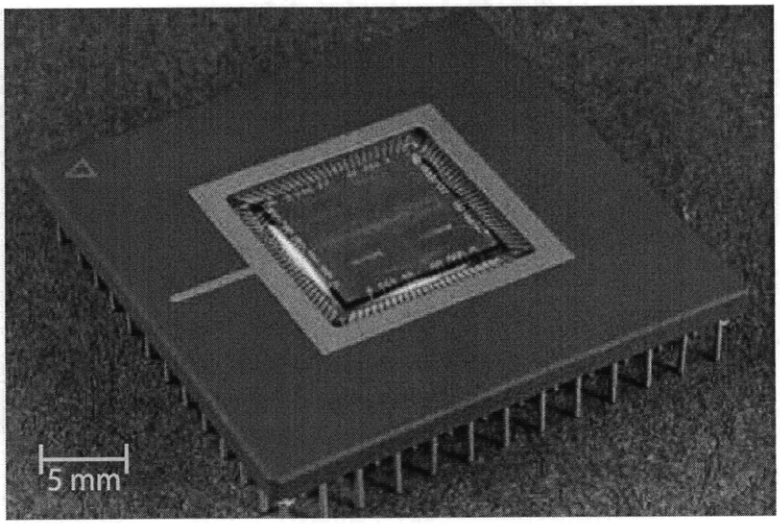

Figure 2-13: Packaged SMIT ion trap. The ion trap is packaged and wire bonded in a 100 pin ceramic pin grid array. This trap chip is mounted with ceramic paste that can be seen around the edges of the chip.

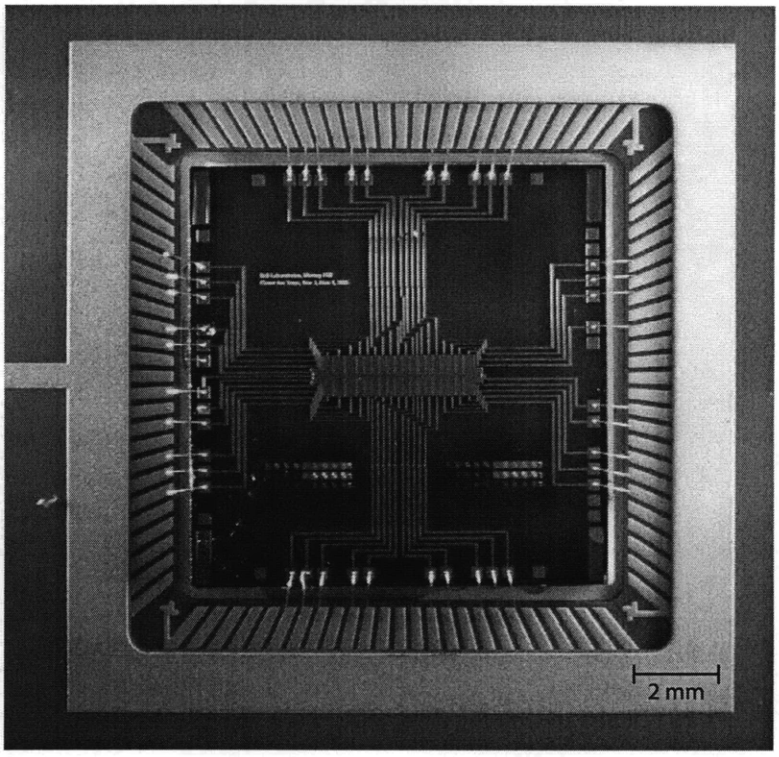

Figure 2-14: Close up of the packaged SMIT ion trap. The details of the electrical leads and wire bonds are visible.

Chapter 3

Trap evaluation and motional heating rate measurements

While some trap properties, namely the secular frequencies and the trap depth, can be calculated with high accuracy, other trap properties must be measured experimentally. Quantum information processing requires ion traps with a long ion lifetime and a low motional heating rate. The ion lifetime must be long compared with the relevant experimental timescales, which include the time required to compensate the stray electric fields and optimize the frequencies of the lasers with respect to the ion in addition to the time required for the experiment. The stray electric fields change each time the trap is loaded due to deposition of charge on dielectric surfaces and must be recompensated, and the laser frequencies drift significantly on a timescale of a few minutes. This results in an ion lifetime cutoff of roughly ten minutes below which it is experimentally very difficult to do any coherent quantum operations. Motional heating of trapped ions causes decoherence of two qubit gates, which rely on the shared motional state as a quantum bus [CZ95, SM99, TKK+99]. Neither the ion lifetime nor the motional heating rate can be predicted with any degree of accuracy.

Evaluating ion traps for quantum information processing requires a complex experimental apparatus. The traps must be mounted in UHV chambers at pressures less than 10^{-9} torr and driven with both low noise DC and high voltage RF sources. Trapping atomic ions also requires a set of frequency stabilized lasers to do detection, cooling, and quantum gates.

This chapter presents measurements of the ion lifetime and motional heating rate in surface-electrode ion traps. Section 3.1 describes the level structure of $^{88}Sr^{+}$, which is used for all of the atomic ion experiments in this thesis, and Section 3.2 describes the lasers used to address the $^{88}Sr^{+}$ transitions. Sections 3.3 and 3.4 describe the UHV chambers used for trap evaluation at room temperature and 6 K, respectively. Finally, Section 3.5 compares three different methods of loading ions into the traps. The trap evaluation results for the SMIT trap are presented in Section 3.6, and trap evaluation results for some other microfabricated traps are presented in Section 3.7. This chapter concludes with some speculation about the source of ion motional heating in Section 3.8 and a discussion of the outlook of surface-electrode ion traps for quantum information processing in Section 3.9.

The work in this chapter is all original except the following. The level structure of $^{88}Sr^{+}$ has been known for a long time [Gal67]. The laser system presented in Section 3.2 was designed and built by Jaroslaw Labaziewicz, and the cryogenic testing setup presented in Section 3.4 was constructed by Waseem Bakr and Paul Antohi. Finally, the MIT micro-

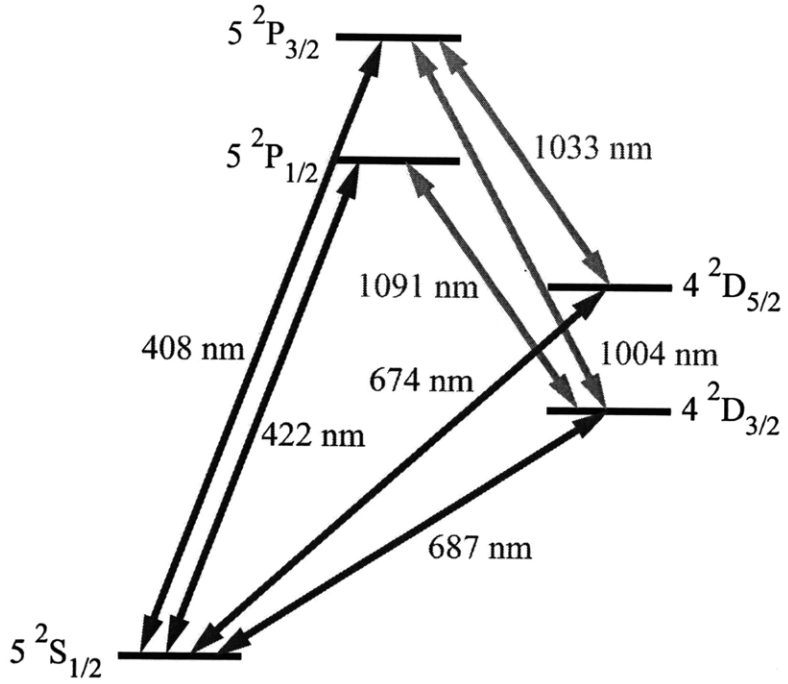

Figure 3-1: $^{88}Sr^+$ level diagram. All of the dipole allowed transitions are shown in blue and gray, together with the quadrupole transitions between the $S_{1/2}$ ground state and the metastable $D_{3/2}$ and $D_{5/2}$ states in red.

fabricated traps discussed in Section 3.7 were fabricated by Yufei Ge.

3.1 $^{88}Sr^+$ level structure

$^{88}Sr^+$ is used for all of the atomic ion experiments in this thesis. It is a convenient choice of ion for quantum information processing because of the simple level structure (no nuclear spin) and because all of the relevant transitions are available as laser diodes. In addition, the transition wavelengths are in the transmission window of common optical glass (BK7) and optical fibers (fused silica). Finally, ^{88}Sr is the most common isotope, with a natural abundance of 83%, eliminating the need for an isotopically selective ion source. The level structure of $^{88}Sr^+$ is shown in Figure 3-1, and the transitions are listed in Table 3.1 [Gal67, GJ91, BWJ+98].

Doppler cooling [MvdS99] is performed on the 422 nm $S_{1/2} \leftrightarrow P_{1/2}$ transition. Once out of every 20 cycles the ion decays to the $D_{3/2}$ state, which has a long spontaneous emission lifetime that disrupts the Doppler cooling process. When this happens, the ion is returned to the $P_{1/2}$ state by a 1091 nm repumper laser which addresses the $D_{3/2} \leftrightarrow P_{1/2}$ transition. Dark states, which are coherent superpositions of the $S_{1/2}$ and $D_{3/2}$ states that do not couple to the 422 nm and 1091 nm lasers, are avoided by detuning the 422 nm laser by $\delta/(2\pi) \sim -10$ MHz from the $S_{1/2} \leftrightarrow P_{1/2}$ transition and the 1091 nm laser by $\delta/(2\pi) \sim +10$ MHz from the $D_{3/2} \leftrightarrow P_{1/2}$ transition [BB02]. The ions are Doppler cooled to near the Doppler limit of $\hbar A_{P_{1/2} \rightarrow S_{1/2}}/2 = 0.48$ mK $= 10$ motional quanta at a secular frequency of 1 MHz.

Sideband cooling [DBIW89] is used to cool the ions from the Doppler limit down to

Wavelength, λ [nm]	Lower state, α	Upper state, β	Frequency, $(\omega_\beta - \omega_\alpha)/(2\pi)$ [THz]	Decay rate, $A_{\beta\to\alpha}$ [s^{-1}]
422	$S_{1/2}$	$P_{1/2}$	710.96282	125.3×10^6
1091	$D_{3/2}$	$P_{1/2}$	274.58924	6.6×10^6
408	$S_{1/2}$	$P_{3/2}$		139.0×10^6
1033	$D_{5/2}$	$P_{3/2}$	290.21085	7.1×10^6
1004	$D_{3/2}$	$P_{3/2}$		0.9×10^6
687	$S_{1/2}$	$D_{3/2}$		2.2
674	$S_{1/2}$	$D_{5/2}$	444.77904	2.5

Table 3.1: $^{88}Sr^+$ transitions. The frequencies listed are the values measured using a Toptica WS7 in this work, while the spontaneous decay rates are from calculations [GJ91, BWJ+98].

the motional ground state. Sideband cooling in this work is performed using a pulsed scheme where first the ion is coherently pumped from the $|S_{1/2}, m = -1/2, n\rangle$ state to the $|D_{5/2}, m = -5/2, n-1\rangle$ state using a π pulse on the red motional sideband of the 674 nm $S_{1/2}, m = -1/2 \leftrightarrow D_{5/2}, m = -5/2$ transition, then the ion is incoherently pumped to the $P_{3/2}, m = -3/2$ state using a pulse on the 1033 nm $D_{5/2}, m = -5/2 \leftrightarrow P_{3/2}, m = -3/2$ transition, and finally the ion spontaneously decays back to the $S_{1/2}, m = -1/2$ ground state. In this notation m is the magnetic quantum number and n and $n-1$ are the number of vibrational quanta in the motional mode of interest. Most of the time the repumping process does not change the vibrational quantum number, so after one cycle the ion is in the $|S_{1/2}, m = -1/2, n-1\rangle$ state. Eventually the ion reaches the vibrational ground state which is decoupled from the laser pulses. Typically, 75 cycles are sufficient to prepare one motional mode in the vibrational ground state with $> 90\%$ probability.

The ion temperature can be measured by looking at the ratio of the Rabi frequencies of the red and blue motional sidebands [WMI+98b] of the $S_{1/2}, m = -1/2 \leftrightarrow D_{5/2}, m = -5/2$ transition. In the Lamb-Dicke regime, where the ion is well-localized with respect to the wavelength of light, the expectation value of the number of motional quanta $\langle n\rangle$ is given by

$$\frac{P_{rsb}}{P_{bsb}} = \frac{\langle n\rangle}{\langle n\rangle + 1} \tag{3.1}$$

where P_{rsb} and P_{bsb} are the probability of making the transition from $S_{1/2}, m = -1/2$ to $D_{5/2}, m = -5/2$ under laser pulses of identical power and duration on the red and blue motional sidebands of the $S_{1/2}, m = -1/2 \leftrightarrow D_{5/2}, m = -5/2$ transition.

The two qubit states are the $S_{1/2}, m = -1/2$ ground state and the $D_{5/2}, m = -5/2$ metastable excited state. While the coherence time is ultimately limited to 400 ms by spontaneous decay of the $D_{5/2}, m = -5/2$ state, in this work the coherence time is limited to a few hundred microseconds by phase noise on the 674 nm laser. Transitions between the qubit states are accomplished using the 674 nm $S_{1/2}, m = -1/2 \leftrightarrow D_{5/2}, m = -5/2$ laser. The qubit state can be measured by applying the Doppler cooling lasers, which couple to the $S_{1/2}, m = -1/2$ state but not to the $D_{5/2}, m = -5/2$ state, and counting the number of 422 nm photons scattered by the ion.

3.2 Lasers

As can be seen from the last section, Doppler cooling, sideband cooling, and qubit manipulation of $^{88}Sr^{+}$ requires four lasers at 422 nm, 674 nm, 1033 nm, and 1091 nm. In this work these lasers are generated by four identical laser systems which use optical feedback to stabilize extended cavity diode lasers (ECDLs) [LRBC07]. ECDLs by themselves have linewidths of order 1 MHz and long term drifts as large as 10 MHz/minute. After optical feedback, the lasers used for this work have linewidths around 20 kHz and long term drifts < 1 MHz/minute. For more details, see References [LRBC07, Lab08].

While 20 kHz linewidths are good enough for the 422 nm, 1033 nm, and 1091 nm lasers, the 674 nm qubit transition laser needs to have a smaller linewidth. In this work, this is accomplished by Pound-Drever-Hall (PDH) locking the output of the laser to a high finesse, stable cavity [LHN+07, She08]. This technique has been used by other groups to achieve sub-Hz linewidth lasers [LHN+07], and in this work the resulting laser linewidth is of order 100 Hz. This is sufficient to achieve qubit coherence times of hundreds of microseconds.

The experiments in this chapter require sequences of laser pulses with precise time and amplitude control. In this work a field programmable gate array (FPGA, OpalKelly XEM3010-1000) is used to control the laser pulses and count photons scattered by the ion into a photo-multiplier tube (PMT). This allows for precise, repeatable timing with a resolution of 16 ns (the FPGA clock runs at 62.5 MHz) and sub 1 ns jitter. The lasers are switched using acousto-optic modulators (AOMs) which are driven by direct digital synthesizers (DDSs, Analog Devices AD9858) controlled by the FPGA. Amplitude control is provided by digital variable attenuators (Honeywell HRF-AT4610) also controlled by the FPGA. The pulse sequencer is described in much more detail in Reference [Lab08].

Two additional lasers at 460 nm and 405 nm can be used for loading by photoionization of a neutral atomic beam [VCLB06, BLW+07]. In this work 405 nm is generated with a bare ECDL, and 460 nm is generated using a frequency doubled titanium sapphire laser [Lab08].

3.3 Room temperature trap evaluation setup

Room temperature trap evaluation is performed in the UHV chamber shown in Figures 3-2 and 3-3. The vacuum chamber is built using standard conflat (CF) components. It is pumped by a combination of a 40 L/s ion pump (Varian VacIon Plus 40 StarCell) and a titanium sublimation pump (Thermionics SB-1020), and has a base pressure below 5×10^{-10} torr. Reaching the base pressure requires baking at 200 C (the bakeout temperature is limited to 200 C by kapton wire insulation in the chamber) for approximately 2 weeks.

The science part of the vacuum chamber is a spherical octagon chamber (Kimball Physics MCF450-SO20008) with two axes of unrestricted optical access at 45 degrees to each other and a home built UHV compatible CPGA socket shown in Figure 3-4 [SHO+06]. The CPGA socket is built by sandwiching gold plated brass alloy pin receptacles (Mill-Max 0672-4-15-15-30-27-100) between two pieces of 0.1 inch thick UHV compatible plastic (Vespel SP3). The plastic parts are mounted to the spherical octagon using some stainless steel mounting parts. Fifty of the 100 pins on the CPGA are fed out of the vacuum chamber by a kapton insulated ribbon cable through a D-sub vacuum feedthrough. Before assembly, the pin receptacles are annealed at 450 C in rough vacuum for 10 minutes with a 0.016 inch diameter steel wire inserted. This softens the springs so that less force is required to insert

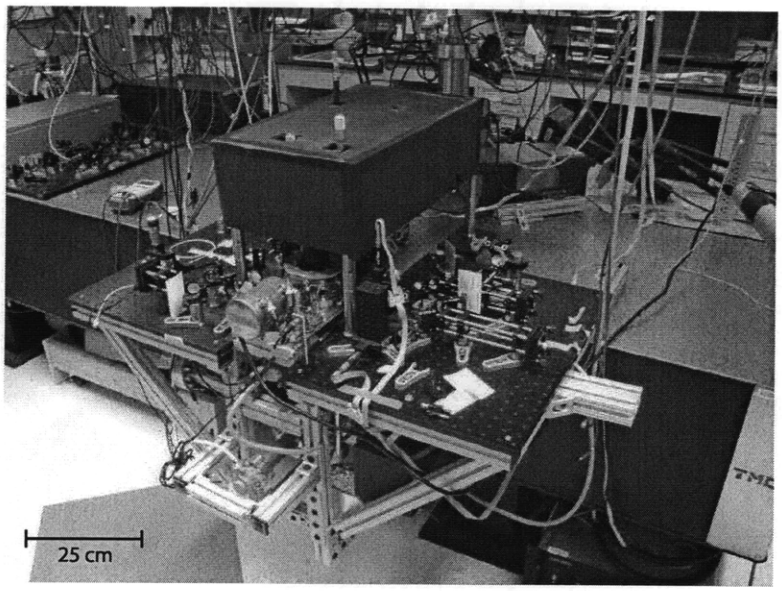

Figure 3-2: Room temperature trap evaluation setup. The vacuum chamber is mounted on the side of the optical table for maximum pumping speed (the largest opening of the spherical octagon vacuum chamber is the bottom flange) and unrestricted optical access in the plane of the optical table. Two breadboards are mounted on either side of the spherical octagon for laser delivery optics, and the imaging system sits above the spherical octagon in a black box used for light shielding. In front of the spherical octagon the helical resonator used to produce the high voltage RF is visible.

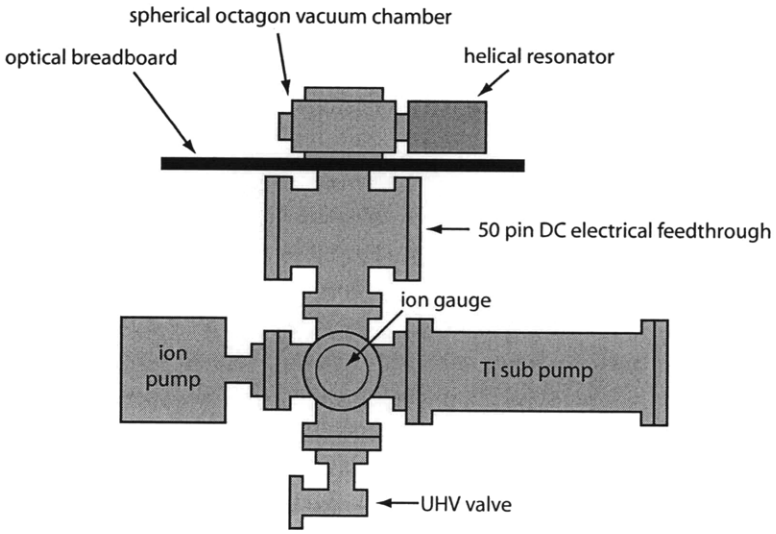

Figure 3-3: Room temperature trap evaluation vacuum chamber.

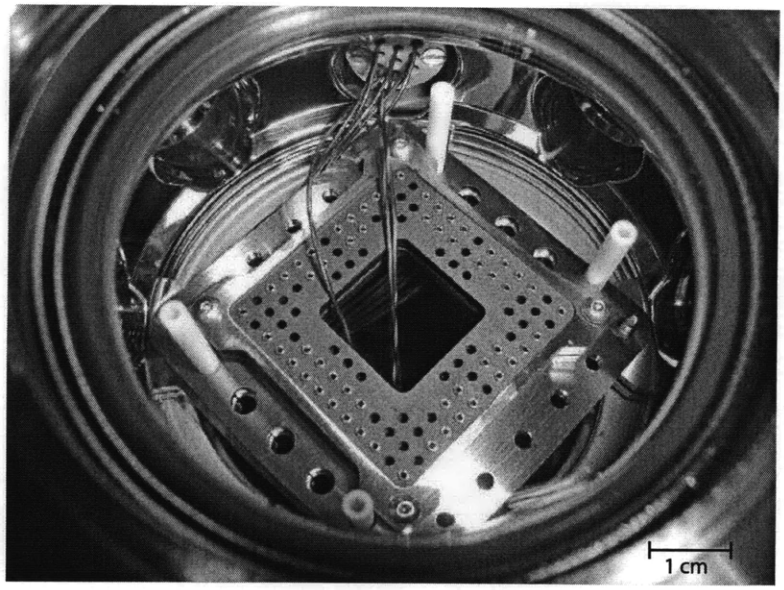

Figure 3-4: Room temperature trap evaluation CPGA socket. This CPGA socket is home built to be UHV compatible. The only materials used in the construction are gold plated pin receptacles, a UHV compatible plastic, and stainless steel.

and remove CPGAs from the CPGA socket. The CPGA socket allows for quickly switching traps without having to rewire the vacuum chamber.

The DC and RF voltages for driving the trap are generated by commercial linear power supplies (Agilent E3631A) and a commercial function generator (Agilent 33250A), respectively. The linear power supplies have a range of -25 to $+25$ V; higher voltages can be obtained if necessary by amplifying the output of the linear power supplies using home built bootstrapped rail amplifiers that go up to ± 200 V. The output of the function generator passes through an RF amplifier (either Amplifier Research 75AP250 or Minicircuits ZHL-1010) and a helical resonator (built following the design in Reference [Fis76] with tapped input coupling) in order to achieve the necessary high voltage and impedance matching to the mostly capacitive trap.

The lasers are delivered from the laser optical table to the trap optical table through polarization maintaining optical fibers, and focused and aligned to the trap using the optics shown in Figure 3-5. For surface-electrode traps with small ion heights, the lasers must be focused very well to avoid scattering off the surface of the trap and into the ion detection optics. At first glance, this might seem to suggest that smaller beam waists are always better, but when the beam waist is too small the Rayleigh length of the laser becomes smaller than the width of the trap and the beam is clipped by the edge of the trap. This leads to more, as opposed to less, scatter at the ion position. The optimum beam waist for 422 nm light passing over a 1 cm wide chip is about 15 μm ($1/e^2$ radius), which results in a beam radius at the edge of the chip of 50 μm. This limits the ion height above the chip to be greater than 50 μm. Smaller ion heights with surface-electrode ion traps will require either smaller width ion trap chips, through chip optical access, or integrated laser delivery optics.

Ion detection is done by either an electron multiplying CCD (Princeton Instruments PhotonMax512) or a photon counting PMT (Hamamatsu H7360-02). Photons scattered

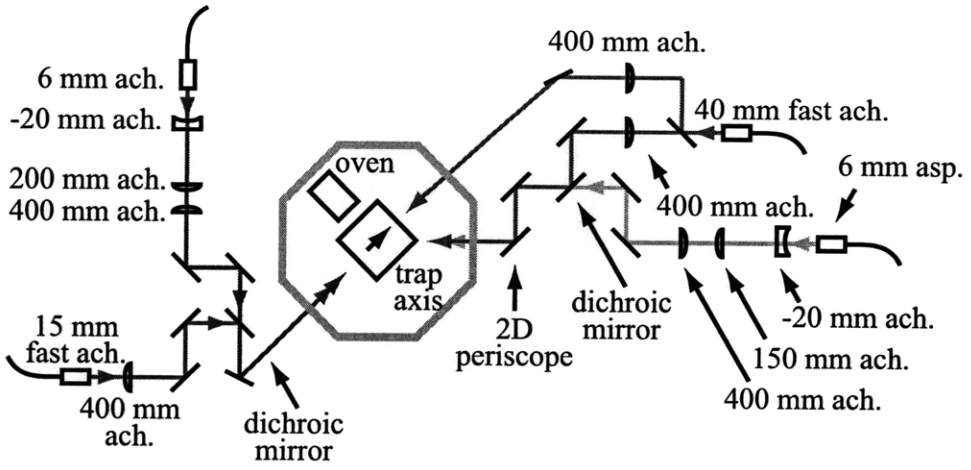

Figure 3-5: Room temperature trap evaluation laser delivery optical layout. The six lasers are delivered from another optical table in four single mode, polarization maintaining optical fibers. The fiber in the upper left contains the 674 nm laser, the fiber in the lower left contains both the 460 nm and 405 nm lasers, the fiber in the upper right contains the 422 nm laser, and the fiber in the lower right contains the 1091 nm and 1033 nm lasers. The optics in this figure focus the lasers and align them to the trap. The beam sizes at the trap are 19 μm ($1/e^2$ radius) for the 674 nm laser, 150 μm for the 460 nm and 405 nm lasers, 15 μm for the 422 nm laser, and 26 μm for the 1091 nm and 1033 nm lasers.

by the ion are collected and focused onto the CCD using the following optical elements: focal plane, 55 mm space (the vacuum window is in this space), 150 mm meniscus lens, 20 mm space, 150 mm achromatic doublet lens, 150 mm space, 400 mm achromatic doublet lens, 453 mm space (there is a 427 nm bandpass filter in this space, Semrock FF01-427/10-25 with 98% transmission at 422 nm), CCD. In the 452 mm space, there is also a 50/50 beamsplitter which directs half of the light to the PMT. The magnification of this imaging system is 5.5, and the resolution is about 7 μm. All of the lenses are 2 inch diameter. With one ion and the 422 nm laser on resonance and above saturation power, the PMT receives about 20,000 counts/s.

3.4 Cryogenic trap evaluation setup

Cryogenic cooling of the trap electrodes has been shown to reduce the motional heating rates of trapped ions [DOS+06]. There is also an experimental advantage to cryogenic ion trapping in that UHV pressures are easily reached without any vacuum bakeout and with non-standard vacuum materials in the vacuum chamber (e.g., plastic and superglue). Going from standard pressure to UHV requires less than 24 hours. Finally, it might be possible to couple trapped ion qubits to superconducting qubits [M+07] in a cryogenic environment.

Cryogenic trap evaluation is performed in the liquid helium bath cryostat shown in Figure 3-6. The innermost layer is a liquid helium dewar, where the trap and electrical filters for the DC electrode sources are mounted. Around the liquid helium dewar is a 77 K radiation shield, which is heat sunk to a liquid nitrogen dewar. Finally, the outermost layer is a vacuum vessel. Vacuum pressures below 2×10^{-12} torr are reached using a combination of two activated charcoal getter pumps which are heat sunk to the liquid nitrogen and

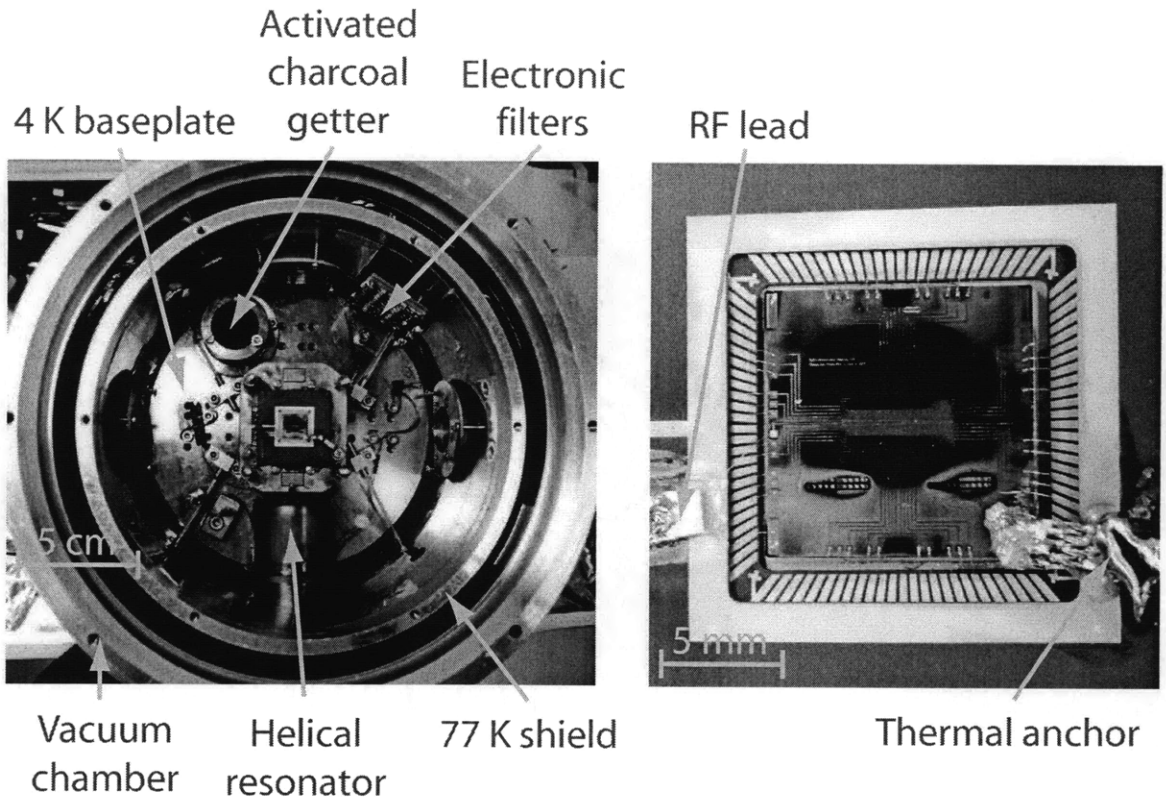

Figure 3-6: Cryogenic trap evaluation setup. The picture on the left shows the inside of the liquid helium bath cryostat. The trap, as well as some electrical filter networks and an activated charcoal getter pump, are heat sunk to the 4 K baseplate of the helium dewar. The helical resonator and oven (not shown, but it is positioned in front of the helical resonator) are mounted to the 77 K radiation shield. The outermost layer is the vacuum chamber. The picture on the right is the SMIT trap used for cryogenic testing. In order to reduce the capacitive load on the helical resonator the RF lead is rerouted on top of the CPGA, and a copper braid is indium soldered to the trap and to the 4 K baseplate for heat sinking.

helium dewars and a turbomolecular pump which does the initial vacuum pumpdown from standard pressure. The trap temperature is typically around 6 K due to heat dissipation in the RF electrodes. For more details, see References [Lab08, ASA+09].

The trap drive electronics as well as the laser delivery and imaging optics are similar to that of the room temperature trap evaluation setup, and are described in detail in Reference [Lab08].

3.5 Loading methods

Three methods are commonly used to load atomic ion traps: electron impact ionization of a neutral atom beam, laser ablation of a solid target, and photoionization of a neutral atom beam. Electron impact ionization is the simplest loading method, but it deposits a large amount of charge on any exposed dielectric surfaces, which results in large stray electric fields that destabilize the ion trap. Laser ablation is useful for cryogenic ion trapping because it does not require a neutral atom beam so the heat load is much lower, but the

stray electric fields are similar to electron bombardment ionization. Photoionization is very efficient, and it produces the smallest stray electric fields.

There is a fourth method, photoionization of atoms in a MOT (magneto-optical trap), which was demonstrated in Reference [CGC+07]. This method is even cleaner than photoionization of a neutral atom beam, but it is significantly more complicated to implement and therefore not used in this work.

3.5.1 Electron impact ionization

Electron impact ionization relies on collisions between an electron beam and a neutral atom beam to strip electrons off of the atoms. Because the collisional cross section is so small, the electron beam flux must be very high. Thus many electrons are deposited on any exposed dielectric surfaces resulting in a large stray electric field. This is a problem in particular for surface-electrode traps, which necessarily have dielectric surfaces that separate the different electrodes. Every time the trap is loaded, the new stray electric field must be measured and compensated [BCL+07]. For this reason, electron impact ionization is not used for trap evaluation in this work.

3.5.2 Laser ablation

Laser ablation of a solid target has been used to load ion traps as early as 1981 [Kni81, KGF+90]. Ablation is a process in which a high-intensity laser strikes a surface, causing the rapid ejection of material that includes neutral atoms, ions, molecules, and electrons [Phi07]. With other methods of ion loading, the neutral atoms are ionized inside the trapping region. This, however, is not the case with ablation. It was shown in [HMO+06] that the electrons from the ablation plume reach the ion trap first and short the trap electrodes for an amount of time of the order of 10 μs, and the ions from the ablation plume which are passing through the trapping region when the trap voltages recover may be captured. This shorting due to the electrons is necessary because the potential of a Paul trap is conservative in the pseudopotential approximation. The pseudopotential approximation is valid for any ions moving slowly enough to be captured by the trap. A recent paper demonstrated an alternative way to load ion traps with ablation which uses photoionization to ionize the neutral atoms in the ablation plume as they pass through the trap region [HGH+07].

Laser ablation loading is potentially advantageous for quantum information processing for two reasons. First, it is very fast: ions can be loaded with a single laser pulse in much less than one second. And second, because the heat load is negligible ablation is a natural solution for loading ion traps in a cryostat. In order to determine the suitability of ablation loading for surface-electrode ion traps, ablation loading was tested with a PCB ion trap in the room temperature trap evaluation setup (see Figures 3-7 and 3-8).

Ablation loading test setup

The laser used for ablation is a pulsed, frequency-tripled Continuum Minilite Nd:YAG laser at 355 nm. No additional photoionization lasers are used. Ions are loaded using a single laser pulse of energy 1-10 mJ and duration 4 ns. Ion numbers ranging from one to a few hundred are obtained with a single pulse.

Firing the ablation laser ten times in ten seconds raises the vacuum pressure from the base pressure of 2×10^{-9} torr to 3×10^{-9} torr. The vacuum pressure drops back down to the base pressure in a few seconds.

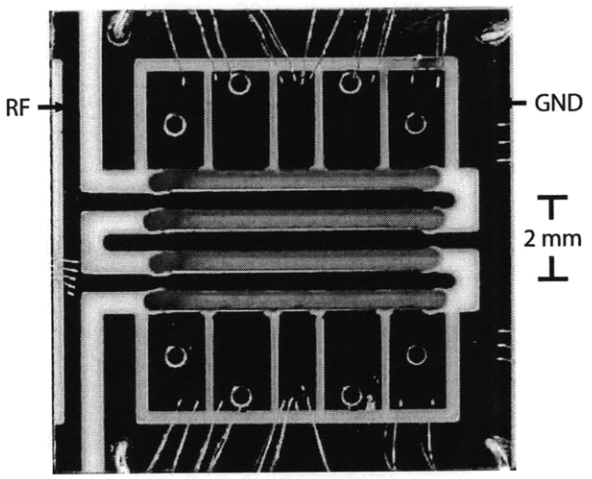

Figure 3-7: Layout of the trap used for testing laser ablation loading. The trap is a PCB surface-electrode ion trap with five control electrodes on each side. The RF electrodes are spaced by 2 mm, leading to an ion height of 0.8 mm above the trap surface.

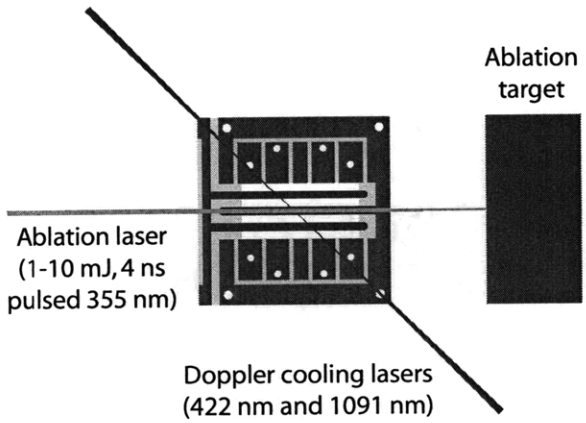

Figure 3-8: Geometry of the laser ablation loading experiment. The ablation target is positioned approximately 25 mm away from the trap center, and the surface of the target is orthogonal to the direction to the trap. Not to scale.

Ablation loading target dependence

The efficiency of laser ablation loading is strongly dependent on the ablation target material. Several target materials are characterized by measuring the trapped ion signal as a function of the number of ablation laser pulses fired on a single spot of the target. Each ablation laser pulse knocks the ions from the previous pulse out of the trap, so the trapped ion signal is roughly proportional to the number of ions loaded by a single ablation pulse. An ideal ablation target would load a constant number of ions per pulse. In practice, the number of ions per pulse is not constant and eventually the target stops producing ions. The target lifetime is different for each target material. Similar changes in yield are observed after many ablation pulses in pulsed laser deposition and is attributed to ablating a profile into the target surface which modifies the ablation process [CH94]. Note that a finite ablation target lifetime is not a fundamental problem because the position of the ablation laser spot on the target can be dithered. This measurement provides a benchmark of the loading efficiency, consistancy, and lifetime of the target.

The target materials studied here are Sr (99% pure from Sigma-Aldrich), Sr/Al alloy (10% Sr, 90% Al by mass from KB Alloys), single crystal $SrTiO_3$ ($\langle 100 \rangle$ crystal orientation from Sigma-Aldrich), and $SrTiO_3$ powder in an epoxy resin (5 μm $SrTiO_3$ powder from Sigma-Aldrich mixed with Loctite 5 minute epoxy). While Sr metal is a natural choice of target material, it is difficult to work with because it oxidizes quickly in air. None of the other targets considered here have that problem. Figure 3-9 shows the experimental results for each target. It is clear from a standpoint of lifetime and consistency that the $SrTiO_3$ crystal is the best choice of target material for loading $^{88}Sr^+$. The relatively lower efficiency of $SrTiO_3$ is not a problem because only small numbers of ions are desired.

Ablation loading trap depth dependence

One of the potential problems of using ablation to load surface-electrode ion traps is the low trap depth. Here, the trapped ion signal is measured as a function of trap depth. In this experiment, ions are loaded into the trap at a series of decreasing RF voltages which correspond to decreasing trap depths. The trap depth is calculated using a boundary element electrostatics solver [Cha], and verified by checking that the numerical model predicts secular frequencies which match the experiment at each RF voltage. The trapped ion signal for each trap depth is plotted in Figure 3-10. The ablation laser pulse energy of 1.1 mJ and spot size of 680 μm are chosen to maximize the ion signal at low trap depth. The lowest trap depth which is loaded here is 40 meV. In contrast, the same experiment using electron impact ionization of a thermal atomic beam loaded a minimum trap depth of 470 meV.

Ablation loading of single ions

Finally, the data presented in Figures 3-9 and 3-10 corresponds to loading hundreds of ions per ablation pulse. Single ions can be loaded with ablation by setting the ablation laser energy such that on average less than one ion is loaded per pulse and alternating ablation laser pulses with ion signal measurements until a single ion is observed. If more than one ion is observed they are ejected from the trap and the loading process restarts. Figure 3-11 shows an example probability distribution of the number of ions loaded with a single ablation laser pulse. This experiment was performed in a smaller ion trap than the one used for the previous experiments with an ablation pulse energy of 2 mJ and spot size of 500 μm. The experimental probability distribution fits well to a Poisson distribution with

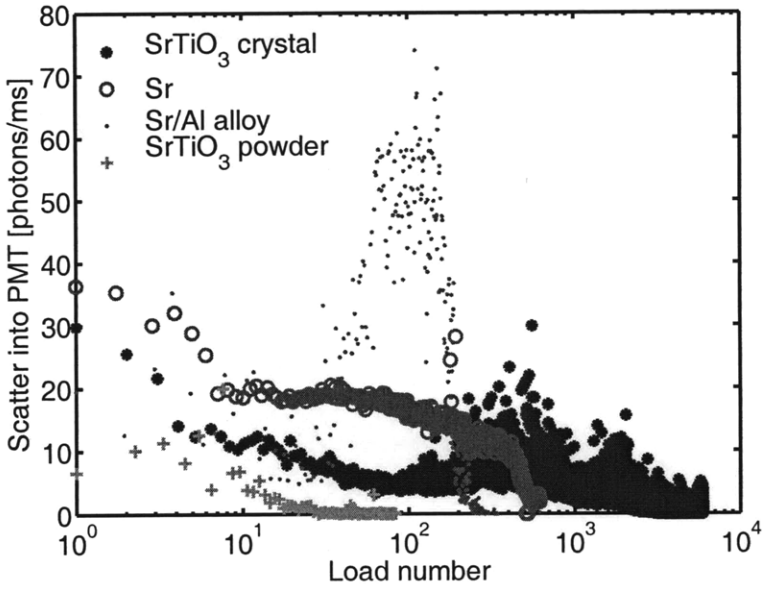

Figure 3-9: Laser ablation loading target lifetime for several different target materials. The trapped ion signal is plotted as a function of the number of ablation pulses fired on a single spot of the target. Each point represents the signal due to a single ablation pulse of energy 8 mJ. The ions from the previous pulse are lost when the electrons in the ablation plume short the trap, so the trapped ion signal is roughly proportional to the number of ions loaded by a single pulse of the ablation laser. For this experiment, the ablation laser was focused to a spot size of 300 μm. For reference, a single ion scatters roughly 0.2 photons/ms into the PMT for the parameters of this measurement.

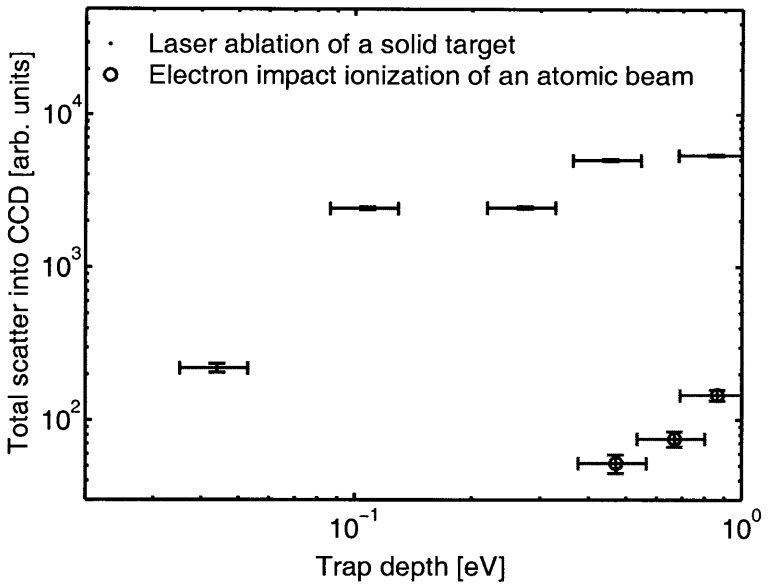

Figure 3-10: Laser ablation loading rate versus trap depth. The trapped ion signal is plotted as a function of the computed trap depth for both ablation and electron impact ionization loading. An ablation pulse energy of 1.1 mJ was used with a spot size of 680 μm. Each point is the ion signal obtained either from a single pulse of the ablation laser or from loading using electron impact ionization until the ion signal stops increasing.

a mean ion number of 0.16. With these parameters it takes on average 7 pulses to load and the probability of loading more than one ion is 8%. The probability of loading more than one ion can be reduced by using a lower ablation laser pulse energy.

While laser ablation loading offers several potential advantages for quantum information processing, more development is required in order to reduce the amount of charge deposited on the exposed dielectrics before it is a practical solution. In particular, ion optics could be used to remove the charged particles from the ablation plume and the neutral atoms could be photoionized when they pass through the trap. This was investigated briefly, but the high voltages required for the ion optics were found to interfere with the trap operation in the simple designs that were tested. Instead of pursuing ablation loading further, the trap evaluation work here used photoionization of a neutral atom beam from an atomic oven for loading.

3.5.3 Photoionization

Photoionization loading works by photoionization of a neutral atomic beam as it passes through the trap. The neutral atomic beam typically comes from a resistive atomic oven similar to that used for electron impact ionization. Photoionization can be very efficient, so the flux of the atomic beam can be made very small. This results in very little deposition of metal from the atomic beam on the trap. Further, because the laser(s) used for photoionization can be tightly focused to overlap with the atomic beam only in the trap, virtually all of the ions which are produced can be trapped resulting in very little charge deposition on exposed dielectric surfaces.

The primary difficulty with photoionization loading is that it requires an extra laser or

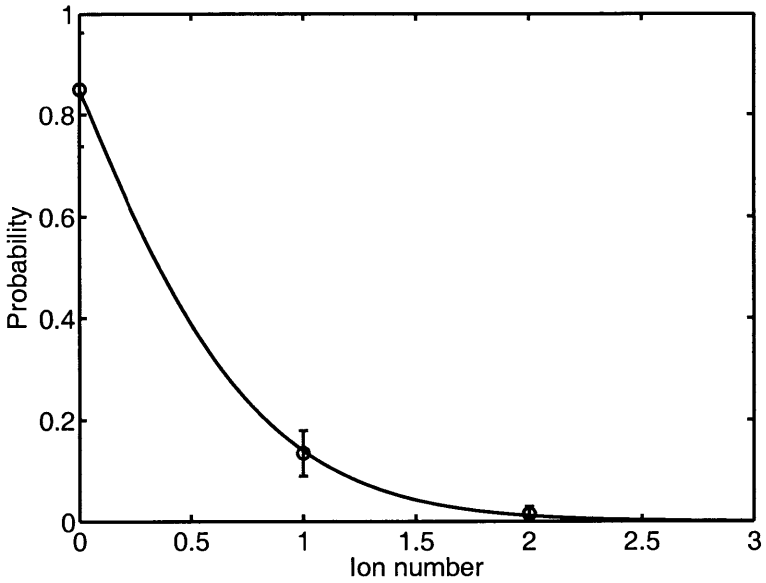

Figure 3-11: Probability distribution of the number of ions loaded with a single ablation laser pulse. The circles are experimental data and the line is a Poisson fit with a mean ion number of 0.16. The experiment was performed with an ablation pulse energy of 2 mJ and a spot size of 500 μm.

two which are specific to the ion species. Neutral ^{88}Sr can be photoionized efficiently using a two photon transition to an autoionizing state in the continuum with lasers at 460 nm and 405 nm [VCLB06, BLW$^+$07]. The autoionizing state quickly decays into an ion and a free electron.

Here photoionization is implemented using the two photon transition. The stray fields generated loading typical surface-electrode traps with photoionization are measured to be of order $O(100)$ V/m as opposed to $O(1000)$ V/m with electron impact and ablation loading. This allows loading of traps with depths as shallow as 20 meV, and the process of compensating for the stray electric fields after loading is much simpler.

3.6 SMIT evaluation results

The SMIT trap was tested both at room temperature and at 6 K.

3.6.1 SMIT at room temperature

The room temperature testing was performed at a vacuum pressure of 5×10^{-10} torr. Ions are loaded into the largest trap region between the electrodes 2B and 2T (see Figure 2-11) by photoionization. At room temperature large stray electric fields of the order of (10 V)/(100 μm) $\sim 10^5$ V/m are observed, indicated by the fact that the trap voltages which compensate the trap experimentally are up to 10 V from the predicted voltages. Further, only up to two ions can be loaded into the trap simultaneously. The SMIT trap used for room temperature testing failed when one of the DC electrodes shorted to the silicon substrate after about 3 weeks of continuous use.

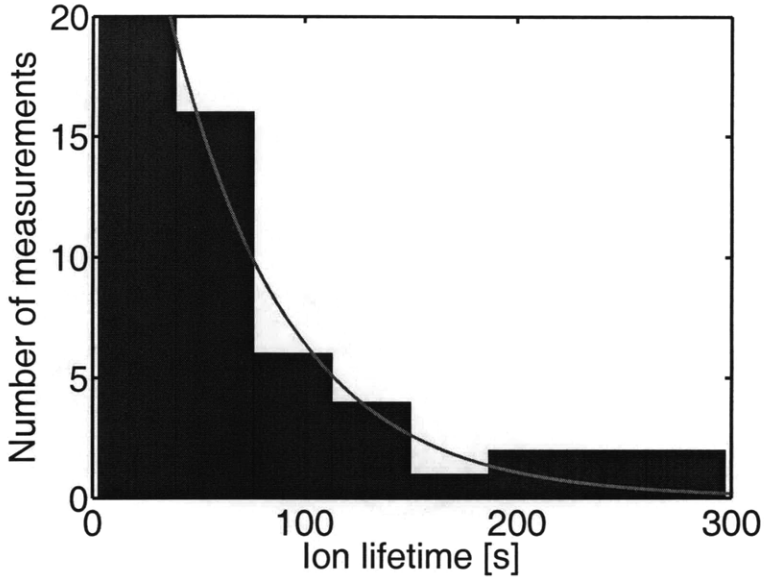

Figure 3-12: Ion lifetime with continuous laser cooling in the SMIT ion trap. Histogram of 59 ion lifetimes measured at room temperature with the Doppler cooling lasers on continuously. An exponential fit with a decay time of 56 ± 6 s is overlaid in red.

The ion lifetime is measured by loading single ions and measuring how long they remain trapped. A histogram of 59 ion lifetimes is shown in Figure 3-12. In this experiment the Doppler cooling lasers remain on continuously. The histogram fits well to an exponential with a decay time of 56 ± 6 s. This ion lifetime is not long enough for heating rate measurements or quantum information processing.

Measurements of the ion lifetime without Doppler cooling can provide insight into the ion loss mechanism. The dark lifetime is measured by loading a single ion, turning off the Doppler cooling lasers for a controlled amount of time, and turning the Doppler cooling lasers back on and observing whether the ion is still trapped. This is repeated many times for each dark time to determine the probability of keeping an ion as a function of the length of time that the Doppler cooling lasers are off, shown in Figure 3-13. This should fit to an exponential if the ion lifetime is limited by background gas collisions or to a step function if the lifetime is limited by ion heating. The data has both exponential and step function components, indicating that the both background gas and ion heating may play a role in the anomalously short ion lifetime. Much longer ion lifetimes are observed in other surface-electrode ion traps at similar vacuum pressures, so the background gas contribution to the short ion lifetime is not due to the base pressure of the vacuum system. One possible explanation is that the ion lifetime is primarily limited by local outgassing of the SiO_2 layer (see Section 2.4.2). Cooling the trap to cryogenic temperatures reduces both local outgassing and ion heating.

3.6.2 SMIT at 6 K

Testing at 6 K was performed in the largest trap region between the electrodes 3B and 3T. Stray electric fields of the order of (0.1 V)/(100 μm) $\sim 10^3$ V/m are observed, and up to 10 ions can be loaded into the trap simultaneously. While this stray electric field is

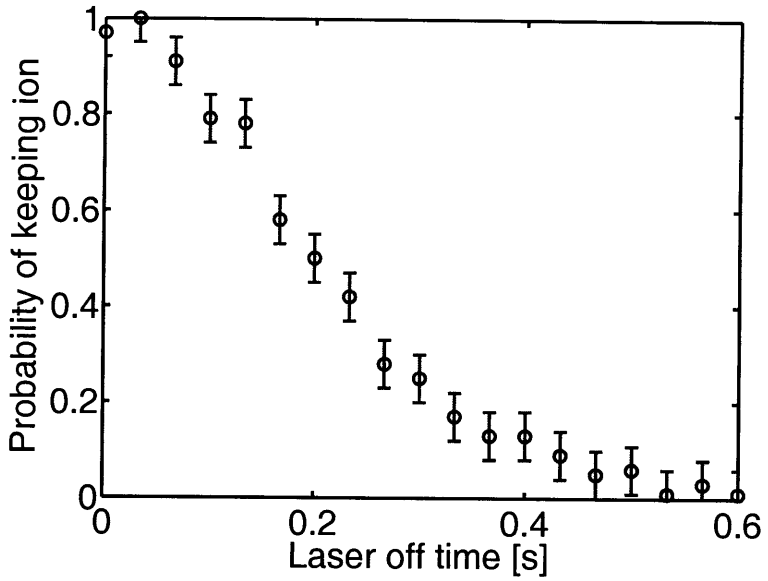

Figure 3-13: Ion lifetime without laser cooling in the SMIT ion trap. The probability of keeping an ion is plotted as a function of the length of time that the Doppler cooling lasers are turned off, measured at room temperature. This should fit to an exponential if the ion lifetime is limited by background gas collisions or to a step function if the lifetime is limited by ion heating. The data has both exponential and step function components, indicating that the both background gas and ion heating may play a role in the anomalously short ion lifetime.

still larger than what is typically observed with photoionization loading, it is two orders of magnitude smaller than that observed at room temperature. The cryogenic testing trap failed when some of the DC electrodes delaminated from the substrate after temperature cycling between room temperature and 6 K five times and cleaning in water and isopropanol (see Figure 3-14).

The ion lifetime was measured at 6 K using the three ions shown in Figure 3-15 to be 4.5 ± 1.1 hours. This ion lifetime is improved by two orders of magnitude over the lifetime at room temperature and is long enough for both heating rate measurements and quantum information processing.

The heating rate is measured by sideband cooling to the ground state of the axial motional mode; waiting 0, 2, or 4 ms; and measuring the relative sizes of the red and blue motional sidebands to determine the expectation value of the number of motional quanta as a function of time. Figure 3-16 shows the red and blue motional sidebands measured immediately after sideband cooling and 2 ms after sideband cooling. The average number of quanta in the axial motional mode as a function of wait time after sideband cooling is shown in Figure 3-17, along with a linear fit which determines the heating rate in quanta per second.

The heating rate, shown in Figure 3-18, is found to be a strong function of the RF amplitude. This is unexpected because the RF amplitude does not affect the frequency of the axial motional mode. This suggests that part of the heating observed here is due to thermalization of the axial motional mode with the radial modes. The radial modes are not sideband cooled and the y' radial mode is only weakly Doppler cooled due to the small

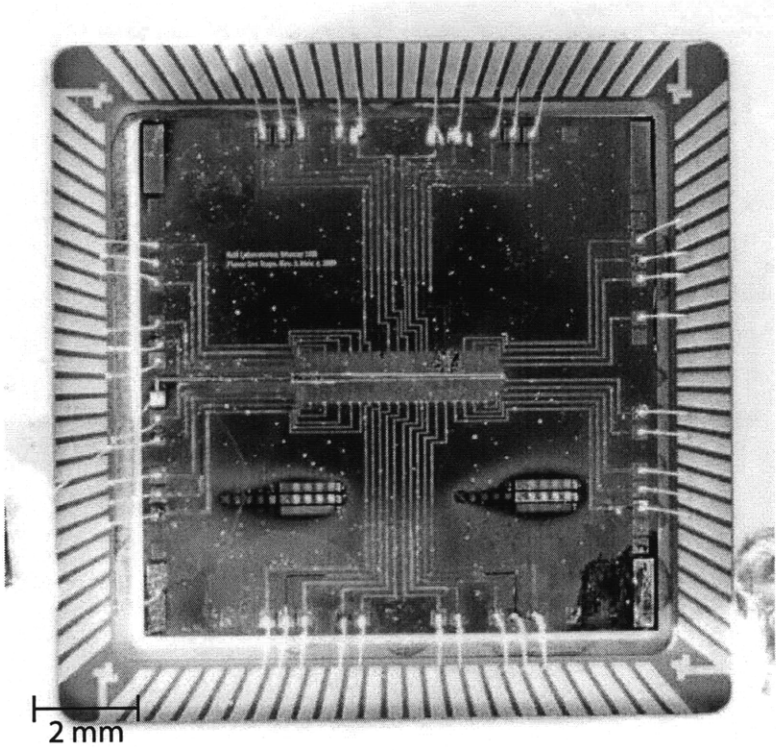

Figure 3-14: SMIT ion trap after failure in the cryogenic testing setup. The delaminated electrodes are near the upper right corner of the trap. The dots visible all over the trap are the result of earlier attempts to load the trap using laser ablation before an oven was installed in the cryostat.

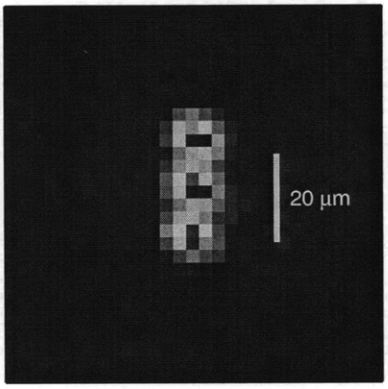

Figure 3-15: Image of three $^{88}Sr^{+}$ ions trapped in the SMIT trap at 6 K. The ion lifetime at 6 K is measured to be 4.5 ± 1.1 hours using these ions.

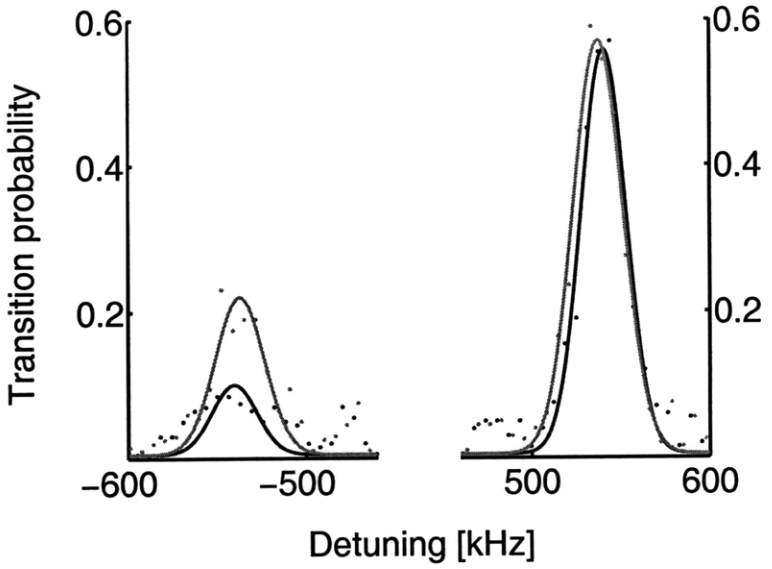

Figure 3-16: Spectra of the 674 nm $^{88}Sr^{+}$ $S_{1/2}, m = -1/2 \leftrightarrow D_{5/2}, m = -5/2$ transition showing the red (left) and blue (right) motional sidebands. The data points in blue (green) are taken with a 0 ms (2 ms) delay between sideband cooling and measurement. The solid lines are fits used to determine the average number of quanta in the axial motional mode.

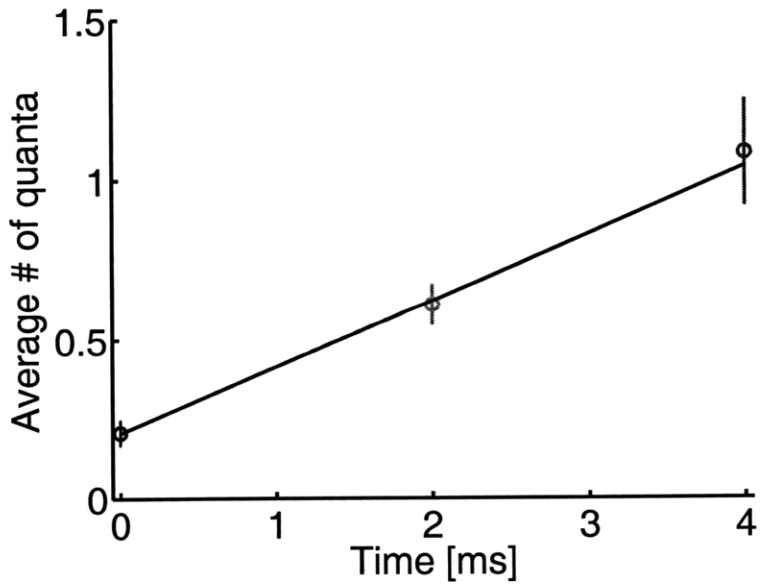

Figure 3-17: Motional heating rate measurement in the SMIT trap at 6 K. The average number of motional quanta in the axial mode is plotted as a function of wait time between sideband cooling and temperature measurement. The slope of the linear fit shown in black gives the heating rate.

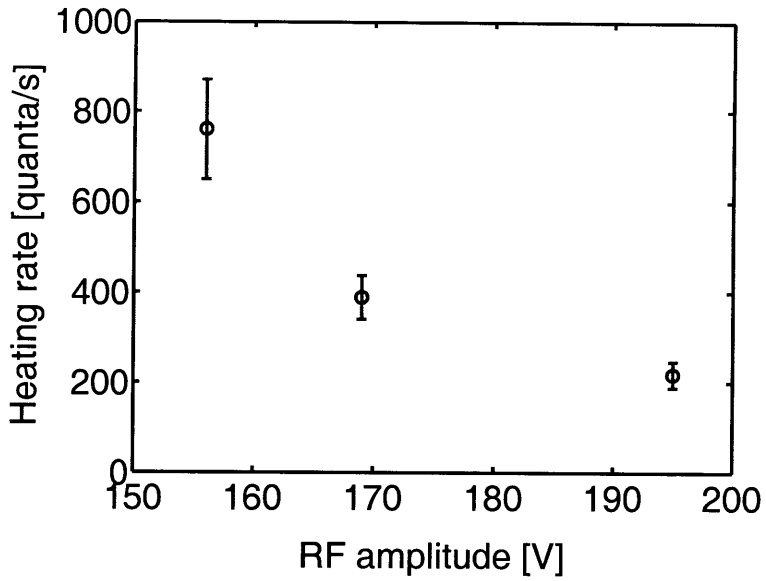

Figure 3-18: Motional heating rate results in the SMIT trap at 6 K. The heating rate of the axial motional mode is plotted as a function of the amplitude of the RF trap drive. The heating rate is smaller at higher RF amplitudes. This suggests that part of the ion heating measured here is due to coupling of the initially cool axial mode to the relatively hot radial modes. The radial modes move further away in frequency at higher RF amplitude, which reduces the coupling. The intrinsic heating rate of the trap is thus $\leq 220 \pm 30$ quanta/s.

projection of the wavevector of the Doppler cooling laser on the y' principal axis. As the RF amplitude is turned up, the radial modes move further away from the axial mode in frequency and the coupling between the radial and axial modes is reduced. The intrinsic heating rate of the trap is upper bounded by the heating rate measured at the highest RF amplitude: 220 ± 30 quanta/s.

While this trap is unsuitable for quantum information processing at room temperature due to the short ion lifetime, its behavior is much improved at 6 K. The stray electric fields are reduced and the ion lifetime is increased by two orders of magnitude. The ion heating rate at 6 K is $\leq 220 \pm 30$ quanta/s at a secular frequency of 540 kHz and an ion height of 79 μm above the trap surface. This is small enough to allow fault tolerant quantum information processing.

3.7 MIT microfabricated trap evaluation results

This section presents the results of testing of some other microfabricated surface-electrode ion traps. These traps were fabricated in the MIT EML (Exploratory Materials Lab) microfabrication facility by Yufei Ge, and are described in detail in References [LGA+08, LGL+08, Lab08]. There are two trap designs. Both designs are single layer metal electrodes on a single crystal quartz substrate, with a single etch step defining the electrodes. While this design is not straightforwardly compatible with integrated optics or electronics like the SMIT trap, it is quick to fabricate and can be used to try different materials for the trap electrodes. The two trap designs tested here are evaporated silver electrodes and electroplated gold electrodes.

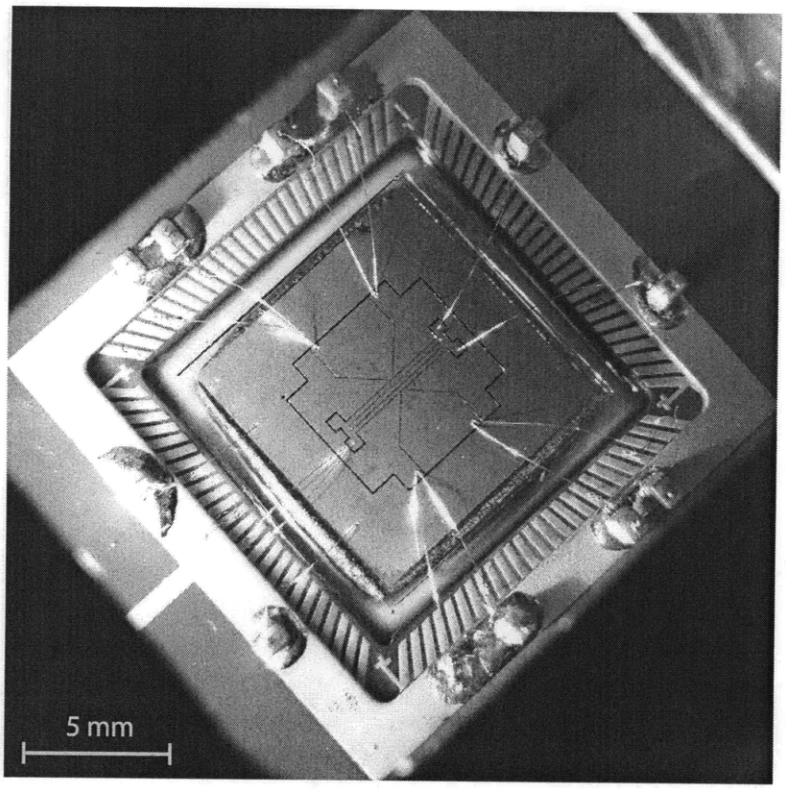

Figure 3-19: Photograph of the silver surface-electrode ion trap mounted in the room temperature trap evaluation setup. The chip is 1 cm by 1 cm, and the ion height above the trap is 150 μm. The capacitors soldered onto the edge of the CPGA are used to filter the RF from the DC electrodes. The frame around the image is a metal plate mounted 1 cm above the trap which partially screens the trap from stray electric fields.

3.7.1 Silver trap at room temperature

Two silver traps were tested at room temperature (see Figure 3-19). The traps were mounted in CPGA chip carriers identical to those used for the SMIT traps using EPO-TEK 353ND epoxy. Ten pF capacitors were soldered to the CPGA ground and wirebonded to the DC electrodes to reduce RF capacitive pickup on the DC electrodes (note that this was not necessary in the SMIT trap due to the built-in capacitive divider). The ion heights in the two traps were 150 μm and 100 μm above the trap surface, and the vacuum pressure was 5×10^{-10} torr. The ion lifetime in both traps was observed to be about 10 minutes.

The motional heating rate was measured by a technique called Doppler recooling [WEL+07]. In this technique the ion is Doppler cooled, then the Doppler cooling laser is turned off for a variable delay time, and finally the Doppler cooling laser is turned back on and the temporal dynamics of the photon scattering rate are measured to determine the temperature. This measurement is repeated for different delay times to determine the motional heating rate. The advantages of Doppler recooling over the sideband technique are that it is simpler and it works for heating rates which are too large to allow sideband cooling.

Figure 3-20 shows an example of the temporal dynamics of the photon scattering rate during Doppler recooling in the 150 μm trap. In order for the data to fit the model presented in Reference [WEL+07], the saturation parameter and atomic linewidth need to be used

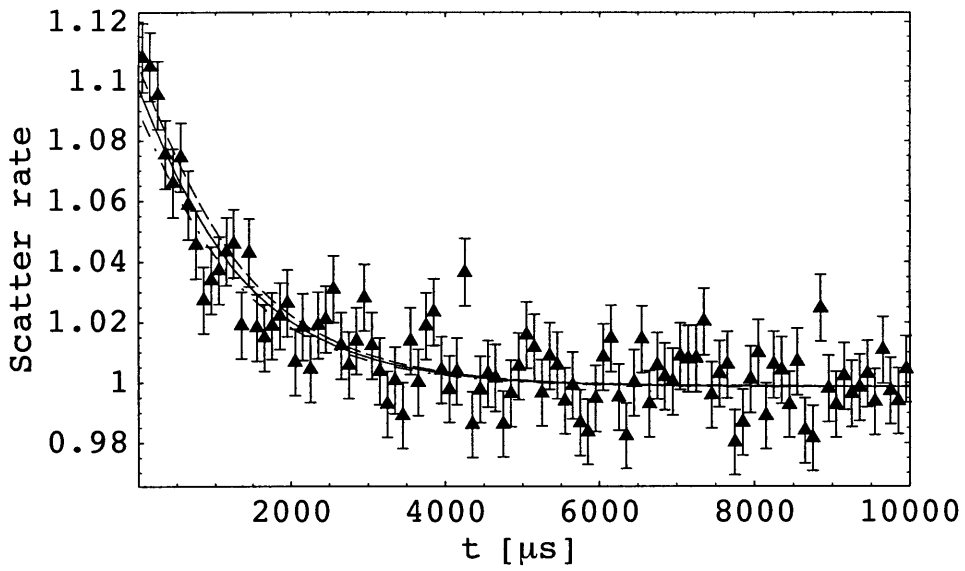

Figure 3-20: Sample Doppler recooling temperature measurement data. The scatter rate, normalized to the steady state scatter rate, is plotted as a function of time starting when the Doppler cooling laser turns on after it has been off for 1 ms. While the Doppler cooling laser is off, the ion heats up and is Doppler shifted into resonance so that when the Doppler cooling laser turns back on the scatter rate is higher than the steady state value. This particular data corresponds to an initial ion temperature $\langle n \rangle = 34000 \pm 3000$ motional quanta.

as fit parameters in addition to the ion temperature. The fitting routine comes up with a saturation parameter of 1326 and an atomic linewidth of 2.4 MHz. These combine to give a power broadened atomic linewidth of 87 MHz, which is the same order of magnitude as the experimentally observed power broadened linewidth of 116 MHz. The interpretation of this is that the repumping rate of the $D_{3/2}$ state limits the scattering rate on the $S_{1/2} \leftrightarrow P_{1/2}$ transition to correspond to that of a 2.4 MHz linewidth transition. The heating rate measured in the 150 μm trap using Doppler recooling is $(30 \pm 1) \times 10^6$ quanta/s at a secular frequency of 860 kHz (see Figure 3-21).

This measurement was confirmed to be consistent with the heating rate measured using another method. In this alternative method the minimum Doppler cooling rate required to keep an ion from boiling out of the trap is determined, and set equal to the heating rate. The heating rate measured using the minimum Doppler cooling power method in the 150 μm silver trap is $(27 \pm 6) \times 10^6$ quanta/s. While this measurement has larger errorbars than the Doppler recooling method, it is a useful check that the Doppler cooling method is still valid despite the fact that the saturation power and the atomic linewidth had to be used as fit parameters.

Because the motional heating rate in the 150 μm silver trap is much higher than would be expected for a trap of its size, a second silver trap was measured. The heating rate in the second trap was $(12.7 \pm 0.3) \times 10^6$ quanta/s with an ion height of 100 μm and a secular frequency of 1.13 MHz. Thus, it seems that silver traps have a very high motional heating rate at room temperature.

Measurement of silver traps at 6 K show a motional heating rate which is suppressed by

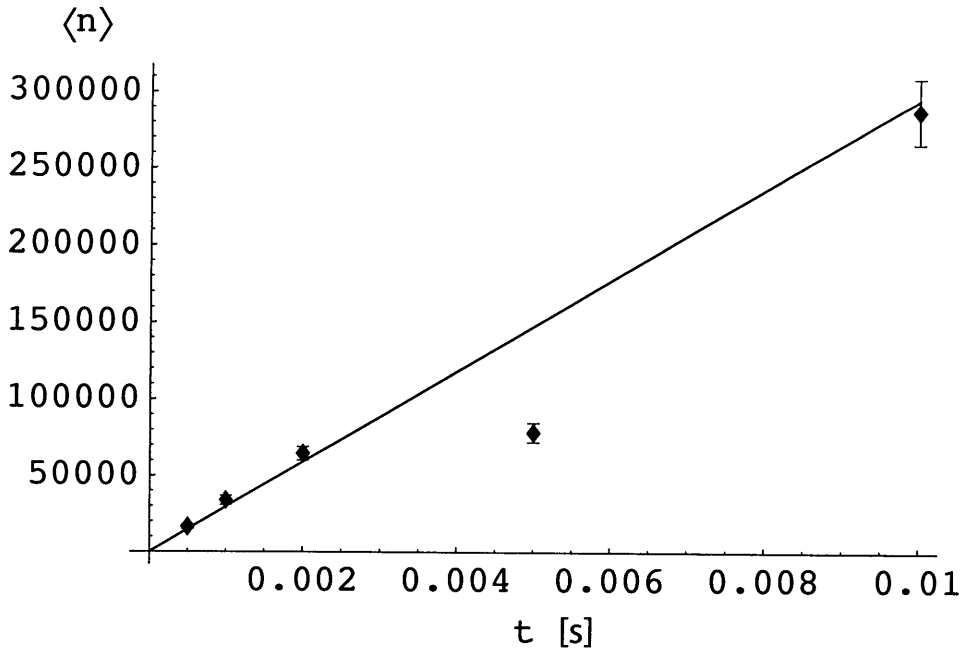

Figure 3-21: Motional heating rate measurement in the silver surface-electrode ion trap at room temperature. The average number of motional quanta in the axial mode is plotted as a function of time that the Doppler cooling laser is off. The slope of the linear fit gives the heating rate $(30 \pm 1) \times 10^6$ quanta/s.

several orders of magnitude to 6.8 ± 0.3 quanta/s in a 150 μm trap with a secular frequency of 1 MHz (see Reference [LGA+08]).

3.7.2 Gold trap at room temperature

One gold trap with an ion height of 75 μm above the trap surface was tested at room temperature (see Figure 3-22). The trap was mounted in a CPGA and RF grounding capacitors were installed identically to the silver traps. Because the trap temperature is found to be so important for the ion heating rate, however, extra heating and temperature measurement elements were added to the CPGA in order to measure the ion motional heating rate as a function of trap temperature for a temperature range between room temperature and a few tens of degrees higher. A heater consisting of a ring of 0.002 inch thick stainless steel foil with resistance 0.5 Ω was epoxied (with EPO-TEK 353ND) to the bottom of the CPGA, and a calibrated silicon diode temperature sensor (Lakeshore DT-670-SD) was epoxied (again, with EPO-TEK 353ND) to the top of the CPGA. The ion lifetime in this trap was about 30 minutes.

The motional heating rate of the axial mode was measured using the sideband method. At room temperature, the heating rate was 5400 ± 400 quanta/s at a secular frequency of 773 kHz. With 2 A going through the heater, the trap temperature was 350 K and there was no change of the ion motional heating rate within the measurement error. With 3 A going through the heater, the ion lifetime dropped to a few seconds and it was impossible to measure the motional heating rate.

Cryogenic cooling of the gold trap to 10 K resulted in suppression of the heating rate

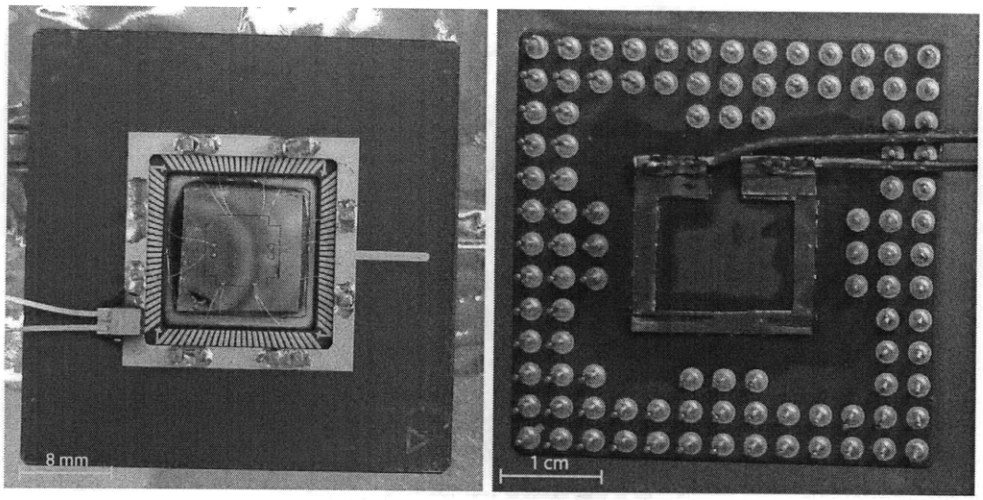

Figure 3-22: Photographs of the gold surface-electrode ion trap. The photograph on the left shows the top of the CPGA with the ion trap and filter capacitors mounted. The chip is 1 cm by 1 cm, and the ion height above the trap is 75 μm. The additional element on the lower left of the CPGA is a calibrated silicon diode temperature sensor. The photograph on the right shows the bottom of the CPGA. There is a stainless steel foil heater glued to the center.

to 2.9 ± 0.2 quanta/s with a 75 μm ion height and a secular frequency of 1 MHz [LGL+08].

3.8 Motional heating sources

All three types of traps evaluated here have motional heating rates which are small enough for large-scale quantum information processing when they are cooled to cryogenic temperatures. Cryogenic cooling, however, adds significant complexity to the experimental apparatus, so it would be beneficial to figure out how to obtain low ion heating rates in small surface-electrode ion traps at room temperature. This requires an understanding of the source of the ion motional heating.

Ion motional heating is caused by electric field fluctuations at the motional frequency of the ion according to [SOT97, WMI+98a, TKK+99]

$$\dot{n}_i = \frac{Q^2}{4m\hbar\omega_i} S_{E_i}(\omega_i) \ . \tag{3.2}$$

Here $\dot{n}_i$ is the motional heating rate of motional mode i in quanta per second, Q is the ion charge, m is the ion mass, $\hbar$ is the Planck constant, ω_i is the secular frequency of motional mode i, and $S_{E_i}(\omega_i)$ is the spectral density of electric field noise along the i direction at the secular frequency of the ion. Understanding the source of the ion motional heating amounts to understanding the source of electric field fluctuations above a metal surface.

3.8.1 Thermal ion heating

One source of ion heating is thermal (Johnson) noise in either the resistance of the trap electrodes or in the resistance of the drive electronics. The geometrical calculation of the magnitude of electric field noise at the ion position given some resistance of an electrode or

voltage source can be carried out either in the straightforward way (electrostatic modeling of the electric field generated by the appropriate voltage noise), or by calculating how much energy would be dissipated in the resistance of the trap electrode or voltage source by ion motion and using the fluctuation-dissipation theorem [CW51, LYS07]. The electric field noise is then inserted into Equation 3.2 to determine the ion motional heating rate.

Unfortunately, when these calculations are carried out, the heating rates due to thermal noise are found to be one or more orders of magnitude smaller than the heating rates observed in experiments. For example, the thermal heating rate in the SMIT trap at room temperature is predicted to be of the order of 10 quanta/s for $^{88}Sr^{+}$ with a secular frequency of 1 MHz. This is reduced to of order 0.01 quanta/s at 6 K (the electrical resistivity of 1 μm aluminum films decreases by about 2 orders of magnitude upon cooling from room temperature to 6 K [SESD81]), which is about four orders of magnitude smaller than what is observed in the experimental measurement.

Furthermore, thermal noise should generate motional heating rates which scale linearly with the temperature times the resistance (which in general depends on temperature), inversely with the trap size squared, and inversely with the secular frequency. All three of these scalings are at odds with what is observed in experiments: temperature scaling which is a power law in temperature with the power changing between measurements in the same trap [LGL+08], trap size scaling which looks like one over the trap size to the fourth power [DOS+06], and secular frequency scaling which looks like one over the secular frequency squared [DOS+06].

3.8.2 Anomalous ion heating

Ion motional heating which is not due to thermal fluctuations is called anomalous ion heating. Several models for anomalous ion heating have been proposed, but experiments thus far have not been able to distinguish between them. Among the more promising models are fluctuating potentials on crystal facets [CDB92], fluctuating charge traps [OCK+06], and fluctuating surface adsorbates [RO92]. All of these models (assuming a small spatial extent and an activation energy driven process) predict the correct trap size and frequency scaling [LGL+08]. The correct temperature scaling can also be obtained from the models by assuming a distribution of fluctuators with different activation energies [LGL+08]. Further understanding will require a more detailed understanding of the surface physics of metal films.

3.9 Discussion

Figure 3-23 summarizes all of the ion motional heating rate measurements discussed in this chapter. Ion heating is suppressed by several orders of magnitude upon cooling to 6 K, where the heating rates are small enough to allow fault-tolerant quantum information processing in all of the traps evaluated here.

The SMIT trap in particular offers a promising direction for future development. This work demonstrates that the concept – an aluminum trap fabricated on a silicon substrate following standard silicon VLSI techniques – is a viable method of producing scalable, multiplexed ion traps with long ion lifetimes and low motional heating rates at cryogenic temperatures. Some things which should be addressed are the room temperature ion lifetime and the trap reliability. The poor room temperature ion lifetime might be improved by reducing the height of the 10 μm SiO_2 pillars which are used to raise the RF electrodes above

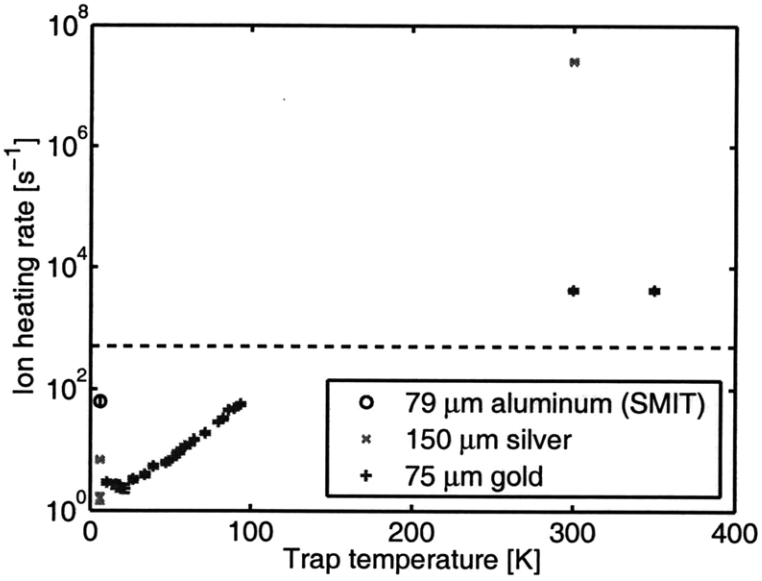

Figure 3-23: Summary of ion motional heating measurements. The ion heating rate scaled to a 1 MHz secular frequency is plotted as a function of trap temperature for the 79 μm ion height SMIT trap, the 100 and 150 μm ion height silver traps, and the 75 μm ion height gold trap. The data for the silver and gold traps at cryogenic temperatures are representative of the results of References [LGA$^+$08] and [LGL$^+$08], respectively, and are not discussed elsewhere in this thesis. Note that the silver trap in particular shows a 7 order of magnitude reduction in the ion motional heating rate upon cooling from room temperature to 6 K. The black dashed line corresponds to the fault tolerance threshold for the parameters given in Reference [Ste07].

the plane of the chip. They could then be deposited in one layer, which might eliminate micro-voids that slowly outgas. This would have the additional benefit of reducing laser scatter from the raised RF electrodes into the ion imaging optics, which was a problem in the cryogenic trap evaluation setup where the laser beam quality is poor due to the multiple layers of windows. The traps might be made more reliable with respect to electrode shorting and delamination by replacing the nitride insulator between the control electrodes and the silicon substrate with SiO_2, which is more robust. The poor trap reliability of the first generation traps prevented testing in more than one trapping zone in this work. Future development can take advantage of the ability to integrate silicon microfabrication with electronics and optics to build an integrated, large-scale trap for trapped ion quantum information processing.

Part II

Trapped ion cavity QED

Chapter 4

Cavity QED

Cavity QED (cavity quantum electrodynamics) is the system of one or more atoms coupled to a small number of modes of the electromagnetic field [MNB+05]. Cavity QED systems can be used for several applications within trapped ion quantum information processing, including quantum non-demolition cooling and quantum interconnects.

Quantum non-demolition cooling is the process of cooling the motional state of a trapped atom or ion without decohering the internal state. Some method of quantum non-demolition cooling will be necessary for large-scale trapped ion quantum information processing because all of the high-fidelity two qubit gates require that the motional state of the ions is cooled to near the quantum mechanical ground state. As the ions heat up during the course of a computation [LGL+08, BVO+09], they will have to be periodically recooled in order to perform quantum gates. Unfortunately, free space sideband cooling [DBIW89], which is typically used to prepare the ions in the motional ground state before the computation begins, cannot be used during the computation because it decoheres the internal qubit state of the trapped ion. Cavity cooling is one possible method quantum non-demolition cooling, and it is the subject of Chapter 5.

Trapped ion quantum interconnects perform coherent mapping between single ion and single photon states, which will be necessary to implement a quantum network [Kim08]. Quantum networks enable long distance quantum communication via quantum repeaters [BDCZ98]. Trapped ion quantum interconnects are the subject of Chapters 6 and 7.

This chapter describes the basic theory of cavity QED. Section 4.1 presents the Hamiltonian of a two-level atom coupled to an optical cavity. Section 4.2 discusses the effects of decoherence in the master equation framework. Section 4.3 describes the quantum Langevin equations for cavity QED with a two-level atom, which can be solved analytically to obtain the expectation values of observables for the cavity QED system. Finally, Section 4.4 specializes to describe cavity QED with $^{88}Sr^{+}$ and quantifies the deviation from the two-level model using a numerical solution of the master equation.

Sections 4.1, 4.2, and 4.3 review previous work. Section 4.4 is original work.

4.1 Hamiltonian

The model cavity QED system consists of a single two-level atom coupled to a single mode of the electromagnetic field (see Figure 4-1). This model system is closely approximated by a single hydrogen-like atom in an optical cavity, where the coupling of the atom to the cavity mode is enhanced relative to its coupling to the free space electromagnetic field.

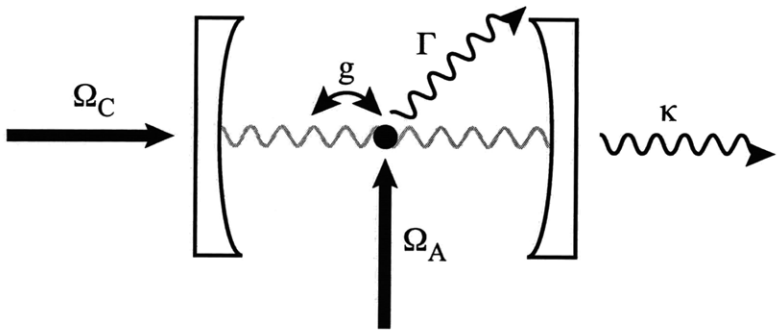

Figure 4-1: Model cavity QED system. A single two-level atom is coupled to a single mode of the electromagnetic field, which is enhanced relative to the free space electromagnetic field by an optical cavity, with coupling strength g. The atom decays into free space with energy decay rate Γ, and the cavity mode decays with energy decay rate κ. The atom is pumped with a laser with Rabi frequency Ω_A, and the cavity is pumped with a laser with Rabi frequency Ω_C.

Either the atom or the cavity is pumped by a laser. The Hamiltonian of this system, in the rotating wave approximation, is [CTDRG98, MvdS99]

$$\begin{aligned} H &= -\hbar\omega_A\sigma^\dagger\sigma - \hbar\omega_C a^\dagger a + \hbar g\left(a^\dagger\sigma + \sigma^\dagger a\right) \\ &\quad + \frac{\hbar\Omega_A}{2}\left(\sigma^\dagger e^{-i\omega_L t} + \sigma e^{i\omega_L t}\right) + \frac{\hbar\Omega_C}{2}\left(a^\dagger e^{-i\omega_L t} + a e^{i\omega_L t}\right) . \end{aligned} \tag{4.1}$$

Here, σ and $\sigma^\dagger$ are the lowering and raising operators for the two-level atom, a and $a^\dagger$ are the lowering and raising operators for the harmonic oscillator cavity mode, ω_A is the atom frequency, ω_C is the cavity frequency, ω_L is the laser frequency, g is the coupling strength between the atom and the cavity, Ω_A is the Rabi frequency of the laser acting on the atom, and Ω_C is the Rabi frequency of the laser acting on the cavity. In this chapter the motion of the atom is neglected.

In the absence of any lasers ($\Omega_A = \Omega_C = 0$), the Hamiltonian in Equation 4.1 reduces to the familiar Jaynes-Cummings Hamiltonian [JC63]. The Jaynes-Cummings Hamiltonian can be decomposed into non-interacting, two-level manifolds spanned by the states $|g,n\rangle$ and $|e,n-1\rangle$. The Hamiltonian acting on manifold n is

$$\begin{aligned} H_n = \hbar n\omega_C|g,n\rangle\langle g,n| \quad &+ \quad \hbar\left[(n-1)\,\omega_C + \omega_A\right]|e,n-1\rangle\langle e,n-1| \\ &+\hbar\sqrt{n}g\left(|e,n-1\rangle\langle g,n| + |g,n\rangle\langle e,n-1|\right) . \end{aligned} \tag{4.2}$$

The energy eigenstates are

$$|\pm,n\rangle = \mp\frac{1}{\sqrt{2}}\sqrt{1 \pm \frac{\delta_{CA}^2}{\sqrt{\delta_{CA}^2 + 4ng^2}}}|g,n\rangle - \frac{1}{\sqrt{2}}\sqrt{1 \mp \frac{\delta_{CA}^2}{\sqrt{\delta_{CA}^2 + 4ng^2}}}|e,n-1\rangle \tag{4.3}$$

and the energy eigenvalues are

$$E_{\pm,n} = \hbar\left(n\omega_C - \frac{\delta_{CA}}{2}\right) \pm \frac{\hbar}{2}\sqrt{\delta_{CA}^2 + 4ng^2} , \tag{4.4}$$

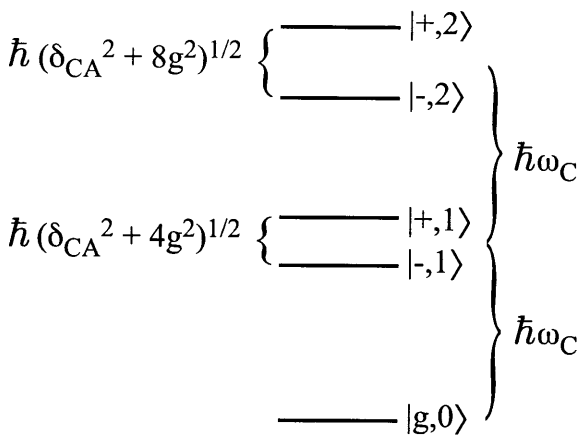

Figure 4-2: Energy eigenstates of the Jaynes-Cummings Hamiltonian. The eigenstates of manifold n are split by $\hbar\sqrt{\delta_{CA}^2 + 4ng^2}$.

where $\delta_{CA} = \omega_C - \omega_A$ is the cavity-atom detuning. The coupling of the atom to the cavity is said to dress the states of the atom, and the energy eigenstates of the combined system are called dressed states. The energy eigenstates of the Jaynes-Cummings Hamiltonian are shown in Figure 4-2.

For the treatment of the master equation in the following section, it is more convenient to transform to the rotating frame using the transformation

$$H \rightarrow UHU^\dagger - i\hbar U\frac{\partial U^\dagger}{\partial t} \tag{4.5}$$

$$|\psi\rangle \rightarrow U|\psi\rangle \tag{4.6}$$

with

$$U = e^{i\omega_L t(\sigma^\dagger\sigma + a^\dagger a)} \ . \tag{4.7}$$

The Hamiltonian in Equation 4.1 becomes

$$H = -\hbar\delta_A\sigma^\dagger\sigma - \hbar\delta_C a^\dagger a + \hbar g\left(a^\dagger\sigma + \sigma^\dagger a\right) + \frac{\hbar\Omega_A}{2}\left(\sigma^\dagger + \sigma\right) + \frac{\hbar\Omega_C}{2}\left(a^\dagger + a\right) \ , \tag{4.8}$$

where $\delta_A = \omega_L - \omega_A$ is the laser-atom detuning and $\delta_C = \omega_L - \omega_C$ is the laser-cavity detuning.

4.2 Decoherence and the master equation

In order to include the effects of decoherence, it is necessary to go the the master equation formalism [GZ04]. Both the atom and the cavity are coupled to the free space electromagnetic field, which acts as a zero temperature reservoir. The atom decays to its ground state with energy decay rate Γ, and the cavity decays to its ground state with energy decay rate κ. The system is described by a density matrix ρ, which evolves according to the master equation

$$\frac{\partial\rho}{\partial t} = -\frac{i}{\hbar}[H,\rho] + \sum_\alpha\left(L_\alpha\rho L_\alpha^\dagger - \rho L_\alpha^\dagger L_\alpha - L_\alpha^\dagger L_\alpha\rho\right) \ . \tag{4.9}$$

The L_α are the Liouvillian operators which describe the effects of decoherence.

4.2.1 Atom and cavity decay

The atom and cavity decay are described by Liouvillian operators

$$L_\sigma = \sqrt{\Gamma}\sigma \tag{4.10}$$

and

$$L_a = \sqrt{\kappa}a \ . \tag{4.11}$$

4.2.2 Laser linewidth

The effects of a non-zero laser linewidth can be included in the master equation model by solving the master equation with a stochastic phase noise added to the laser [LDP87, MBR+04]. For Lorentzian phase noise with FWHM Γ_L and restricting the system to the manifold spanned by $|g,0\rangle$, $|e,0\rangle$, and $|g,1\rangle$, it turns out that this is equivalent to including an extra Liouvillian operator

$$L_{=}\sqrt{\Gamma_L}|g,0\rangle\langle g,0| \ . \tag{4.12}$$

In general the master equation in Equation 4.9 is difficult to solve, and expectation values must be computed numerically.

4.3 Quantum Langevin equations

If the non-zero laser linewidth is neglected and the laser Rabi frequencies are small compared with the atom and cavity decay rates, then it is possible to solve for the expectation values of the system analytically using the quantum Langevin equations [MNP+06]. The expectation value of a time-independent operator $\mathcal{O}$ evolves according to

$$\frac{d}{dt}\mathcal{O} = \mathrm{tr}\left(\mathcal{O}\frac{\partial\rho}{\partial t}\right) \ . \tag{4.13}$$

Substituting the master equation into the above expression and evaluating the commutators results in the following expressions for the time evolution of the operators $\langle\sigma\rangle$ and $\langle a\rangle$:

$$\frac{d}{dt}\langle\sigma\rangle = i\tilde{\delta}_A\left(\langle\sigma\rangle - \frac{g}{\tilde{\delta}_A}\langle a\rangle - \frac{\Omega_A}{2\tilde{\delta}_A}\right) \tag{4.14}$$

and

$$\frac{d}{dt}\langle a\rangle = i\tilde{\delta}_C\left(\langle a\rangle - \frac{g}{\tilde{\delta}_C}\langle\sigma\rangle - \frac{\Omega_C}{2\tilde{\delta}_C}\right) \tag{4.15}$$

where $\tilde{\delta}_A = \delta_A + i\Gamma/2$ and $\tilde{\delta}_C = \delta_C + i\kappa/2$. Here the fact that the laser Rabi frequencies are small compared with the atom and cavity decay rates has been used to set $[\sigma,\sigma^\dagger] = 1$. This amounts to assuming that the two level atom can be approximated as a harmonic oscillator, which is reasonable as long as the population of the atomic excited state much less than one. The steady state values of the population of the atomic excited state $\langle\sigma^\dagger\sigma\rangle$ and the

number of photons in the cavity $\langle a^\dagger a \rangle$ are then

$$\left\langle \sigma^\dagger \sigma \right\rangle = |\langle \sigma \rangle|^2 = \left| \frac{\frac{\Omega_A}{2\tilde{\delta}_A} + \frac{g\Omega_C}{2\tilde{\delta}_A\tilde{\delta}_C}}{1 - \frac{g^2}{\tilde{\delta}_A\tilde{\delta}_C}} \right|^2 \tag{4.16}$$

and

$$\left\langle a^\dagger a \right\rangle = |\langle a \rangle|^2 = \left| \frac{\frac{\Omega_C}{2\tilde{\delta}_C} + \frac{g\Omega_A}{2\tilde{\delta}_A\tilde{\delta}_C}}{1 - \frac{g^2}{\tilde{\delta}_A\tilde{\delta}_C}} \right|^2 . \tag{4.17}$$

4.3.1 Cooperativity

The cooperativity, η_C, is defined as the ratio of the rate of scattering photons into the cavity over the rate of scattering photons into free space. Here $\Omega_C = 0$. The rate of scattering photons into the cavity is $\kappa \langle a^\dagger a \rangle$ and the rate of scattering photons into free space is $\Gamma \langle \sigma^\dagger \sigma \rangle$, so the cooperativity is

$$\eta_C = \frac{\kappa \langle a^\dagger a \rangle}{\Gamma \langle \sigma^\dagger \sigma \rangle} = \frac{4g^2}{\kappa\Gamma} . \tag{4.18}$$

4.3.2 Spectra

The cavity transmission spectra with $\Omega_A = 0$ is given by

$$T = \left(\frac{\kappa}{\Omega_C}\right)^2 \left\langle a^\dagger a \right\rangle = \left| \frac{\frac{\kappa}{2\tilde{\delta}_C}}{1 - \frac{g^2}{\tilde{\delta}_A\tilde{\delta}_C}} \right|^2 . \tag{4.19}$$

The cavity transmission spectra is plotted in Figure 4-3 for several values of the cooperativity. When the cooperativity is zero (equivalent to the situation without an atom in the cavity), the transmission is a Lorentzian with a FWHM of κ. As the cooperativity increases the single Lorentzian transmission peak first reduces in amplitude, then splits into two peaks separated by $\sqrt{\delta_{CA}^2 + 4g^2}$. These two peaks correspond to the dressed states calculated in Section 4.1.

4.4 Cavity QED with $^{88}Sr^+$

The next chapter describes a cavity QED experiment with $^{88}Sr^+$ and a cavity near resonance with the $S_{1/2} \leftrightarrow P_{1/2}$ transition. This situation differs from the simple model of described in the previous sections of this chapter both because $^{88}Sr^+$ is not a two-level atom and the cavity has more than one mode. This section describes a master equation model of cavity QED with $^{88}Sr^+$ and a cavity near resonance with the $S_{1/2} \leftrightarrow P_{1/2}$ transition and how it differs from the simple model in the previous sections.

4.4.1 Master equation

The relevant atomic states are the strontium $S_{1/2}$, $P_{1/2}$, and $D_{3/2}$ states including magnetic sublevels (see Figure 3-1), for a total of 8 states. The cavity is assumed to have two

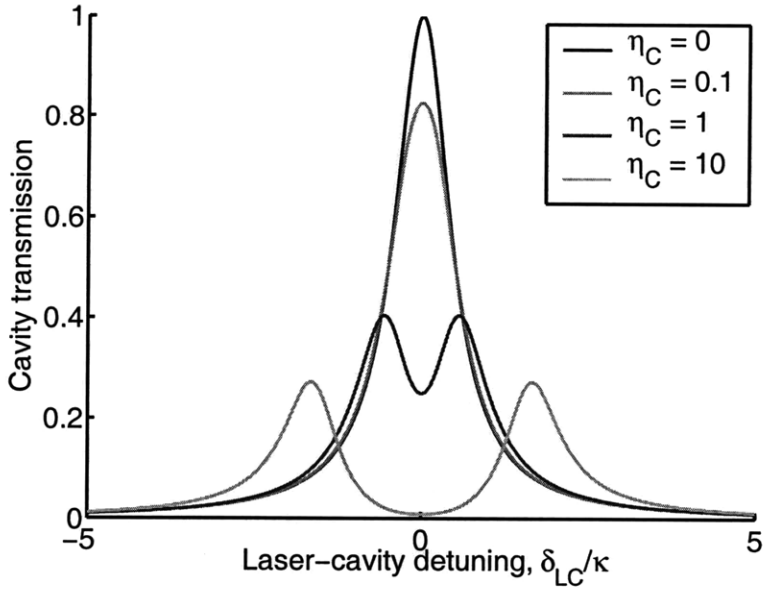

Figure 4-3: Model cavity QED transmission spectra. The transmission of a cavity coupled to a two-level atom is plotted as a function of the laser-cavity detuning δ_{LC} with the cavity-atom detuning $\delta_{CA} = 0$ and $\Gamma = \kappa$.

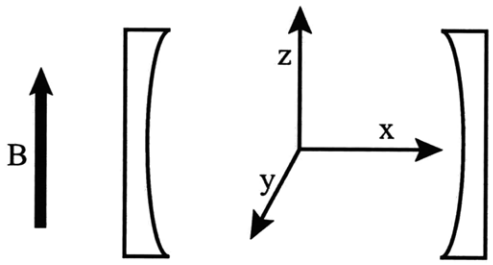

Figure 4-4: $^{88}Sr^{+}$ cavity QED geometry. The magnetic field is along the z-axis and the cavity axis is along the x-axis. The two polarization modes of the cavity are linear polarization along the y and z-axes.

degenerate modes which differ in polarization. In the low saturation limit each of these modes can have zero or one photons, for a total of 4 cavity states. States where both the atom and the cavity are excited (atom in the $P_{1/2}$ state, one or both of the cavity modes have one photon) can be neglected in the low saturation limit, so the total number of states considered in this model is $8 \times 4 - 6 = 26$.

The geometry is shown in Figure 4-4. The magnetic field, which sets the quantization axis of the atom, is along the z-axis. The cavity axis is along the x-axis, Finally, the two polarization modes of the cavity are linear polarization along the y and z-axes.

Hamiltonian

The Hamiltonian, in the rotating frame and under the rotating wave approximation, can be broken up into the following terms:

$$H = H_A + H_C + H_{AC} + H_{AL} + H_{CL} \ . \tag{4.20}$$

The Hamiltonian of the atom, H_A, is given by

$$\begin{aligned} H_A &= \Bigg(\sum_{m_J=\pm 1/2} (\hbar\delta_{SP} + 2\hbar m_J \delta_B)|S, m_J\rangle\langle S, m_J| + \\ &\quad \sum_{m_J=\pm 1/2} \frac{2}{3}\hbar m_J \delta_B |P, m_J\rangle\langle P, m_J| + \\ &\quad \sum_{m_J=\pm 1/2,\pm 3/2} (\hbar\delta_{DP} + \frac{4}{5}\hbar m_J \delta_B)|D, m_J\rangle\langle D, m_J|\Bigg) \otimes \mathbb{1}_A \ . \end{aligned} \tag{4.21}$$

The Hamiltonian of the cavity, H_C, is given by

$$H_C = -\hbar\delta_C \left(a_y^\dagger a_y + a_z^\dagger a_z\right) \otimes \mathbb{1}_A \ . \tag{4.22}$$

The Hamiltonian of the atom-cavity interaction, H_{AC}, is given by

$$\begin{aligned} H_{AC} &= \sum_{\substack{m_J=\pm 1/2 \\ m'_J=\pm 1/2}} \left(\hbar g_{P,m'_J;S,m_J;y} |P, m'_J\rangle\langle S, m_J| \otimes a_y + \hbar g^*_{P,m'_J;S,m_J;y} |S, m_J\rangle\langle P, m'_J| \otimes a_y^\dagger\right) \\ &\quad \sum_{\substack{m_J=\pm 1/2 \\ m'_J=\pm 1/2}} \left(\hbar g_{P,m'_J;S,m_J;z} |P, m'_J\rangle\langle S, m_J| \otimes a_z + \hbar g^*_{P,m'_J;S,m_J;z} |S, m_J\rangle\langle P, m'_J| \otimes a_z^\dagger\right) \ . \end{aligned} \tag{4.23}$$

The Hamiltonian of the atom-laser interaction, H_{AL}, is given by

$$\begin{aligned} H_{AL} &= \Bigg(\frac{1}{2} \sum_{\substack{m_J=\pm 1/2 \\ m'_J=\pm 1/2}} (\hbar\Omega_{P,m'_J;S,m_J} |P, m'_J\rangle\langle S, m_J| + \hbar\Omega^*_{P,m'_J;S,m_J} |S, m_J\rangle\langle P, m'_J| + \\ &\quad \frac{1}{2} \sum_{\substack{m_J=\pm 1/2,\pm 3/2 \\ m'_J=\pm 1/2}} (\hbar\Omega_{P,m'_J;D,m_J} |P, m'_J\rangle\langle D, m_J| + \hbar\Omega^*_{P,m'_J;D,m_J} |D, m_J\rangle\langle P, m'_J|\Bigg) \otimes \mathbb{1}_C \ . \end{aligned} \tag{4.24}$$

Finally, the Hamiltonian of the cavity-laser interaction, H_{CL}, is given by

$$H_{CL} = \frac{1}{2} \sum_{\mu=y,z} \left(\hbar\Omega_v a_\mu^\dagger + \hbar\Omega_\mu^* a_\mu\right) \otimes \mathbb{1}_A \ . \tag{4.25}$$

Here, δ_{SP} and δ_{SP} are the detunings of the 422 nm and 1091 nm lasers from the $S_{1/2} \leftrightarrow P_{1/2}$ and $D_{3/2} \leftrightarrow P_{1/2}$ transitions, respectively; $\delta_B = \mu_B B/\hbar$ is the magnetic field strength in units of frequency, where μ_B is the Bohr magneton and B is the magnetic field; and δ_C is the detuning of the 422 nm laser from the cavity. The Rabi frequencies of the 422 nm and 1091 nm lasers, $\Omega_{P,m'_J;S,m_J}$ and $\Omega_{P,m'_J;D,m_J}$, are defined such that they include the selection

rules appropriate for the laser polarization, and can be written as

$$\Omega_{L',m'_J;L,m_J} = \sqrt{3}\Omega_{L'L}(-1)^{m_J} \sum_{q=-1,0,1} (-1)^q \epsilon_q \begin{pmatrix} J & 1 & J' \\ m_J & q & -m'_J \end{pmatrix} \tag{4.26}$$

where $\Omega_{L'L}$ is the Rabi frequency for a two-level atom and the laser polarization is

$$\hat{\epsilon} = \sum_{q=-1,0,1} \epsilon_q \hat{u}_q \tag{4.27}$$

with $\hat{u}_{-1} = (\hat{x} - i\hat{y})/\sqrt{2}$, $\hat{u}_0 = \hat{z}$, and $\hat{u}_{+1} = -(\hat{x} + i\hat{y})/\sqrt{2}$. The term in brackets on the right of Equation 4.26 is a three-J symbol. The atom-cavity interaction strength can be written as

$$g_{P,m'_J;S,m_J;y} = \sqrt{\frac{2}{3}} g|m'_J - m_J| \tag{4.28}$$

$$g_{P,m'_J;S,m_J;z} = \sqrt{\frac{1}{3}} g|m'_J + m_J| \tag{4.29}$$

where g is the interaction strength for a two-level atom.

Liouvillian

The Liouvillian operators for the atom decay are

$$L_{L',m'_J;L,m_J} = \sqrt{2A_{L\to L'} \sum_{q=-1,0,1} \left| (-1)^q \begin{pmatrix} J & 1 & J' \\ m_J & q & -m_J \end{pmatrix} \right|^2} |L', m'_J\rangle\langle L, m_J| \otimes \mathbb{1}_C \ . \tag{4.30}$$

The possible values of $L', m'_J; L, m_J$ are

$$\begin{array}{l} S, 1/2; P, 1/2 \ , \\ S, -1/2; P, 1/2 \ , \\ S, 1/2; P, -1/2 \ , \\ S, -1/2; P, -1/2 \ , \\ D, 3/2; P, 1/2 \ , \\ D, 1/2; P, 1/2 \ , \\ D, -1/2; P, 1/2 \ , \\ D, 1/2; P, -1/2 \ , \\ D, -1/2; P, -1/2 \ , \text{ and} \\ D, -3/2; P, -1/2 \ . \end{array}$$

The spontaneous decay rates $A_{P_{1/2}\to S_{1/2}}$ and $A_{P_{1/2}\to D_{3/2}}$ can be found in Table 3.1. The Liouvillian operators for the cavity decay are

$$L_\mu = \sqrt{\kappa} a_\mu \otimes \mathbb{1}_A \tag{4.31}$$

where μ can be y or z. Finally, the Liouvillian operators for the laser linewidths are

$$L_{\Gamma_{PS}} = (1 - N_y - N_z)\sqrt{\Gamma_{PS}}|S, m_J, N_y, N_z\rangle\langle S, m_J, N_y, N_z| \,, \tag{4.32}$$

$$L_{\Gamma_{PS}} = (-N_y - N_z)\sqrt{\Gamma_{PS}}|D, m_J, N_y, N_z\rangle\langle D, m_J, N_y, N_z| \tag{4.33}$$

and

$$L_{\Gamma_{PD}} = \sqrt{\Gamma_{PD}}|D, m_J, N_y, N_z\rangle\langle D, m_J, N_y, N_z| \,, \tag{4.34}$$

where Γ_{PS} and Γ_{PD} are the laser linewidths of the 422 nm and 1091 nm lasers, and m_J, N_y, and N_z run over all possible values.

4.4.2 Numerical solution

The master equation is solved with the Hamiltonian and Liouvillian above using a Mathematica script provided in Appendix A. For experimentally reasonable laser powers and detunings, but zero laser linewidths, the cooperativity of $^{88}Sr^+$ is 0.31×0.93 that of a two-level atom, where the factor $\eta_{cg} = 0.31$ comes from the Clebsch-Gordan coefficient for π polarized light on the $^{88}Sr^+$ $S_{1/2} \leftrightarrow P_{1/2}$ transition and the factor $\eta_r = 0.93$ comes from imperfect repumping. The addition of 20 kHz laser linewidths results in an additional reduction of cooperativity $\eta_l = 0.82$, for a total reduction of 0.24 for $^{88}Sr^+$ relative to a two-level atom. The relatively close agreement of this master equation model with the simple two-level atom model presented earlier suggests that the two-level atom theory is sufficient for most of the calculations of cavity QED with $^{88}Sr^+$ in this thesis, provided that the cooperativity η_C is replaced by the effective cooperativity $\eta_{C,eff} = \eta_{cg}\eta_r\eta_l\eta_C$.

Chapter 5

Implementation of resolved sideband cavity cooling

Cavity cooling is a method of laser cooling which uses coherent scattering into an optical cavity to cool particles [HHG+97, VC00, VCB01]. The particle to be cooled is placed in a cavity and excited with a laser tuned to the red of a cavity resonance. The function of the cavity is to enhance the density of modes at the frequency of the cavity resonance [Pur46], so photons scattered into the cavity are preferentially blue shifted relative to the incident photons. Thus, on average, scattering events which remove a photon from the laser and put it into the optical cavity cool the particle.

Cavity cooling can be used to perform quantum non-demolition cooling because the photons that are scattered into the cavity and implement cooling carry away no information about the internal state of the ion. Thus, if all of the scattered photons end up in the cavity, the internal qubit state of the ion is perfectly preserved. Some photons, however, are scattered into free space, and these scattering events can potentially decohere the internal state of the ion. Fortunately, decoherence of the ground state hyperfine manifold due to free space scattering can be suppressed by using a laser which is far detuned from any atomic optical transitions [CMMH94, OLJ+05]. While for free space laser cooling this would cause the cooling limit to increase, the cavity cooling limit is set by the cavity properties and the detuning between the laser and the cavity so the temperature limit of cavity cooling can be low even for large detunings between the laser and any atomic transitions.

An alternative method for quantum non-demolition cooling of trapped ion qubits is sympathetic cooling, where the qubit ions are co-trapped with cooling ions of a different atomic species. Because the Coulomb interaction couples the motional modes of the qubit ions with the cooling ions, the motion of the qubit ion can be cooled by resolved sideband laser cooling of only the cooling ions with little effect on the qubit coherence [HMS+08]. This ability, however, comes at the cost of an extra set of lasers for addressing the cooling ion transitions. In a large scale quantum information processor, it is likely that high finesse optical cavities will already be integrated for quantum communication [Kim08, RBS+08, OMM+09]. This makes cavity cooling relatively easier to implement, requiring only one extra laser.

Previous experiments have demonstrated cavity cooling of neutral atom clouds [CBV03, BCV03] and single neutral atoms [MPS+04, NMH+05, FKG+07]. They have all been in the strong coupling regime, either by using superradiant collective states of many atoms [CBV03, BCV03] or high finesse, low mode volume optical resonators [MPS+04, NMH+05,

FKG+07], and the weak trapping regime. In the strong coupling regime, recoil heating is suppressed relative to cavity cooling, and the cavity cooling limit is set by the cavity linewidth. It is very difficult to reach the strong coupling regime with trapped ions. In the weak trapping regime, the motional frequency of the trapped particles is smaller than the cavity linewidth, and it is impossible to cool to the motional ground state. With trapped ions, it is relatively easier to reach the strong trapping, or resolved sideband regime.

This chapter presents an experimental demonstration of cavity cooling in the resolved sideband regime, where the motional frequency of the trapped particles is larger than the cavity linewidth, and where cavity cooling to the motional ground state is possible. Sections 5.1 and 5.2 describe the experimental setup and the optical cavity. Section 5.3 describes the alignment of the ion position with the cavity standing wave. Section 5.4 presents two measurements of the cooperativity, and Sections 5.5 and 5.6 present measurements of the cavity cooling spectra and the cavity cooling dynamics. Finally, Section 5.7 puts the cavity cooling results in context.

All of the work described in this chapter is original.

5.1 Experimental setup

The experimental setup is shown schematically in Figure 5-1. Ions are confined in a linear RF Paul trap with principle motional axes x, y, and z shown. Both the trap axis and the cavity are oriented along the z axis. The cavity cooling laser propagates along $(\hat{x}+\hat{y})/\sqrt{2}$ and is polarized parallel to the magnetic field direction $(\hat{x}-\hat{y})/\sqrt{2}$. The remaining lasers for Doppler cooling, state preparation and temperature measurement, and repumping all propagate along $\pm(\hat{x}/\sqrt{4}+\hat{y}/\sqrt{4}+\hat{z}/\sqrt{2})$ so that they have nonzero projections along all of the ion motional axes.

5.1.1 Ion trap geometry and trapping parameters

The ion trap is a four rod trap fabricated by the research group of S. Urabe at Osaka University, similar to the one used in Reference [FNTU05] with stainless steel knife blade electrodes held in place by ceramic spacers (see Figure 5-2). It was decided to use a four rod trap instead of a surface-electrode trap so that the ion is well shielded by the trap electrodes from any stray electric charges which might accumulate on the dielectric mirror surfaces. The distance from the trap axis to the electrodes is $r_0 = 0.6$ mm, and the two DC electrodes are divided into five segments of lengths 5, 2, 2, 2, and 5 mm. There is an additional DC electrode at a distance 3 mm from the trap axis located between the bottom two knife blades to allow compensation of any stray electric field along the y-axis without applying a DC bias to one of the RF electrodes. The RF electrodes are driven with ~ 390 V at $2\pi \times 14.3$ MHz using a helical resonator and the two end DC electrodes are biased at 150 V; the remaining DC electrodes are biased to compensate stray electric fields so that the ion is located at the null of the RF electric field [BMB+98]. The resulting motional frequencies of the trapped ion are $(\omega_z, \omega_y, \omega_x) = 2\pi \times (0.87, 1.20, 1.45)$ MHz.

5.1.2 Ion trap mount and ion imaging system

Figure 5-3 shows a photograph of the ion trap mounted in the vacuum chamber. In this setup, the first two lenses of the imaging system are mounted to the trap inside the vacuum chamber for improved light collection efficiency and can be seen above the trap in Figure

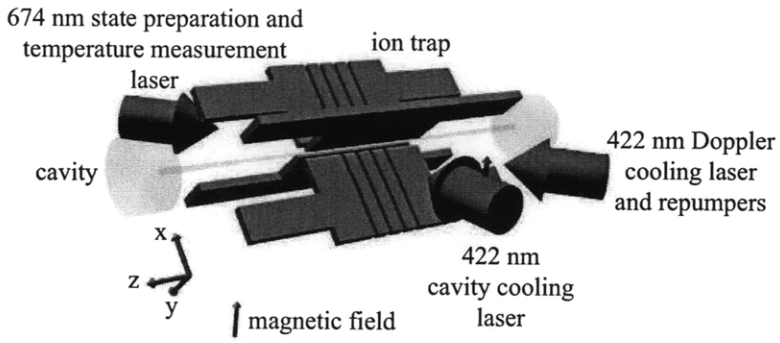

Figure 5-1: Schematic of the cavity cooling experimental setup. A single $^{88}Sr^{+}$ ion is confined in the center of the ion trap electrodes. The optical cavity is oriented along the ion trap axis and the 422 nm cavity cooling laser is perpendicular to the ion trap axis. The 422 nm Doppler cooling laser, 1033 nm and 1091 nm repumpers, and 674 nm state preparation and temperature measurement laser are all at 45 degrees to the trap axis such that they have projections along all of the ion motional principal axes. The coordinate system shown in the lower left corner corresponds to the principal motional axes of the ion trap.

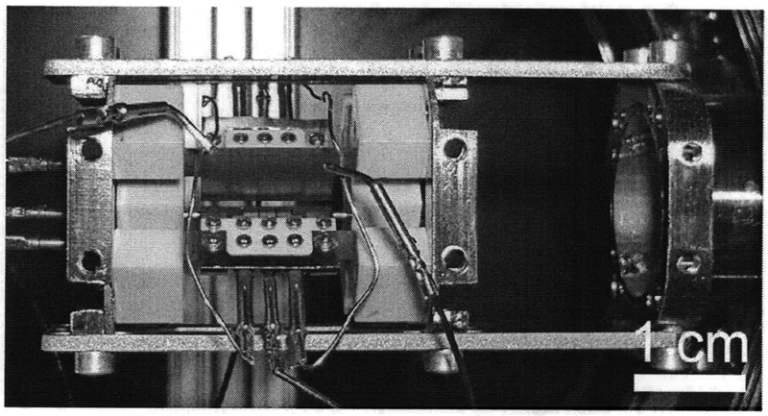

Figure 5-2: Photograph of the cavity cooling ion trap. It is a four rod ion trap with stainless steel knife blade electrodes held in place by ceramic spacers. The two DC electrodes are divided into five segments.

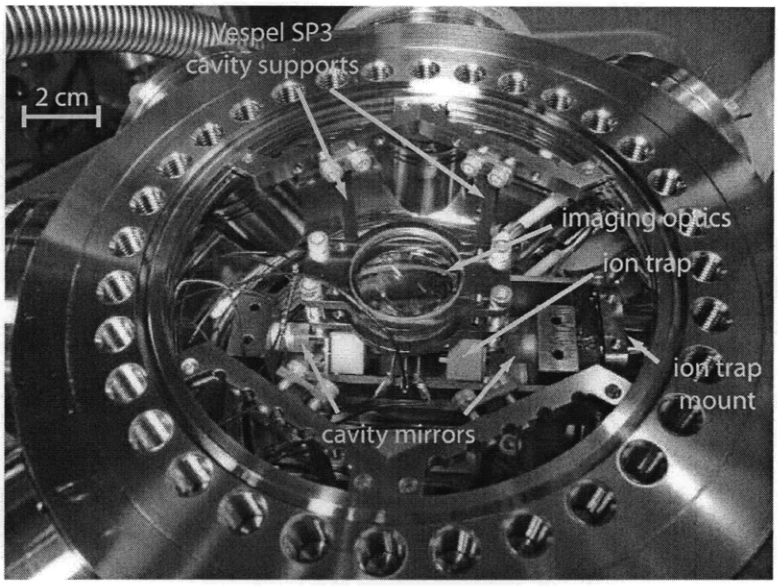

Figure 5-3: Photograph of the cavity cooling ion trap and cavity. The ion trap is in the center of the vacuum chamber underneath the imaging lenses. Both the ion trap and the imaging lenses are mounted to a vacuum flange off the right side of the photograph with a bellows in between the mounting flange and the spherical octagon vacuum chamber so that the trap can be moved with respect to the cavity. The two cavity mirrors are visible to the left and right of the ion trap. The cavity is hung from the top of the vacuum chamber on four Vespel SP3 rods (brown) which are visible in the photograph.

5-3. The imaging system consists of: focal plane, 20.28 mm space, 25 mm aspheric lens (Edmunds 49102, 20.28 mm back focal length), 1 mm space, 200 mm plano-convex lens, 300 mm space (the vacuum window is in this space), 100 mm plano-convex lens, 100 mm space (two mirrors used for alignment and a 427 nm bandpass filter are in this space, Semrock FF01-427/10-25 with 98% transmission at 422 nm), 100 mm plano-convex lens, 100 mm space, CCD (Princeton Instruments PhotonMax512). In the final 100 mm space there is a 75/25 beamsplitter which directs 75% of the light to a photon counting PMT (Hamamatsu H7360-02). The magnification of this imaging system is 8, and the resolution is about 7 μm. All of the optics are 1 inch diameter. With one ion and the 422 nm laser on resonance and above saturation power, the PMT receives about 140,000 counts/s.

Either the ion trap or the cavity position must be adjustable in order to align the ion position with the center of the cavity mode. This can be accomplished by moving the ion trap electrodes, moving the RF null by using independent RF drive circuits to apply different RF amplitudes to each of the electrodes, or moving the cavity. Here it was decided that a translatable cavity mount would be more sensitive to vibrations and it would be difficult to phase match independent RF drive circuits, so the trap electrodes are mounted in a way which is possible to translate. The trap and first two imaging lenses are mounted to a vacuum flange which is separated from the spherical octagon vacuum chamber by a flexible edge-welded bellows. The vacuum flange is held in place using the mount shown in Figure 5-4, and can be moved in two dimensions using the translation stages shown. This allows the ion position to be aligned with the center of the cavity in the x and y-directions for optimal coupling strength.

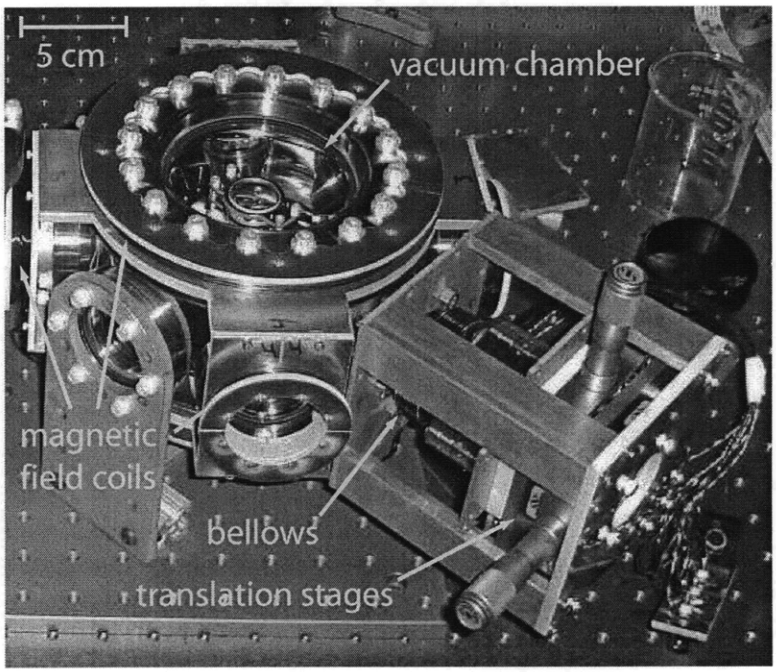

Figure 5-4: Translation stages for moving the cavity cooling ion trap relative to the cavity. The ion trap is mounted to the vacuum flange on the right side of the bellows, which can be moved around in the two dimensions perpendicular to the trap axis using the two translation stages. The coils around the vacuum chamber are used to cancel the ambient magnetic field and add a bias magnetic field in the vertical direction.

The laser delivery optics are identical to those in the room temperature surface-electrode trap evaluation setup (see Section 3.3), and the cavity is described in detail in the next section.

5.2 Cavity

While the temperature limit of cavity cooling is independent of the level structure of the atom and the detuning of the cavity from any of the atomic transitions, the cavity cooling rate is proportional to the photon scattering rate which depends very strongly on the atomic properties. For this demonstration experiment, the cavity is designed to be near resonant with the 422 nm $^{88}Sr^{+}$ $S_{1/2} \leftrightarrow P_{1/2}$ electric dipole transition to allow a large cavity cooling rate without using very much laser power.

5.2.1 Design

Cavity mirrors in the blue are limited to a finesse [Sie86]

$$F = \frac{\pi\sqrt{\mathcal{R}}}{1-\mathcal{R}} = \frac{\Delta\omega_{FSR}}{\kappa} \tag{5.1}$$

of a few tens of thousand by photon scattering losses which scale like one over the wavelength squared [CSL06]. Here $\mathcal{R}$ is the mirror power reflectivity, $\Delta\omega_{FSR} = 2\pi \times c/(2L)$ is the cavity free spectral range, κ is the cavity transmission FWHM, and L is the cavity length. In order to reach the resolved sideband regime, where $\kappa \ll \omega$, this imposes a requirement that the length of the cavity satisfy $L \gg 5$ mm. Here a cavity length $L \sim 5$ cm is selected.

The cavity cooling temperature limit is inversely proportional to the cavity cooperativity. For a two-level atom at an antinode of the cavity coupled to a single cavity TEM_{00} mode, the cooperativity is given by [VCB01]

$$\eta_C = \frac{24F}{\pi k^2 w_0^2} \tag{5.2}$$

where $k = 2\pi/\lambda$ is the magnitude of the wavevector of the light and w_0 is the $1/e^2$ cavity mode radius. The cavity waist is related to the cavity length and mirror radius of curvature R by [Sie86]

$$w_0^2 = \frac{\lambda}{2\pi}\sqrt{L(2R-L)}\ . \tag{5.3}$$

Optical cavities are stable for the parameter $g = 1 - L/R$ in the range $-1 < g < 1$, with the most stable configuration being $g = 0$ which is called confocal. While the cooperativity would be larger and hence the cavity cooling temperature limit would be smaller for a near-concentric cavity with $g \sim -1$, here the cavity is designed to be near-confocal with $g \sim 0$ for better stability and easier alignment. This results in a cooperativity $\eta_C = 0.26$ for an ideal two-level atom.

The frequencies of the modes of a cavity are given by [Sie86]

$$\omega_{kmn} = 2\pi \times \omega_{FSR}\left[(k+1) + \frac{m+n+1}{\pi}\cos^{-1}(g)\right] \tag{5.4}$$

where the subscript k denotes the longitudinal modes and the subscripts m and n denote

the transverse modes. For a perfectly confocal cavity, the transverse modes with $m + n$ even are degenerate with the TEM_{00} mode and the transverse modes with $m + n$ odd are degenerate with a frequency halfway between two TEM_{00} modes. Cavity cooling in a perfectly confocal cavity has the advantage that the cooperativity is enhanced by coupling to all of the transverse modes with $m+n$ even. In practice, however, it is impossible to make the cavity perfectly confocal and the deviation from confocality spreads out the transverse modes in frequency. This effectively broadens the cavity linewidth, potentially taking the system out of the resolved sideband regime. Here, the cavity mirror radius of curvature is $R = 5$ cm and the cavity length is $L = R + 250$ μm, resulting in a TEM_{00} mode waist $w_0 = 58$ μm and a 9.4 MHz frequency interval between the TEM_{00} and TEM_{11} modes. The TEM_{00} mode is the mode which is used for cavity cooling, and the fact that the frequency interval between the TEM_{00} and TEM_{11} modes is large compared with the cavity linewidth and the ion trap motional frequencies ensures that the transverse modes do not effectively broaden the cavity linewidth.

5.2.2 Assembly

The cavity mirrors were purchased from AT Films. The substrates are super polished fused silica with a diameter of 7.75 mm and a thickness of 4 mm. The mirror side is concave with a radius of curvature of 5 cm and is coated with a high reflectance (quoted reflectivity $\mathcal{R} > 0.9997$) coating centered at 422 nm. The back side is flat and is coated with an AR (antireflection) coating centered at 422 nm. The optical coatings are ion beam sputtered. (In addition to having the lowest scattering losses, ion beam sputtered coatings are stable under vacuum. Electron beam evaporation coatings for blue light, for instance, exhibit higher losses when placed in vacuum.)

The mirrors are mounted on cylindrical piezos which are used for locking the cavity length. The piezos have an outer diameter of 7.7 mm and an inner diameter of 6.2 mm, and they are made of the piezoceramic material Pz27 from Ferroperm. This material is selected for its high Curie temperature of > 350 C. One of the piezos is 6.2 mm long for a large travel range and the other piezo is 3.15 mm long for a higher actuation bandwidth.

The cavity mount consists of three parts: a baseplate and two arms which hold the cavity mirrors. The arms are fixed to the baseplate with screws that go through slots in the baseplate and screw into the arms. This allows the length of the cavity to be adjusted by a small amount to allow for machining tolerances of the cavity mount baseplate and the mirror radius of curvature and still satisfy $L = R + 250$ μm.

The cavity was assembled according to the following procedure:

0. Wear clean lab coat, hair net, face mask, and gloves and assemble the cavity on the optical table with curtains and an air purifier.

1. Make the electrical leads for the piezos by crimping Accu-Glass 100170 pins onto MDC 680500 kapton coated wire.

2. Clean the leads by sonicating for 10 minutes each in soapy water, clean water, acetone, and methanol.

3. Clean the piezos by soaking for 20 minutes each in acetone then methanol (the sonicator is not used because it causes the electrode coatings to come off of the piezos).

4. Solder the leads onto the piezos with 80/20 Au/Sn solder using a soldering iron with a clean tip set to 400 C; do not heat the piezos any longer than necessary to melt the solder as there is a risk of heating them above their Curie temperature.

5. Glue the mirrors onto the piezos using Varian Torr Seal epoxy; cure on a hot plate at 80 C for 1 hour.

6. Clean the pencil marks off of the sides of the mirrors using clean cotton swabs and methanol.

7. Glue the long piezo onto one of the cavity mount arms using Torr Seal; cure on a hot plate at 80 C for 1 hour.

8. Clean both mirrors using clean cotton swabs and ultra-high purity dry methanol (note that methanol absorbs a lot of water if exposed to air for more than a few minutes).

   (a) Put the mirror under a microscope.

   (b) Adjust the microscope focus to the mirror surface by looking at the edge of the mirror under low magnification.

   (c) Use high magnification with lots of light (here a bright flashlight was used to supplement the microscope light) to see if there are any dust spots.

   (d) If there are dust spots put some methanol on a cotton swab and run it across the mirror; only run each cotton swab across the mirror once.

   (e) Repeat until there are no more dust spots.

9. Screw the cavity mount arm which already has a mirror attached to it onto the cavity mount baseplate; hold the other mirror in place with a three-dimensional translation stage.

10. Align the cavity by adjusting the position of the mirror held by the translation stage.

    (a) Rough align the cavity with 460 nm light; ensure that the cavity mode is centered on the cavity mirrors.

    (b) Fine align the cavity with 422 nm light.

    (c) Set the length of the cavity by first tweaking the cavity length until all of the transverse modes with $m + n$ even are degenerate (this is where the cavity is confocal), then moving the mirror on the translation stage such that the cavity is 250 μm longer than confocal.

11. Measure the cavity finesse by ringdown (see Section 5.2.3); if the finesse is too low go back to step 8.

12. Apply Torr Seal epoxy to the second cavity mount arm, position it behind the mirror on the translation stage, and screw it to the cavity mount baseplate; cure at room temperature for 24 hours.

The time between cavity assembly and closing the vacuum chamber was made as short as possible to avoid contamination of the cavity mirrors by dust in the air. Further, the vacuum chamber was rough pumped very slowly (standard pressure to 1 torr over about 1 hour) to avoid shock waves which can condense water on the cavity mirrors during pumpdown. Finally, the vacuum chamber was baked only up to 115 C after the cavity was installed to avoid damage of the Torr Seal epoxy.

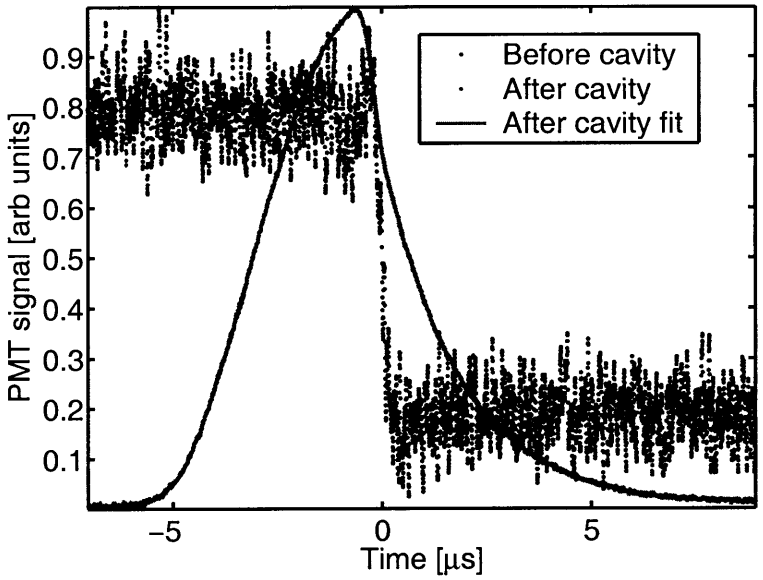

Figure 5-5: Ringdown measurement of the cavity cooling cavity finesse. The cavity transmission (green) and the laser power (blue) are plotted as a function of time, with the laser switched off at time zero. The two measurements are made using the same PMT, and the laser power measurement switches very rapidly, so the relatively slower decay of the cavity transmission can be attributed to the cavity ringdown as opposed to the PMT or laser switching speed. (The laser power measurement is much noisier than the cavity transmission measurement because much less power is used.) The portion of the cavity transmission curve in red is fit to determine the cavity ringdown time $\tau = 1.83 \pm 0.03$ μs. The resulting finesse is 34500 ± 500.

5.2.3 Characterization

The cavity finesse was measured using ringdown. In this technique, light is coupled to the cavity and the transmission is monitored on the far side of the cavity using a fast photodiode or PMT. The light is quickly switched off and the decay time of the transmitted light is measured (see Figure 5-5). The cavity finesse is related to the cavity mode power decay time constant by

$$F = \frac{\pi c \tau}{L} , \tag{5.5}$$

where the cavity transmission goes like $e^{-t/\tau}$. The cavity finesse measured using ringdown slowly decayed over time, presumably due to accumulation of strontium atoms on the mirror surfaces. The finesse measured after the cavity was put in the vacuum chamber and baked out, but before firing the strontium oven at all, was 34500 ± 500. Approximately 8 months later, around which time most of the cavity cooling measurements were taken, the finesse was remeasured to be 25600 ± 100.

The finesse $F = 25600$ implies a cavity transmission linewidth $\kappa = 2\pi \times 117$ KHz. Direct measurement reveals a cavity transmission linewidth of $2\pi \times 136$ kHz. This increase in linewidth is attributed to the linewidth of the cavity cooling laser. The two polarization modes of the cavity TEM_{00} mode are measured to be degenerate.

Following the procedure presented in Reference [HKY01], the cavity mirror transmission was measured to be $\mathcal{T} = 38$ ppm (parts per million) and the cavity mirror loss was measured

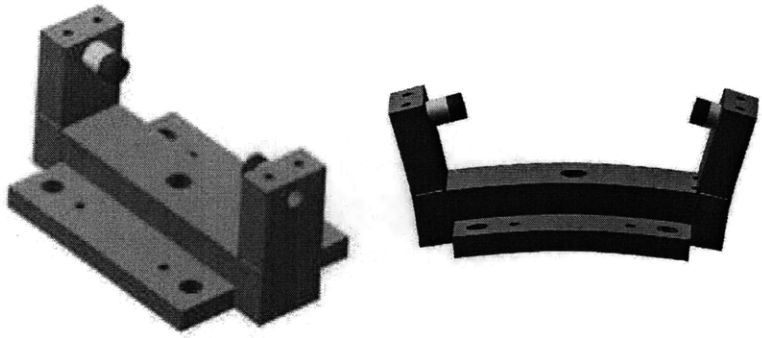

Figure 5-6: Cavity cooling cavity mount. On the left, a Solidworks rendering of the cavity mount is shown. The gray part is the stainless steel spacer, the yellow parts are piezos, and the blue parts are the cavity mirrors. On the right, a rendering of the shape of the lowest frequency vibrational mode of the cavity mount is shown (greatly exaggerated in amplitude). This mode was computed using Cosmosworks (an extension package of Solidworks) and has a calculated frequency of 4.4 kHz.

to be $\mathcal{L} = 53$ ppm. (This measurement of the transmission agrees well with the value specified by AT Films, which is $\mathcal{T} = 41$ ppm.) This implies that a photon in the cavity has a 21% chance of coming out each end of the cavity and a 58% chance of being lost.

5.2.4 Mount and vibrational isolation

The cavity mount is shaped like a tuning fork in order to fit around the ion trap. This has the unfortunate consequence of possessing a low frequency vibrational mode which changes the length of the cavity (see Figure 5-6). The vibrational modes of the cavity mount were modeled using Cosmosworks (an extension package of Solidworks), and the low frequency tuning fork mode was predicted to be at 4.4 kHz. Experimentally, this mode can be excited acoustically by playing a tone on a speaker and it is observed to be at 4.3 kHz.

In order to passively isolate the cavity mount from acoustic noise in the lab, the cavity mount is hung on four 0.1 by 0.15 by 2.6 inch rods made of Vespel SP3 (a UHV compatible plastic). The soft plastic rods do not transmit vibrations above their resonant frequency of approximately 50 Hz. The Vespel SP3 rods are visible in Figure 5-3.

5.2.5 Lock

The cavity length is locked using a modified form of the Pound-Drever-Hall method [DHK+83] shown in Figures 5-7 and 5-8. This lock is designed to minimize the scattering rate of the cavity lock beam by the ion and to allow detection of the photons scattered by the ion from the cavity cooling beam into the cavity. Two pairs of sidebands are added to the cavity lock beam by an electro-optic modulator (EOM) driven with a sum of sine waves at $9.1750 + 0.0060$ and $9.1750 - 0.0060$ GHz, the $-9.1750 + 0.0060$ GHz sideband is injected into one of the cavity TEM_{11} modes, and the reflected beam is beat with the $-9.1750 - 0.0060$ GHz sideband on an avalanche photodiode (APD) to get an error signal at 12 MHz. Fast feedback is applied to correct the frequency of the cavity lock beam so that the cavity does not fall out of lock, and slow feedback is applied correct the cavity length using cavity piezo. The amount of lock light in the cavity TEM_{11} mode is $\sim (80\ \mathrm{nW}) \times F \sim 2\ \mathrm{mW}$, but the light is detuned by ~ 9 GHz from the $^{88}\mathrm{Sr}^{+}$ transition and the ion is located at a

node of the TEM_{11} mode so the scattering rate of lock light by the ion is only ~ 10 photons/s. The photons scattered by the ion from the cavity cooling beam into the cavity TEM_{00} mode are detected using the photon counting PMT (Hamamatsu H7360-02SELECT) located on the right side of the cavity in Figure 5-7. The cavity lock beam is removed from the scattered cavity cooling beam with 99.998% efficiency by filtering the polarization using a polarizing beamsplitter and the spatial mode using a single mode optical fiber.

The TEM_{00} output mode of the laser is mode matched with the TEM_{11} mode of the cavity for locking using a binary phase hologram [Soi02, MSH+05]. The binary phase hologram was fabricated in the MIT EML by Yufei Ge. It consists of a 0.57 μm thick layer of MgF_2 (refractive index 1.37) applied to opposite quadrants of a substrate (see Figure 5-9). This thickness of MgF_2 applies a π phase shift to the light. The substrate is a AR coated piece of glass. The TEM_{00} output mode of the laser passes through the center of the binary phase hologram and is transformed into a superposition of transverse modes with the dominant mode being the TEM_{11} mode. This phase hologram allows coupling of the TEM_{00} output mode of the laser to the TEM_{11} mode of the cavity with $\sim 40\%$ efficiency.

5.3 Alignment of ion to cavity mode

In order to achieve maximum coupling between the ion and the cavity, the ion must be positioned in the center of the cavity mode at an antinode of the cavity standing wave.

5.3.1 Transverse position

Alignment of the ion to the center of the cavity mode in the transverse directions is accomplished by moving the ion trap using the translation stages shown in Figure 5-4. The cavity-atom detuning is set to $\delta_{CA}/(2\pi) = -10$ MHz and light is coupled into the cavity TEM_{00} mode. The scatter of the light from the cavity into the free space imaging system is monitored. Before the system has been aligned for the first time, there is no scatter of the light in the cavity TEM_{00} mode by the ion and the ion trap position must be randomly searched. Once the ion is close enough to the center of the cavity mode that some of the light in the cavity TEM_{00} mode is scattered by the ion, the ion trap position is optimized to maximize the scatter, making sure that the optical power in the cavity is small enough that it does not saturate the ion.

After the ion trap has been aligned to the cavity, the ion trap position can be systematically varied to check that the size of the cavity TEM_{00} mode as seen by the ion matches the expected value of $w_0 = 58$ μm. Within the 10 μm accuracy of the translation stages, this is indeed observed to be the case.

5.3.2 Longitudinal position

Alignment of the ion to an antinode of the cavity standing wave is accomplished by moving the ion within the trap using a small additional voltage on one of the endcap electrodes. To measure the ion position relative to the cavity standing wave, the ion is pumped by the cavity cooling beam with the laser-cavity detuning $\delta_{LC} = 0$ and the scatter into the cavity is monitored. The scattering rate is maximized when the ion is located at an antinode of the cavity standing wave (see Section 5.5).

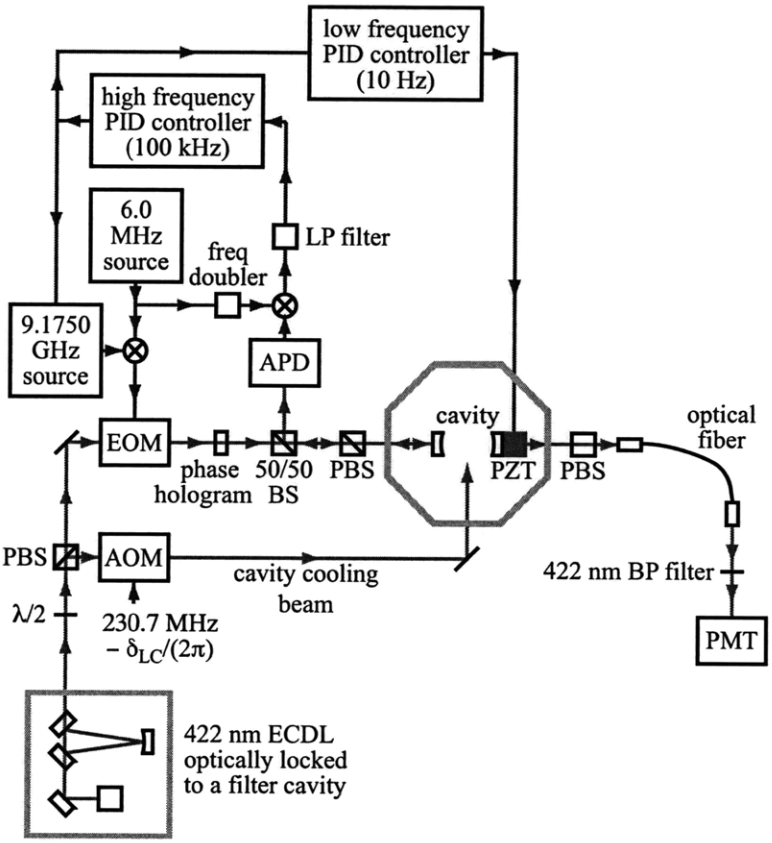

Figure 5-7: Schematic of the laser system used for locking the cavity and generating the cavity cooling beam. The cavity TEM_{11} mode is locked to the $9.1750-0.0060$ GHz red EOM sideband of the laser using a form of PDH with only two relevant frequency components. The cavity probe beam is generated with an AOM which frequency shifts the laser by 230.7 MHz $-\ \delta_{LC}/(2\pi)$. The lock beam is horizontally polarized and the cavity cooling beam is vertically polarized. The PBS on the right side of the cavity is oriented such that vertically polarized light is transmitted, so the PMT detects photons which are scattered from the cavity cooling beam into the cavity but not photons from the cavity lock beam. The cavity cooling beam is detuned by δ_{LC} from one of the cavity TEM_{00} modes, and the cavity lock beam is resonant with one of the cavity TEM_{11} modes three free spectral ranges to the red.

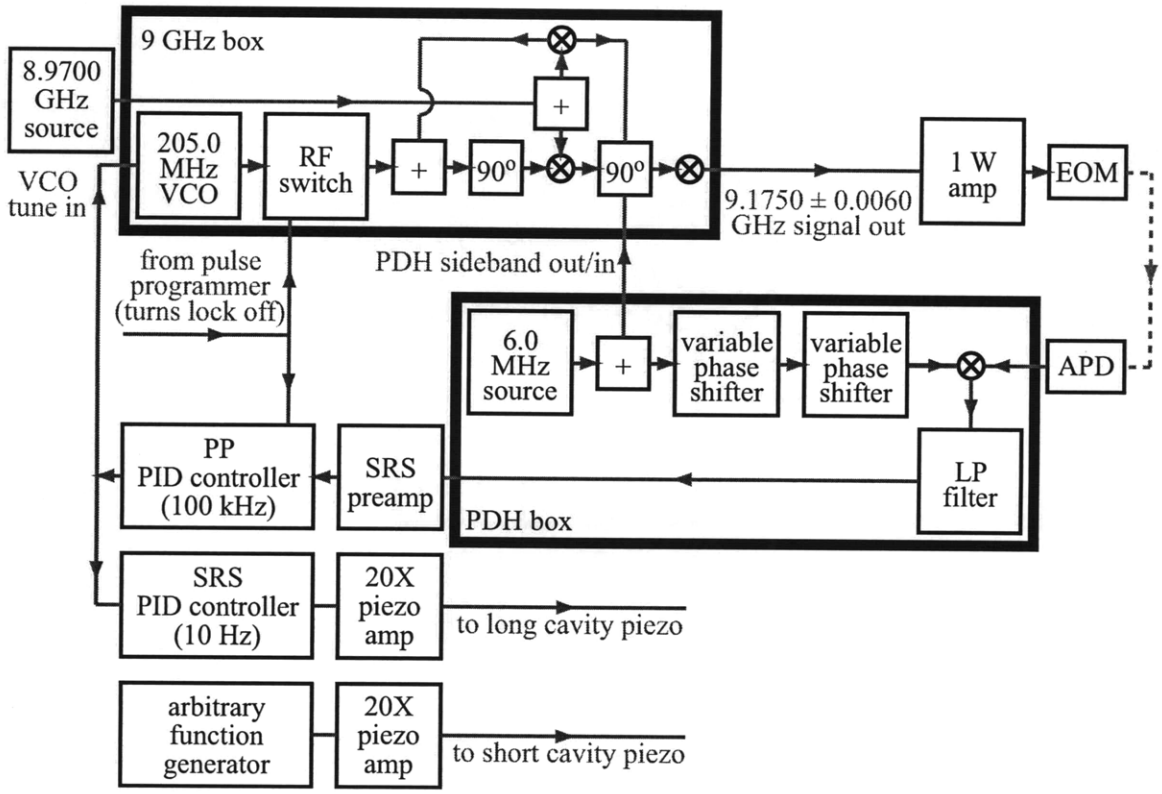

Figure 5-8: Block diagram of the electronics used for locking the cavity. On fast time scales the laser is locked to the cavity using the Precision Photonics lock box, and on slow time scales the cavity is locked to the laser using the SRS lock box.

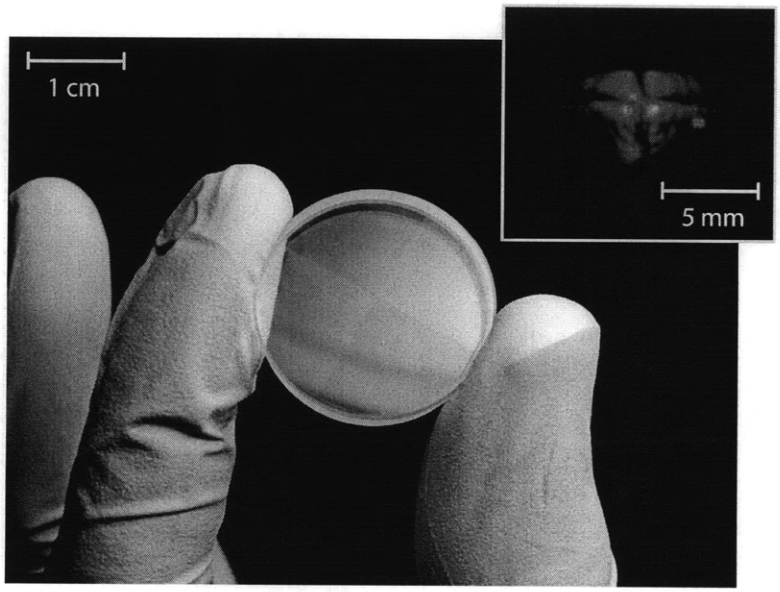

Figure 5-9: Binary phase hologram used for mode matching to the TEM_{11} mode of the cavity. The inset in the upper right corner shows the beam shape of the cavity lock laser about 50 cm after passing through the binary phase hologram.

5.4 Cooperativity measurements

The effective cooperativity, $\eta_{C,eff}$ is reduced from the cooperativity of a two-level atom $\eta_C = 0.26$ according to $\eta_{C,eff} = \eta_{cg}\eta_p\eta_l\eta_t\eta_C$. Here $\eta_{cg} = 0.31$ is the reduction in cooperativity due to the Clebsch-Gordan coefficient for π polarized light on the $^{88}Sr^+$ $S_{1/2} \leftrightarrow P_{1/2}$ transition. The transverse positioning error of the ion relative to the center of the cavity mode is about 10 μm in each direction, which results in a random reduction of cooperativity between $\eta_p = 1$ and $\eta_p = 0.89$. The reduction in cooperativity due to the $2\pi \times 19$ kHz linewidth of the cavity cooling laser $\eta_l = 0.82$ is calculated by solving the master equation with a stochastic phase noise added to the laser (see Section 4.4). Finally, the non-zero Doppler cooled ion temperature reduces the cooperativity by a factor $\eta_t = 0.32$ (see Section 5.5). These effects combine to result in a theoretical effective cooperativity $\eta_{C,eff} = 0.019$.

The cooperativity is measured using two methods. The first method is perhaps the more straightforward of the two, which is to directly measure the ratio of the scatter rate into the cavity over the scatter rate into free space. While this method has the advantages of being conceptually simple and measurable with a high signal to noise ratio, it suffers from the disadvantage that it is very difficult to know the free space and cavity photon collection efficiencies very accurately. This results in a relatively large systematic error. The second method is to measure the modification of the cavity transmission lineshape with an ion in the cavity (see Section 4.3.2). While this method has less systematic errors to worry about, it suffers from a very large statistical error because the modification of the cavity transmission lineshape is very small for the low cooperativity of this experiment.

5.4.1 Ratio of scatter

For the ratio of scatter measurement of the effective cooperativity, first the free space scatter collection efficiency is measured using a pulsed optical pumping experiment where the 422 nm and 1091 nm lasers are applied in succession and the mean number of 422 nm photons detected during the 1091 nm laser pulses gives the collection efficiency. The collection efficiency measured using this method is 0.0043 ± 0.0004 PMT counts per photon scattered by the ion into free space. Next, the collection efficiency for photons scattered into the cavity is calculated as the product of several factors: (0.21 photons come out of the back of the cavity per photon scattered into the cavity, see Section 5.2.3) $\times$ (0.995 is the transmission of the vacuum window specified by the company that did the AR coating) $\times$ (0.25 ± 0.05 is the measured fiber coupling efficiency for photons which make it out of the vacuum chamber) $\times$ (0.185 ± 0.028 is the measured product of the 422 nm bandpass filter transmission and the PMT quantum efficiency) $= 0.0097 \pm 0.0019$ PMT counts per photon scattered by the ion into the cavity.

The effective cooperativity is measured by pumping the ion with the cavity cooling beam on resonance ($\delta_{LC} = 0$) and measuring the ratio of scatter into the cavity versus into free space. Figure 5-10 shows the scatter into the cavity as a function of the scatter into free space for several values of the cavity-atom detuning. The slope of the fit at small values of the free space scattering rate is the effective cooperativity $\eta_{C,eff} = 0.0180 \pm 0.0002$. The errorbars here represent the statistical error of the fit; when the systematic error is taken into account the effective cooperativity is $\eta_{C,eff} = 0.018 \pm 0.004$. This measurement agrees with the theoretically calculated value. The saturation behaviour of Figure 5-10 at high free space scattering rate is due to the finite repumping rate of the $D_{3/2}$ state.

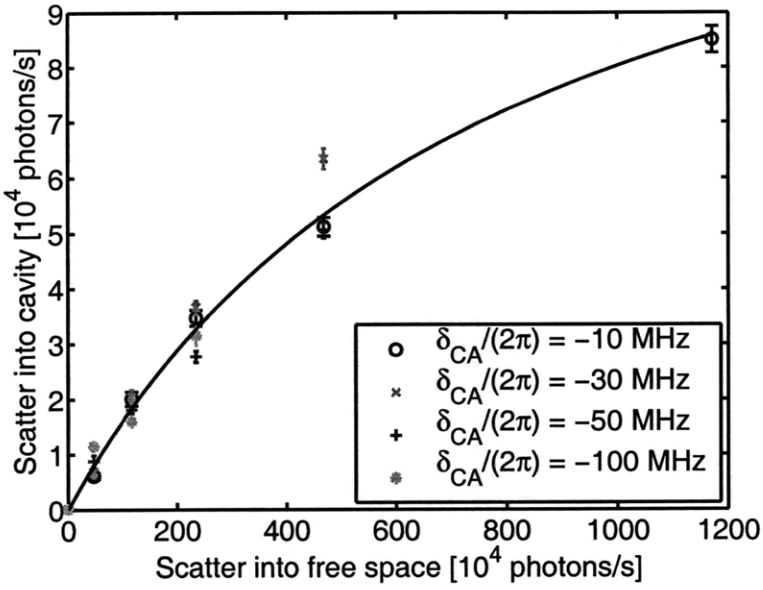

Figure 5-10: Scatter into the cavity as a function of scatter into free space (Γ_{sc}) with $\delta_{LC} = 0$ and for several values of δ_{CA}. The line is a fit to the form $\eta_{C,eff}\Gamma_{sc}/(1+\Gamma_{sc}/\Gamma_{sat})$ with fit parameters $\eta_{C,eff} = 0.0180 \pm 0.0002$ and $\Gamma_{sat} = (8.0 \pm 0.2) \times 10^6$ photons/s.

5.4.2 Cavity transmission spectra

For the cavity transmission spectra measurement of the effective cooperativity, the differential cavity transmission is measured with the ion at a node and at an antinode of the cavity standing wave. This can be done much faster than a differential measurement with and without an ion, so the error due to power fluctuations of the probe laser is reduced. Figure 5-11 shows both the average cavity transmission with the ion at the cavity standing wave node and antinode, and the differential cavity transmission with the ion at the cavity standing wave node and antinode. The differential transmission is fit to Equation 4.19 with fit parameters $\delta_{CA}/(2\pi) = -21 \pm 4$ MHz and $\eta_{C,eff} = 0.014 \pm 0.003$ (statistical error).

While this type of differential measurement removes much of the statistical error which would be present in a measurement with and without an ion in the cavity, it adds an unknown systematic error because it is impossible to verify that the ion is at exactly the node or antinode of the cavity standing wave. Furthermore, because the cavity transmission spectra measurement must be performed at small cavity-atom detunings, it is susceptible to systematic errors caused by dark states of the $S_{1/2}$, $P_{1/2}$, $D_{3/2}$ manifold. Thus, the ratio of scatter measurement of the effective cooperativity is assumed to be more accurate.

5.5 Cavity scatter spectra

The rate of scattering photons from the cavity cooling laser into the cavity depends on the ion position relative to the cavity mode and on the laser-cavity detuning.

Figure 5-12 shows the rate of scattering photons from the cavity cooling laser into the cavity with $\delta_{CA}/(2\pi) = -40$ MHz and $\delta_{LC} = 0$ as a function of ion position along the cavity axis. The scatter is minimized when the ion is located at a cavity standing wave node and maximized when the ion is located at a cavity standing wave antinode. The data for Figure

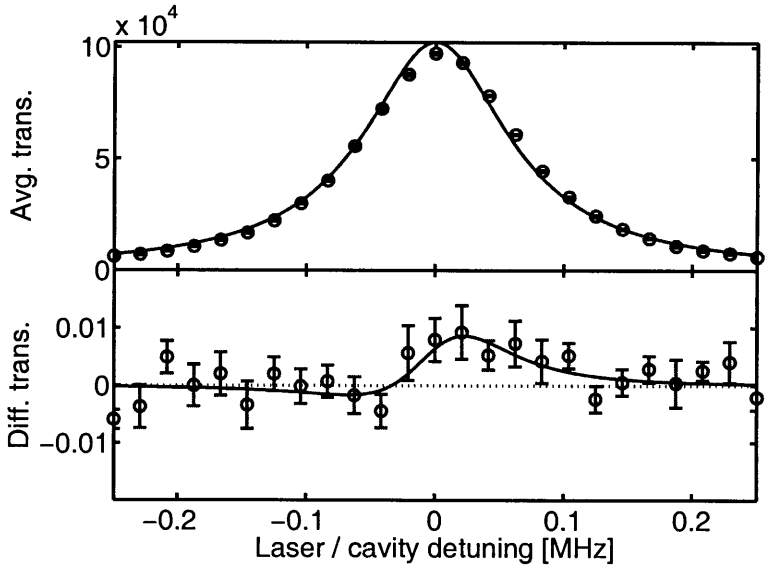

Figure 5-11: Cavity transmission spectra with an ion inside. The ion is moved between the cavity standing wave node and cavity standing wave antinode approximately every 20 ms. In the top panel, the cavity transmission averaged over the ion being at the node and the antinode is plotted as a function of the laser-cavity detuning δ_{LC}. The units of the average cavity transmission are PMT counts/s. In the bottom panel, the cavity transmission with the ion at the antinode minus the cavity transmission with the ion at the node divided by the average cavity transmission is plotted as a function of the laser-cavity detuning δ_{LC}. The bottom panel is fit to the two-level atom model described in the text with fit parameters $\delta_{CA}/(2\pi) = -21 \pm 4$ MHz and $\eta_{C,eff} = 0.014 \pm 0.003$. (This measurement is performed at $\delta_{CA} < 0$ to avoid dark states of the $S_{1/2}$, $P_{1/2}$, $D_{3/2}$ manifold.)

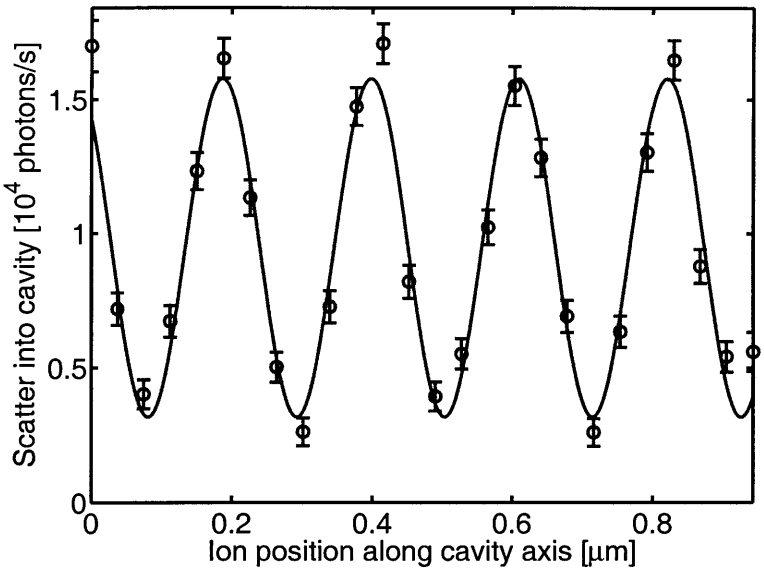

Figure 5-12: Photon scattering rate from the cavity cooling beam into the cavity as a function of the ion position along the cavity axis. This data is taken with $\delta_{CA}/(2\pi) = -40$ MHz and $\delta_{LC} = 0$ MHz. In addition to the cavity cooling beam, the Doppler cooling beam is also on during this measurement, but it does not contribute to the signal because it is off resonant with the cavity. The line is a fit from which the contrast is determined to be $V = 0.67 \pm 0.02$.

5-12 was taken with the ion Doppler cooled. The contrast V is reduced by the non-zero width of the ion wavefunction according to

$$V = e^{-2\left(\frac{2\pi\sqrt{\langle z^2\rangle}}{\lambda}\right)^2}. \tag{5.6}$$

The contrast $V = 0.67 \pm 0.02$ of Figure 5-12 corresponds to an RMS ion wavefunction size $\sqrt{\langle z^2\rangle} = 31 \pm 1$ nm, which is due to a temperature a little below the Doppler limit (39 nm) [GKH$^+$01, MKB$^+$02].

Figure 5-13 shows the rate of scattering photons from the cavity cooling laser into the cavity with $\delta_{CA}/(2\pi) = -60$ MHz as a function of the laser-cavity detuning δ_{LC}. The carrier and all three first order motional sideband transitions are clearly visible, as well as some of the second order motional sideband transitions. Russo et al. [RBS$^+$08] recently observed a similar spectra of scatter into a cavity with resolved motional sidebands. Cavity cooling of motional mode i takes place when the laser-cavity detuning is set to $\delta_{LC} = -\omega_i$.

The selection rules for scattering from the cavity cooling laser into the cavity are those of a stimulated Raman transition where the first laser is the traveling wave cavity cooling laser and the second laser is the standing wave cavity vacuum field. Carrier transitions and first order motional sideband transitions on the x and y motional modes are allowed when the ion is located at a cavity standing wave antinode (Figure 5-13(a)) and forbidden when the ion is located at a cavity standing wave node (Figure 5-13(c)). First order motional sideband transitions on the z motional mode, however, are allowed when the ion is located at a cavity standing wave node (Figure 5-13(c)) and forbidden when the ion is located at a cavity standing wave antinode (Figure 5-13(a)). These selection rules are easily understood

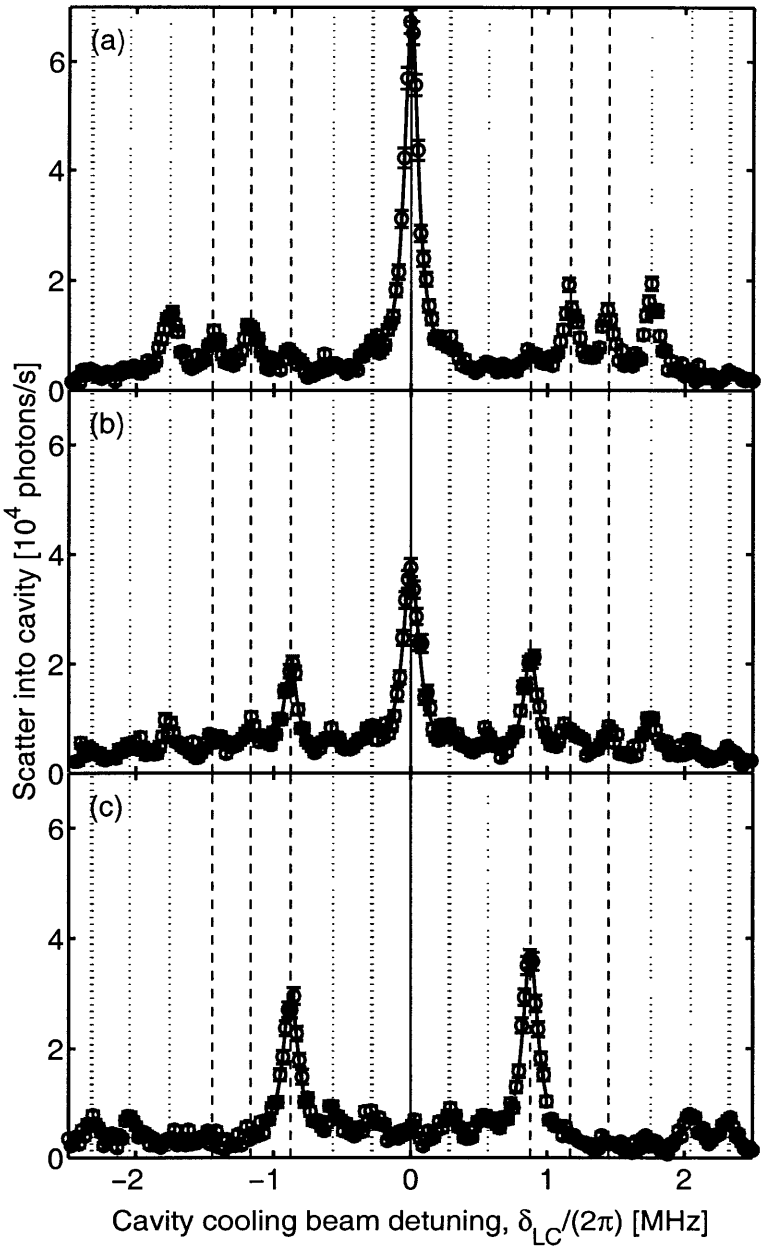

Figure 5-13: Photon scattering rate from the cavity cooling beam into the cavity as a function of the the detuning between the cavity cooling beam and the cavity, δ_{LC}. This data is taken with $\delta_{CA}/(2\pi) = -60$ MHz and $\Gamma_{sc} = 1.2 \times 10^7$ photons/s. In order to keep the ion cold during the measurement, this data is taken in a pulsed fashion: Doppler cool for 200 μs with the cavity cooling beam off, measure for 50 μs with the Doppler cooling beam off, then repeat. The solid vertical line is at the carrier transition frequency, the dashed vertical lines are at the first order motional sideband transition frequencies, and the dotted vertical lines are at the second order motional sideband transition frequencies. The curves are fits used to determine the linewidths of the carrier and lowest frequency motional sidebands. (a) Ion located at a cavity standing wave antinode. (b) Ion located halfway between a cavity standing wave node and antinode. (c) Ion located at a cavity standing wave node.

by noticing that first order sideband transitions on the x and y motional modes change the phonon number when the photon is absorbed from the cavity cooling laser, but first order sideband transitions on the z motional mode change the phonon number when the photon is emitted into the cavity. In a standing wave, transitions which do not change the phonon number are only allowed at an antinode and transitions which do change the phonon number are only allowed at a node.

The carrier and motional sideband linewidths are not broadened by transitions between the two ground states $S_{1/2}, m = \pm 1/2$, but the motional sideband linewidths are broadened by transitions to different motional states [PS76, CB78, JGL+92]. For the data of Figure 5-13, however, the motional sideband transition rate is too small to broaden the motional sideband linewidths observably. The carrier and z motional sidebands are fit to determine the linewidths $2\pi \times (120 \pm 15)$ kHz at the antinode and $2\pi \times (144 \pm 15)$ kHz halfway between the node and antinode for the cavity carrier transition, and $2\pi \times (117 \pm 15)$ kHz halfway between the node and antinode and $2\pi \times (137 \pm 15)$ kHz at the node for the z motional sideband transition. These values are all equal to the measured cavity linewidth within the experimental uncertainty.

5.6 Cavity cooling experiment

This section describes the experiment used to demonstrate and quantitatively characterize cavity cooling. It begins with an overview of the experiment. Then, Section 5.6.1 describes the method used to measure the ion temperature in detail. Section 5.6.2 presents the experimental results. Finally, Section 5.6.3 presents a theoretical model that describes the data.

One-dimensional cavity cooling of the z motional mode is demonstrated by measuring separately the recoil heating rate and the cavity cooling and heating rates for pumping on the cavity red ($\delta_{LC} = -\omega_z$) and blue ($\delta_{LC} = +\omega_z$) motional sidebands. The experiment starts by sideband cooling to the three-dimensional motional ground state on the $S_{1/2}, m = -1/2 \leftrightarrow D_{5/2}, m = -5/2$ transition. Then a variable length pulse of the cavity cooling laser is applied with detunings $\delta_{LC} = 0$ or $\pm\omega_z$ and $\delta_{CA}/(2\pi) = -10$ MHz. Finally, the temperature is measured by measuring the Rabi frequency of the red and blue motional sidebands of the $S_{1/2}, m = -1/2 \leftrightarrow D_{5/2}, m = -5/2$ transition. This cavity-atom detuning is the optimum value for Doppler cooling, but the geometry of the setup dictates that the cavity cooling laser Doppler cools the x and y motional modes but does not Doppler cool the z motional mode. The recoil heating rate is the slope of the temperature versus cavity cooling pulse length for $\delta_{LC} = 0$ and the cavity cooling and heating rates are the differences of the slopes of the temperature versus cavity cooling pulse length for $\delta_{LC} = \pm\omega_z$ and the recoil heating rate. The signature of cavity cooling is that the temperature after pumping on the cavity red motional sideband is smaller than the temperature after pumping on the cavity carrier, which is smaller than the temperature after pumping on the cavity blue motional sideband.

5.6.1 Temperature measurement method

The mean number of quanta $\langle n \rangle$ in any of the motional modes is measured by observing Rabi flops on the red and blue motional sidebands of the $S_{1/2}, m = -1/2 \leftrightarrow D_{5/2}, m = -5/2$ transition. The probability of being in the excited state after a Rabi pulse of length t is

given by

$$p_{D_{5/2}}(t) = A\sum_n p_n \frac{1-\cos(\Omega_{n,n'}t)}{2}\ , \tag{5.7}$$

where A accounts for population in the $S_{1/2}, m = +1/2$ state which is not excited to the $D_{5/2}$ state, $p_n = \langle n\rangle^n/(\langle n\rangle+1)^{n+1}$ is the population in motional state n for a thermal distribution, and $\Omega_{n,n'}$ is the Rabi frequency for Rabi flopping from motional state n to motional state n'. For the red sideband $n' = n-1$ and the sum runs from $n = 1$ to ∞, and for the blue sideband $n' = n+1$ and the sum runs from $n = 0$ to ∞. The Rabi frequency is related to the motional states n and n' and the Lamb-Dicke parameter $\eta_{LD} = \sqrt{\hbar k^2/(2m\omega)}$ by [WMI+98b]

$$\Omega_{n,n'} = \Omega e^{-\eta_{LD}^2/2}\sqrt{\frac{n_<!}{n_>!}}\eta_{LD}^{|n'-n|}L_{n_<}^{|n'-n|}(\eta_{LD}^2) \tag{5.8}$$

where $n_<$ ($n_>$) is the smaller (larger) of n and n' and $L_n^\alpha(X)$ is the generalized Laguerre polynomial

$$L_n^\alpha(X) = \sum_{m=0}^{n}(-1)^m\begin{pmatrix} n+\alpha \\ n-m\end{pmatrix}\frac{X^m}{m!}\ . \tag{5.9}$$

In the above equations $\hbar$ is the Planck constant, k is the projection of the wavevector on the motional axis, and m is the ion mass. Figure 5-14 shows an example of such a temperature measurement on the z motional mode. The data is fit to the model above with fit parameters A and $\langle n\rangle$.

5.6.2 Cavity cooling results

Figure 5-15 shows the temperature of the z motional mode as a function of cavity cooling pulse length for pumping on the cavity carrier and red and blue motional sidebands. This data is taken with the ion position locked to a cavity node, where the first order z motional sideband transitions are allowed. The cavity cooling rate, which is the slope of the difference between pumping on the cavity carrier and the cavity red sideband, is positive. This confirms that cavity cooling is taking place.

In order to demonstrate cavity cooling under more useful circumstances, Figure 5-16 shows the temperature of the z motional mode as a function of cavity cooling pulse length for pumping on the cavity red sideband starting from an initial temperature of 50 motional quanta. The initial state is prepared by first sideband cooling all three motional modes to the motional ground state on the $S_{1/2}, m = -1/2 \leftrightarrow D_{5/2}, m = -5/2$ transition as before, then applying 50 sideband heating cycles on only the z motional mode. This prepares an approximately Gaussian distribution of motional states with a mean of 49.6 ± 0.5 motional quanta and a standard deviation of 7.2 ± 0.3 motional quanta. Cavity cooling reduces the temperature from 50 quanta to about 45 quanta in 4 ms.

5.6.3 Resolved sideband cavity cooling model

The cavity cooling dynamics in Figure 5-15 are fit to a rate equation model parameterized by the effective cooperativity $\eta_{C,eff}$ [VCB01]. This rate equation model agrees with the model of Zippilli and Morigi [ZM05a, ZM05b], which includes coherences, for the weak coupling regime of this experiment.

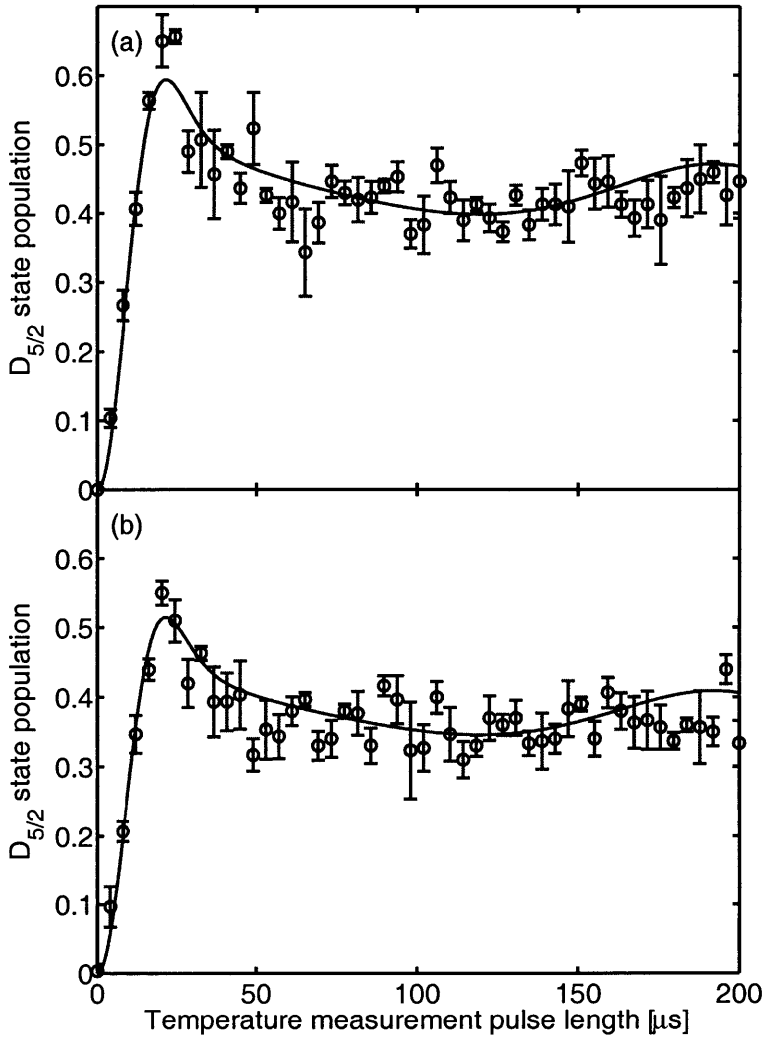

Figure 5-14: Example temperature measurement data showing Rabi flopping on the (a) blue and (b) red axial motional sidebands of the 674 nm transition. The temperature is obtained from this data using a global fit of both sidebands with the amplitude of the Rabi flopping A and the expectation value of the number of quanta in the motional mode $\langle n_z \rangle$ as fit parameters, assuming that the number of quanta in the motional mode follows a thermal distribution. The fit for this particular data returns $A = 0.856 \pm 0.004$ and $\langle n_z \rangle = 6.5 \pm 0.2$. The reduced χ^2 of the fit is 3.2.

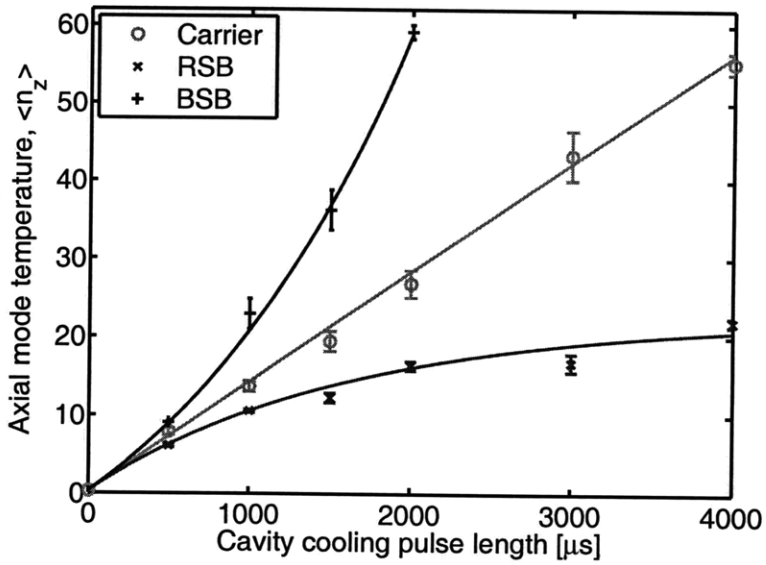

Figure 5-15: Cavity cooling dynamics. The ion is sideband cooled to the three-dimensional motional ground state; a cavity cooling pulse with detuning $\delta_{LC} = 0$ (carrier), $\delta_{LC} = -\omega_z$ (red axial sideband), or $\delta_{LC} = +\omega_z$ (blue axial sideband) is applied; and the number of motional quanta in the z mode is measured. The cavity is detuned by $\delta_{CA}/(2\pi) = -10$ MHz from the atomic transition and the cavity cooling beam has nonzero projections along the radial motional modes but not along the axial motional mode, so the radial motional modes are maintained at $\langle n_{x,y} \rangle \lesssim 10$ by Doppler cooling but the axial motional mode is not Doppler cooled. The lines are a fit to the model described in the text with fit parameters $\langle n \rangle_{t=0} = 0.30 \pm 0.06$, $\Gamma_{sc} = (2.87 \pm 0.02) \times 10^6$ photons/s, and $\eta_{C,eff} = 0.0148 \pm 0.0002$. The reduced χ^2 of the fit is 1.7.

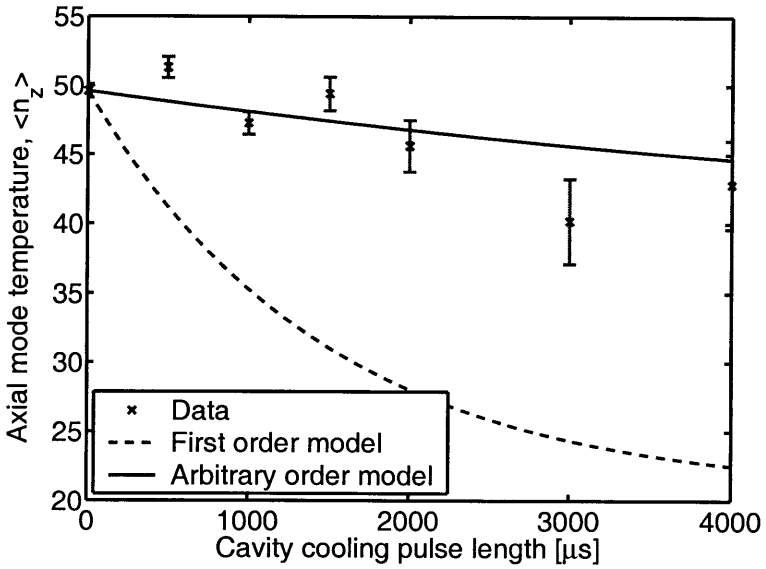

Figure 5-16: Cavity cooling demonstration. The ion is sideband cooled to the three-dimensional motional ground state; the z motional mode is sideband heated to 50 motional quanta; a cavity cooling pulse with detuning $\delta_{LC} = -\omega_z$ is applied; and the number of motional quanta in the z mode is measured. The cavity-atom detuning and cavity cooling beam power are the same as in Figure 5-15. The data is fit to the modified cavity cooling rate equation model described in the text (valid to all orders in the Lamb-Dicke parameter, solid black line) with input parameters $\langle n \rangle_{t=0} = 49.6$ and $\Gamma_{sc} = 2.87 \times 10^6$ photons/s and fit parameter $\eta_{C,eff} = 0.0162 \pm 0.0004$. The ion is cavity cooled from the initial temperature of 50 quanta to about 45 quanta in 4 ms. The reduced χ^2 of the fit is 3.0. For reference, the simpler model which is correct only to first order in the Lamb-Dicke parameter is also shown (dashed black line).

Vuletić et al. model

The rate of transitions from motional state n to $n-1$ is

$$\Gamma_{sc}\eta_{C,eff}\eta_{LD}^2 n \frac{1}{1+\left(\frac{\delta_{LC}+\omega}{\kappa/2}\right)^2} \equiv R^- n \tag{5.10}$$

and the rate of transitions from motional state n to $n+1$ is

$$\Gamma_{sc}\eta_{C,eff}\eta_{LD}^2 (n+1) \frac{1}{1+\left(\frac{\delta_{LC}-\omega}{\kappa/2}\right)^2} + \Gamma_{sc} C \eta_{LD}^2 + \dot{n} \equiv R^+(n+1) + N^+ \tag{5.11}$$

where Γ_{sc} is the free space scattering rate, C is defined such that $C\eta_{LD}^2\hbar\omega$ is the average recoil heating of the motional mode of interest per free space scattering event and $\dot{n}$ is the heating rate in motional quanta per second of the motional mode of interest due to environmental electric field fluctuations. The expectation value of the number of motional quanta evolves according to

$$\frac{d}{dt}\langle n\rangle = -(R^- - R^+)\langle n\rangle + R^+ + N^+ \,. \tag{5.12}$$

Integrating Equation 5.12 results in closed form expressions for the mean ion temperature as a function of time:

$$\langle n\rangle_t = \langle n\rangle_{t=0} e^{-Wt} + \langle n\rangle_{SS}\left(1-e^{-Wt}\right) \tag{5.13}$$

for $\delta_{LC} = -\omega$,

$$\langle n\rangle_t = \langle n\rangle_{t=0} + \left(R^+ + N^+\right) t \tag{5.14}$$

for $\delta_{LC} = 0$, and

$$\langle n\rangle_t = \left(\langle n\rangle_{t=0} + \langle n\rangle_{SS} + 1\right) e^{Wt} - \left(\langle n\rangle_{SS} + 1\right) \tag{5.15}$$

for $\delta_{LC} = +\omega$. The cavity cooling rate W is given by

$$W = \frac{\Gamma_{sc}\eta_{C,eff}\eta_{LD}^2}{1+\left(\frac{\kappa/2}{2\omega}\right)^2} \tag{5.16}$$

and the steady state temperature $\langle n\rangle_{SS}$ is given by

$$\langle n\rangle_{SS} = \left(\frac{\kappa/2}{2\omega}\right)^2 + \left[\frac{C+\frac{\dot{n}}{\Gamma_{SC}\eta_{LD}^2}}{\eta_{C,eff}}\right]\left[1+\left(\frac{\kappa/2}{2\omega}\right)^2\right] \,. \tag{5.17}$$

For cavity cooling of the z motional mode, $C = 1/3$ (photons are scattered isotropically for a $J = 1/2 \leftrightarrow J' = 1/2$ transition [MJMD01, BKD04]) and $\dot{n} = 17 \pm 2$ (measured using the same technique as in Chapter 3). The data in Figure 5-15 fits the above model with fit parameters $\langle n\rangle_{t=0} = 0.30 \pm 0.06$, $\Gamma_{sc} = (2.87 \pm 0.02) \times 10^6$ photons/s, and $\eta_{C,eff} = 0.0148 \pm 0.0002$. This value of the scattering rate is consistent with what is measured using the free space imaging system and this value of the effective cooperativity is within the errorbars of the value measured in Section 5.4. Thus, the cavity cooling rate equation model fits the cavity cooling dynamics data without any free parameters.

Extension to beyond the Lamb-Dicke regime

The data in Figure 5-16 does not fit very well to the model above because the data is outside the Lamb-Dicke regime ($\eta_{LD}^2 \langle n \rangle = 0.73 \not\ll 1$ for $\langle n \rangle = 50$). This results in a reduction of the motional sideband transition rate relative to that in the model which is correct only to first order in $\eta_{LD}^2 \langle n \rangle$. In this case, Equations 5.10 and 5.11 must be replaced by

$$\Gamma_{sc}\eta_{C,eff}\eta_{LD}^2 n \left[\frac{e^{-\eta_{LD}^2/2} L_{n-1}^1(\eta_{LD}^2)}{n}\right]^2 \frac{1}{1+\left(\frac{\delta_{LC}+\omega}{\kappa/2}\right)^2} \equiv R^-(n)n \tag{5.18}$$

and

$$\Gamma_{sc}\eta_{C,eff}\eta_{LD}^2(n+1) \left[\frac{e^{-\eta_{LD}^2/2} L_n^1(\eta_{LD}^2)}{n+1}\right]^2 \frac{1}{1+\left(\frac{\delta_{LC}-\omega}{\kappa/2}\right)^2} + \Gamma_{sc}C\eta_{LD}^2 + \dot{n} \equiv R^+(n)(n+1) + N^+ , \tag{5.19}$$

and the resulting set of differential equations for the population of each motional state must be numerically integrated. The data in Figure 5-16 fits the modified model with input parameters $\langle n \rangle_{t=0} = 49.6$ and $\Gamma_{sc} = 2.87 \times 10^6$ photons/s and fit parameter $\eta_{C,eff} = 0.0162 \pm 0.0004$. Again, since this value of the cooperativity is within the errorbars of the value measured in Section 5.4, this represents parameter free agreement between the cavity cooling data and model.

5.7 Discussion

This experiment is the first demonstration of cavity cooling of a trapped ion and the first demonstration of cavity cooling in the resolved sideband regime. While the small effective cooperativity prevents cavity cooling to the motional ground state, the measured cooling dynamics agree with the rate equation model proposed by Vuletić et al. [VCB01] without any free parameters. This serves as a validation test of the rate equation model, which predicts that with a higher effective cooperativity it should be possible to cavity cool to the motional ground state.

While the next logical step to demonstrate quantum non-demolition cavity cooling, this will require switching to a different qubit scheme. The detuning of the cavity from any atomic transitions must be large compared with the spacing between the qubit states, which is not experimentally possible with an optical qubit. Thus, a demonstration of quantum non-demolition cooling with strontium ions would require using either the two Zeeman levels of the $^{88}Sr^+$ ground state or two levels of the $^{87}Sr^+$ ground state hyperfine manifold as the qubit.

An interesting alternative direction to pursue is cavity cooling of a molecular ion. Because the temperature limit of cavity cooling is independent of the energy level structure of the particle, cavity cooling is in principle applicable to complicated atoms or molecules without closed optical transitions [MPKdVR07, KMPdVR07, LVH+08]. One particularly interesting molecule to consider is C_{60}, also known as buckeyballs. The ion C_{60}^+ has been trapped in an ion trap [RZS06] and studied spectroscopically [TWMK93, FJM93]. It is astrophysically interesting in that it may be present in significant quantities in the interstellar medium, but the spectroscopic properties are not known well enough to tell [FE94, Her00].

Because it can be assumed that none of the transitions are closed, cavity cooling of C_{60}^+ would require a cavity far off resonance from any of its transitions and a very high laser intensity. Ziliang Lin calculated the optical polarizibility of C_{60}^+ using the Hartree-Fock method (following the technique of Reference [RJT01]) to be 72 Å^3 at 532 nm and 65 Å^3 at 492 nm. These values are close to the measured polarizibility of neutral C_{60} which is 90 ± 11 Å^3 at 532 nm [HHG$^+$07]. The cavity can be used to enhance the intensity of the cavity cooling beam by putting the cavity cooling beam in the cavity. For cavity parameters $F = 50000$ at 493 nm, $L = 4.95$ cm, $R = 2.5$ cm, and $w_0 = 20$ μm; a free space scattering rate of 1500 photons/s could be achieved with 6 mW of input power and 300 W of circulating power. The laser intensity on the cavity mirror surface is about half of the damage threshold for these parameters. Cavity cooling of C_{60}^+ would be an interesting, but challenging, direction for further research.

Part III

Future directions

Chapter 6

Coherent mapping between single ions and single photons via collective states

One exciting application of quantum information science is quantum networks. Quantum networks enable both long distance quantum communication [BDCZ98], which can perform provably secure cryptographic key distribution [BB84], and distributed quantum computation, which can overcome any size constraints on the individual quantum computers making up the network [CEHM99]. In the trapped ion implementation, the nodes of quantum networks are trapped ion quantum computers and the channels are optical fibers. The nodes and channels are connected by quantum interconnects, which perform coherent mapping between single ion and single photon states. Trapped ion quantum interconnects can be implemented using controlled vacuum Rabi flopping of a cavity QED system in the strong coupling regime [CZKM97, Pel97].

While Boozer et al. have accomplished coherent mapping between single atom and single photon states in the strong coupling regime [BBM+07], the experimental difficulty of achieving strong coupling with a single atom or ion has led other groups explore the use of superradiant states of atomic ensembles [Dic54] in cavity QED. The coupling of superradiant states to the electromagnetic field is enhanced by the square root of the number of atoms in the ensemble, making it easier to reach the strong coupling regime. Several groups have implemented coherent mapping between collective atom and single photon states in the collective strong coupling regime [CPKK04, CMJ+05, EAM+05, STTV07].

So far, however, there has been little progress in performing local gates with collective states. There is a theoretical proposal for neutral atom Rydberg gates with collective states, but each qubit must be encoded in a collective state involving a different pair of atomic energy levels which limits the number of collective state qubits to of the order of 10 [BMS07, SM08]. In contrast, high fidelity trapped ion local gates have been accomplished by several groups [TWK+98, BKRB08] and there are no fundamental limits to scaling to large numbers of qubits, but there has been much less success in mapping between single ion and single photon states.

This chapter describes a proposal for implementing trapped ion quantum networks which combines the strengths of collective state strong coupling with photons and single trapped ion quantum gates. The basic idea is to construct a quantum gate which maps a single ion state onto a superradient collective state of several ions, then to follow the neutral atom

procedure for mapping the collective ion state to a single photon state in the collective strong coupling regime of cavity QED. Section 6.1 describes the Cirac et al. proposal for quantum interconnects between single ions and single photons [CZKM97]. Section 6.2 describes the use of collective states for enhanced cavity coupling and the gate which maps single ion states to collective ion states. Finally, Section 6.3 presents a detailed proposal for a demonstration experiment with $^{88}Sr^{+}$, including a calculation of the fidelity of mapping between two single ions via collective states and a single photon.

For completeness it is noted that there is an alternative approach for implementing quantum networks with trapped atoms or ions which generates entanglement between nodes probabilistically using interference of spontaneously emitted photons [DLCZ01]. Both quantum communication and distributed quantum computation are possible despite the probabilistic nature of entanglement [DR05, DMM^{+}06], and the advantages of this approach are that it does not require the strong coupling regime and it can be implemented in a way which is insensitive to the photon phase (so that the lengths of the optical fibers between nodes do not need to be stabilized) [DK03, SI03]. Several groups are pursuing this approach experimentally and have observed entanglement between a single ion and its spontaneous emission photons [BMDM04] and interference between spontaneous emission photons from two ions [MMO^{+}07] or atomic ensembles [CMJ^{+}07]. The disadvantage of this approach is that the entanglement is probabilistic, with a probability of success that goes like the efficiency of collecting the spontaneously emitted photons squared. Typically the collection efficiency is $\sim 10^{-2}$ which results in a success probability $\lesssim 10^{-4}$. This imposes a stiff overhead for the probabilistic approach to quantum networks.

Section 6.1 is a review of previous work by Cirac et al., and Sections 6.2 and 6.3 are original work.

6.1 Coherent mapping between single ions and single photons

This section begins by presenting a simplified version of the Cirac et al. proposal for a two node quantum network [CZKM97].

6.1.1 Quantum network model

The setup of the Cirac et al. proposal is shown in Figure 6-1. It consists of two identical two-level ions coupled with optical cavities connected by an optical fiber. This is the simplest possible quantum network, but together with local operations it contains all of the components required to build an arbitrarily complex quantum network. The desired operation is the mapping

$$(c_g|g\rangle_1 + c_e|e\rangle_1)\,|0\rangle_1 \otimes |g\rangle_2|0\rangle_2 \rightarrow |g\rangle_1|0\rangle_1 \otimes (c_g|g\rangle_2 + c_e|e\rangle_2)\,|0\rangle_2 \tag{6.1}$$

where from left to right the kets denote the state of the ion at node 1, the cavity at node 1, the ion at node 2, and the cavity at node 2.

The Hamiltonian for each node, assuming that the cavities are on resonance with the atomic transitions and in the rotating frame, is

$$H_i = \hbar g_i(t)\left[|e\rangle_{ii}\langle g|a_i + |g\rangle_{ii}\langle e|a_i^{\dagger}\right] . \tag{6.2}$$

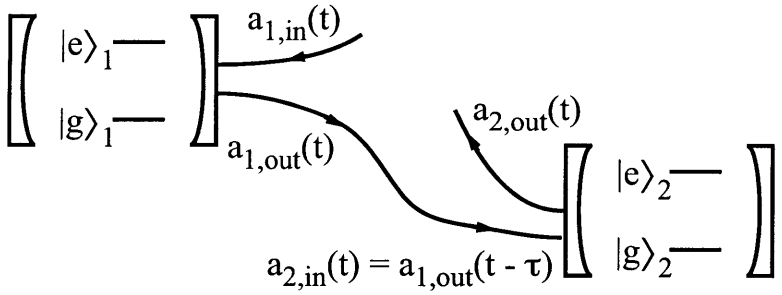

Figure 6-1: Simplified version of the setup of the Cirac et al. proposal [CZKM97] for a two node quantum network. Each node consists of a two-level atom in an optical cavity. Each node has input and output electric field modes $a_{i,in}(t)$ and $a_{i,out}(t)$, and the output mode of node 1 is coupled to the input mode of node 2 with an optical fiber. Note that the input and output modes of an optical cavity can be separated experimentally with a Faraday rotator.

Here, $g_i(t)$ is the (time-dependent) ion-cavity coupling and a_i is the annihilation operator for the cavity mode at node i.

In the Heisenberg picture, the annihilation operators of the cavity modes evolve according to the quantum Langevin equations [CZKM97, GZ04]

$$\frac{da_i}{dt} = -\frac{i}{\hbar}[a_i, H_i] - \frac{\kappa}{2}a_i - \sqrt{\kappa}a_{i,in}(t) \tag{6.3}$$

where κ is the spontaneous decay rate of the cavity (energy, not field). The output of each cavity is [CZKM97, GZ04]

$$a_{i,out}(t) = a_{i,in}(t) + \sqrt{\kappa}a_i(t) \tag{6.4}$$

and the input of the second cavity is the output of the first cavity ($a_{2,in}(t) = a_{1,out}(t-\tau)$), so the quantum Langevin equations can be rewritten as [CZKM97, GZ04]

$$\frac{da_1}{dt} = -\frac{i}{\hbar}[a_1, H_1] - \frac{\kappa}{2}a_1 - \sqrt{\kappa}a_{1,in}(t) \tag{6.5}$$

and

$$\frac{da_2}{dt} = -\frac{i}{\hbar}[a_2, H_2] - \frac{\kappa}{2}a_2 - \kappa a_1(t-\tau) - \sqrt{\kappa}a_{1,in}(t-\tau)\ . \tag{6.6}$$

For simplicity of notation in the following equations, the operators and functions for the first node are redefined using the transformations $a_1(t-\tau) \rightarrow a_1(t)$, $a_{1,in}(t-\tau) \rightarrow a_{1,in}(t)$, and $g_1(t-\tau) \rightarrow g_1(t)$.

The correct waveforms for the functions $g_i(t)$ are determined by considering the evolution of the system in the framework of quantum trajectories. The input mode of the first node is the vacuum state, $a_{1,in}(t)|\psi(t)\rangle = 0$, and the output mode of the second node is monitored by a hypothetical photodetector. During the time when no counts are detected, the system evolves according the the effective Hamiltonian [CZKM97, GZ04]

$$H_{eff} = H_1 + H_2 - i\hbar\frac{\kappa}{2}\left(a_1^\dagger a_1 + a_2^\dagger a_2 + 2a_2^\dagger a_1\right)\ . \tag{6.7}$$

Equation 6.4 gives [CZKM97, GZ04]

$$a_{2,out}(t) = a_{1,in}(t) + \sqrt{\kappa}\,[a_1(t) + a_2(t)] \ , \tag{6.8}$$

so the probability per unit time for a count to be detected is [CZKM97, GZ04]

$$\langle\psi(t)|(a_1 + a_2)^\dagger(a_1 + a_2)|\psi(t)\rangle \ . \tag{6.9}$$

The mapping in Equation 6.1 is accomplished if and only if no counts are detected, so the correct waveforms for the functions $g_i(t)$ can be constructed by solving for the time evolution of the state $|\psi(t)\rangle$ under the effective Hamiltonian in Equation 6.7 subject to the constraint $(a_1 + a_2)|\psi(t)\rangle = 0$.

Solving for the waveforms $g_i(t)$ is a complicated mathematical problem. One way to proceed is to impose two additional conditions: $g_2(t) = g_1(-t)$, which results in a time-symmetric photon wavepacket, and $g_1(t > 0) =$ constant. These two conditions are sufficient to completely determine the waveforms $g_i(t)$ [CZKM97, GZ04]. The control waveforms $g_1(t) = g_2(-t)$ and photon wavepackets $\langle\psi(t)|a_1^\dagger a_1|\psi(t)\rangle$ are shown in Figure 6-2 for several values of $g_1(t > 0)$. The time required to map the ion state onto the photon state is of the order of $\max[1/\kappa, 1/g_1(t > 0)]$.

6.1.2 Vacuum-stimulated Raman transitions

The Cirac et al. quantum interconnect requires experimental control over the ion-cavity coupling as a function of time. While it might be possible to accomplish this by moving the ion in and out of the cavity mode, this would constrain the time for mapping the ion state onto the photon state to be much greater than the reciprocal of the ion motional frequency. A more general method of controlling the ion-cavity coupling is with vacuum-stimulated Raman transitions [MBR+04].

Figure 6-3 shows an energy level diagram for vacuum-stimulated Raman transitions. A laser couples the ground state $|g\rangle$ to an auxiliary state $|r\rangle$ and the cavity couples the auxiliary state $|r\rangle$ to the excited state $|e\rangle$. The auxiliary state spontaneously decays to states $|g\rangle$ and $|e\rangle$ with rates Γ_g and Γ_e. Assuming that $\delta_g = \delta_e \equiv \delta$ and that $\delta \gg \Omega, g, \Gamma_g, \Gamma_e$, the auxiliary state $|r\rangle$ can be adiabatically eliminated from the equations of motion to form an effective two-level system with Hamiltonian [MBR+04]

$$H = \hbar\frac{\Omega g}{2\delta_g}\left(|e\rangle\langle g|a^\dagger + |g\rangle\langle e|a\right) \tag{6.10}$$

where a is the annihilation operator for the cavity mode. The probability of being in the auxiliary state is $(\Omega^2 + 4g^2)/(4\delta^2)$, and the spontaneous decay rate is $(\Gamma_g + \Gamma_e)(\Omega^2 + 4g^2)/(4\delta^2)$.

The Hamiltonian in Equation 6.10 looks identical to the Hamiltonian in Equation 6.2 with the substitutions $g \rightarrow \Omega g/(2\delta)$ and $|g\rangle \leftrightarrow |e\rangle$. Thus, stimulated Raman transitions can be used to implement the Cirac et al. proposal for a two node quantum network. The effective ion cavity coupling $\Omega g/(2\delta)$ is controlled by changing the intensity of the laser used to connect states $|g\rangle$ and $|r\rangle$, so that $\Omega = \Omega(t)$ is a function of time.

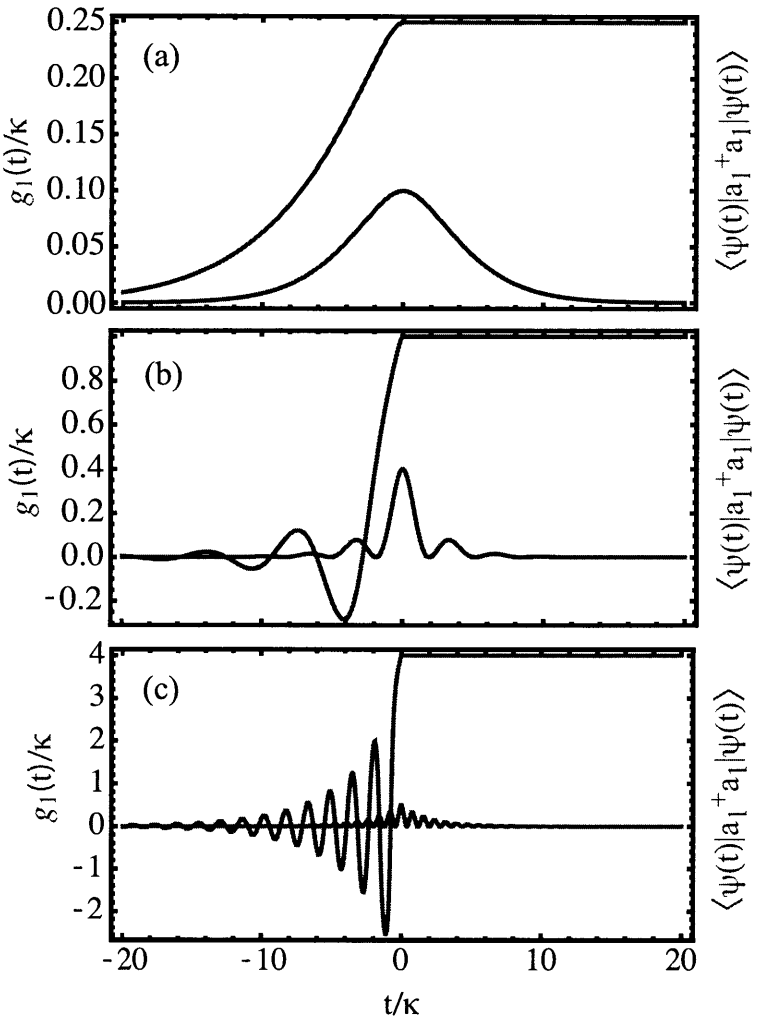

Figure 6-2: Control waveforms $g_1(t) = g_2(-t)$ and photon wavepackets $\langle\psi(t)|a_1^\dagger a_1|\psi(t)\rangle$ as a function of time for quantum state transfer in a two node quantum network. (a) $g_1(t > 0) = \kappa/4$. (b) $g_1(t > 0) = \kappa$. (c) $g_1(t > 0) = 4\kappa$.

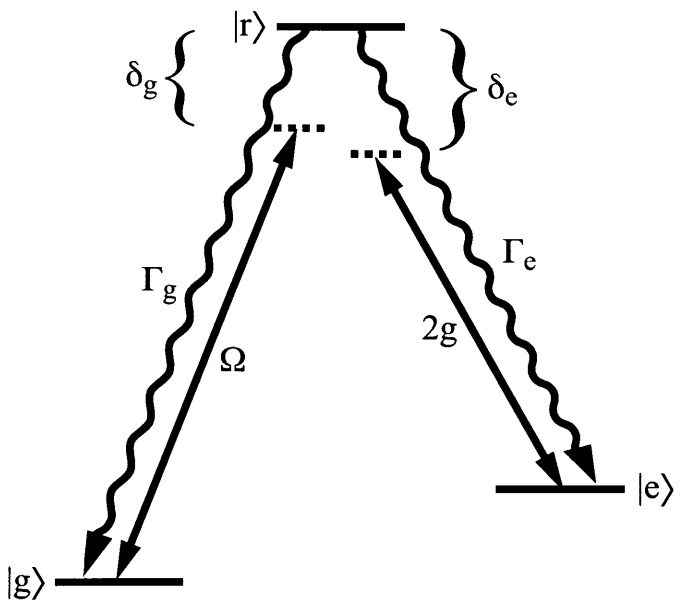

Figure 6-3: Energy level diagram for vacuum-stimulated Raman transitions. A laser with Rabi frequency Ω and detuning δ_g couples the ground state $|g\rangle$ to an auxiliary state $|r\rangle$ and a cavity with coupling g and detuning δ_e couples the auxiliary state $|r\rangle$ to the excited state $|e\rangle$.

6.1.3 Requirements for implementation

Assuming that the control waveforms can be implemented perfectly, the remaining sources of error for the Cirac et al. quantum interconnect are:

1. Spontaneous decay of the auxiliary state $|r\rangle$. The error due to spontaneous decay is small if

$$(\text{probability of spontaneous decay}) \sim (\Gamma_g + \Gamma_e)\frac{\Omega^2 + 4g^2}{4\delta^2} \max\left[\frac{1}{\kappa}, \frac{\delta}{g\Omega}\right] \ll 1 \ . \quad (6.11)$$

2. Decoherence of the $|g\rangle$ and $|e\rangle$ states due to imperfect laser frequency stabilization, cavity frequency stabilization, and magnetic field stabilization. Suppression of decoherence requires that

$$\max\left[\frac{1}{\kappa}, \frac{\delta}{g\Omega}\right] \ll \frac{1}{(\text{laser linewidth}) + (\text{cavity lock linewidth}) + \mu_B(\text{magnetic field noise})} \quad (6.12)$$

   where μ_B is the Bohr magneton.

3. Photon loss in the cavity mirrors. The probability of photon loss in the cavity mirrors is small if

$$(\text{loss of both mirrors}) + (\text{transmission of non-output mirror}) \ll (\text{transmission of output mirror}) \ . \quad (6.13)$$

The requirements in Equations 6.11 through 6.13 can be simplified by selecting Ω such that $\Omega g/\delta \sim \kappa$, which minimizes the time required to map the ion state onto the photon state. In this case, Equation 6.11 simplifies to

$$\frac{4g^2}{\kappa(\Gamma_g + \Gamma_e)} \gg 1 \ , \tag{6.14}$$

which is the definition of the strong coupling regime, and

$$\delta \gg \sqrt{\frac{g^2(\Gamma_g + \Gamma_e)}{\kappa}} \ . \tag{6.15}$$

Equation 6.12 simplifies to

$$\text{(laser linewidth)} + \text{(cavity lock linewidth)} + \mu_B\text{(magnetic field noise)} \ll \kappa \ . \tag{6.16}$$

With trapped ions, usually the strong coupling regime (Equation 6.14) is the most difficult requirement to fulfill.

Another type of error to consider is that the presence of the cavity causes decoherence of the ion by coupling the $|e\rangle$ state to the $|r\rangle$ state, which suffers from spontaneous decay. This will be small if

$$(\Gamma_g + \Gamma_e)\frac{g^2}{\delta^2}\text{(storage time)} \ll 1 \ , \tag{6.17}$$

and could be avoided altogether if the ion is moved out of the cavity when mapping between photons and ions is not taking place.

6.2 Collective ion states

The coupling of superradiant collective states of several ions to the electromagnetic field is enhanced by the square root of the number of ions, N [Dic54]. The use of collective states for a quantum interconnect would relax the strong coupling requirement (Equation 6.14) to

$$\frac{N4g^2}{\kappa(\Gamma_g + \Gamma_e)} \gg 1 \ . \tag{6.18}$$

This is called the collective strong coupling regime.

This section describes the use of collective states for a quantum interconnect. Single ion states are mapped to collective states of several ions, which are then mapped to single photons. Section 6.2.1 describes the mapping between collective ion states and single photon states, and Section 6.2.2 describes the mapping between single ion states and collective ion states. Section 6.2.3 describes how to match the phases of the collective ion state which couples to single photons and the collective ion state which couples to single ions.

6.2.1 Mapping between collective ion states and single photon states

The Hamiltonian for the interaction of several three-level ions with a cavity mode in the rotating frame is simply the sum of the interaction Hamiltonians for each ion:

$$H = \sum_{k=1}^{N} \left(\hbar \frac{\Omega_{k,C} g_k}{2\delta} |e\rangle_{kk}\langle g| a^\dagger + \hbar \frac{\Omega_{k,C}^* g_k^*}{2\delta} |g\rangle_{kk}\langle e| a \right) \bigotimes_{\substack{l=1 \\ l \neq k}}^{N} (|g\rangle_{ll}\langle g| + |e\rangle_{ll}\langle e|) \ . \tag{6.19}$$

Here the auxiliary state $|r\rangle$ has already been adiabatically eliminated (but it will be important in Section 6.2.3 for phase matching) and $\Omega_{k,C}$ and g_k are the Rabi frequency and cavity coupling at the location of ion k. (The subscript C stands for the laser which controls the collective cavity coupling, to be differentiated from the laser which maps single ion states onto collective ion states in Section 6.2.2.) If the quantum state of the system is in the manifold spanned by

$$|\tilde{g}_C\rangle|0\rangle = |ggg\cdots g\rangle|0\rangle \tag{6.20}$$

and

$$|\tilde{e}_C\rangle|1\rangle = \sum_{k=1}^{N} \frac{\Omega_{k,C} g_k/(2\delta)}{\tilde{g}} |e\rangle_k \left(\bigotimes_{\substack{l=1 \\ l \neq k}}^{N} |g\rangle_l \right) |1\rangle \ , \tag{6.21}$$

the Hamiltonian in Equation 6.19 reduces to

$$H = \hbar\tilde{g} \left(|\tilde{e}_C\rangle\langle\tilde{g}_C| a^\dagger + |\tilde{g}_C\rangle\langle\tilde{e}_C| a \right) \tag{6.22}$$

and the ion Rabi flops between the collective states $|\tilde{g}_C\rangle|0\rangle$ and $|\tilde{e}_C\rangle|1\rangle$ with Rabi frequency $2\tilde{g}$. Here, $\tilde{g}$ is given by

$$\tilde{g} = \sqrt{\sum_{k=1}^{N} \left| \frac{\Omega_{k,C} g_k}{2\delta} \right|^2} \ . \tag{6.23}$$

Note that the Hamiltonian in Equation 6.22 does not take the system out of the manifold spanned by $|\tilde{g}_C\rangle|0\rangle$ and $|\tilde{e}_C\rangle|1\rangle$. If $\Omega_{k,C} = \Omega_C$ and $g_k = g$ are uniform over all the ions, then $\tilde{g} = \sqrt{N}\Omega_C g/(2\delta)$ and the coupling of the superradiant collective states to the electromagnetic field is enhanced by a factor of the square root of the number of ions relative to the coupling of a single ion as advertised.

6.2.2 Mapping between single ion states and collective ion states

In order to use the enhanced coupling described in the previous section for a trapped ion quantum interconnect, it is necessary to be able to perform coherent mapping between single ion states (which are used for quantum information processing locally at each node) and collective ion states (which couple strongly to the electromagnetic field). This can be accomplished in two steps as follows.

The first step is to apply a red motional sideband π pulse on the ion which stores the qubit to be transmitted. This performs the mapping

$$(c_g|g\rangle + c_e|e\rangle)|gg\cdots g\rangle|0\rangle \rightarrow |ggg\cdots g\rangle(c_g|0\rangle + c_e|1\rangle) \ , \tag{6.24}$$

where in this section the rightmost ket represents the motional state of the ion chain.

The second step is to apply a collective red sideband π pulse on all of the ions. A single laser is simultaneously incident on all of the ions with Hamiltonian

$$H = \sum_{k=1}^{N} \left(\hbar \frac{\eta_{LD}\Omega_{k,L}/\sqrt{N}}{2} |e\rangle_{kk}\langle g|b + \hbar \frac{\eta_{LD}\Omega^*_{k,L}/\sqrt{N}}{2} |g\rangle_{kk}\langle e|b^\dagger \right) \bigotimes_{\substack{l=1 \\ l\neq k}}^{N} (|g\rangle_{ll}\langle g| + |e\rangle_{ll}\langle e|) \tag{6.25}$$

where b is the annihilation operator for the motional mode, $\eta_{LD}/\sqrt{N}$ is the Lamb-Dicke parameter for an N ion crystal, and $\Omega_{k,L}$ is the Rabi frequency of the laser at the position of ion k. The form of this Hamiltonian is identical to that of Equation 6.19, where the cavity (harmonic oscillator) mode has been replaced by the motional (harmonic oscillator) mode. The same analysis can be carried out. If the ion is in the manifold spanned by

$$|\tilde{g}_L\rangle|1\rangle = |ggg\cdots g\rangle|1\rangle \tag{6.26}$$

and

$$|\tilde{e}_L\rangle|0\rangle = \sum_{k=1}^{N} \frac{\Omega_{k,L}}{\tilde{\Omega}} |e\rangle_k \left(\bigotimes_{\substack{l=1 \\ l\neq k}}^{N} |g\rangle_l \right) |0\rangle \ , \tag{6.27}$$

the Hamiltonian reduces to

$$H = \hbar \frac{\eta_{LD}\tilde{\Omega}}{2} \left(|\tilde{e}_L\rangle\langle\tilde{g}_L|b + |\tilde{g}_L\rangle\langle\tilde{e}_L|b^\dagger \right) \tag{6.28}$$

and the ion Rabi flops between the collective states $|\tilde{g}_L\rangle|1\rangle$ and $|\tilde{e}_L\rangle|0\rangle$ with Rabi frequency

$$\tilde{\Omega} = \sqrt{\frac{\sum_{k=1}^{N} |\Omega_{k,L}|^2}{N}} \ . \tag{6.29}$$

Note that the Hamiltonian in Equation 6.25 does nothing to the state $|ggg\cdots g\rangle|0\rangle$. A collective red sideband π pulse is accomplished by applying the laser for a time $\pi/(\eta_{LD}\tilde{\Omega})$ and the associated mapping is

$$|ggg\cdots g\rangle(c_g|0\rangle + c_e|1\rangle) \rightarrow (c_g|\tilde{g}_L\rangle + c_e|\tilde{e}_L\rangle)|0\rangle \ . \tag{6.30}$$

An alternative method for mapping between single ion and collective ion states is a series of laser pulses each acting on a single ion. Häffner et al. [HHR+05] has generated and verified collective states of the form $|\tilde{e}_L\rangle$ of up to 8 ions using this method. While this method is significantly more complicated than the method proposed above, it allows arbitrary phase matching.

6.2.3 Phase matching

If $|\tilde{g}_C\rangle = |\tilde{g}_L\rangle$ and $|\tilde{e}_C\rangle = |\tilde{e}_L\rangle$, then the mappings in Sections 6.2.1 and 6.2.2 can be combined to map from a single ion state to a single photon state via a collective ion state with enhanced coupling to the cavity mode. This condition is called phase matching, and

can be explicitly stated as

$$\frac{\Omega_{k,C} g_k/(2\delta)}{\tilde{g}} = \frac{\eta_{LD}\Omega_{k,L}}{\tilde{\Omega}} \tag{6.31}$$

for all k. The amplitude and phase of $\Omega_{k,C}$, g_k, and $\Omega_{k,L}$ depend on position, so phase matching is only possible for some special geometries.

The cavity mode is a standing wave, so the position dependence of g_k is

$$g_k \sim \cos^2(\vec{k}_0 \cdot \vec{r}_k) e^{-|\vec{r}_k - \vec{r}_k \cdot \hat{k}_0|^2/w_0^2} \tag{6.32}$$

where k_0 is the wavevector of the cavity mode and w_0 is the cavity waist. The lasers can be either standing or traveling waves, with associated position dependence

$$\Omega_{k,\alpha} \sim \cos^2(\vec{k}_\alpha \cdot \vec{r}_k) e^{-|\vec{r}_k - \vec{r}_k \cdot \hat{k}_\alpha|^2/w_\alpha^2} \tag{6.33}$$

or

$$\Omega_{k,\alpha} \sim e^{i\vec{k}_\alpha \cdot \vec{r}_k} e^{-|\vec{r}_k - \vec{r}_k \cdot \hat{k}_\alpha|^2/w_\alpha^2} \tag{6.34}$$

where $\alpha = C$ or L and k_C and k_L are the laser wavevectors. Typically, the cavity waist w_0 is of the order of tens of microns and the laser spot sizes w_C and w_L can be made as small or as large as desired.

If the ion chain is parallel to the cavity axis, phase matching can be accomplished with the laser geometry shown in Figure 6-4(a). The vacuum-stimulated Raman laser is a standing wave while the collective state generation laser is a traveling wave. The laser spot sizes w_C and w_L must be much larger than the total ion chain length, and $\theta = \cos^{-1}(|\vec{k}_0|/|\vec{k}_L|)$. The number of ions is limited only such that the total ion chain length is much less than the Rayleigh length of the cavity.

If, on the other hand, the ion chain is perpendicular to the cavity axis, phase matching can be accomplished with the laser geometry shown in Figure 6-4(b). Both lasers are traveling waves. The laser spot size w_C must be much larger than the total ion chain length but w_L can be smaller. The angle $\theta = \cos^{-1}(|\vec{k}_L|/|\vec{k}_C|)$. In this geometry, the number of ions is limited such that the total ion chain length is much less than the cavity waist w_0.

6.3 Proposed implementation with $^{88}Sr^+$

This section details an experimental proposal for implementing coherent mapping between single ions and single photons via collective states with $^{88}Sr^+$. The relevant energy levels are shown in Figure 6-5. The collective state generation laser connects the two qubit states $S_{1/2}$ and $D_{5/2}$, the cavity connects states $D_{5/2}$ and $P_{3/2}$, and the vacuum-stimulated Raman laser connects states $S_{1/2}$ and $P_{3/2}$. This energy level scheme is advantageous because the ion state is mapped to a photon at 1033 nm, which has a relatively low attenuation in optical fibers ($\sim$ 1 dB/km).

6.3.1 Pulse sequence for coherent mapping between single ions and single photons via collective states

The complete pulse sequence for coherent mapping from single ions to single photons via collective states follows:

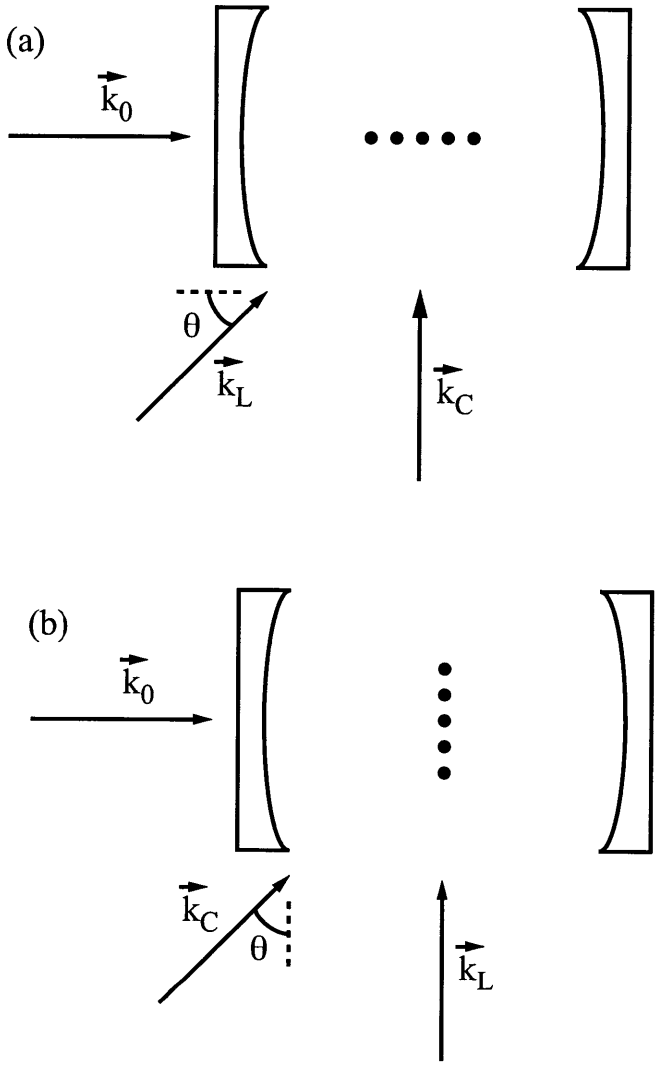

Figure 6-4: Two possible geometries for phase matching cavity and laser collective states. The wavevectors $\vec{k}_0$, $\vec{k}_C$, and $\vec{k}_L$ correspond to the cavity mode, the vacuum-stimulated Raman laser, and the collective state generation laser. (a) Ion chain parallel to the cavity axis. (b) Ion chain perpendicular to the cavity axis.

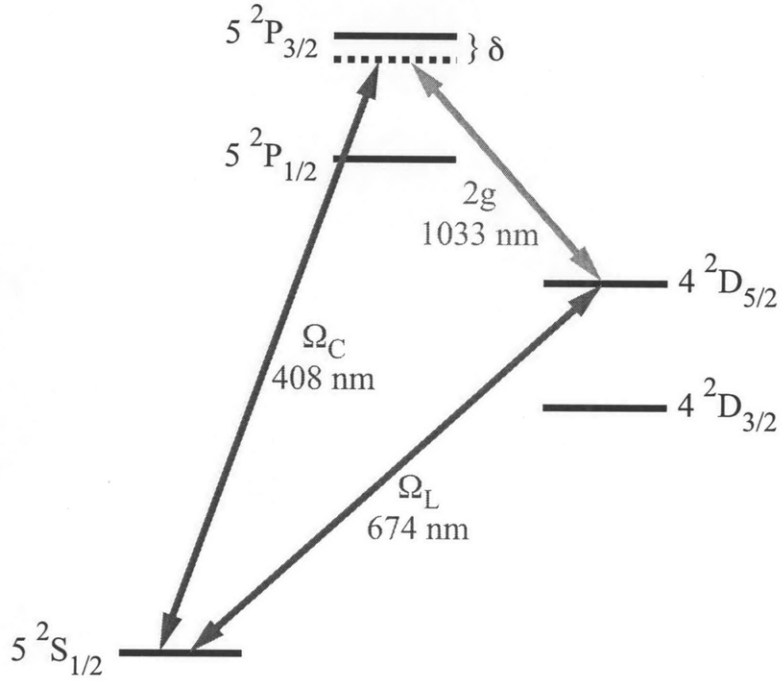

Figure 6-5: Energy level diagram for mapping between single ions and single photons with $^{88}Sr^+$. The collective state generation laser connects the two qubit states $S_{1/2}$ and $D_{5/2}$, the cavity connects states $D_{5/2}$ and $P_{3/2}$, and the vacuum-stimulated Raman laser connects states $S_{1/2}$ and $P_{3/2}$.

1. Single ion π pulse on the motional red sideband

$$(c_g|g\rangle + c_e|e\rangle)|gg\cdots g\rangle|0\rangle|0\rangle \rightarrow |ggg\cdots g\rangle(c_g|0\rangle + c_e|1\rangle)|0\rangle \ . \tag{6.35}$$

2. Collective π pulse on the motional red sideband

$$|ggg\cdots g\rangle(c_g|0\rangle + c_e|1\rangle)|0\rangle \rightarrow (c_g|\tilde{g}\rangle + c_e|\tilde{e}\rangle)|0\rangle|0\rangle \ . \tag{6.36}$$

3. Collective mapping from collective ion state to single photon state

$$(c_g|\tilde{g}\rangle + c_e|\tilde{e}\rangle)|0\rangle|0\rangle \rightarrow |\tilde{e}\rangle|0\rangle(c_g|1\rangle + c_e|0\rangle) \ . \tag{6.37}$$

Reading from left to right the kets represent the ion state, the motional state, and the cavity mode state. Here it is assumed that $|\tilde{g}_L\rangle = |\tilde{g}_C\rangle \equiv |\tilde{g}\rangle$ and $|\tilde{e}_L\rangle = |\tilde{e}_C\rangle \equiv |\tilde{e}\rangle$. Coherent mapping from single photons to single ions via collective states is accomplished by implementing the above pulse sequence in the reverse order.

6.3.2 Experimental requirements

The experimental requirements for implementing the above pulse sequence with high fidelity are:

1. Collective strong coupling,

$$\frac{N4g^2}{\kappa A_{P_{3/2}}} \gg 1 \tag{6.38}$$

where N is the number of ions and $A_{P_{3/2}}$ is the total spontaneous emission rate of the $P_{3/2}$ state.

2. Large vacuum-stimulated Raman detuning,

$$\delta \gg \sqrt{\frac{g^2 A_{P_{3/2}}}{\kappa}} \ . \tag{6.39}$$

3. Small decoherence rates,

$$\text{(laser linewidth)} + \text{(cavity lock linewidth)} + \mu_B\text{(magnetic field noise)} \ll \kappa \ . \tag{6.40}$$

4. Small mirror loss,

$$\begin{aligned}\text{(loss of both mirrors)} + \text{(transmission of non-output mirror)} \\ \ll \text{(transmission of output mirror)} \ .\end{aligned} \tag{6.41}$$

5. Linear chain of N ions [WMI+98b],

$$\text{(radial trap frequency)} > 0.73N^{0.86}\text{(axial trap frequency)} \ . \tag{6.42}$$

6. Ground state cooling of an N ion chain.

7. Individual addressing (this would not require tightly focused lasers if different ion species are used for the single ion qubit and the several ion collective state which couples to the cavity).

8. Frequency discrimination of the center of mass motional mode.

9. Spatially uniform magnetic field,

$$\mu_B(\text{magnetic field uniformity}) \ll \kappa \ . \tag{6.43}$$

10. Phase matching,

$$1 - |\langle \tilde{e}_L | \tilde{e}_C \rangle|^2 \ll 1 \ . \tag{6.44}$$

6.3.3 Ion trap, cavity, and states

While requirement 1 favors a large number of ions, requirements 5, 6, 7, and 8 all favor a small number of ions. An appropriate compromise is $N = 10$. An axial trap frequency of $2\pi \times 500$ kHz then imposes that the radial trap frequencies are $> 2\pi \times 2.6$ MHz, which is experimentally feasible.

For this number of ions, the phase matching geometry in Figure 6-4(b) is selected. This allows all of the ions to be located at an antinode of the cavity mode, which maximizes the collective cavity coupling $\tilde{g}$. Even with a cavity waist as small as $w_0 = 15$ μm, the phase matching fidelity is

$$|\langle \tilde{e}_L | \tilde{e}_C \rangle|^2 = \frac{\left(\sum_{i=1}^{N} e^{-z_i^2/w_0^2}\right)^2}{N \sum_{i=1}^{N} e^{-2z_i^2/w_0^2}} = 0.98 \ . \tag{6.45}$$

Here z_i is the position of ion i along the trap axis and is obtained by solving a set of equations which balance the Coulomb repulsion between ions with the trap potential [Jam98].

The collective strong coupling requirement can be rewritten as

$$\frac{24F}{\pi k_0^2 w_0^2} \frac{A_{P_{3/2} \to D_{5/2}}}{A_{P_{3/2}}} \frac{A_{P_{3/2},m=-3/2 \to D_{5/2},m=-5/2}}{A_{P_{3/2} \to D_{5/2}}} \gg 1 \ . \tag{6.46}$$

Here F is the cavity finesse. The second and third terms are due to the branching ratio and the Clebsch-Gordan coefficient for the particular transition selected. The choice of the magnetic sublevels $P_{3/2}, m = -3/2$ and $D_{5/2}, m = -5/2$ results in the largest possible value for the third term $A_{P_{3/2},m=-3/2 \to D_{5/2},m=-5/2}/A_{P_{3/2} \to D_{5/2}} = 2/3$ (see Figure 6-6), while the second term is fixed by the branching ratio to be $A_{P_{3/2} \to D_{5/2}}/A_{P_{3/2}} = 0.048$ (see Table 3.1).

While the collective strong coupling requirement demands a high cavity finesse, if the finesse is too high the losses in the cavity mirrors will dominate the transmission and the photon will be lost. A finesse $F = 50000$ is selected for this proposal, with contributions from the transmission of the mirrors $\mathcal{T}_1 = 120$ ppm and $\mathcal{T}_2 = 2$ ppm and contributions form the loss of the mirrors $\mathcal{L}_1 = \mathcal{L}_2 = 2$ ppm. High finesse cavities with 2 ppm mirror loss have been demonstrated at 854 nm [HKY01]. Since both absorption and scattering losses get smaller with increasing wavelength, it should be easier to obtain 2 ppm loss mirrors at 1033 nm. The resulting reduction of fidelity of mapping from a collective ion state to a single ion state is $\mathcal{T}_1/(\mathcal{T}_1 + \mathcal{T}_2 + \mathcal{L}_1 + \mathcal{L}_2) = 0.95$

The cavity geometry is selected to achieve a mode waist of $w_0 = 15$ μm with as large of a cavity decay rate κ as possible. The cavity mirrors have radii $R_1 = 5$ mm and $R_2 = \infty$,

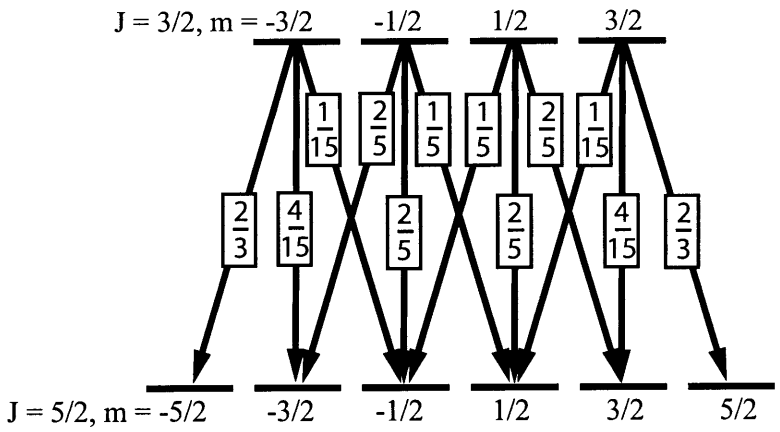

Figure 6-6: Clebsch-Gordan coefficients for the relative spontaneous decay rates of the magnetic sublevels of a $J = 5/2$ to $J = 3/2$ transition.

and the cavity length is $L = R_1 - 95$ μm. This results in a cavity decay rate of $\kappa/(2\pi) = 0.612$ MHz.

The resulting collective cavity cooperativity is

$$\eta_C = N\frac{24F}{\pi k_0^2 w_0^2}\frac{A_{P_{3/2}\rightarrow D_{5/2}}}{A_{P_{3/2}}}\frac{A_{P_{3/2},m=-3/2\rightarrow D_{5/2},m=-5/2}}{A_{P_{3/2}\rightarrow D_{5/2}}} = 14.7\ , \tag{6.47}$$

and the collective cavity coupling is $\tilde{g}/(2\pi) = 7.25$ MHz.

6.3.4 Schrödinger equation model

The fidelity of coherent mapping between two collective ion states via a single photon is calculated by numerical integration of the Schrödinger equation. Following Section 6.1.1, the non-Hermitian effective Hamiltonian is

$$H_{eff} = H_1 + H_2 - i\hbar\frac{\kappa_t}{2}\left(a_1^\dagger a_1 + a_2^\dagger a_2 + 2a_2^\dagger a_1\right) \tag{6.48}$$

and the Hamiltonian for each node is

$$H_i = \hbar\delta_{i,g}|\tilde{g}\rangle_{ii}\langle\tilde{g}| + \hbar\delta_{i,e}|\tilde{e}\rangle_{ii}\langle\tilde{e}| + \hbar\frac{\Omega_i}{2}\left[|\tilde{r}\rangle_{ii}\langle\tilde{g}| + |\tilde{g}\rangle_{ii}\langle\tilde{r}|\right] + \hbar\tilde{g}\left[|\tilde{r}\rangle_{ii}\langle\tilde{e}|a_i + |\tilde{e}\rangle_{ii}\langle\tilde{r}|a_i^\dagger\right]$$
$$-i\hbar\frac{\kappa_l}{2}a_i^\dagger a_i - i\hbar\frac{A_{P_{3/2}}}{2}|\tilde{r}\rangle_{ii}\langle\tilde{r}| - i\hbar\frac{\Gamma_\Omega}{2}|\tilde{g}\rangle_{ii}\langle\tilde{g}| - i\hbar\frac{\Gamma_g}{2}|\tilde{e}\rangle_{ii}\langle\tilde{e}|\ . \tag{6.49}$$

Here $\kappa_t = \kappa\mathcal{T}_1/(\mathcal{T}_1 + \mathcal{T}_2 + \mathcal{L}_1 + \mathcal{L}_2)$ is the fraction of the cavity decay rate which comes from transmission of the input-output mirror, $\kappa_l = \kappa(\mathcal{T}_2 + \mathcal{L}_1 + \mathcal{L}_2)/(\mathcal{T}_1 + \mathcal{T}_2 + \mathcal{L}_1 + \mathcal{L}_2)$ is the fraction of the cavity decay rate which comes from transmission of the non-input-output mirror and loss of both mirrors, $\delta_{i,g}$ is the detuning of the vacuum-stimulated Raman laser from the $S_{1/2} \leftrightarrow P_{3/2}$ transition, $\delta_{i,e}$ is the detuning of the cavity from the $D_{5/2} \leftrightarrow P_{3/2}$ transition, Γ_Ω is the linewidth of the vacuum-stimulated Raman laser, and Γ_g is the linewidth of the cavity lock.

It is important to take the AC Stark shift of the states into account when selecting the detunings $\delta_{i,g}$ and $\delta_{i,e}$. The vacuum-stimulated Raman transition is driven on resonance

with $\delta_{1,g} = \delta_{2,g} = \delta$ and $\delta_{i,e} = \delta - \tilde{g}^2/\delta + \Omega_i^2/(4\delta)$.

The state of the system is decomposed as

$$\begin{aligned} |\psi(t)\rangle &= c_g \left[c_{\tilde{g}0\tilde{e}0}|\tilde{g}0\tilde{e}0\rangle + c_{\tilde{r}0\tilde{e}0}|\tilde{r}0\tilde{e}0\rangle + c_{\tilde{e}1\tilde{e}0}|\tilde{e}1\tilde{e}0\rangle + c_{\tilde{e}0\tilde{e}1}|\tilde{e}0\tilde{e}1\rangle + c_{\tilde{e}0\tilde{r}0}|\tilde{e}0\tilde{r}0\rangle + c_{\tilde{e}0\tilde{g}0}|\tilde{e}0\tilde{g}0\rangle\right] \\ &\quad + c_e|\tilde{e}0\tilde{e}0\rangle \end{aligned} \tag{6.50}$$

where from left to right the symbols in each ket denote the state of the ions at node 1, the state of the cavity mode at node 1, the state of the ions at node 2, and the state of the cavity mode at node 2. The Schrödinger equation is numerically integrated using the vacuum-stimulated Raman laser pulse shapes calculated in Section 6.1.1.

The resulting expected fidelity of mapping between two collective ion states via a single photon, for realistic experimental parameters, is 0.69. This includes the decoherence due to spontaneous decay of the $P_{3/2}$ state, laser and cavity lock linewidths, and cavity loss.

6.3.5 Summary

The experimental parameters of the proposed implementation of coherent mapping between two single ions via collective states and a single photon are summarized in Table 6.1, and the fidelity is tabulated in Table 6.3.4. The total fidelity of 0.67 includes the decoherence due to phase matching, spontaneous decay of the $P_{3/2}$ state, laser and cavity lock linewidths, and cavity loss. This is an ambitious experiment, but the expected fidelity of coherent mapping between two single ions is much higher than previous experiments [BBM+07].

Parameter	Value
Cavity finesse, F	50000
Cavity mirror 1 transmission, $\mathcal{T}_1$	120×10^{-6}
Cavity mirror 2 transmission, $\mathcal{T}_2$	2×10^{-6}
Cavity mirror 1 loss, $\mathcal{L}_1$	2×10^{-6}
Cavity mirror 2 loss, $\mathcal{L}_2$	2×10^{-6}
Cavity waist, w_0	15 μm
Cavity mirror 1 radius of curvature, R_1	5 mm
Cavity mirror 2 radius of curvature, R_2	∞
Cavity length, L	$R_1 - 95$ μm
Cavity decay rate, $\kappa/(2\pi)$	0.612 MHz
Trap axial secular frequency, $\omega_z/(2\pi)$	500 kHz
Trap radial secular frequencies, $\omega_{x,y}/(2\pi)$	3.0 MHz
Number of ions, N	10
Auxiliary state decay rate, $A_{P_{3/2}}/(2\pi)$	23.4 MHz
Branching ratio, $A_{P_{3/2}\rightarrow D_{5/2}}/A_{P_{3/2}}$	0.048
Clebsch-Gordan coefficient, $A_{P_{3/2},m=-3/2\rightarrow D_{5/2},m=-5/2}/A_{P_{3/2}\rightarrow D_{5/2}}$	2/3
Collective cavity coupling, $\tilde{g}/(2\pi)$	7.25 MHz
Collective cavity cooperativity, $4\tilde{g}^2/(\kappa\Gamma)$	14.7
Vacuum-stimulated Raman detuning, $\delta/(2\pi)$	500 MHz
Vacuum-stimulated Raman laser power (100 μm Gaussian mode)	22.1 μW
Vacuum-stimulated Raman laser linewidth, $\Gamma_\Omega/(2\pi)$	1 kHz
Cavity lock linewidth, $\Gamma_\Omega/(2\pi)$	1 kHz

Table 6.1: Experimental parameters of proposed implementation of mapping between two single ions via collective states and a single photon.

Decoherence mechanism	Fidelity
Phase matching between laser and cavity collective states	0.98^2
Spontaneous decay of the $P_{3/2}$ state	0.86
Laser and cavity lock linewidths	0.89
Cavity loss	0.95^2
Mapping between two single ions via collective states and a single photon	0.67

Table 6.2: Fidelity of coherent mapping between two single ion states via collective states and a single photon. The phase matching fidelity is calculated in Section 6.3.3 and the other fidelities are calculated in Section 6.3.4.

Chapter 7

Ion trap chips with integrated cavities

In order to scale the trapped ion quantum networks proposed in the previous chapter to many nodes, the ion traps and optical cavities at each node will have to be microfabricated and integrated as much as possible. As noted in Chapter 2, surface-electrode ion trap chips are amenable to modern microfabrication techniques. Optical cavities can be integrated with surface-electrode ion trap chips in a variety of ways.

This chapter discusses a few ideas for how to integrate optical cavities with ion trap chips. Section 7.1 presents an idea to build a fiber cavity on an ion trap chip, and an experimental attempt to develop a method for attaching fibers to surface-electrode ion traps in a way which does not interfere with trap operation. Section 7.2 presents an idea to microfabricate a surface-electrode ion trap directly on top of a cavity mirror such that the ion is located above a region of exposed mirror surface. This can be combined with a second (bulk) mirror to form an integrated ion trap-cavity system. Section 7.2 goes on to mention some similar ideas: one idea combines an ion trap chip with an aperture with two bulk mirrors, and the other idea is to fabricate a surface-electrode ion trap on the tip of a mirrored optical fiber and combine it with one bulk mirror. Finally, Section 7.3 compares and contrasts the relative merits of the various designs.

The ideas in this chapter are original except for the following. The idea for fiber cavities on ion trap chips was inspired by similar neutral atom experiments [SCH+06]. The implementation of fibers for light collection on a surface-electrode trap described in Section 7.1.2 was primarily carried out by Elizabeth George and Yufei Ge. And the idea for ion traps microfabricated on the tip of an optical fiber described in Section 7.2.3 comes from Isaac Chuang.

7.1 Surface-electrode trap with a fiber cavity

Neutral atom chip traps have been integrated with fiber cavities with remarkable success [SCH+06]. The ends of two optical fibers are laser machined to have the desired radius of curvature and coated with dielectric mirror stacks. The fibers are then secured to the surface of the atom chip using microfabricated alignment structures [LBW+05]. A natural extension of this idea is to build fiber cavities on surface-electrode ion traps (see Figure 7-1).

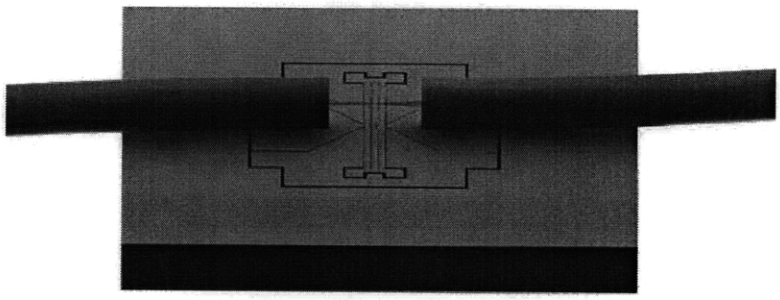

Figure 7-1: Schematic of a surface-electrode ion trap with an integrated fiber cavity. The ends of the optical fibers (grey) are laser machined to have the correct radius of curvature and coated with dielectric mirror stacks. They are secured to the trap surface using microfabricated alignment structures (not shown). Figure not to scale.

7.1.1 Geometry and cavity parameters

Experimentally feasible sets of parameters for an integrated ion trap chip-fiber cavity system can be identified by considering the design constraints. The cavity geometry is constrained both by the geometry of the trap and by the requirement to mode match the cavity mode to the input-output fiber mode. In addition, the trap geometry is constrained by the cavity geometry because the ion height above the chip surface must be equal to half the diameter of the optical fibers. An ion height of 62.5 μm is selected because off-the-shelf single mode optical fibers have a diameter of 125 μm. If the cavity is too short, then the non-unity dielectric constant of the optical fibers as well as any surface charges which accumulate on the optical fibers will destroy the ion trapping potential. However, if the cavity is too long, then the cavity mode will be larger and mode matching to the optical fiber will be more difficult. For the selected ion height the width of the three center electrodes together is about 300 μm, so the shortest reasonable cavity length is about 500 μm. Assuming that the ion is $^{88}Sr^{+}$ and the cavity wavelength is 1033 nm, the radius of the fiber mode is ≈ 3.0 μm. The input-output fiber mode must be mode matched to the cavity mode, so the input-output fiber end is flat and the other fiber end is concave with a radius of curvature 501.5 μm. The resulting cavity mode has a radius of 3.0 μm at the input-output fiber end, 27 μm at the ion position, and 55 μm at the other fiber end. With a finesse of 50000 this results in a single ion cooperativity of $4g^2/(\kappa\Gamma) = 0.44$. (A symmetric fiber cavity with a slightly smaller waist and higher single ion cooperativity could be made by attaching GRIN lenses to the fiber ends [WHS+06], but this has not been demonstrated experimentally.) Table 7.1 summarizes the set of parameters discussed here.

Parameter	Value
Fiber diameter	125 μm
Fiber mode radius	$\approx$ 3.0 μm
Trap ion height	62.5 μm
Cavity finesse	50000
Cavity length	500 μm
Cavity mirror 1 radius of curvature	∞
Cavity mirror 2 radius of curvature	501.5 μm
Cavity mode radius at mirror 1	3.0 μm
Cavity mode radius at mirror 2	55 μm
Cavity mode radius at ion position	27 μm
Single ion cooperativity	0.44

Table 7.1: Experimentally feasible parameters for a surface-electrode ion trap with an integrated fiber cavity for the 1033 nm transition of $^{88}Sr^{+}$. The cavity finesse of 50000 is very optimistic because the scattering losses of the fiber mirrors are likely to be much higher than on bulk mirrors with super-polished substrates. Mirror 1 is the input-output mirror.

7.1.2 Experimental implementation of fibers on a surface-electrode trap

This section presents an experimental attempt to develop a method for attaching fibers to surface-electrode ion traps in a way which does not interfere with trap operation. The objective of this particular experiment is to use a large core multimode fiber to collect light scattered by the ion. This objective was chosen in order to develop some of the techniques necessary for a fiber cavity on a surface-electrode ion trap without all of the experimental complications of an optical cavity. This experiment is covered in much greater detail in Reference [Geo08].

The multimode fiber used for this experiment has an outer diameter of 260 μm and a core diameter of 200 μm. The end of the fiber is positioned 650 μm from the center of the trap, resulting in a collection efficiency of 6×10^{-3}. The trap is a gold electrode surface-electrode ion trap with an ion height of 130 μm. The fabrication process for the trap is identical to that described briefly in Section 3.7. Alignment structures for the fiber are fabricated out of SU-8 2100 photoresist using a procedure adapted from [LBW+05]. First, a 170 μm thick layer of SU-8 is spun onto the finished trap surface and set by baking. This thickness is not critical, but it must be thicker than half the fiber diameter. Then, the regions of SU-8 which are to become alignment structures are lithographically exposed to ultraviolet light and the SU-8 is baked again. The exposure time is intentionally chosen to underexpose the SU-8 so that the walls of the alignment structures are slightly under-etched (see Figure 7-2). This holds the fiber down against the surface of the trap. Finally, the unexposed SU-8 is removed and the SU-8 is baked a third time. After waiting a few days for the SU-8 alignment structures to fully harden, the fiber is inserted and glued in place.

Figure 7-3 shows a top view and Figure 7-4 shows a wide view of the finished trap with the fiber attached. The trap is mounted in a CPGA chip carrier and the fiber is stress relieved by the dot of glue holding it to the CPGA.

Because SU-8 is known to outgas at the UHV pressures required for trapping ions, the surface-electrode trap with an integrated fiber was tested in the cryogenic setup described in Section 3.4. Outgassing is very heavily suppressed at the $\sim$ 6 K operating temperature of the trap in the cryostat. A custom fiber feedthrough was constructed to connect the fiber

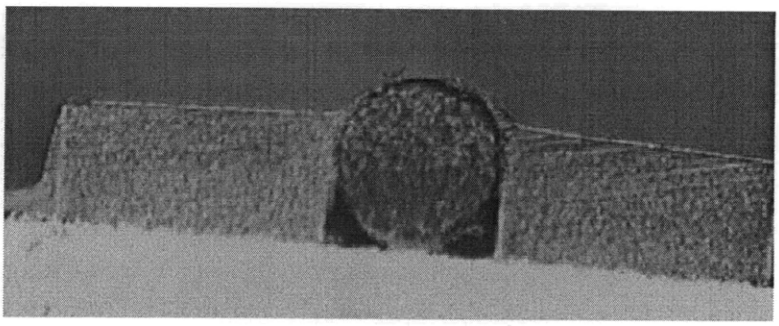

Figure 7-2: Cross-sectional view of SU-8 fiber alignment structures. These test alignment structures have been cut in half with a die saw and photographed under an optical microscope. The fiber diameter for this particular test is 125 μm. Reproduced with permission from Reference [Geo08].

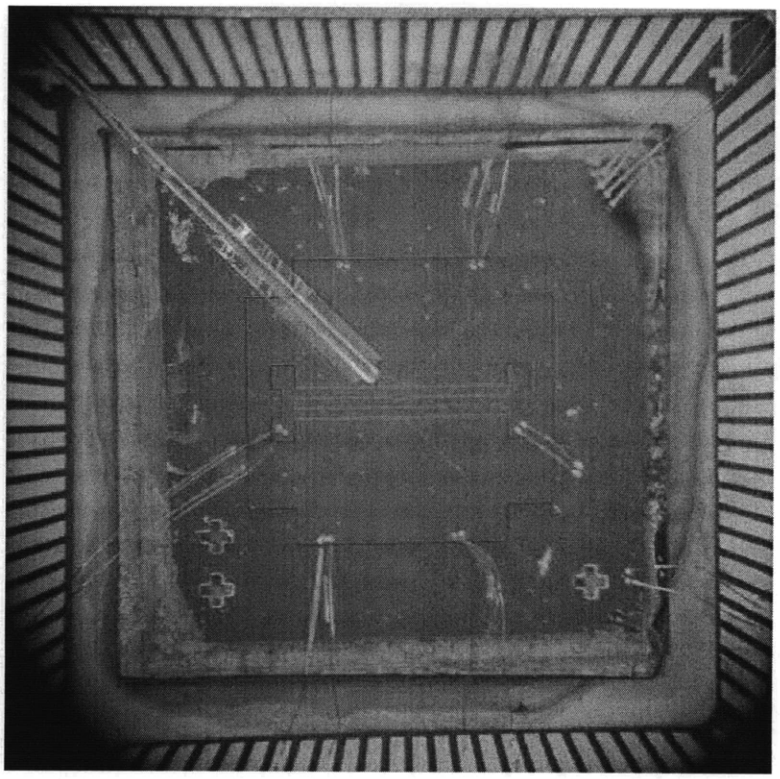

Figure 7-3: Top view of a surface-electrode ion trap with an integrated optical fiber for light collection. The ion trap chip is 1 cm by 1 cm. Reproduced with permission from Reference [Geo08].

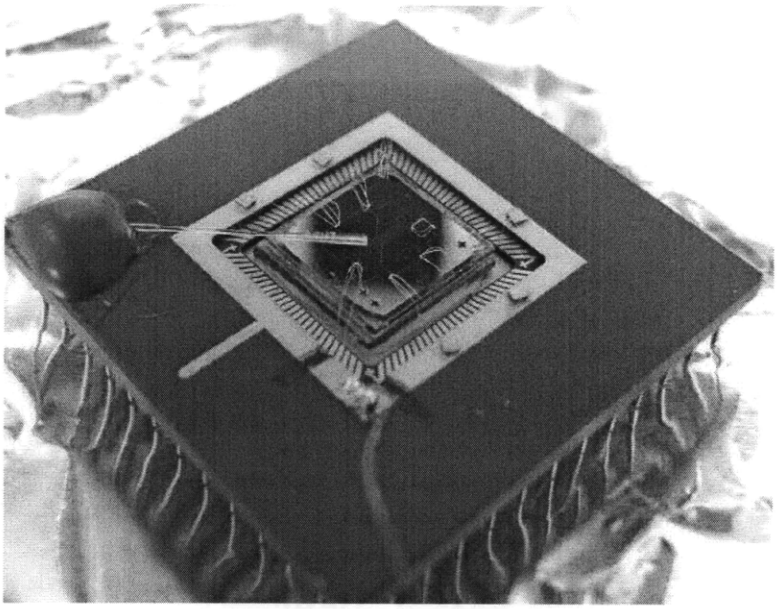

Figure 7-4: Wide view of a surface-electrode ion trap with an integrated optical fiber for light collection. The ion trap chip is 1 cm by 1 cm. Reproduced with permission from Reference [Geo08].

on the trap to a PMT outside the cryostat by potting a length of bare fiber in an aluminum window blank using Torr Seal.

Unfortunately, no ions were trapped in the surface-electrode trap with the integrated optical fiber. The typical culprits were ruled out: the vacuum pressure was good (5×10^{-8} torr measured outside the cryostat, which is within the normal range), the oven was producing neutral ^{88}Sr atoms (confirmed by observing scattered light on the 460 nm transition of the neutral ^{88}Sr atomic beam), and the laser alignment was checked and methodically scanned several times. The probable reason is that stray charge accumulated on the fiber and SU-8 alignment structure and destroyed the trapping potential. A potential solution for this problem in future iterations of the experiment might be to coat the alignment structure and fiber (except for the tip) with a conductor to dissipate the stray charges.

The integrated fiber, however, was successfully used to collect light. By deliberately misaligning the 422 nm laser to scatter off of an imperfection on the trap surface, an artificial ion was created. The scattered light was collected by the fiber and detected by a PMT located outside the cryostat.

7.2 Surface-electrode trap fabricated on a cavity mirror

This section presents an alternative idea for integration of a surface-electrode ion trap with an optical cavity. In this design, the surface-electrode trap is fabricated on top of a mirror, and a hole is etched in the center electrode such that the ion sits above a small area of exposed mirror surface. A second (bulk) mirror is positioned above the trap to complete the optical cavity (see Figure 7-5). This idea is motivated by work with neutral atom chips, where metallic [RHH99] and more recently dielectric [PSK08] mirrors have been patterned on atom chips. Section 7.2.1 describes the trap geometry and the cavity parameters. Section

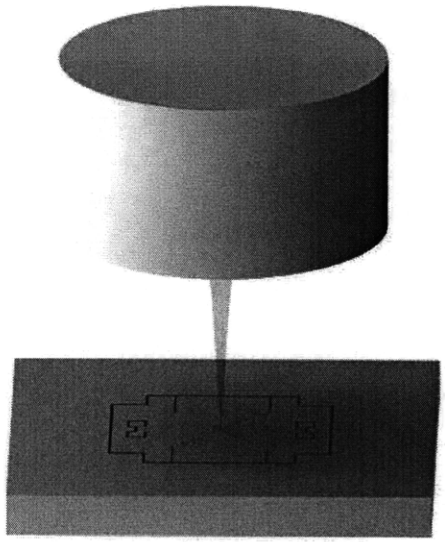

Figure 7-5: Schematic of a surface-electrode trap fabricated on a cavity mirror together with a second (bulk) mirror forming a integrated ion trap chip-optical cavity system. Figure not to scale.

7.2.2 presents CPO simulations of the ion trap potential. Finally, Section 7.2.3 describes some similar alternative integrated ion trap-optical cavity systems.

7.2.1 Geometry and cavity parameters

The primary design constraint for this integrated ion trap chip-optical cavity system is that the hole in the center electrode must be small enough that it does not affect the trapping potential but large enough that it does not affect the cavity mode. The center electrode around the exposed mirror acts as an aperture for the cavity mode, which results in an additional loss mechanism

$$\mathcal{L}_{aperture} = \frac{\int_{R_{aperture}}^{\infty} 2\pi r dr e^{-2r^2/w_0^2}}{\int_0^{\infty} 2\pi r dr e^{-2r^2/w_0^2}} = e^{-2R_{aperture}^2/w_0^2} \tag{7.1}$$

where $R_{aperture}$ is the radius of the hole in the center electrode and w_0 is the radius of the cavity mode at the surface of the ion trap. Using the cavity parameters from Chapter 6 – mirror radii of curvature 5 mm and ∞, cavity length 4.905 mm, and mode waist 15 μm – an aperture radius $R_{aperture} = 40$ μm results in an acceptable loss loss due to the aperture $\mathcal{L}_{aperture} < 10^{-6}$. The trap size must be selected to be large enough that a 40 μm radius hole in the center electrode does not adversely affect the performance of the trap.

7.2.2 CPO simulations

It is important to confirm that the hole in the center electrode of the ion trap does not ruin the trapping potential. Figure 7-6 shows the central region of the standard surface-electrode ion trap design with a hole in the center electrode. The trapping potential is computed using CPO following the procedure described in Section 2.1 and the resulting trapping potential

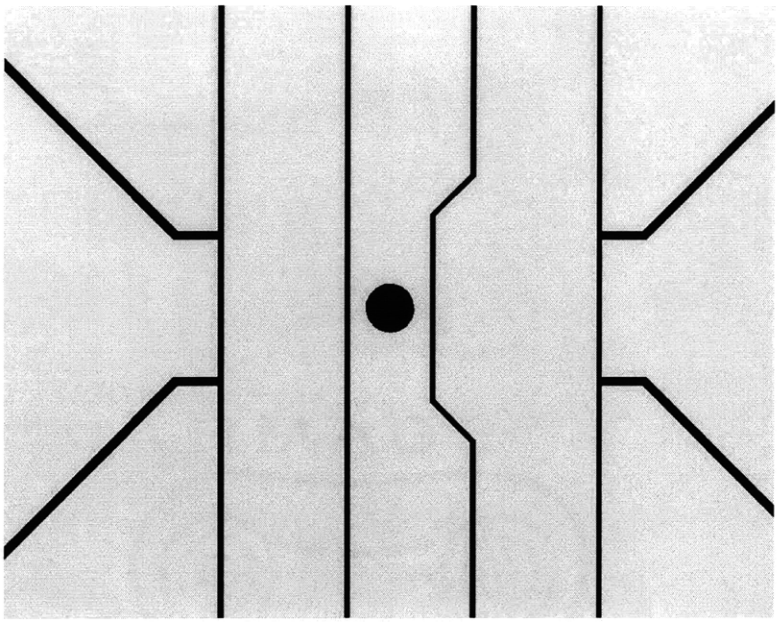

Figure 7-6: Schematic of the central region of a surface-electrode trap fabricated on a mirror showing the details of the center of the trap. The yellow areas are gold electrodes, and the black areas are where the gold has been etched away to reveal the mirror underneath. The hole in the center electrode is used as one of the mirrors for the cavity, and the ion is trapped above it. Figure not to scale.

is shown in Figure 7-7. For a center electrode width of 160 μm (at the notch in the center of the trap) and an aperture radius of 40 μm, the presence of the aperture modifies the ion position, secular frequencies, and trap depth by less than 2%.

One thing to note is that the standard surface-electrode ion trap design shown in Figure 7-6 has a notch in the center electrode which adds some RF confinement in the axial direction. If this were not present then the leads to the RF electrodes which are located only at one end of the trap would generate a component of the RF electric field along the trap axis, and there would be micromotion along the trap axis. The notch ensures that there is a three-dimensional RF null in the center of the trap, and hence a single location without micromotion. The relatively large RF confinement along the trap axis provided by the notch, however, will be a problem for this work because for a long ion chain the end ions will experience micromotion. Thus, some design work will have to be done in order to reduce the RF field along the trap axis.

Table 7.2 summarizes the set of parameters discussed here.

7.2.3 Variations

This section discusses some variations of integrated ion trap chip-optical cavity systems which are similar to the surface-electrode trap fabricated on a cavity mirror.

Surface-electrode trap with an aperture for a cavity mode

If it turns out to be too difficult to fabricate a surface-electrode ion trap on a cavity mirror without substantially degrading the quality of the mirror, one alternative would be to make

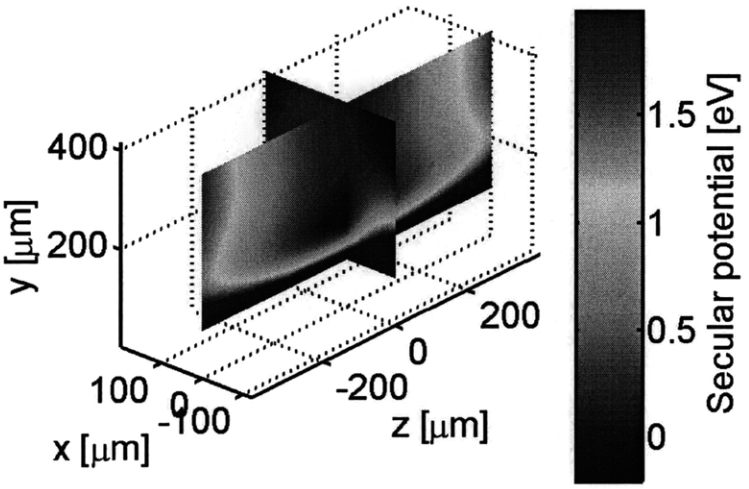

Figure 7-7: Secular potential of a surface-electrode trap with a hole in the center electrode. Ions are trapped in the center of the trap at $(x, y, z) = (35, 176, 5)$ μm in the coordinate system shown. The presence of the hole modifies the ion position, secular frequencies, and trap depth by less than 2%.

Parameter	Value
Center electrode width	160 μm
Aperture radius	40 μm
Trap ion height	176 μm
Cavity finesse	50000
Cavity length	4.905 mm
Cavity mirror 1 radius of curvature	5 mm
Cavity mirror 2 radius of curvature	∞
Cavity mode radius at mirror 1	15 μm
Cavity mode radius at mirror 2	109 μm
Cavity mode radius at ion position	15 μm
Single ion cooperativity	1.5

Table 7.2: Experimentally feasible parameters for a surface-electrode ion trap fabricated on one of the mirrors of a cavity for the 1033 nm transition of $^{88}Sr^{+}$. Mirror 1 is the mirror that the trap is fabricated on.

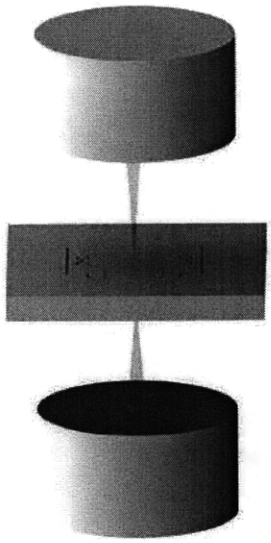

Figure 7-8: Schematic of a surface-electrode trap with an aperture through the substrate for the cavity mode. The two cavity mirrors are placed on either side of the ion trap chip to form the optical cavity. Figure not to scale.

the hole in the center electrode go all the way through the substrate. If the ion trap is fabricated on a silicon substrate, deep reactive ion etching (DRIE) can be used to etch holes in the substrate with walls that are very close to vertical. Cavity mirrors can then be positioned on either side of the ion trap chip such that the cavity mode goes through the hole in the surface-electrode ion trap. Figure 7-8 shows a schematic of this design.

Surface-electrode trap fabricated on a mirrored optical fiber

A second variation is currently being developed by a collaboration between Taehyun Kim and Jungsang Kim at Duke University along with Yufei Ge and Isaac Chuang at MIT. This design embeds an optical fiber with a mirrored surface in the substrate and fabricates a surface-electrode ion trap on top. The mirrored fiber tip forms one of the cavity mirrors and the second (bulk) cavity mirror is positioned above the trap. Figure 7-9 shows a schematic of this design.

This design is more ambitious than the surface-electrode trap fabricated on a cavity mirror for two reasons. First, it requires fabrication of electrodes on the tip of an optical fiber, which is small enough that it is difficult to eliminate edge effects. And second, the cavity must be much closer to concentric in order to mode match the cavity mode with the fiber mode, making the cavity alignment much more difficult. On the positive side, however, the closer the cavity is to concentric, the smaller its waist will be and the cavity-ion coupling will be stronger.

7.3 Discussion

While the fiber cavity on a surface-electrode ion trap appears to be a viable route to achieve an integrated ion trap chip-cavity system, it leaves a lot of exposed dielectric close to the ion

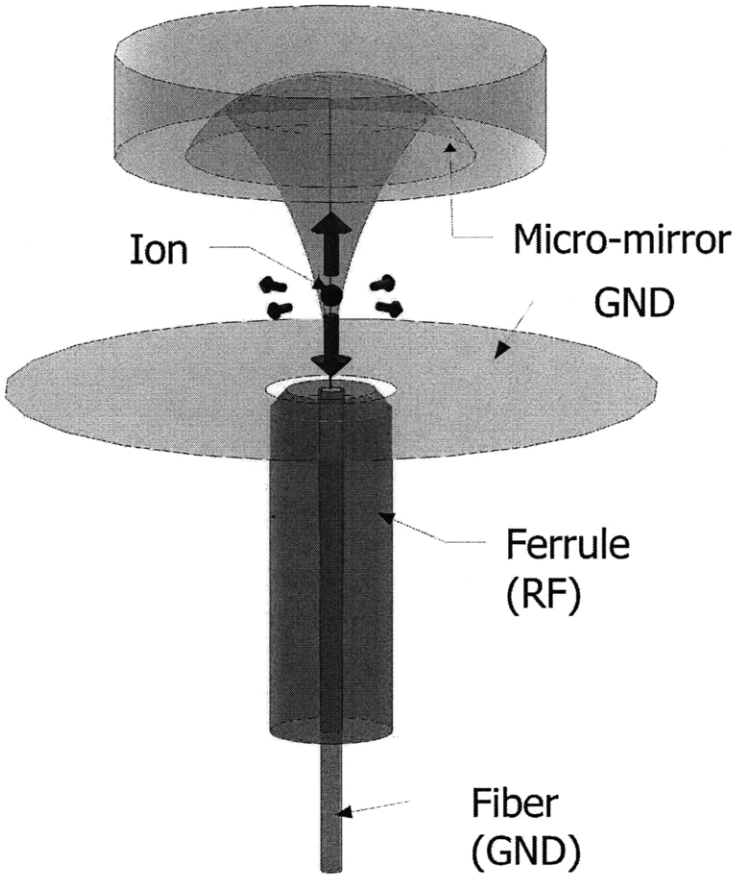

Figure 7-9: Schematic of a surface-electrode trap fabricated on a mirrored optical fiber. The tip of the fiber is embedded in a substrate and a surface-electrode ion trap is microfabricated on top. Figure courtesy of Taehyun Kim, Duke University.

which can adversely affect the trapping potential. In addition, it is not clear how to integrate piezoelectric actuators to actively stabilize the cavity length. The surface-electrode ion trap fabricated on a cavity mirror is a promising alternative which leaves a much smaller area of exposed dielectric close to the ion position.

The variations of the surface-electrode ion trap fabricated on a cavity mirror presented at the end of the previous section are not selected for the following reasons. The surface-electrode ion trap with an aperture for the cavity mode adds additional fabrication complexity (it is difficult to make precisely positioned and sized holes through substrates) and is a less scalable design without any functional benefits. The surface-electrode trap fabricated on a mirrored optical fiber has a smaller mode waist and hence a stronger cavity-ion coupling, but the cavity must be very close to concentric which makes alignment very difficult. Thus the surface-electrode ion trap fabricated on a cavity mirror is selected as the most promising design for an integrated ion trap chip-optical cavity system to be realized in the near future.

The surface-electrode ion trap fabricated on a cavity mirror system is ideal for the implementation of an interconnect between trapped ion qubits and photonic qubits as discussed in the previous chapter. This would be a significant step towards large-scale trapped ion quantum information processing.

Chapter 8

Conclusions and future work

This thesis explores some of the challenges associated with scaling and interconversion for trapped ion quantum information processing. Scaling was addressed by the development of microfabricated ion trap chips and the demonstration of a method of quantum non-demolition cooling, and interconversion was addressed by a theoretical proposal for mapping between single ion qubits and single photon qubits via collective states.

The first part of this thesis describes the development of scalable, multiplexed ion trap chips. Surface-electrodes ion traps were designed, fabricated, and tested using macroscopic charged particles and atomic ions. Testing with atomic ions was performed both at room temperature and with the trap electrodes cryogenically cooled to 6 K for reduced ion motional heating rates. This part culminates with the successful demonstration of the SMIT ion trap – which is a surface-electrode ion trap chip fabricated on a silicon substrate using standard VLSI techniques – including a measurement of the motional heating rate at 6 K showing that the trap is suitable for high fidelity quantum gates.

The demonstration of a scalable, multiplexed ion trap, however, is only one step on the road to a scalable trapped ion quantum information processor. For the SMIT trap to be truly scalable, the materials selection and fabrication process will have to be optimized to improve the reliability. Testing of the first generation SMIT trap found that the thin nitride insulator has an unacceptably high probability of developing electrical shorts and delaminating from the substrate, so perhaps in future generations of the SMIT trap the nitride should be replaced with SiO_2. The upper limit to the total number of trap electrodes, and hence the number of ions, is of the order of one over the probability of electrode failure. Finally, a scalable trap is not enough. To achieve large-scale quantum information processing with trapped ions, the control electronics and optics will also have to be designed and built in a scalable way. The SMIT trap is compatible with integrated CMOS control electronics and MEMs optics, but it remains for future work to integrate the electronics and optics and see if they are compatible with the trapped ions.

The second part of this thesis presents an experimental demonstration of cavity cooling. An integrated ion trap-optical cavity setup was designed and built, and the ion-cavity coupling was carefully characterized. The cavity cooling dynamics were measured to be consistent with the theoretical predictions without any free parameters. This experiment is the first demonstration of cavity cooling with trapped ions, and the first demonstration of cavity cooling in the resolved sideband regime where it is possible to cavity cool to the motional ground state.

In addition to these exciting scientific results, part of the motivation for this experiment

is to develop some of the tools which will be necessary for an experimental implementation of the theoretical proposal in the third part of this thesis. There are a couple of lessons which are particularly relevant. First, locking the cavity in a way which does not decohere the state of the ion was more difficult than anticipated. The locking scheme used in this work is already the second generation to be built, and it still causes too much decoherence of the qubit for high fidelity gates while the cavity is locked. A more sophisticated lock using a second laser which is offset locked to the cavity probe laser will be required for the proposal in the third part of this thesis. The second lesson is that there are many effects which reduce the cooperativity below the value given by the simple formula for a two-level atom. In this experiment the two-level cooperativity would have allowed near ground state cavity cooling, but the effective cooperativity set the cavity cooling limit at a few times the Doppler limit.

The third part of this thesis proposes a method of interconversion between single ion qubits and single photon qubits via collective states of several trapped ions. The new idea is to use single and collective motional sideband laser pulses to map from single ion qubits, with which high fidelity quantum gates have been demonstrated, to collective ion qubits, which couple strongly to single photons in cavity QED. Experimental parameters are suggested for a potential demonstration experiment.

There are some significant technical challenges which will have to be met in order to carry out an experiment to demonstrate mapping between single ions qubits and single photon qubits via collective states. First and foremost, the collective strong coupling regime must be achieved. This will require a small mode volume cavity, which can probably only be achieved by integrating the cavity with a microfabricated ion trap. Other technical challenges include single ion addressing and ground state cooling of several ion crystals.

While some questions are answered in this thesis, several more questions are asked. The SMIT trap was designed and built in a scalable way – but ion movement, integration with control electronics and optics, and high fidelity gates still need to be demonstrated in a scalable ion trap. Cavity cooling was implemented – but the preservation of qubit coherence was not demonstrated. Finally, a quantum gate for mapping between collective and single ion states was proposed – but mapping from single ion qubits to single photon qubits via collective states has not yet been realized. Questions about if and how well these ideas will work remain to be answered in future work.

In 2004, the same year that this thesis work began, a panel of experts in quantum information processing produced version 2.0 of the "Quantum Information Science and Technology Roadmap" [H+04]. The panel established a desired future objective of developing by 2012 a "suite of viable emerging quantum computing technologies of sufficient complexity to function as quantum computer-science test-beds in which architectural and algorithmic issues can be explored." The ultimate goal of this work has been to contribute to the body of knowledge that results in such "test-beds". The rapidly evolving field of trapped ion quantum information processing continues to yield positive results that indicate it will be an important component in the quest to realize a large-scale quantum information processor. It is hoped that this thesis represents a significant step forward on the roadmap.

Bibliography

[ABO08] D. Aharonov and M. Ben-Or. Fault-tolerant quantum computation with constant error rate. *SIAM J. on Comp.*, **38**, 1207, 2008.

[ALB+07] M. Anderlini, P. J. Lee, B. L. Brown, J. Sebby-Strabley, W. D. Phillips, and J. V. Porto. Controlled exchange interaction between pairs of neutral atoms in an optical lattice. *Nature*, **448**, 452, 2007.

[ASA+09] P. B. Antohi, D. Schuster, G. M. Akselrod, J. Labaziewicz, Y. Ge, Z. Lin, W. S. Bakr, and I. L. Chuang. Cryogenic ion trapping systems with surface-electrode traps. *Rev. Sci. Instr.*, **80**, 013103, 2009.

[BB84] C. H. Bennett and G. Brassard. Quantum cryptography: Public key distribution and coin tossing. In *Proceedings of IEEE International Conference on Computers, Systems, and Signal Processing*, p. 175, 1984.

[BB02] D. J. Berkeland and M. G. Boshier. Destabilization of dark states and optical spectroscopy in zeeman-degenerate atomic systems. *Phys. Rev. A*, **65**, 033413, 2002.

[BBM+07] A. D. Boozer, A. Boca, R. Miller, T. E. Northup, and H. J. Kimble. Reversible state transfer between light and a single trapped atom. *Phys. Rev. Lett.*, **98**, 193601, 2007.

[BCJD99] G. K. Brennen, C. M. Caves, P. S. Jessen, and I. H. Deutsch. Quantum logic gates in optical lattices. *Phys. Rev. Lett.*, **82**, 1060, 1999.

[BCL+07] K. R. Brown, R. J. Clark, J. Labaziewicz, P. Richerme, D. R. Leibrandt, and I. L. Chuang. Loading and characterization of a printed-circuit-board atomic ion trap. *Phys. Rev. A*, **75**, 015401, 2007.

[BCS+04] M. D. Barrett, J. Chiaverini, T. Schaetz, J. Britton, W. M. Itano, J. D. Jost, E. Knill, C. Langer, D. Leibfried, R. Ozeri, and D. J. Wineland. Deterministic quantum teleportation of atomic qubits. *Nature*, **429**, 737, 2004.

[BCV03] A. T. Black, H. W. Chan, and V. Vuletic. Observation of collective friction forces due to spatial self-organization of atoms: from Rayleigh to Bragg scattering. *Phys. Rev. Lett.*, **91**, 203001, 2003.

[BDCZ98] H.-J. Briegel, W. Dür, J. I. Cirac, and P. Zoller. Quantum repeaters: the role of imperfect local operations in quantum communication. *Phys. Rev. Lett.*, **81**, 5932, 1998.

[BHI+91] J. J. Bollinger, D. J. Heinzen, W. M. Itano, S. L. Gilbert, and D. J. Wineland. A 303-MHz frequency standard based on trapped Be^+ ions. *IEEE Trans. Instr. Meas.*, **40**, 126, 1991.

[BHIW86] J. C. Bergquist, R. G. Hulet, W. M. Itano, and D. J. Wineland. Observation of quantum jumps in a single atom. *Phys. Rev. Lett.*, **57**, 1699, 1986.

[BHL+05] K.-A. Brickman, P. C. Haljan, P. J. Lee, M. Acton, L. Deslauriers, and C. Monroe. Implementation of Grovers quantum search algorithm in a scalable system. *Phys. Rev. A*, **72**, 050306, 2005.

[BKD04] D. Budker, D. F. Kimball, and D. P. DeMille. *Atomic physics: an exploration through problems and solutions.* Oxford University Press, 2004.

[BKRB08] J. Benhelm, G. Kirchmair, C. F. Roos, and R. Blatt. Towards fault-tolerant quantum computing with trapped ions. *Nature Phys.*, **4**, 463, 2008.

[BLB+06] J. Britton, D. Leibfried, J. Beall, R. B. Blakestad, J. J. Bollinger, J. Chiaverini, R. J. Epstein, J. D. Jost, D. Kielpinski, C. Langer, R. Ozeri, R. Reichle, S. Seidelin, N. Shiga, J. H. Wesenberg, and D. J. Wineland. A microfabricated surface-electrode ion trap in silicon. arXiv:quant-ph/0605170, 2006.

[BLW+07] M. Brownnutt, V. Letchumanan, G. Wilpers, R. C. Thompson, P. Gill, and A. G. Sinclair. Controlled photoionization loading of $^{88}Sr^+$ for precision ion-trap experiments. *Appl. Phys. B*, **87**, 411, 2007.

[BMB+98] D. J. Berkeland, J. D. Miller, J. C. Bergquist, W. M. Itano, and D. J. Wineland. Minimization of ion micromotion in a Paul trap. *J. Appl. Phys.*, **83**, 5025, 1998.

[BMDM04] B. B. Blinov, D. L. Moehring, L.-M. Duan, and C. Monroe. Observation of entanglement between a single trapped atom and a single photon. *Nature*, **428**, 153, 2004.

[BMS07] E. Brion, K. Mølmer, and M. Saffman. Quantum computing with collective ensembles of multilevel systems. *Phys. Rev. Lett.*, **99**, 260501, 2007.

[BPR+99] M. P. Bradley, J. V. Porto, S. Rainville, J. K. Thompson, and D. E. Prichard. Penning trap measurements of the masses of ^{133}Cs, $^{87,85}Rb$, and ^{23}Na with uncertainties ≤ 0.2 ppb. *Phys. Rev. Lett.*, **83**, 4510, 1999.

[BRC+04] M. G. Blain, L. S. Riter, D. Cruz, D. E. Austin, G. Wu, W. R. Plass, and R. G. Cooks. Towards the hand-held mass spectrometer: design considerations, simulation, and fabrication of micrometer-scaled cylindrical ion traps. *Int. J. Mass Spect.*, **236**, 91, 2004.

[BS98] C. H. Bennett and P. W. Shor. Quantum information theory. *IEEE Trans. Info. Theory*, **44**, 2724, 1998.

[BVO+09] R. B. Blakestad, A. P. VanDevender, C. Ospelkaus, J. M. Amini, J. Britton, D. Leibfried, and D. J. Wineland. High fidelity transport of trapped-ion

qubits through an X-junction trap array. *Phys. Rev. Lett.*, **102**, 153002, 2009.

[BWJ+98] T. Brage, G. M. Wahlgren, S. G. Johansson, D. S. Leckrone, and C. R. Proffitt. Theoretical oscillator strengths for Sr II and Y III, with application to abundances in the HgMn-type star χ Lupi. *Astrophys. J.*, **496**, 1051, 1998.

[CB78] J. Cooper and R. J. Ballagh. Role of collisional repopulation of atomic levels on coherent and redistributed components in resonant light scattering. *Phys. Rev. A*, **18**, 1302, 1978.

[CBB+05] J. Chiaverini, R. B. Blakestad, J. Britton, J. D. Jost, C. Langer, D. Leibfried, R. Ozeri, and D. J. Wineland. Surface-electrode architecture for ion-trap quantum information processing. *Quant. Inf. Comput.*, **5**, 419, 2005.

[CBL+05] J. Chiaverini, J. Britton, D. Leibfried, E. Knill, M. D. Barrett, R. B. Blakestad, W. M. Itano, J. D. Jost, C. Langer, R. Ozeri, T. Schaetz, and D. J. Wineland. Implementation of the semiclassical quantum fourier transform in a scalable system. *Science*, **308**, 5724, 2005.

[CBV03] H. W. Chan, A. T. Black, and V. Vuletic. Observation of collective-emission-induced cooling of atoms in an optical cavity. *Phys. Rev. Lett.*, **90**, 063003, 2003.

[CDB92] J. B. Camp, T. W. Darling, and R. E. Brown. Effect of crystallites on surface potential cariations of Au and graphite. *J. Appl. Phys.*, **71**, 783, 1992.

[CEHM99] J. I. Cirac, A. K. Ekert, S. F. Huelga, and C. Macchiavello. Distributed quantum computation over noisy channels. *Phys. Rev. A*, **59**, 4249, 1999.

[CGC+07] M. Cetina, A. Grier, J. Campbell, I. Chuang, and V. Vuletić. Bright source of cold ions for surface-electrode traps. *Phys. Rev. A*, **76**, 041401(R), 2007.

[CH94] D. B. Chrisey and G. K. Hubler, editors. *Pulsed Laser Deposition of Thin Films.* Wiley, 1994.

[Cha] Charged Particle Optics programs. http://www.electronoptics.com.

[Chu36] A. Church. An unsolvable problem of elementary number theory. *Am. J. Math*, **58**, 345, 1936.

[CK85] R. J. Cook and H. J. Kimble. Possibility of direct observation of quantum jumps. *Phys. Rev. Lett.*, **54**, 1023, 1985.

[Cla09] R. J. Clark. *An Investigation of Precision and Scaling Issues in Nuclear Spin and Trapped-ion Quantum Simulators.* Ph.D. thesis, Massachusetts Institute of Technology, 2009.

[CLS+04] J. Chiaverini, D. Leibfried, T. Schaetz, M. D. Barrett, R. B. Blakestad, J. Britton, W. M. Itano, J. D. Jost, E. Knill, C. Langer, R. Ozeri, and D. J. Wineland. Realization of quantum error correction. *Nature*, **432**, 602, 2004.

[CMJ+05] T. Chaneliere, D. N. Matsukevich, S. D. Jenkins, S. Y. Lan, T. A. B. Kennedy, and A. Kuzmich. Storage and retrieval of single photons transmitted between remote quantum memories. *Nature*, **438**, 833, 2005.

[CMJ+07] T. Chaneliere, D. N. Matsukevich, S. D. Jenkins, S.-Y. Lan, R. Zhao, T. A. B. Kennedy, and A. Kuzmich. Quantum interference of electromagnetic fields from remote quantum memories. *Phys. Rev. Lett.*, **98**, 113602, 2007.

[CMMH94] R. A. Cline, J. D. Miller, M. R. Matthews, and D. J. Heinzen. Spin relaxation of optically trapped atoms by light scattering. *Opt. Lett.*, **19**, 207, 1994.

[CP01] R. Crandall and C. Pomerance. *Prime numbers: a computational perspective.* Springer, New York, 2001.

[CPK+02] Y. Cai, W.-P. Peng, S.-J. Kuo, Y. T. Lee, and H.-C. Chang. Single-particle mass spectrometry of polystyrene microspheres and diamond nanocrystals. *Anal. Chem.*, **74**, 232, 2002.

[CPKK04] C. W. Chou, S. V. Polyakov, A. Kuzmich, and H. J. Kimble. Single-photon generation from stored excitation in an atomic ensemble. *Phys. Rev. Lett.*, **92**, 213601, 2004.

[Cro05] A. W. Cross. Synthesis and evaluation of fault-tolerant quantum computer architectures. M. S. thesis, Massachusetts Institute of Technology, 2005.

[CSL06] H. Cho, M. Shin, and J. Lee. Effects of substrate and deposition method onto the mirror scattering. *Appl. Opt.*, **45**, 1440, 2006.

[CTDRG98] C. Cohen-Tannoudji, J. Dupont-Roc, and G. Grynberg. *Atom-photon interactions.* Wiley Science, 1998.

[CW51] H. B. Callen and T. A. Welton. Irreversibility and generalized noise. *Phys. Rev.*, **83**, 34, 1951.

[CY95] I. L. Chuang and Y. Yamamoto. Simple quantum computer. *Phys. Rev. A*, **52**, 3489, 1995.

[CZ95] J. I. Cirac and P. Zoller. Quantum computations with cold trapped ions. *Phys. Rev. Lett.*, **74**, 4091, 1995.

[CZ00] J. I. Cirac and P. Zoller. A scalable quantum computer with ions in an array of microtraps. *Nature*, **404**, 579, 2000.

[CZKM97] J. I. Cirac, P. Zoller, H. J. Kimble, and H. Mabuchi. Quantum state transfer and entanglement distribution among distant nodes in a quantum network. *Phys. Rev. Lett.*, **78**, 3221, 1997.

[DBIW89] F. Diedrich, J. C. Bergquist, W. M. Itano, and D. J. Wineland. Laser cooling to the zero point energy of motion. *Phys. Rev. Lett.*, **62**, 403, 1989.

[Deh67] H. G. Dehmelt. Radiofrequency spectroscopy of stored ions I: Storage. *Adv. Atom. Mol. Phys.*, **3**, 53, 1967.

[Deu85] D. Deutsch. Quantum theory, the Church-Turing Principle and the universal quantum computer. *Proc. Roy. Soc. London Ser. A*, **400**, 97, 1985.

[DHK+83] R. W. P. Drever, J. L. Hall, F. V. Kowalski, J. Hough, G. M Ford, A. J. Munley, and H. Ward. Laser phase and frequency stabilization using an optical resonator. *Appl. Phys. B*, **31**, 97, 1983.

[Dic54] R. H. Dicke. Coherence in spontaneous radiation processes. *Phys. Rev.*, **93**, 99, 1954.

[DiV00] D. P. DiVincenzo. The physical implementation of quantum computation. *Fortschritte der Physik*, **48**, 771, 2000.

[DK03] L.-M. Duan and J. Kimble. Efficient engineering of multiatom entanglement through single-photon detections. *Phys. Rev. Lett.*, **90**, 253601, 2003.

[DLC+09] N. Daniilidis, T. Lee, R. Clark, S. Narayanan, and H. Häffner. Wiring up trapped ions to study aspects of quantum information. arXiv:0903.3834, 2009.

[DLCZ01] L.-M. Duan, M. D. Lukin, J. I. Cirac, and P. Zoller. Long-distance quantum communication with atomic ensembles and linear optics. *Nature*, **414**, 413, 2001.

[DMM+06] L.-M. Duan, M. J. Madsen, D. L. Moehring, P. Maunz, Jr. R. N. Kohn, and C. Monroe. Probabilistic quantum gates between remote atoms through interference of optical frequency qubits. *Phys. Rev. A*, **73**, 062324, 2006.

[DOS+06] L. Deslauriers, S. Olmschenk, D. Stick, W. K. Hensinger, J. Sterk, and C. Monroe. Scaling and suppression of anomalous heating in ion traps. *Phys. Rev. Lett.*, **97**, 103007, 2006.

[DR05] L.-M. Duan and R. Raussendorf. Efficient quantum computation with probabilistic quantum gates. *Phys. Rev. Lett.*, **95**, 080503, 2005.

[EAM+05] M. D. Eisaman, A. André, F. Massou, M. Fleischhauer, A. S. Zibrov, and M. D. Lukin. Electromagnetically induced transparency with tunable single-photon pulses. *Nature*, **438**, 837, 2005.

[FE94] B. H. Foing and P. Ehrenfreund. Detection of two interstellar absorption bands coincident with spectral features of C_{60}^{+}. *Nature*, **369**, 296, 1994.

[Fey82] R. P. Feynman. Simulating physics with computers. *Intl. J. Theor. Phys.*, **21**, 467, 1982.

[Fis76] J. R. Fisk. Helical-resonator design techniques. *QST*, p. 11, June 1976.

[FJM93] J. Fulara, M. Jakobi, and J. P. Maier. Electronic and infrared spectra of C_{60}^{+} and C_{60}^{-} in neon and argon matrices. *Chem. Phys. Lett.*, **211**, 227, 1993.

[FKG+07] K. M. Fortier, S. Y. Kim, M. J. Gibbons, P. Ahmadi, and M. S. Chapman. Deterministic loading of individual atoms to a high-finesse optical cavity. *Phys. Rev. Lett.*, **98**, 233601, 2007.

[FNTU05] T. Furukawa, J. Nishimura, U. Tanaka, and S. Urabe. Design and characteristic measurement of miniature three-segment linear Paul trap. *Japanese J. Appl. Phys.*, **44**, 7619, 2005.

[FSLC97] P. T. H. Fisk, M. J. Sellars, M. A. Lawn, and C. Coles. Accurate measurement of the 12.6 GHz clock transition in trapped $^{171}Yb^{+}$ ions. *IEEE Trans. Ultrason. Ferroelectr. Freq. Control*, **44**, 344, 1997.

[Gal67] A. Gallagher. Oscillator strengths of Ca II, Sr II, and Ba II. *Phys. Rev.*, **157**, 24, 1967.

[GC97] N. Gershenfeld and I. L. Chuang. Bulk spin resonance quantum computation. *Science*, **275**, 350, 1997.

[Geo08] E. M. George. Fiber optic integration in planar ion traps. B. S. thesis, Massachusetts Institute of Technology, 2008.

[GH02] C. G. Granqvist and A. Hultåker. Transparent and conducting ito films: new devolepments and applications. *Thin Solid Films*, **411**, 1, 2002.

[Gho95] P. K. Ghosh. *Ion Traps.* Clarendon Press, Oxford, 1995.

[GJ91] C. Guet and W. R. Johnson. Relativistic many-body calculations of transition rates for Ca^{+}, Sr^{+}, and Ba^{+}. *Phys. Rev. A*, **44**, 1531, 1991.

[GKH+01] G. R. Guthöhrlein, M. Keller, K. Hayasaka, W. Lange, and H. Walther. A single ion as a nanoscopic probe of an optical field. *Nature*, **2001**, 49, 2001.

[Gor00] R. G. Gordon. Criteria for choosing transparent conductors. *MRS Bulletin*, p. 52, August 2000.

[Gro96] L. K. Grover. A fast quantum mechanical algorithm for database search. In *Proceedings of the 28th Annual ACM Symposium on the Theory of Computing*, p. 212, 1996.

[GZ04] C. W. Gardiner and P. Zoller. *Quantum noise.* Springer-Verlag, Berlin, 3rd edition, 2004.

[H+04] R. Hughes et al. A quantum information science and technology roadmap. http://qist.lanl.gov, 2004.

[HDLL+08] P. Herskind, A. Dantan, M. B. Langkilde-Lauesen, A. Mortensen, J. L. Sørensen, and M. Drewsen. Loading of large ion Coulomb crystals into a linear Paul trap incorporating an optical cavity for cavity QED studies. *Appl. Phys. B*, **93**, 373, 2008.

[HDM+09] P. F. Herskind, A. Dantan, J. P. Marler, M. Albert, and M. Drewsen. Realization of collective strong coupling with ion Coulomb crystals in an optical cavity. In preparation, 2009.

[Her00] G. H. Herbig. The search for interstellar C_{60}. *Astrophys. J.*, **542**, 334, 2000.

[HGH+07] R. J. Hendricks, D. M. Grant, P. F. Herskind, A. Dantan, and M. Drewsen. An all-optical ion-loading technique for scalable microtrap architectures. *Appl. Phys. B*, **88**, 507, 2007.

[HHG+97] P. Horak, G. Hechenblaikner, K. M. Gheri, H. Stecher, and H. Ritsch. Cavity-induced atom cooling in the strong coupling regime. *Phys. Rev. Lett.*, **79**, 4974, 1997.

[HHG+07] L. Hackermüller, K. Hornberger, S. Gerlich, M. Gring, H. Ulbricht, and M. Arndt. Optical polarizabilities of large molecules measured in near-field interferometry. *Appl. Phys. B*, **89**, 469, 2007.

[HHR+05] H. Häffner, W. Hänsel, C. F. Roos, J. Benhelm, D. Chek al kar, M. Chwalla, T. Körber, U. D. Rapol, M. Riebe, P. O. Schmidt, C. Becher, O. Gühne, W. Dür, and R. Blatt. Scalable multiparticle entanglement of trapped ions. *Nature*, **438**, 643, 2005.

[HKY01] C. J. Hood, H. J. Kimble, and J. Ye. Characterization of high-finesse mirrors: loss, phase shifts, and mode structure in an optical cavity. *Phys. Rev. A*, **64**, 033804, 2001.

[HMO+06] Y. Hashimoto, L. Matsuoka, H. Osaki, Y. Fukushima, and S. Hasegawa. Trapping laser ablated Ca^+ ions in linear paul trap. *Japanese J. Appl. Phys.*, **45**, 7108, 2006.

[HMS+08] J. P. Home, M. J. McDonnell, D. J. Szwer, B. C. Keitch, D. M. Lucas, D. N. Stacey, and A. M. Steane. Memory coherence of a sympathetically cooled trapped-ion qubit. arXiv:0810.1036, 2008.

[HOS+06] W. K. Hensinger, S. Olmschenk, D. Stick, D. Hucul, M. Yeo, M. Acton, L. Deslauriers, and C. Monroe. T-junction ion trap array for two-dimensional ion shuttling, storage, and manipulation. *Appl. Phys. Letters*, **88**, 034101, 2006.

[HRB08] H. Häffner, C. F. Roos, and R. Blatt. Quantum computing with trapped ions. *Phys. Rep.*, **469**, 155, 2008.

[HYH+08] D. Hucul, M. Yeo, W. K. Hensinger, J. Rabchuk, S. Olmschenk, and C. Monroe. On the transport of atomic ions in linear and multidimensinal ion trap arrays. *Quant. Inf. Comput.*, **8**, 501, 2008.

[Jam98] D. F. V. James. Quantum dynamics of cold trapped ions with application to quantum computation. *Appl. Phys. B*, **66**, 181, 1998.

[JC63] E. T. Jaynes and F. W. Cummings. Comparison of quantum and semiclassical radiation theories with application to the beam maser. *Proc. IEEE*, **51**, 89, 1963.

[JGL+92] P. S. Jessen, C. Gerz, P. D. Lett, W. D. Phillips, S. L. Rolston, R. J. C. Spreeuw, and C. I. Westbrook. Observation of quantized motion of Rb atoms in an optical field. *Phys. Rev. Lett.*, **69**, 49, 1992.

[Jor08] S. P. Jordan. *Quantum computation beyond the circuit model.* Ph.D. thesis, Massachusetts Institute of Technology, 2008.

[KGF+90] V. H. S. Kwong, T. T. Gibbons, Z. Fang, J. Jiang, H. Knocke, Y. Jiang, and B. Ruger. Experimental apparatus for production, cooling, and storing multiply charged ions for charge-transfer measurements. *Rev. Sci. Instr.*, **61**, 1931, 1990.

[Kim08] H. J. Kimble. The quantum internet. *Nature*, **453**, 1023, 2008.

[KK09] J. Kim and C. Kim. Integrated optical approach to trapped ion quantum computation. *Quant. Inf. Comput.*, **9**, 181, 2009.

[KKM+00] D. Kielpinski, B. E. King, C. J. Myatt, C. A. Sackett, Q. A. Turchette, W. M. Itano, C. Monroe, D. J. Wineland, and W. H. Zurek. Sympathetic cooling of trapped ions for quantum logic. *Phys. Rev. A*, **61**, 032310, 2000.

[KMPdVR07] K. Kowalewski, G. Morigi, P. W. H. Pinkse, and R. de Vivie-Riedle. Cavity cooling of translational and ro-vibrational motion of molecules: ab initio-based simulations for OH and NO. *Appl. Phys. B*, **89**, 459, 2007.

[KMW02] D. Kielpinski, C. Monroe, and D. J. Wineland. Architecture for a large-scale ion-trap quantum computer. *Nature*, **417**, 709, 2002.

[Kni81] R. D. Knight. Storage of ions from laser-produced plasmas. *Appl. Phys. Letters*, **38**, 221, 1981.

[Kni05] E. Knill. Quantum computing with realistically noisy devices. *Nature*, **434**, 39, 2005.

[KPM+05] J. Kim, S. Pau, Z. Ma, H. R. Mclellan, J. V. Gates, A. Kornblit, R. E. Slusher, R. M. Jopson, I. Kang, and M. Dinu. System design for large-scale ion trap quantum information processor. *Quant. Inf. Comput.*, **5**, 515, 2005.

[Lab08] J. Labaziewicz. *High Fidelity Quantum Gates with Ions in Cryogenic Microfabricated Ion Traps.* Ph.D. thesis, Massachusetts Institute of Technology, 2008.

[LBMW03] D. Leibfried, R. Blatt, C. Monroe, and D. J. Wineland. Quantum dynamics of single trapped ions. *Rev. Mod. Phys.*, **75**, 281, 2003.

[LBW+05] X. Liu, K. Brenner, M. Wilzbach, M. Schwarz, T. Fernholz, and J. Schmiedmayer. Fabrication of alignment structures for a fiber resonator by use of deep-ultraviolet lithography. *Appl. Opt.*, **44**, 6857, 2005.

[LDM+03] D. Leibfried, B. DeMarco, V. Meyer, D. Lucas, M. Barrett, J. Britton, W. M. Itano, B. Jelenkovi, C. Langer, T. Rosenband, and D. J. Wineland. Experimental demonstration of a robust, high-fidelity geometric two ion-qubit phase gate. *Nature*, **422**, 412, 2003.

[LDP87] S. V. Lawande, R. D'Souza, and R. R. Puri. Effects of detuning and fluctuations on fluorescence radiation from a strongly driven three-level atom: some analytical results. *Phys. Rev. A*, **36**, 3228, 1987.

[LGA+08] J. Labaziewicz, Y. Ge, P. Antohi, D. Leibrandt, K. R. Brown, and I. L. Chuang. Suppression of heating rates in cryogenic surface-electrode ion traps. *Phys. Rev. Lett.*, **100**, 13001, 2008.

[LGL+08] J. Labaziewicz, Y. Ge, D. R. Leibrandt, S. X. Wang, R. Shewmon, and I. L. Chuang. Temperature dependence of electric field noise above gold surfaces. *Phys. Rev. Lett.*, **101**, 180602, 2008.

[LHN+07] A. D. Ludlow, X. Huang, M. Notcutt, T. Zanon-Willette, S. M. Foreman, M. M. Boyd, S. Blatt, and J. Ye. Compact, thermal-noise-limited optical cavity for diode laser stabilization at 1×10^{-15}. *Opt. Lett.*, **32**, 641, 2007.

[LKS+05] D. Leibfried, E. Knill, S. Seidelin, J. Britton, R. B. Blakestad, J. Chiaverini, D. B. Hume, W. M. Itano, J. Jost, C. Langer, R. Ozeri, R. Reichle, and D. J. Wineland. Creation of a six-atom 'schrödinger cat' state. *Nature*, **438**, 639, 2005.

[Llo96] S. Lloyd. Universal quantum simulators. *Science*, **273**, 1073, 1996.

[LRBC07] J. Labaziewicz, P. Richerme, K. R. Brown, and I. L. Chuang. Compact, filtered diode laser system for precision spectroscopy. *Opt. Lett.*, **32**, 572, 2007.

[LVH+08] B. L. Lev, A. Vukics, E. R. Hudson, B. C. Sawyer, P. Domokos, H. Ritsch, and J. Ye. Prospects for the cavity-assisted laser cooling of molecules. *Phys. Rev. A*, **77**, 023402, 2008.

[LYS07] D. Leibrandt, B. Yurke, and R. Slusher. Modeling ion trap thermal noise decoherence. *Quant. Inf. Comput.*, **7**, 052, 2007.

[M+07] J. Majer et al. Coupling superconducting qubits via a cavity bus. *Nature*, **449**, 443, 2007.

[MBR+04] C. Maurer, C. Becher, C. Russo, J. Eschner, and R. Blatt. A single-photon source based on a single Ca^+ ion. *New J. Phys.*, **6**, 94, 2004.

[MJMD01] C. A. Müller, T. Jonckheere, C. Miniatura, and D. Delande. Weak localization of light by cold atoms: the impact of quantum internal structure. *Phys. Rev. A*, **64**, 053804, 2001.

[MKB+02] A. B. Mundt, A. Kreuter, C. Becher, D. Leibfried, J. Eschner, F. Schmidt-Kaler, and R. Blatt. Coupling a single atomic quantum bit to a high finesse optical cavity. *Phys. Rev. Lett.*, **89**, 103001, 2002.

[MMK+95] C. Monroe, D. M. Meekhof, B. E. King, W. M. Itano, and D. J. Wineland. Demonstration of a fundamental quantum logic gate. *Phys. Rev. Lett.*, **75**, 4714, 1995.

[MMO+07] P. Maunz, D. L. Moehring, S. Olmschenk, K. C. Younge, D. N. Matsukevich, and C. Monroe. Quantum interference of photon pairs from two remote trapped atomic ions. *Nature Phys.*, **3**, 538, 2007.

[MNAU02] J. M. Martinis, S. Nam, J. Aumentado, and C. Urbina. Rabi oscillations in a large Josephson-junction qubit. *Phys. Rev. Lett.*, **89**, 117901, 2002.

[MNB+05] R. Miller, T. E. Northup, K. M. Birnbaum, A. Boca, A. D. Boozer, and H. J. Kimble. Trapped atoms in cavity QED: coupling quantized light and matter. *J. Phys. B: At. Mol. Opt. Phys.*, **38**, S551, 2005.

[MNP+06] K. Murr, S. Nußmann, T. Puppe, M. Hijlkema, B. Weber, S. C. Webster, A. Kuhn, and G. Rempe. Three-dimensional cavity cooling and trapping in an optical lattice. *Phys. Rev. A*, **73**, 063415, 2006.

[MOL+99] J. E. Mooij, T. P. Orlando, L. Levitov, L. Tian, C. H. van der Wal, and S. Lloyd. Josephson persistent-current qubit. *Science*, **285**, 1036, 1999.

[MPKdVR07] G. Morigi, P. W. H. Pinkse, M. Kowalewski, and R. de Vivie-Riedle. Cavity cooling of internal molecular motion. *Phys. Rev. Lett.*, **99**, 073001, 2007.

[MPS+04] P. Maunz, T. Puppe, I. Schuster, N. Syassen, P. W. H. Pinkse, and G. Rempe. Cavity cooling of a single atom. *Nature*, **428**, 50, 2004.

[MSH+05] T. P. Meyrath, F. Schreck, J. L. Hanssen, C.-S. Chuu, and M. G. Raizen. A high frequency optical trap for atoms using Hermite-Gaussian beams. *Opt. Exp.*, **13**, 2843, 2005.

[MSW+08] A. H. Myerson, D. J. Szwer, S. C. Webster, D. T. C. Allcock, M. J. Curtis, G. Imreh, J. A. Sherman, D. N. Stacey, A. M. Steane, and D. M. Lucas. High-fidelity readout of trapped-ion qubits. *Phys. Rev. Lett.*, **100**, 200502, 2008.

[MvdS99] H. J. Metcalf and P. van der Straten. *Laser Cooling and Trapping.* Springer-Verleg, New York, 1999.

[MW01] G. Morigi and H. Walther. Two-species Coulomb chains for quantum information. *Eur. Phys. J. D*, **13**, 261, 2001.

[NC00] M. A. Nielsen and I. L. Chuang. *Quantum computation and quantum information.* Cambridge University Press, 2000.

[NMH+05] S. Nußmann, K. Murr, M. Hijlkema, B. Weber, A. Kuhn, and G. Rempe. Vacuum-stimulated cooling of single atoms in three dimensions. *Nature Phys.*, **1**, 122, 2005.

[O'B07] J. L. O'Brien. Optical quantum computing. *Science*, **318**, 1567, 2007.

[OCK+06] S. Oh, K. Cicak, J. S. Kline, M. A. Sillanp, K. D. Osborn, J. D. Whittaker, R. W. Simmonds, and D. P. Pappas. Elimination of two level fluctuators in superconducting quantum bits by an epitaxial tunnel barrier. *Phys. Rev. B*, **74**, 100502, 2006.

[OLJ+05] R. Ozeri, C. Langer, J. D. Jost, B. DeMarco, A. Ben-Kish, B. R. Blakestad, J. Britton, J. Chiaverini, W. M. Itano, D. B. Hume, D. Leibfried, T. Rosenband, P. O. Schmidt, and D. J. Wineland. Hyperfine coherence in the presence of spontaneous photon scattering. *Phys. Rev. Lett.*, **95**, 030403, 2005.

[OMM+09] S. Olmschenk, D. N. Matsukevich, P. Maunz, D. Hayes, L.-M. Duan, and C. Monroe. Quantum teleportation between distant matter qubits. *Science*, **323**, 486, 2009.

[Pau90] W. Paul. Electromagnetic traps for charged and neutral particles. *Rev. Mod. Phys.*, **62**, 531, 1990.

[Pel97] T. Pellizzari. Quantum networking with optical fibers. *Phys. Rev. Lett.*, **79**, 839, 1997.

[Phi07] C. R. Phipps. *Laser Ablation and Applications.* Springer, 2007.

[PLB+06] C. E. Pearson, D. R. Leibrandt, W. S. Bakr, W. J. Mallard, K. R. Brown, and I. L. Chuang. Experimental investigation of planar ion traps. *Phys. Rev. A*, **73**, 032307, 2006.

[PS76] D. Polder and M. F. H. Schuurmans. Resonance fluorescence from a $j = 1/2$ to $j = 1/2$ transition. *Phys. Rev. A*, **14**, 1486, 1976.

[PSK08] T. P. Purdy and D. M. Stamper-Kurn. Integrating cavity quantum electrodynamics and ultracold-atom chips with on-chip dielectric mirrors and temperature stabilization. *Appl. Phys. B*, **90**, 401, 2008.

[Pur46] E. M. Purcell. Spontaneous emission probabilities at radio frequencies. *Phys. Rev.*, **69**, 681, 1946.

[RBKD+02] M. A. Rowe, A. Ben-Kish, B. DeMarco, D. Leibfried, V. Meyer, J. Beall, J. Britton, J. Hughes, W. M. Itano, B. Jelenkovic, C. Langer, T. Rosenband, and D. J. Wineland. Transport of quantum states and separation of ions in a dual rf ion trap. *Quant. Inf. Comput.*, **2**, 257, 2002.

[RBS+08] C. Russo, H. G. Barros, A. Stute, F. Dubin, E. S. Phillips, T. Monz, T. E. Northup, C. Becher, T. Salzburger, H. Ritsch, P. O. Schmidt, and R. Blatt. Raman spectroscopy of a single ion coupled to a high-finesse cavity. *Appl. Phys. B*, **95**, 205, 2008.

[RHH99] J. Reichel, W. Hänsel, and T. W. Hänsch. Atomic micromanipulation with magnetic surface traps. *Phys. Rev. Lett.*, **83**, 3398, 1999.

[RHR+04] M. Riebe, H. Häffner, C. F. Roos, W. Hänsel, J. Benhelm, G. P. T. Lancaster, T. W. Körber, C. Becher, F. Schmidt-Kaler, D. F. V. James, and R. Blatt. Deterministic quantum teleportation with atoms. *Nature*, **429**, 734, 2004.

[RJT01] K. Ruud, D. Jonsson, and P. R. Taylor. The dispersion of the polarizability of C_{60}: A confirmation of recent experimental results through theoretical calculations. *J. Chem. Phys.*, **114**, 4331, 2001.

[RO92] F. Rossi and G. I. Opat. Observations of the effects of adsorbates on patch potentials. *J. Phys. D: Appl. Phys.*, **25**, 1349, 1992.

[Roo00] C. F. Roos. *Controlling the quantum state of trapped ions.* Ph.D. thesis, University of Innsbruck, 2000.

[RZS06] V. L. Ryjkov, X. Z. Zhao, and H. A. Schuessler. Sympathetic cooling of fullerene ions by laser-cooled Mg^+ ions in a linear rf trap. *Phys. Rev. A*, **74**, 023401, 2006.

[SCH+06] T. Steinmetz, Y. Colombe, D. Hunger, T. W. Hänsch, A. Balocchi, R. J. Warburton, and J. Reichel. Stable fiber-based Fabry-Pérot cavity. *Appl. Phys. Letters*, **89**, 111110, 2006.

[SCR+06] S. Seidelin, J. Chiaverini, R. Reichle, J. J. Bollinger, D. Leibfried, J. Britton, J. H. Wesenberg, R. B. Blakestad, R. J. Epstein, D. B. Hume, W. M. Itano, J. D. Jost, C. Langer, R. Ozeri, N. Shiga, and D. J. Wineland. Microfabricated surface-electrode ion trap for scalable quantum information processing. *Phys. Rev. Lett.*, **96**, 253003, 2006.

[SESD81] J. R. Sambles, K. C. Elsom, and G. Sharp-Dent. The effect of sample thickness on the resistivity of aluminum. *J. Phys. F*, **11**, 31075, 1981.

[Sha48] C. E. Shannon. A mathematical theory of communication. *Bell System Tech. J.*, **27**, 379,623, 1948.

[She08] R. Shewmon. Coherent manipulations of trapped $^{88}Sr^+$ using the $4D_{5/2} \rightarrow 5S_{1/2}$ transition. B. S. thesis, Massachusetts Institute of Technology, 2008.

[SHKS01] M. Sawada, M. Higuchi, S. Kondo, and H. Saka. Characteristics of indium-tin-oxide/silver/indium-tin-oxide sandwich films and their application to simple-matrix liquid-crystal displays. *Jpn. J. Appl. Phys.*, **40**, 3332, 2001.

[Sho94] P. W. Shor. Algorithms for quantum computation: Discrete logarithms and factoring. In *Proceedings of the 35th Annual Symposium on the Foundations of Computer Science*, p. 124, 1994.

[Sho95] P. Shor. Scheme for reducing decoherence in quantum computer memory. *Phys. Rev. A*, **52**, R2493, 1995.

[SHO+06] D. Stick, W. K. Hensinger, S. Olmschenk, M. J. Madsen, K. Schwab, and C. Monroe. Ion trap in a semiconductor chip. *Nature Phys.*, **2**, 36, 2006.

[SI03] C. Simon and W. T. M. Irvine. Robust long-distance entanglement and a loophole-free bell test with ions and photons. *Phys. Rev. Lett.*, **91**, 110405, 2003.

[Sie86] A. E. Siegman. *Lasers.* University Science Books, 1986.

[SKHR+03] F. Schmidt-Kaler, H. Häffner, M. Riebe, S. Gulde, G. P. T. Lancaster, T. Deuschle, C. Becher, C. F. Roos, J. Eschner, and R. Blatt. Realization of the Cirac-Zoller controlled-NOT quantum gate. *Nature*, **422**, 408, 2003.

[SL00] A. M. Steane and D. M. Lucas. Quantum computing with trapped ions, atoms, and light. *Fortschritte der Physik*, **48**, 839, 2000.

[SM99] A. Sørensen and K. Mølmer. Quantum computation with ions in thermal motion. *Phys. Rev. Lett.*, **82**, 1971, 1999.

[SM00] A. Sørensen and K. Mølmer. Entanglement and quantum computation with ions in thermal motion. *Phys. Rev. A*, **62**, 022311, 2000.

[SM08] M. Saffman and K. Mølmer. Scaling the neutral-atom rydberg gate quantum computer by collective encoding in holmium atoms. *Phys. Rev. A*, **78**, 012336, 2008.

[Soi02] V. A. Soifer. *Methods of computer design of diffractive optical elements.* John Wiley & Sons, 2002.

[SOT97] T. A. Savard, K. M. O'Hara, and J. E. Thomas. Laser-noise induced heating in far-off resonance optical traps. *Phys. Rev. A*, **56**, R1095, 1997.

[Ste07] A. M. Steane. How to build a 300 bit, 1 giga-operation quantum computer. *Quant. Inf. Comput.*, **7**, 171, 2007.

[STTV07] J. Simon, H. Tanji, J. K. Thompson, and V. Vuletić. Interfacing collective atomic excitations and single photons. *Phys. Rev. Lett.*, **98**, 183601, 2007.

[SvdWCL04] A. S. Sørensen, C. H. van der Wal, L. I. Childress, and M. D. Lukin. Capacitive coupling of atomic systems to mesoscopic conductors. *Phys. Rev. Lett.*, **92**, 063601, 2004.

[TBZ05] L. Tian, R. Blatt, and P. Zoller. Scalable ion trap quantum computing without moving ions. *Eur. Phys. J. D*, **32**, 201, 2005.

[TKK+99] Q. A. Turchette, D. Kielpinski, B. E. King, D. Leibfried, D. M. Meekhof, C. J. Myatt, M. A. Rowe, C. A. Sackett, C. S. Wood, W. M. Itano, C. Monroe, and D. J. Wineland. Heating of trapped ions from the quantum ground state. *Phys. Rev. A*, **61**, 2000, 1999.

[TRBZ04] L. Tian, P. Rabl, R. Blatt, and P. Zoller. Interfacing quantum-optical and solid-state qubits. *Phys. Rev. Lett.*, **92**, 247902, 2004.

[Tur36] A. M. Turing. On computable numbers, with an application to the entscheidungsproblem. *Proc. London Math Soc.*, **42**, 230, 1936.

[TWK+98] Q. A. Turchette, C. S. Wood, B. E. King, C. J. Myatt, D. Leibfried, W. M. Itano, C. Monroe, and D. J. Wineland. Deterministic entanglement of two trapped ions. *Phys. Rev. Lett.*, **81**, 3631, 1998.

[TWMK93] S. Trajmar, S. Wang, K. F. Man, and M. A. Khakoo. Fluorescence of buckminsterfullerenes: UV emission of C_{60}^+ and C_{70}^+. http://trs-new.jpl.nasa.gov/dspace/handle/2014/34907, 1993.

[VC00] V. Vuletić and S. Chu. Laser cooling of atoms, ions, or molecules by coherent scattering. *Phys. Rev. Lett.*, **84**, 3787, 2000.

[VCB01] V. Vuletić, H. W. Chan, and A. T. Black. Three-dimensional cavity doppler cooling and cavity sideband cooling by coherent scattering. *Phys. Rev. A*, **64**, 033405, 2001.

[VCLB06] K. Vant, J. Chiaverini, W. Lybarger, and D. J. Berkeland. Photoionization of strontium for trapped-ion quantum information processing. arXiv:quant-ph/0607055v1, 2006.

[VSB+01] L. M. K. Vandersypen, M. Steffen, G. Breyta, C. S. Yannoni, R. Cleve, and I. L. Chuang. Experimental realization of shor's quantum factoring algorithm using nuclear magnetic resonance. *Nature*, **883**, 350, 2001.

[WDW78] D. J. Wineland, R. E. Drullinger, and F. L. Walls. Radiation-pressure cooling of bound resonant absorbers. *Phys. Rev. Lett.*, **78**, 1639, 1978.

[WEL+07] J. H. Wesenberg, R. J. Epstein, D. Leibfried, R. B. Blakestad, J. Britton, J. P. Home, W. M. Itano, J. D. Jost, E. Knill, C. Langer, R. Ozeri, S. Seidelin, and D. J. Wineland. Fluorescence during doppler cooling of a single trapped atom. *Phys. Rev. A*, **76**, 053416, 2007.

[WHS+06] M. Wilzbach, A. Haase, M. Schwarz, D. Heine, K. Wicker, X. Liu, K.-H. Brenner, S. Groth, T. Fernholz, B. Hessmo, and J. Schmiedmayer. Detecting neutral atoms on an atom chip. *Fortschritte der Physik*, **54**, 746, 2006.

[WMI+98a] D. J. Wineland, C. Monroe, W. M. Itano, B. E. King, D. Leibfried, D. M. Meekhof, C. Myatt, and C. Wood. Experimental primer on the trapped ion quantum computer. *Fortschritte der Physik*, **46**, 363, 1998.

[WMI+98b] D. J. Wineland, C. Monroe, W. M. Itano, D. Leibfried, B. E. King, and D. M. Meekhof. Experimental issues in coherent quantum-state manipulation of trapped atomic ions. *J. Res. Natl. Inst. Stand. Technol.*, **103**, 259, 1998.

[ZM05a] S. Zippilli and G. Morigi. Cooling trapped atoms in optical resonators. *Phys. Rev. Lett.*, **95**, 143001, 2005.

[ZM05b] S. Zippilli and G. Morigi. Mechanical effects of optical resonators on driven trapped atoms: ground-state cooling in a high finesse cavity. *Phys. Rev. A*, **72**, 053408, 2005.

Appendix A

Numerical solution of the master equation for $^{88}Sr^{+}$ in a cavity

The following is Mathematica 6.0.1 code for the numerical solution of the master equation for an $^{88}Sr^{+}$ ion in a cavity as described in Chapter 4.

Set up the equations of motion

```
(* fix the function ThreeJSymbol - it returns indeterminate when it should return zero *)
ThreeJ[x1_, x2_, x3_] := If[x1[[2]] + x2[[2]] + x3[[2]] == 0, ThreeJSymbol[x1, x2, x3], 0];

(* States are in the order
   01: S1/2,mJ=-1/2,NY=0,NZ=0
   02: S1/2,mJ=+1/2,NY=0,NZ=0
   03: P1/2,mJ=-1/2,NY=0,NZ=0
   04: P1/2,mJ=+1/2,NY=0,NZ=0
   05: D3/2,mJ=-3/2,NY=0,NZ=0
   06: D3/2,mJ=-1/2,NY=0,NZ=0
   07: D3/2,mJ=+1/2,NY=0,NZ=0
   08: D3/2,mJ=+3/2,NY=0,NZ=0
   09: S1/2,mJ=-1/2,NY=1,NZ=0
   10: S1/2,mJ=+1/2,NY=1,NZ=0
   11: D3/2,mJ=-3/2,NY=1,NZ=0
   12: D3/2,mJ=-1/2,NY=1,NZ=0
   13: D3/2,mJ=+1/2,NY=1,NZ=0
   14: D3/2,mJ=+3/2,NY=1,NZ=0
   15: S1/2,mJ=-1/2,NY=0,NZ=1
   16: S1/2,mJ=+1/2,NY=0,NZ=1
   17: D3/2,mJ=-3/2,NY=0,NZ=1
   18: D3/2,mJ=-1/2,NY=0,NZ=1
   19: D3/2,mJ=+1/2,NY=0,NZ=1
   20: D3/2,mJ=+3/2,NY=0,NZ=1
   21: S1/2,mJ=-1/2,NY=1,NZ=1
   22: S1/2,mJ=+1/2,NY=1,NZ=1
   23: D3/2,mJ=-3/2,NY=1,NZ=1
   24: D3/2,mJ=-1/2,NY=1,NZ=1
   25: D3/2,mJ=+1/2,NY=1,NZ=1
   26: D3/2,mJ=+3/2,NY=1,NZ=1
*)

Nstates = 26;
Llist = {0, 0, 1, 1, 2, 2, 2, 2, 0, 0, 2, 2, 2, 2, 0, 0, 2, 2, 2, 2, 0, 0, 2, 2, 2, 2};
mJlist = {-1/2, 1/2, -1/2, 1/2, -3/2, -1/2, 1/2, 3/2, -1/2, 1/2, -3/2, -1/2, 1/2,
   3/2, -1/2, 1/2, -3/2, -1/2, 1/2, 3/2, -1/2, 1/2, -3/2, -1/2, 1/2, 3/2};
Nylist = {0, 0, 0, 0, 0, 0, 0, 0, 1, 1, 1, 1, 1, 1, 0, 0, 0, 0, 0, 0, 1, 1, 1, 1, 1, 1};
Nzlist = {0, 0, 0, 0, 0, 0, 0, 0, 0, 0, 0, 0, 0, 0, 1, 1, 1, 1, 1, 1, 1, 1, 1, 1, 1, 1};

Sstates = Position[Llist, 0][[All, 1]];
Pstates = Position[Llist, 1][[All, 1]];
Dstates = Position[Llist, 2][[All, 1]];

(* Ranges of selected variables *)
assumptions = {APS ≥ 0, APD ≥ 0, κ ≥ 0, ΩSP ≥ 0, ΩDP ≥ 0, Ωy ≥ 0, Ωz ≥ 0, g ≥ 0};

(* Preliminary definitions and tests *)
Coeff[J_, mJ_, Jp_, mJp_, ϵM1_, ϵ0_, ϵP1_] :=
  (-1)^mJ * ((-1)^(-1) * ϵM1 * ThreeJ[{J, mJ}, {1, -1}, {Jp, -mJp}] + (-1)^(0) * ϵ0 * ThreeJ[{J, mJ},
      {1, 0}, {Jp, -mJp}] + (-1)^(-1) * ϵP1 * ThreeJ[{J, mJ}, {1, +1}, {Jp, -mJp}]);

Simplify[Sum[Abs[Coeff[1/2, mJ, 3/2, mJp, ϵM1, ϵ0, ϵP1]]^2,
   {mJ, -1/2, 1/2}, {mJp, -3/2, 3/2}], Abs[ϵM1]^2 + Abs[ϵ0]^2 + Abs[ϵP1]^2 = 1];
Sum[(Abs[Coeff[1/2, mJ, 3/2, mJp, 1, 0, 0]]^2 + Abs[Coeff[1/2, mJ, 3/2, mJp, 0, 1, 0]]^2 +
     Abs[Coeff[1/2, mJ, 3/2, mJp, 0, 0, 1]]^2) /. mJ → 1/2, {mJp, -3/2, 3/2}];

ΩFun[Ω_, J_, mJ_, Jp_, mJp_, ϵM1_, ϵ0_, ϵP1_] := Sqrt[3] * Ω * Coeff[J, mJ, Jp, mJp, ϵM1, ϵ0, ϵP1];
ΓFun[ALLp_, J_, mJ_, Jp_, mJp_] := 2 * ALLp * (Abs[Coeff[J, mJ, Jp, mJp, 1, 0, 0]]^2 +
     Abs[Coeff[J, mJ, Jp, mJp, 0, 1, 0]]^2 + Abs[Coeff[J, mJ, Jp, mJp, 0, 0, 1]]^2);
```

```
gFun[g_, mJ_, mJp_, μ_] := Switch[μ,
   "y", g * Abs[mJp - mJ] * Sqrt[(2 / 3) * (13 / 14)],
   "z", g * Abs[mJp + mJ] * Sqrt[(1 / 3) * (13 / 14)],
   _, 0
  ];

(* Hamiltonian *)
HA = ħ * Normal[
    Sum[(δSP + 2 * mJlist[[i]] * δB) * SparseArray[{i, i} → 1, {Nstates, Nstates}], {i, Sstates}] + Sum
      (2 / 3) * mJlist[[i]] * δB * SparseArray[{i, i} → 1, {Nstates, Nstates}], {i, Pstates}] + Sum[
      (δDP + (4 / 5) * mJlist[[i]] * δB) * SparseArray[{i, i} → 1, {Nstates, Nstates}], {i, Dstates}]
   ];
HC = ħ * Normal[Sum[-δC * (Nylist[[i]] + Nzlist[[i]]) *
      SparseArray[{i, i} → 1, {Nstates, Nstates}], {i, 1, Nstates}]];
HAC = ħ * Normal[Sum[KroneckerDelta[Nylist[[i]], 1] * KroneckerDelta[Nylist[[j]], 0] *
       KroneckerDelta[Nzlist[[i]], Nzlist[[j]]] * gFun[g, mJlist[[i]], mJlist[[j]], "y"] *
       SparseArray[{i, j} → 1, {Nstates, Nstates}], {i, Sstates}, {j, Pstates}] +
     Sum[Conjugate[KroneckerDelta[Nylist[[i]], 1] * KroneckerDelta[Nylist[[j]], 0] *
         KroneckerDelta[Nzlist[[i]], Nzlist[[j]]] * gFun[g, mJlist[[i]], mJlist[[j]], "y"]] *
       SparseArray[{j, i} → 1, {Nstates, Nstates}], {i, Sstates}, {j, Pstates}] +
     Sum[KroneckerDelta[Nylist[[i]], Nylist[[j]]] * KroneckerDelta[Nzlist[[i]], 1] *
       KroneckerDelta[Nzlist[[j]], 0] * gFun[g, mJlist[[i]], mJlist[[j]], "z"] *
       SparseArray[{i, j} → 1, {Nstates, Nstates}], {i, Sstates}, {j, Pstates}] +
     Sum[Conjugate[KroneckerDelta[Nylist[[i]], Nylist[[j]]] * KroneckerDelta[Nzlist[[i]], 1] *
         KroneckerDelta[Nzlist[[j]], 0] * gFun[g, mJlist[[i]], mJlist[[j]], "z"]] *
       SparseArray[{j, i} → 1, {Nstates, Nstates}], {i, Sstates}, {j, Pstates}]
   ];
HAL =
  ħ * Normal[(1 / 2) * Sum[KroneckerDelta[Nylist[[i]], Nylist[[j]]] * KroneckerDelta[Nzlist[[i]],
         Nzlist[[j]]] * ΩFun[ΩSP, 1 / 2, mJlist[[i]], 1 / 2, mJlist[[j]], ϵSPM1, ϵSP0, ϵSPP1] *
       SparseArray[{i, j} → 1, {Nstates, Nstates}], {i, Pstates}, {j, Sstates}] + (1 / 2) *
      Sum[Conjugate[KroneckerDelta[Nylist[[i]], Nylist[[j]]] * KroneckerDelta[Nzlist[[i]],
          Nzlist[[j]]] * ΩFun[ΩSP, 1 / 2, mJlist[[i]], 1 / 2, mJlist[[j]], ϵSPM1, ϵSP0, ϵSPP1]] *
       SparseArray[{j, i} → 1, {Nstates, Nstates}], {i, Pstates}, {j, Sstates}] +
     (1 / 2) * Sum[KroneckerDelta[Nylist[[i]], Nylist[[j]]] * KroneckerDelta[Nzlist[[i]],
         Nzlist[[j]]] * ΩFun[ΩDP, 1 / 2, mJlist[[i]], 3 / 2, mJlist[[j]], ϵDPM1, ϵDP0, ϵDPP1] *
       SparseArray[{i, j} → 1, {Nstates, Nstates}], {i, Pstates}, {j, Dstates}] + (1 / 2) *
      Sum[Conjugate[KroneckerDelta[Nylist[[i]], Nylist[[j]]] * KroneckerDelta[Nzlist[[i]],
          Nzlist[[j]]] * ΩFun[ΩDP, 1 / 2, mJlist[[i]], 3 / 2, mJlist[[j]], ϵDPM1, ϵDP0, ϵDPP1]] *
       SparseArray[{j, i} → 1, {Nstates, Nstates}], {i, Pstates}, {j, Dstates}]];
HCL = ħ * Normal[
    (1 / 2) * Ωy *
      Sum[KroneckerDelta[Llist[[i]], Llist[[j]]] * KroneckerDelta[mJlist[[i]], mJlist[[j]]] *
        KroneckerDelta[Nzlist[[i]], Nzlist[[j]]] * SparseArray[{i, j} → 1, {Nstates, Nstates}],
       {i, Position[Nylist, 1][[All, 1]]}, {j, Position[Nylist, 0][[All, 1]]}] +
     (1 / 2) * Conjugate[Ωy] * Sum[KroneckerDelta[Llist[[i]], Llist[[j]]] *
        KroneckerDelta[mJlist[[i]], mJlist[[j]]] * KroneckerDelta[Nzlist[[i]], Nzlist[[j]]] *
        SparseArray[{j, i} → 1, {Nstates, Nstates}],
       {i, Position[Nylist, 1][[All, 1]]}, {j, Position[Nylist, 0][[All, 1]]}] + (1 / 2) * Ωz *
      Sum[KroneckerDelta[Llist[[i]], Llist[[j]]] * KroneckerDelta[mJlist[[i]], mJlist[[j]]] *
        KroneckerDelta[Nylist[[i]], Nylist[[j]]] * SparseArray[{i, j} → 1, {Nstates, Nstates}],
       {i, Position[Nzlist, 1][[All, 1]]}, {j, Position[Nzlist, 0][[All, 1]]}] +
     (1 / 2) * Conjugate[Ωz] * Sum[KroneckerDelta[Llist[[i]], Llist[[j]]] *
        KroneckerDelta[mJlist[[i]], mJlist[[j]]] * KroneckerDelta[Nylist[[i]], Nylist[[j]]] *
        SparseArray[{j, i} → 1, {Nstates, Nstates}],
       {i, Position[Nzlist, 1][[All, 1]]}, {j, Position[Nzlist, 0][[All, 1]]}]
   ];
H = Evaluate[Simplify[HA + HC + HAC + HAL + HCL, assumptions]];

(* Louivillian *)
(* LS and LD take into account the laser linewidths and the jitter of the cavity lock:
   δS/(2π) =
 (FWHM 422 nm laser) + (FWHM cavity jitter) and δD/(2π) = (FWHM 1092 nm laser) *)
LAPS = Flatten[Table[KroneckerDelta[Nylist[[i]], Nylist[[j]]] * KroneckerDelta[
```

```
      Nzlist[[i]], Nzlist[[j]]] * Sqrt[ΓFun[APS, 1 / 2, mJlist[[i]], 1 / 2, mJlist[[j]]]] *
     Normal[SparseArray[{j, i} → 1, {Nstates, Nstates}]], {i, Pstates}, {j, Sstates}], 1];
LAPD = Flatten[Table[KroneckerDelta[Nylist[[i]], Nylist[[j]]] * KroneckerDelta[
      Nzlist[[i]], Nzlist[[j]]] * Sqrt[ΓFun[APD, 1 / 2, mJlist[[i]], 3 / 2, mJlist[[j]]]] *
     Normal[SparseArray[{j, i} → 1, {Nstates, Nstates}]], {i, Pstates}, {j, Dstates}], 1];
Lκy = Flatten[Table[KroneckerDelta[Llist[[i]], Llist[[j]]] *
     KroneckerDelta[mJlist[[i]], mJlist[[j]]] * KroneckerDelta[Nzlist[[i]], Nzlist[[j]]] *
     Sqrt[κ] * Normal[SparseArray[{j, i} → 1, {Nstates, Nstates}]],
    {i, Position[Nylist, 1][[All, 1]]}, {j, Position[Nylist, 0][[All, 1]]}], 1];
Lκz = Flatten[Table[KroneckerDelta[Llist[[i]], Llist[[j]]] *
     KroneckerDelta[mJlist[[i]], mJlist[[j]]] * KroneckerDelta[Nylist[[i]], Nylist[[j]]] *
     Sqrt[κ] * Normal[SparseArray[{j, i} → 1, {Nstates, Nstates}]],
    {i, Position[Nzlist, 1][[All, 1]]}, {j, Position[Nzlist, 0][[All, 1]]}], 1];
LS = Sqrt[δS] * Table[Normal[SparseArray[{i, i} → 1 - Nylist[[i]] - Nzlist[[i]],
      {Nstates, Nstates}]], {i, Sstates}];
LD = Sqrt[δD] * Table[Normal[SparseArray[{i, i} → 1, {Nstates, Nstates}]], {i, Dstates}];
L = Complement[Flatten[{LAPS, LAPD, Lκy, Lκz, LS, LD}, 1], {Table[0, {Nstates}, {Nstates}]}];

(* Explicit density matrix *)
SubscriptFun[i_, j_, Nstates_] := Module[{NsubscriptDigits, is, js},
   NsubscriptDigits = StringLength[ToString[Nstates]];
   is = ToString[i];
   While[StringLength[is] < NsubscriptDigits, is = "0" <> is];
   js = ToString[j];
   While[StringLength[js] < NsubscriptDigits, js = "0" <> js];
   is <> js
  ];
ρ = Table[Which[
    i == j, ToExpression["ρ" <> SubscriptFun[i, j, Nstates]],
    i < j, ToExpression[
     "ρ" <> SubscriptFun[i, j, Nstates] <> "R+i*ρ" <> SubscriptFun[i, j, Nstates] <> "I"],
    i > j, ToExpression["ρ" <> SubscriptFun[j, i, Nstates] <>
      "R-i*ρ" <> SubscriptFun[j, i, Nstates] <> "I"]
   ],
   {i, 1, Nstates}, {j, 1, Nstates}];

(* Equations of motion *)
ρDOTspont = Evaluate[Simplify[
    Sum[L[[i]].ρ.ConjugateTranspose[L[[i]]] - (ConjugateTranspose[L[[i]]].L[[i]].ρ +
        ρ.ConjugateTranspose[L[[i]]].L[[i]]) / 2, {i, 1, Length[L]}]
    , assumptions]];
ρDOT = Evaluate[Simplify[(1 / (i * ħ)) * (H.ρ - ρ.H) + ρDOTspont, assumptions]];
```

Construct a function which solves for the steady state density matrix by numerical function minimization

```
(* Here are the parameters which are allowed to be complex *)
complex = {ϵSPM1, ϵSP0, ϵSPP1, ϵDPM1, ϵDP0, ϵDPP1};

realEquations = {};
Do[
  If[i ≥ j, AppendTo[realEquations, ComplexExpand[Re[ρDOT[[i, j]]], complex]]]
  , {i, 1, Nstates}, {j, 1, Nstates}];
imaginaryEquations = {};
Do[
  If[i > j, AppendTo[imaginaryEquations, ComplexExpand[Im[ρDOT[[i, j]]], complex]]]
  , {i, 1, Nstates}, {j, 1, Nstates}];
normalizationEquation =
  Sum[ToExpression["ρ" <> SubscriptFun[i, i, Nstates]], {i, 1, Nstates}] == 1;
constraintEquations = Table[0 ≤ ToExpression["ρ" <> SubscriptFun[i, i, Nstates]] ≤ 1,
   {i, 1, Nstates}];
equations[ΩSP_, ϵSPM1_, ϵSP0_, ϵSPP1_, δSP_, ΩDP_, ϵDPM1_, ϵDP0_,
   ϵDPP1_, δDP_, δB_, Ωy_, Ωz_, δC_, g_, APS_, APD_, κ_, δS_, δD_] :=
  Evaluate[Flatten[{Sum[realEquations[[i]]^2, {i, 1, Length[realEquations]}] +
      Sum[imaginaryEquations[[i]]^2, {i, 1, Length[imaginaryEquations]}],
     normalizationEquation, constraintEquations}]];

VariablesAndGuesses[ρ_] := Module[{ρv},
   ρv = Variables[ρ];
   Table[{ρv[[i]], If[ToString[ρv[[i]]] == "ρ0101" || ToString[ρv[[i]]] == "ρ0202", 1/2, 0]},
    {i, 1, Length[ρv]}]
  ];

(* Solve the equations *)
ρSS[ΩSP_, ϵSPM1_, ϵSP0_, ϵSPP1_, δSP_, ΩDP_, ϵDPM1_,
   ϵDP0_, ϵDPP1_, δDP_, δB_, Ωy_, Ωz_, δC_, g_, APS_, APD_, κ_, δS_, δD_] :=
  FindMinimum[equations[ΩSP, ϵSPM1, ϵSP0, ϵSPP1, δSP, ΩDP, ϵDPM1, ϵDP0, ϵDPP1, δDP,
     δB, Ωy, Ωz, δC, g, APS, APD, κ, δS, δD], VariablesAndGuesses[ρ], AccuracyGoal → 12,
    PrecisionGoal → 12, WorkingPrecision → 15, MaxIterations → 100][[2]];
```

Reproduce curve A from Berkeland' s paper about dark states, using g = 0, to verify that the Sr is behaving properly

```
(* Total decay rate *)
γ = 127*^6;

(* x polarization *)
εXM1 = 1 / Sqrt[2];
εX0 = 0;
εXP1 = -1 / Sqrt[2];

(* Arbitrary polarization in the x-z plane at angle θBE from the z-axis *)
εARBM1[θBE_] := Sin[θBE] / Sqrt[2];
εARB0[θBE_] := Cos[θBE];
εARBP1[θBE_] := -Sin[θBE] / Sqrt[2];

(* Berkeland curve A *)
t1 = AbsoluteTime[];
Plot[(ρ0303 + ρ0404) /. ρSS[(Sqrt[2] / 5) * γ, εXM1, εX0, εXP1, γ * normilizedδSP,
   (Sqrt[2] / 5) * γ, εXM1, εX0, εXP1, γ / 2, 0.1 * γ, 0, 0, 0, 0, (13 / 14) * γ, (1 / 14) * γ, γ],
 {normilizedδSP, -2, 1}, PlotRange → {All, All}, PlotPoints → 25, MaxRecursion → 3]
Print["Computation time = " <> ToString[AbsoluteTime[] - t1] <> " s"];
```

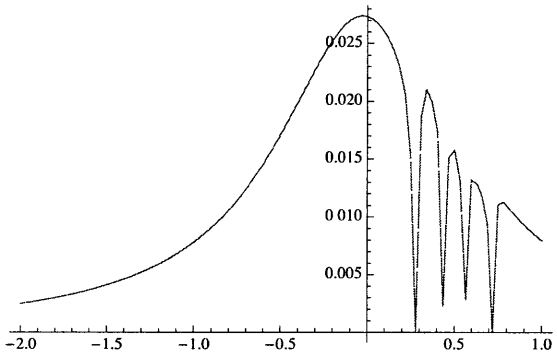

Computation time = 5032.705846 s

Plot the cavity transmission, using g = 0, to verify that the cavity is behaving properly

```
κP = 2 * π * 164.*^3;
gP = 0.;
ΩP = 2 * π * 1.*^3;

t1 = AbsoluteTime[];
Plot[
 (κP / 2)^2 / (ΩP / 2)^2 * Sum[(Nylist[[i]] + Nzlist[[i]]) * ToExpression["ρ" <> SubscriptFun[i, i, Nstates]],
    {i, 1, Nstates}] /. ρSS[0, ϵXM1, ϵX0, ϵXP1, -γ / 2, (Sqrt[2] / 5) * γ, ϵXM1, ϵX0,
   ϵXP1, γ / 2, 0.1 * γ, 0, ΩP, 2 * π * 1*^3 * detuning, gP, (13 / 14) * γ, (1 / 14) * γ, κP],
 {detuning, -500, 500}, PlotRange → {All, All}, PlotPoints → 25, MaxRecursion → 2]
Print["Computation time = " <> ToString[AbsoluteTime[] - t1] <> " s"];
```

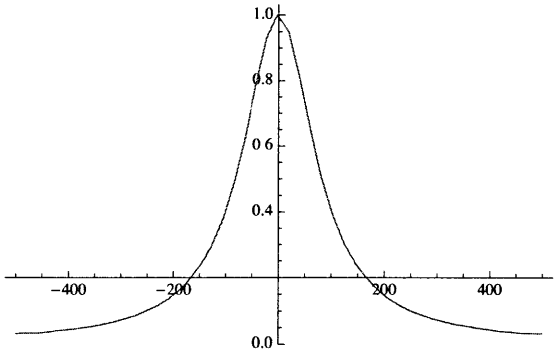

Computation time = 4128.695114 s

Calculate the cavity transmission

```
(* Total decay rate *)
γ = 127*^6;

(* x polarization *)
εXM1 = 1 / Sqrt[2];
εX0 = 0;
εXP1 = -1 / Sqrt[2];

(* z polarization *)
εZM1 = 0;
εZ0 = 1;
εZP1 = 0;

(* other parameters *)
κP = 2 * π * 164.*^3;
gP = 2 * π * 460.*^3;
ΩP = 2 * π * 1.*^3;
δP = 0;

(* cavity transmission with g = 0 *)
(κP / 2)^2 / (ΩP / 2)^2 * Sum[(Nylist[[i]] + Nzlist[[i]]) * ToExpression["ρ" <> SubscriptFun[i, i, Nstates]],
   {i, 1, Nstates}] /. ρSS[0, εXM1, εX0, εXP1, -γ / 2, (Sqrt[2] / 5) * γ, εXM1,
  εX0, εXP1, γ / 2, 0.1 * γ, 0, ΩP, δP, 0 * gP, (13 / 14) * γ, (1 / 14) * γ, κP, 0, 0]
```

```
1.00008
```

```
(* cavity transmission with g > 0,
but with the spontaneous decay rate to the D state set equal to zero *)
(κP / 2)^2 / (ΩP / 2)^2 * Sum[(Nylist[[i]] + Nzlist[[i]]) * ToExpression["ρ" <> SubscriptFun[i, i, Nstates]],
   {i, 1, Nstates}] /. ρSS[0, εZM1, εZ0, εZP1, 0, (Sqrt[2] / 5) * γ, εXM1,
  εX0, εXP1, γ / 2, 0.1 * γ, 0, ΩP, δP, gP, (13 / 14) * γ, 0 * (1 / 14) * γ, κP, 0, 0]
```

```
0.852259
```

```
(* cavity transmission with g > 0 and including spontaneous decay to the D state *)
(κP / 2)^2 / (ΩP / 2)^2 * Sum[(Nylist[[i]] + Nzlist[[i]]) * ToExpression["ρ" <> SubscriptFun[i, i, Nstates]],
   {i, 1, Nstates}] /. ρSS[0, εZM1, εZ0, εZP1, 0, (Sqrt[2] / 5) * γ, εXM1,
  εX0, εXP1, γ / 2, 0.1 * γ, 0, ΩP, δP, gP, (13 / 14) * γ, (1 / 14) * γ, κP, 0, 0]
```

```
0.86171
```

```
(* cavity transmission for a two-level atom *)
analyticTransmission[ΩA_, ΩC_, g_, δA_, δC_, κ_, Γ_] := Abs[ κ/(2*(δC+i κ/2)) / (1 - g^2/((δA+i Γ/2)(δC+i κ/2))) ]^2;
```

```
analyticTransmission[0, ΩP, gP / (Sqrt[3]), 0, 0, κP, (13 / 14) * γ]
```

```
0.839125
```

OK; the extra levels only raise the cavity transmission on resonance from 0.84 to 0.86

Calculate the cooperativity

```
(* Fundamental constants, SI units *)
e = 1.60*^-19;
m = 9.11*^-31;
c = 3*^8;
hbar = 1.05*^-34;
bohrMagneton = (e * hbar) / (2 * m);

(* Total decay rate of the P states *)
γ = 127*^6;

(* Transition parameters *)
BLUEfreq = 2 * Pi * c / 422*^-9;
BLUEdecay = (13 / 14) * γ;
IRfreq = 2 * Pi * c / 1092*^-9;
IRdecay = (1 / 14) * γ;

(* Magnetic field, T *)
Bfield = 4.1*^-4; (* T *)
δBfield = Bfield * bohrMagneton / hbar;
Print["δB = " <> ToString[δBfield / γ] <> " γ"];

(* Blue power *)
BLUEpow = 1*^-6; (* W *)
BLUEwaist = 15*^-6; (* m *)
ΩBLUE = Sqrt[(12 * c^2 * BLUEdecay * BLUEpow) / (hbar * BLUEwaist^2 * BLUEfreq^3)];
Print["ΩSP = " <> ToString[ΩBLUE / γ] <> " γ"];

(* IR power *)
IRpow = 10*^-6; (* W *)
IRwaist = 30*^-6; (* m *)
ΩIR = Sqrt[(12 * c^2 * IRdecay * IRpow) / (hbar * IRwaist^2 * IRfreq^3)];
Print["ΩDP = " <> ToString[ΩIR / γ] <> " γ"];
```

$\delta B = 0.283499\,\gamma$

$\Omega SP = 1.93664\,\gamma$

$\Omega DP = 3.53519\,\gamma$

```
(* other parameters *)
κP = 2 * π * 117.*^3;
gP = 2 * π * 460.*^3;
ΩP = 2 * π * 1.*^6;
δP = 0;

(* solution *)
sol = ρSS[ΩP, ϵZM1, ϵZ0, ϵZP1, -5 * γ / 2, 3.4 * γ, ϵXM1,
   ϵX0, ϵXP1, γ / 2, 0.26 * γ, 0, 0, δP, gP, (13 / 14) * γ, (1 / 14) * γ, κP, 0, 0];

(* populations *)
Table[ToExpression["ρ" <> SubscriptFun[i, i, Nstates]], {i, 1, Nstates}] /. sol

(* cooperativity *)
κP * Sum[(Nylist[[i]] + Nzlist[[i]]) * ToExpression["ρ" <> SubscriptFun[i, i, Nstates]], {i, 1,
     Nstates}] / (γ * Sum[ToExpression["ρ" <> SubscriptFun[i, i, Nstates]], {i, Pstates}]) /. sol
```

Out[84]= {0.582263, 0.416217, 0.0000374207, 0.0000374207, 0.0000215599, 0.0000550871, 0.0000365096, 0.0000196823, 3.2686×10^{-7}, 3.25456×10^{-7}, 3.35614×10^{-7}, 3.356×10^{-7}, 3.35604×10^{-7}, 3.35607×10^{-7}, 0.000655863, 0.000652403, 3.35614×10^{-7}, 3.356×10^{-7}, 3.35604×10^{-7}, 3.35607×10^{-7}, 1.7004×10^{-7}, 1.69691×10^{-7}, 2.27106×10^{-7}, 2.27102×10^{-7}, 2.27103×10^{-7}, 2.27105×10^{-7}}

Out[81]= 0.101636

This result seems to be stable over a couple orders of magnitude in ΩP, so I'll buy it

In[82]:=
$$\frac{4 * (gP / Sqrt[3])^2}{\kappa P * \gamma}$$

Out[82]= 0.119301

OK; (cooperativity of strontium)/(cooperativity of a two-level atom) = 0.102/0.119 = 0.86

Calculate the cooperativity, including the effect of non - zero laser linewidths

```
(* laser linewidths *)
δSS = 2 * π * 20.*^3;
δDD = 2 * π * 20.*^3;

(* solution *)
sol = ρSS[ΩP, εZM1, εZ0, εZP1, -γ / 2, 3.4 * γ, εXM1, εX0,
   εXP1, γ / 2, 0.26 * γ, 0, 0, δP, gP, (13 / 14) * γ, (1 / 14) * γ, κP, δSS, δDD];

(* populations *)
Table[ToExpression["ρ" <> SubscriptFun[i, i, Nstates]], {i, 1, Nstates}] /. sol

(* cooperativity *)
κP * Sum[(Nylist[[i]] + Nzlist[[i]]) * ToExpression["ρ" <> SubscriptFun[i, i, Nstates]], {i, 1,
     Nstates}] / (γ * Sum[ToExpression["ρ" <> SubscriptFun[i, i, Nstates]], {i, Pstates}]) /. sol
```

Out[92] $\{0.303001, 0.692548, 0.000120059, 0.000120055, 0.000189401, 0.000271543, 0.000134939,$
$0.00015957, 7.58644 \times 10^{-7}, 3.2932 \times 10^{-7}, 1.52622 \times 10^{-7}, 1.52617 \times 10^{-7}, 1.52617 \times 10^{-7},$
$1.52615 \times 10^{-7}, 0.00169473, 0.00175781, 1.52622 \times 10^{-7}, 1.52617 \times 10^{-7}, 1.52617 \times 10^{-7}, 1.52615 \times 10^{-7},$
$5.74506 \times 10^{-8}, 6.23726 \times 10^{-8}, 9.80359 \times 10^{-8}, 9.8035 \times 10^{-8}, 9.80348 \times 10^{-8}, 9.80344 \times 10^{-8}\}$

Out[93] 0.0833109

OK; (cooperativity of strontium including laser linewidths)/(cooperativity of a two-level atom) = 0.083/0.119 = 0.70